Deformation Mechanisms of Nanocrystalline Nickel Studied by In-situ X-Ray Diffraction

THÈSE N^{O} 4158 (2008)

PRÉSENTÉE LE 28 JUILLET 2008
À LA FACULTE SCIENCES ET TECHNIQUES DE L'INGÉNIEUR
LABORATOIRE DE MÉTALLURGIE MÉCANIQUE
PROGRAMME DOCTORAL EN SCIENCE ET GÉNIE DES MATÉRIAUX

ÉCOLE POLYTECHNIQUE FÉDÉRALE DE LAUSANNE

POUR L'OBTENTION DU GRADE DE DOCTEUR ÈS SCIENCES

PAR

Stefan BRANDSTETTER

M. Eng. in materials science, Montanuniversität Leoben, Autriche
et de nationalité autrichienne

acceptée sur proposition du jury:

Prof. H. Hofmann, président du jury
Prof. H. Van Swygenhoven, directrice de thèse
Prof. A. Mortensen, rapporteur
Prof. R. Pippan, rapporteur
Prof. G. Saada, rapporteur

ÉCOLE POLYTECHNIQUE
FÉDÉRALE DE LAUSANNE

Suisse
2008

Abstract

Materials consisting of grains or crystallites with sizes below a hundred nanometers have exhibited unique physical and mechanical properties in comparison to their coarse-grained counterparts. As a result, considerable effort has been put into uncovering the new deformation mechanisms that give rise to this outstanding response of nanocrystalline materials. Moreover, the production of nanocrystalline materials of reasonable sizes for structural applications remains a challenge. However, the size limitation is of no issue for their present application in the growing field of MEMS and NEMS devices. Ultimately, the reliability and lifetime prediction of these devices will depend on the accurate knowledge of their mechanical response.

This dissertation addresses experimental and simulation procedures used to understand the fundamental deformation mechanisms operating in bulk nanocrystalline Nickel. Recent results from simulations suggested dislocations as a dominant carrier of plasticity in nanocrystalline materials. In contrast to coarse-grained materials, these dislocations are nucleated at grain boundaries and, after propagating through the nano grains, they are absorbed there as well. Deformation experiments during in-situ X-ray diffraction strengthened the predicted outcome from simulation but many open questions remained.

Within this thesis a more extensive range of in-situ testing experiments are performed that aim to systematically investigate the nanocrystalline deformation mechanism in terms of both temperature and external loading conditions. The development of a low temperature tensile test set-up allowed to study temperature dependent behavior and revealed that dislocation activity in nanocrystalline Nickel is a strongly thermally activated process where propagation of dislocation seems to be as important as nucleation from dislocations at the grain boundary. This finding is further supported by strain-dip tests, which revealed that pinning points strongly influence dislocation propagation.

Nanocrystalline Nickel exhibits, in its as prepared state, large internal stress variations. These stress variations and the small grain size are most likely responsible for the microplastic regime characterized by an extended macroscopic strain, making the usage of the classical definition of yield questionable. Furthermore it could be shown that upon annealing, which reduces the samples’ internal stress, this extended microplastic regime was observed to be less pronounced. To study the structural stability of nanocrystalline Nickel at large strains, the material was investigated by compression experiments, revealing no changes in mean grain size. Furthermore, the three dimensional atomic probe technique was utilized for localizing impurity concentrations. The program was rounded by calculating diffraction peaks from simulated nanocrystalline structures with a single type of defect. This allowed investigating the characteristics of the diffraction pattern of nanocrystalline systems in a bottom up approach.

Finally, the results of the thesis are discussed in terms of a thermally activated deformation mechanism that involves the nucleation, propagation and absorption of dislocation within the nanocrystalline environment.

KEYWORDS: X-ray diffraction (XRD), Mechanical properties, Nanocrystalline materials, Nickel, Low temperature deformation, Molecular dynamics

Kurzfassung

Metallische Materialien mit Korngrössen kleiner als hundert Nanometer besitzen einzigartige physikalische und mechanische Eigenschaften verglichen mit ihrem grobkörnigen Pendant. Diese aussergewöhnlichen Eigenschaften von sogenannten nanokristallinen Materialen gaben unter anderem den Anstoss, deren Verformungsmechanismen zu erforschen. Für die strukturelle Anwendung dieser Materialien würde eine industrielle Herstellung von grossen Teilen, welche bis jetzt eine unlösbare Aufgabe ist, notwendig sein. Jedoch stellt dies bei dem derzeitigen Anwendungsbereich der MEMS und NEMS Technologie kein Problem dar. Die Zuverlässigkeit solcher technologisch wichtiger Elemente wird letztendlich davon abhängen ob es möglich ist, deren Verformungsverhalten genau zu beschreiben.

Diese Doktorarbeit beschäftigt sich mit dem grundlegenden Verformungsverhalten von nanokristallinem Nickel und verwendet sowohl Experimente als auch Simulationen, um tiefere Einblicke in die elementaren Verformungsmechanismen zu gewinnen. Neueste Simulationserkenntnisse ergaben, dass die für grobkörnige Materialien übliche Versetzungsbewegung, entgegen ursprünglichen Annnahmen, auch bei nanokristallinen Materialien massgebend an deren Verformung ist. Jedoch werden diese Versetzungen, nicht wie im grobkörnigen Material üblich innerhalb des Korns erzeugt, sondern an deren Korngrenzen. Diese erzeugten Versetzungen durchwandern das Korn und werden letztendlich an der gegenüberliegenden Korngrenze absorbiert. Verformungsexperimente mit simultanen Röntgenbeugungsuntersuchungen haben die oben genannten Simulationsergebnisse erhärtet, konnten jedoch bei weitem nicht alle Fragen beantworten.

Mit systematischen Untersuchungen konnte dazu beigetragen werden, den Einfluss von Temperatur und Ladeabfolge auf die Verformung von nanokristallinem Nickel zu verstehen. Die Entwicklung einer Zugversuchsmaschine für Tieftemperatur ermöglichte temperaturabhängige Untersuchungen von Werkstoffen. Damit konnte gezeigt werden, dass die Versetzungsbewegung in nanokristallinen Materialien stark von der Temperatur beeinflusst ist und die Bewegung zumindest gleichbedeutend wie deren Erzeugung ist. Auch sogenannte Dehnungsverringerungstests lieferten mehrere Anzeichen daraufhin, dass die von Haftpunkten kontrollierte Versetzungsbewegung bei der Verformung massgebend ist.

Nanokristallines Nickel besitzt in seinem Lieferzustand hohe Eigenspannungen, welche in Verbindung mit der geringen Korngrösse, höchstwahrscheinlich die Hauptursachen für einen ausgeprägten mikroplastischen Bereich sind. Dieser Bereich ist durch eine ausgedehnte makroskopische Dehnung charakterisiert, weshalb eine exakte Definition der Streckgrenze unzulänglich ist. Des Weiteren konnte noch gezeigt werden, dass im angelassenen Zustand dieser microplastische Bereich stark verringert ist. Nanokristallines Nickel bricht im Zugversuch nach nur geringer plastischer Dehnung. Um einen höhere plastische Umformung zu studieren wurden Kompressionsversuche durchgeführt, welche zeigten, dass keine Kornvergröberung statt fand. Weiters wurden an nanokristallinem Nickel Atomsondenmessungen bewerkstelligt, die dazu dienten, Verunreinigungen zu lokalisieren und quantifizieren. Um die Einflüsse von speziellen Kristallfehlern auf das Röntgenbeugungsspektrum zu beschreiben, wurde es von mehreren, eigens dafür konstruierten, fehlerbehafteten dreidimensionalen Atomkonfigurationen berechnet.

Am Ende dieser Arbeit werden die gewonnen Ergebnisse in Form eines thermisch aktivierten Verformungsmechanismus diskutiert, welcher die Erzeugung, die Fortbewegung und die Absorption von Versetzungen in der nanokristallinen Umgebung beinhaltet.

STICHWÖRTER: Röntgenbeugung, mechanische Eigenschaften, nanokristalline Materialien, Nickel, Tieftemperaturverformung, Molekulardynamik

List of Abbreviations

3DAP	3-dimensional atom probe
CG	Coarse-grained
ED	Electrodeposited
EDM	Electrical-discharge machining
FCC	Faced-centered cubic
FIM	Field ion microscope
GB	Grain boundary
HCP	Hexagonal close-packed
HP	Hall-Petch
HPT	High-pressure torsion
HREM	High resolution transmission electron microscopy
LT	Low temperature
LED	Light-emitting diode
MCP	Micro channel plate
MEMS	Micro-Electro-Mechanical Systems
MS beam line	Materials science beam line
MTM	Micro tensile-test machine
NC	Nanocrystalline
P-VII	Pearson-VII
PID controller	Proportional-integral-derivative controller
PSI	Paul Scherrer Institut
RMS	Root-mean-square
RT	Room temperature
SEM	Scanning electron microscope
SLS	Swiss light source
TEM	Transmission electron microscope
UFG	Ultra fine grained
UTS	Ultimate tensile strength
WH	Williamson-Hall
XRD	X-ray diffraction

Table of contents

ABSTRACT .... **I**

KURZFASSUNG .... **III**

LIST OF ABBREVIATIONS .... **V**

TABLE OF CONTENTS .... **VII**

1. INTRODUCTION **1**

- 1.1. BACKGROUND 1
  - *1.1.1. Influence of grain size and microstructure 2*
  - *1.1.2. Deformation processes in nanocrystalline materials 3*
  - *1.1.3. Proposed deformation models 6*
- 1.2. RESEARCH OUTLINE 8

2. EXPERIMENTAL AND TECHNICAL DETAILS **11**

- 2.1. MATERIALS DESCRIPTION 11
  - *2.1.1. Nanocrystalline-electrodeposited Nickel 11*
  - *2.1.2. Ultra fine-grained Nickel 13*
  - *2.1.3. Specimen preparation 14*
- 2.2. MECHANICAL TESTING 16
  - *2.2.1. Tensile testing 16*
  - *2.2.2. Low Temperature Set-up 26*
  - *2.2.3. Compression testing 31*
- 2.3. X-RAY POWDER DIFFRACTION 35
  - *2.3.1. General 35*
  - *2.3.2. X-Ray sources 35*
  - *2.3.3. Experimental set-up 36*
  - *2.3.4. Data treatment 41*
  - *2.3.5. Extracting structural parameters 43*
- 2.4. 3-DIMENSIONAL ATOM PROBE 49
  - *2.4.1. FIM 49*
  - *2.4.2. 3DAP 50*
- 2.5. SIMULATED DIFFRACTION PATTERN 52
  - *2.5.1. Molecular dynamics (general) 52*
  - *2.5.2. Sample construction 52*
  - *2.5.3. moldyPSI 53*
  - *2.5.4. Deforming computational samples 54*
  - *2.5.5. Calculating XRD diffraction pattern 54*
  - *2.5.6. Calculating internal stress 54*

3. RESULTS **57**

- 3.1. PLASTIC DEFORMATION OF NANOCRYSTALLINE NICKEL 57
  - *3.1.1. Load-unload cycles in the microplastic regime 59*
  - *3.1.2. Influence of waiting time between two loading cycles 64*
  - *3.1.3. Load-unload cycles in the transient region 67*
  - *3.1.4. Effect of pre-annealing 72*
  - *3.1.5. Summary 79*
- 3.2. TEMPERATURE INFLUENCE ON THE DEFORMATION BEHAVIOR 80
  - *3.2.1. Multiple load-unload cycles at 180K 80*
  - *3.2.2. Single load-unload cycles at LT with subsequent load-unload at RT 85*
  - *3.2.3. Load-unload cycles in the microplastic regime at low temperature 87*
  - *3.2.4. Loading cycles on UFG-Nickel 92*
  - *3.2.5. Tensile failure of nanocrystalline Nickel 94*

3.2.6. Summary 95

3.3. TRANSIENT MECHANICAL TEST 96

3.3.1. Separation of internal and effective stresses 96

3.3.2. Activation volume measurements 98

3.3.3. Summary 99

3.4. COMPRESSION RESULTS 100

3.4.1. Load-unload cycles 100

3.4.2. Stress relaxation test 104

3.4.3. Creep test 105

3.4.4. Summary 107

3.5. XRD CALCULATION PLUS WILLIAMSON-HALL ANALYSIS 109

3.5.1. Introducing dislocation defects 109

3.5.2. Introducing twin defects 112

3.5.3. X-ray calculations from MD simulation cells 112

3.5.4. WH anisotropy from calculated spectra 114

3.5.5. Summary 120

3.6. 3D ATOM PROBE INVESTIGATIONS 122

3.6.1. Impurities in as prepared material 123

3.6.2. Impurities in deformed material 127

3.6.3. Impurities in material annealed at 140ºC 128

3.6.4. Impurities material annealed at 180ºC 128

3.6.5. Summary 129

4. DISCUSSION 131

4.1. STRESSES IN POLYCRYSTALLINE MATERIALS 131

4.1.1. Relation between internal stresses and X-ray peak parameters: unloaded sample 133

4.1.2. Relation between internal stresses and X-ray peak parameters: during loading 135

4.1.3. Influence of dislocations and twins on the X-ray profile: Calculations from atomistic configurations 139

4.2. THE XRD VIEW ON DEFORMATION REGIMES 142

4.2.1. Microplastic regime 142

4.2.2. Macroplastic regime 150

4.2.3. Summary 157

4.3. DEFORMATION MECHANISMS: A VIEW PROVIDED BY TRANSIENT TEST 159

4.3.1. Separation of athermal and thermal stress component with Dip tests 159

4.3.2. Elaborating the activation volume with successive relaxations 161

4.4. DEFORMATION BEHAVIOR: A COMBINED VIEW 163

5. SUMMARY 167

6. OUTLOOK 169

APPENDIX A 171

DISLOCATION RESPONSE TO THERMAL AND ATHERMAL STRESSES 171

APPENDIX B 178

GRAIN SIZE DISTRIBUTIONS 178

APPENDIX C 179

DIFFERENT SURFACES OF NANOCRYSTALLINE NICKEL 179

REFERENCES 183

LIST OF PUBLICATIONS 193

ACKNOWLEDGEMENTS 194

CURRICULUM VITAE 195

1. Introduction

In the beginning of the twenty-first century, the iPod generation calls their music player “nano” to be progressive and modern. However, already 50 years ago the science community anticipated the great possibilities of materials with a length scales close to the atomic distances [1]. Subsequently, structures with sizes of 10^{-9} meters had been named according to their SI (Système International d'Unités) definition, nano. This word has then been utilized for a wide range of research in the last decades. One of them is the investigation of metallic materials.

The outstanding properties of nanocrystalline (NC) materials was first pointed out by Gleiter [2] in 1989. Since them, a great amount of research has been carried out in this field. In the beginning, the NC regime covered various types of materials containing features with sizes below one micrometer. Nowadays the NC regime addresses only those materials for which the grain size is below 100nm. Materials with grain sizes between 100nm and one micrometer are termed ultra fine-grained (UFG).

Strong interest in nano-structured materials arose with the development of Micro-Electro-Mechanical Systems (MEMS). These MEMS are an integration of mechanical elements, sensors, actuators, and electronics on a common chip technology. If in MEMS structures metals are used, they are applied through different adsorption processes, which often result in a NC-structure. MEMS are an enabling technology allowing the development of smart products, enhancing the computational ability of microelectronics with the perception and control capabilities of microsensors and microactuators and expanding the space of possible designs and applications. In order to employ such actuators and sensors the underlying mechanical principles of utilized NC-materials have to be understood. The interest in the deformation behavior of NC materials is also evident by more than 500 published papers dealing with this field [3].

1.1. Background

Before starting with NC structures, a short essay is given on the deformation of faced centered cubic (FCC) metals. It is well established that single crystal FCC materials deform via slip events carried by dislocations. The stress that the dislocation feels on the slip plane in the slip direction is called the lattice resistance. This resistance is 10^{-5} times lower than the shear modulus [4] and independent of the dislocation character, screw or edge. Assuming that the applied stress is higher than the lattice resistance, the movement of a dislocation is controlled by intersections with statistically stored dislocations. If the grain is in a multi-slip-orientation, forest hardening will be dominating in the beginning of the plastic deformation. For further reading on basic concepts of dislocations and their properties the author refers to [5, 6].

In a very simple approach, these basic principles are also valid if the material is built of many crystallites, i.e. a polycrystalline aggregate. In such an agglomerate of grains, the present grain boundaries (GBs) serve as obstacles and hinder, additionally to the forest dislocations, the easy slip of a dislocation. Moreover, during deformation the materials anisotropy cause incompatibilities at the GBs [7, 8] resulting in stress fields which can as well influence the easy slip of a dislocation. In an alloy, additional obstacles like precipitates or phase boundaries can be present and hinder the dislocation motion.

1.1.1. Influence of grain size and microstructure

It is well known that the yield strength of polycrystalline materials increases with decreasing grain size. The behavior can be described by an empirical relation named after Hall and Petch (HP) [9, 10]. This dependency had been verified for several metals over large grain size regions. However, if the material approaches grain sizes below approximately 100nm deviations had been observed (summarized by [3, 11]).

In comparison with conventional coarse-grained (CG) polycrystalline materials, NC-materials exhibit a significant fraction of GB atoms [12, 13] independent of their defined width [14]. The high amount of GB atoms or the related interface density was considered as one of the key points controlling the mechanical behavior for very small grain sizes. Early molecular dynamics (MD) simulations for grains below 10nm suggest GB accommodation processes as a main deformation mechanism [15-17]. From these results, Conrad et al. [18] deduced a phenomenological model explaining softening behavior at grain sizes smaller than a material dependent critical value. Yip discussed this issue and formulated a concept named the “strongest size” [19, 20]. It describes a grain size region between 10 and 20nm, where a transformation from slip mechanism to GB mediated processes takes place. Experimentally a reduction was also observed and called the inverse HP effect [21, 22]. For very small grain sizes not much data is available and is often connected with a rather broad grain size distribution [23]. Therefore, the existence of such an inverse effect is questioned [24], but a deviation from the conventional HP relation seems to be present [3, 25]. However, for grain sizes bigger than 20nm, no extended GB regions or randomly arranged atoms could be found with HRTEM [26], as it was assumed in early works [27, 28].

NC materials are produced by different ways such as compaction of ball milled or inert gas condensed powder [29], electrodeposition [30], pulsed-laser deposition, ion sputtering, or annealing from amorphous metallic glasses [31, 32]. It can be expected that the different fabrication pathways will lead to dissimilar microstructures and GB networks. Furthermore, these techniques will cause different impurity content and local distributions. Therefore, it is often difficult to compare results from various studies because initial microstructural conditions may be different.

1.1.2. Deformation processes in nanocrystalline materials

The plastic deformation of NC materials has already been reviewed several times [3, 11, 33], but no general and comprehensive understanding of the deformation mechanism could be given, even for the simple case of pure FCC materials. Possible deformation processes of NC materials will be elaborated in the following. These processes are: nucleation and propagation of dislocations [34], twinning of FCC crystals [35], GB motion [36], grain rotation [37], grain growth [38], and diffusion mechanisms [39].

Considering the last point first, diffusion based mechanisms usually operate at high homologues temperatures. In the beginning of NC research, investigations on NC-Copper revealed that GB diffusion constants are three magnitudes higher than in their CG counterpart at 359K [40]. These results were utilized to explain the deformation behavior of NC materials [21]. However, these early results were later ascribed to the sample processing and not to an intrinsic property [41]. Markmann et al. [39] suggests a deformation mechanism controlled by GB diffusion in NC-Palladium under creep conditions (strain rate 10^{-10} s^{-1}). If a diffusion constant is extrapolated from this creep experiments, it leads to unreasonable high stresses for technical strain rates even with the large errors connect to such measurements. Moreover, the measured activation volume (for details see Appendix A) should be of the order of one Burgers vector cube for Coble creep, which is not the case in NC metals with grain sizes above 20nm [42-46]. Therefore, it can be safely assumed that such diffusion based deformation mechanism play only a minor role in NC metals tested at room temperature.

Dislocation based deformation process are the main carrier of plasticity in CG materials. There nucleation of a dislocation is often described in terms of Frank-Read sources where the average distance between two obstacles defines the necessary force to bulge and finally propagate a dislocation. Zhu et al. [47] calculated the forces to bow out a dislocation in a Nickel grain with 1μm and 30nm. The forces are 82MPa and 3.28GPa respectively wherefrom the first one is plausible but the second one is much higher than any measured flow stress. On a GB ledge in NC grains a nucleation of a dislocations could be accomplished much easier. Already in 1963, Li proposed the possibility of nucleating dislocations on GB ledges to explain the HP relation [48]. This is supported by MD simulation suggesting as well nucleation of perfect dislocations from GBs in NC materials [49]. The contribution of dislocations to the deformation of NC material could be revealed by post mortem TEM analysis where dislocations have been found in NC-Nickel at least after deformation at liquid nitrogen temperatures [50, 51].

In-situ TEM investigations can give an insight into the microscopic processes during deformation. However, such results have to be taken with care when compared to bulk mechanisms. TEM studies have to be obtained on electron transparent layers of a few tens of nm, i.e. there are maximum three, four grains stacked above each other in the case of NC materials. The actual test is then performed on a thin slice of material with a relatively huge surface area. Moreover, the stress in such an in-situ TEM experiment is usually applied in a complicated crack configuration [52]. Haque [53, 54] developed a novel method for uni-axial tensile testing in the TEM, but the thin film aspect is still present thus the results may not be directly related to bulk properties. These open issues demand other experimental techniques probing the bulk properties of metallic materials. In-situ X-ray measurements during deformation do not provide a visual picture but probe the bulk material. The strain field of some deformation constituents is then reflected in their characteristic peak profile. This is the reason why in-situ X-ray analyses are employed within this thesis.

Deformation twinning is well known, however, the material parameters causing it are not well understood. The concept of deformation twinning is based on the emission of a partial dislocation, which is followed by a twin partial as opposed to the partial being followed by a trailing partial on the same slip plane resulting in the creation of a perfect dislocation. Atomistic simulations locate the reason for one or the other process occurring in the stacking fault energy and the ratio between the stable and the unstable configuration as well as the unstable twin fault energy [55, 56]. These energies are relatively insensitive to isotropic volume changes and simple shear [57]. A multiscale simulation approach suggests that nucleation of a trailing partial dislocation or a twin partial dislocation at a crack tip is in general rate dependent, where the trailing partial is preferable at lower loads and/or lower loading rates [58]. This could be important for NC materials due to their high density of GBs and triple junctions, which exhibits stress intensities similar as crack tip. The observation of deformation twinning is easy in post mortem TEM analyses. Especially because any relaxation process as it could happen for dislocations by preparing the TEM lamella can be safely ignored for twins since it is known from CG materials that twins are difficult to anneal even at high homologous temperatures. Twins have been observed after deformation in NC-Nickel [50] as well as in NC-Tantalum [59] although under the stress state of an indenter. Also in the as prepared material of a NC Nickel-Iron alloy [60] a high density of twins were observed. Within this thesis TEM analyses are utilized to evidence the existence and/or the increase of twins in NC-Nickel specimens.

GB accommodation processes such as grain rotation and GB sliding are assumed to occur in NC materials. A significant contribution from GB sliding or coupled GB motion was suggested by experiments through the absence of a rolling texture and the retention of the equiaxed grain shape after large deformation in NC-Palladium [39] and by MD simulation [61, 62]. Moreover, TEM observation of grain rotation in dark field imaging was reported [37] although the interpretation of the contrast changes from these in-situ TEM experiments was questioned [11, 63].

It is well known that NC material can exhibit grain growth if they are pure enough [38, 64, 65]. This can happen at room temperature (RT) without any external load. During deformation, grain growth was observed in NC-Copper under an indenter [66] in NC-Nickel under very high deformation levels using high pressure torsion (HPT) [67] as well as in NC Aluminum layers [68]. During tensile deformation of NC Nickel no grain growth had been observed [69]. However, the plastic strain achieved through uni-axial tensile testing is in the order of a few percent. Therefore, compression test are carried out to investigate inter alia grain growth in higher deformation regimes.

Another important issue present in NC materials is the initial structure. In annealed CG structures, dislocations are predominately influenced by friction forces and obstacles. This picture changes if for example the material is cold worked. Then long-range internal stress fields arise through dislocation patterning acting e.g. with back stress on sessile dislocation segments. In the as prepared situation of NC materials an increase in root-mean-square (RMS) strain goes along with the reduction in grain size [70]. This high RMS-strain quantifies the pre-existent enhanced fluctuation of stress fields at small grain sizes and has to be taken into account when describing the overall deformation behavior. Furthermore, it is possible that anelasticity in NC materials influences the apparent Young's modulus and moreover the dynamic behavior [71, 72]. For the latter, also the dynamics of dislocations generated during deformation can cause time dependent changes [73].

All mentioned processes including the diffusion based ones could occur for a specific grain size and their distribution under certain conditions of temperature, pressure, stress, and strain rate. Transient tests are usually utilized to pin down the rate limiting process for one material at certain external conditions [43, 74, 75]. Therefore, they are applied within this work on NC-Nickel. However, to obtain reliable conclusions experimental results have to be associated with models explaining elementary processes with a physical background.

1.1.3. Proposed deformation models

So-called two-phase models are often used to explain the behavior of NC-materials. The basic principle is to distinguish between a bulk phase and a boundary phase with different properties. These models are mainly utilized to explain a deviation or an inverse HP slope [12, 76-80]. One of them described by Meyers et al. [80] distinguishes between a core and a mantle phase. The model describes a core phase with a homogeneous stress state and a mantle region around the GB. The latter is more subjected to the elastic anisotropic effect and additionally the GB acts as a source of dislocations. These effects combined with the activation of two or more slip systems in a polycrystal are responsible for the formation of a work hardened layer along the GBs, already in the microplastic region. Benson et al. [81] extended this approach to the "NC" regime, down to 100nm grain size. They found good agreement with experimental data in the UFG regime. However, it is doubtful whether this model can be extended to real NC regime since materials with 30nm grain size deform heterogeneous and only a small fraction of the grains have to yield in the early stage of deformation [82]. This early stage of deformation which is suspected to built up a mantle layer in NC materials has never been addressed experimentally. Inter alia load-unload cycles in the initial deformation stage were studied within this thesis.

Asaro et al. [83] formulated a model to describe the emission of a partial/perfect dislocation into a NC grain by creating two trailing segments in the “side GBs” whereby the athermal nucleation is considered as the rate limiting process. In addition, the model includes a GB sliding process for sufficiently small grain sizes based on kinetic relations proposed by Conrad [18]. With the combination of both mechanisms, they were able to describe the strain rate sensitivity of the material because sliding is an activated mechanism and depends on strain rate and temperature. Zhu et al. [47, 84] incorporated this results together with realistic grain size distributions to formulate a model describing experimentally observed stress strain data. Based on the model the authors pointed out that the grain size distribution is important to describe the experimentally observed data.

MD simulation revealed that NC materials can deform by nucleating a stable dislocation at a GB ledge (nucleation) which successively travels trough the grain and is finally absorbed at the “opposite” GB [34]. The nucleation of the leading partial through a stress concentration changes the preexisting ledge so that the trailing partial does not necessarily nucleates at the same ledge. Moreover, it could be shown that the propagation of a dislocation can be hindered by other GB ledges in the slip plane of the dislocation. This pinning and depinning of the dislocation involves a complex process of kink dynamics as well as discrete atomic activity. In other words, the dislocation has to overcome a local energy barrier that will be strain rate and temperature dependent. In fact, it could be shown with MD simulations that the depinning time of the dislocation is strongly temperature dependent [34].

Whether one or the other proposed model can be seen as reliable depends on further findings substantiating or extending the already gained knowledge. In particular, the early stage of deformation – the microplastic regime – is investigated with load-unload cycles. Deformation experiments at temperatures well below RT and so called transient tests are utilized to study the importance and nature of the thermal component in the NC deformation.

1.2. Research outline

The main idea followed within this thesis originates from the mentioned MD simulations [34, 49]. In a former PhD work [85], deformation experiments on NC Nickel during in-situ X-ray diffraction revealed a reversibility of the peak broadening upon unloading after RT deformation supporting the suggested MD ideas.

Within this thesis, investigations have been pursued by performing experiments in the early stages of plastic deformation, the microplastic regime of NC-Nickel. Furthermore, the influence of lowering the temperature has been studied with a newly designed set-up. With transient tests, the internal stress fields of NC-Nickel as well their activation volumes were measured. Compression tests were performed to investigate the material at large strains, which cannot be obtained by tensile testing due to limited ductility. Calculations of X-ray diffraction profiles from atomistic simulation configurations obtained from MD are used to assist the experimental results and a 3-dimensional atom probe (3DAP) technique is applied to investigate impurities in NC-Nickel. All experiments are assisted and supported by SEM and TEM analysis of the specimens. Figure 1 outlines graphically the studied fields to determine deformation processes of NC Nickel. The starting knowledge of research obtained until now is sketched in the middle of the diagram. To obtain an overview, the following areas are listed not necessarily in order of priority.

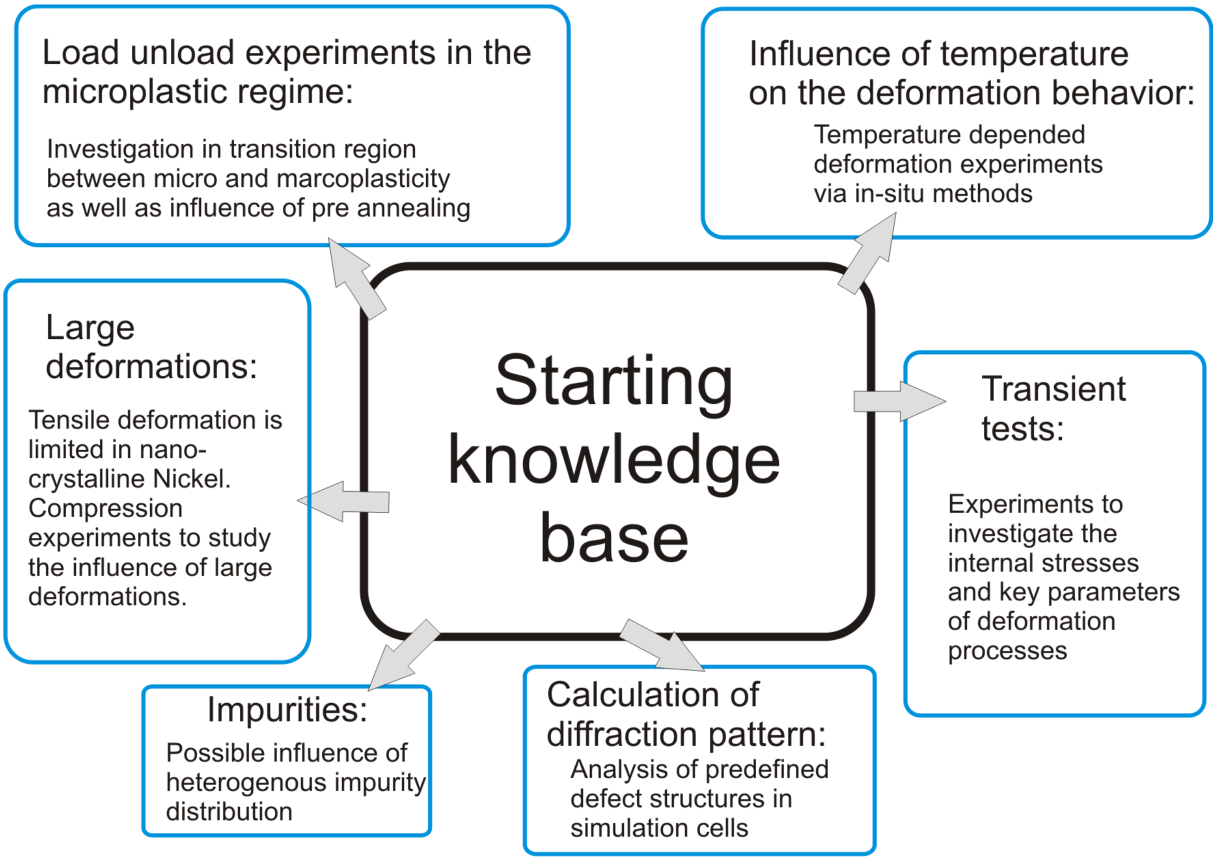
Load unload experiments in the microplastic regime:
Investigation in transition region between micro and marcoplasticity as well as influence of pre annealing
Influence of temperature on the deformation behavior:
Temperature depended deformation experiments via in-situ methods
Large deformations:
Tensile deformation is limited in nano-crystalline Nickel. Compression experiments to study the influence of large deformations.
Starting knowledge base
Transient tests:
Experiments to investigate the internal stresses and key parameters of deformation processes
Impurities:
Possible influence of heterogenous impurity distribution
Calculation of diffraction pattern:
Analysis of predefined defect structures in simulation cells

Figure 1: A graphical outline of the thesis structure.

A) Studying the evolution of the internal stresses in the microplastic regime by load-unload experiments. Moreover, studying the influence of annealing on the related parameters.

B) To discern key values of the dominating deformation processes transition tests are used to evaluate the material.

C) Investigating the thermal dependence of deformation parameters in terms of internal effects measured with X-ray diffraction by different load and temperature cycles.

D) Tensile tests are restricted in deformation. Therefore, compression experiments are performed to study the microstructure and evolution of internal processes at large deformations.

E) An important issue is the interpretation of diffraction peak profiles: An attempt is made via the calculation of diffraction peaks from simulated NC samples with defined defect structures. A “bottom-up” approach to study peak profiles from NC bulk materials.

F) It is know that NC Nickel produced via electrodeposition contains a certain amount of impurities. Their amount and distribution probably plays an important role in the deformation mechanisms. Therefore, the tested materials are studied via adapted 3D-atom probe technique.

The following Chapter describes the applied techniques used within this thesis. Adjacent to this description the results are presented. In the subsequent discussion Chapter, outcomes are critically reviewed.

2. Experimental and technical details

2.1. Materials description

2.1.1. Nanocrystalline-electrodeposited Nickel

To study fundamental aspects of NC FCC metals, electrodeposited (ED) Nickel [22, 43, 45, 69, 86-90] is frequently used as an example material. By using pulse deposition techniques [91], NC-ED Nickel can be easy synthesized pore-free and can be made without texture. Furthermore, it exhibits a stable nanostructure at RT without spontaneous grain growth. This stability depends partly on the melting temperature [92] where nickel has an advantage compared to other FCC metals e.g. Copper or Aluminum.

It has to be mentioned however that not all process conditions result in the high quality NC structure and that often texture [93] and/or nanovoids [94] are present. Normally a small amount of saccharin inhibitor ($C_7H_4NO_3S$) is added to establish a certain grain size [95]. This inhibitor is a source of impurities incorporated in the NC-ED bulk material. The distribution of the impurities in the material is addressed in Section 3.6.

The ED material used within this thesis is purchased from Goodfellow$^{®}$ in sheet form with the dimensions of 80mm x 80mm x 0.2mm. From the production process, no further details are available. A TEM picture and a grain size distribution obtained from several dark field images are shown in Figure 2b.

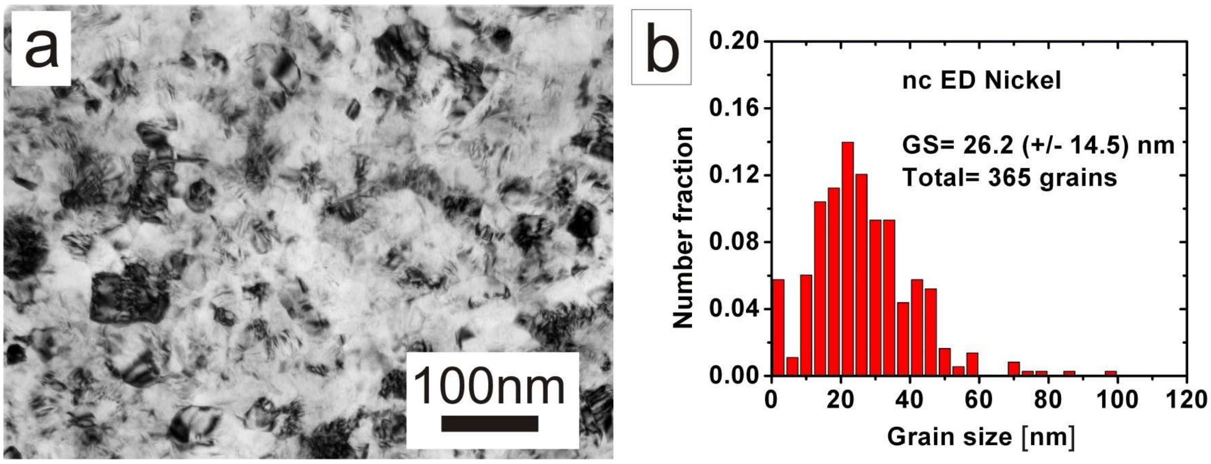

Figure 2: a) A bright field TEM picture (in plane view) of NC-Nickel as purchased and b) its grain size distribution.

In a bright field TEM picture (Figure 2a), no clear grain structure can be observed. Some areas appear mainly dark and can be interpret as grains. The dominating feature in the TEM pictures are the frequent changing black white contrasts (see Figure 3a). Such changes in contrast within a crystallite/grain usually originate in CG material from the strain fields of various defects e.g. dislocations. HRTEM performed by Wu et al. [51] revealed that there are only very few full lattice dislocations present in NC-Nickel. The contrast changes, which are present everywhere in TEM bright field images originate from extrinsic GB dislocations or from strain fields stored in the GB of the material, e.g. a delocalized dislocation core [96]. Such strain fields do not allow a proper grain size determination in bright field images. Therefore, grain size distributions are taken from dark field images where a better determination of the GB is possible. Figure 3b (from the same area as Figure 3a) shows the boundary of a NC grain outlined with a red polygon. The dark field image is obtained with a selected area diffraction (SAD) aperture on the 111 ring.

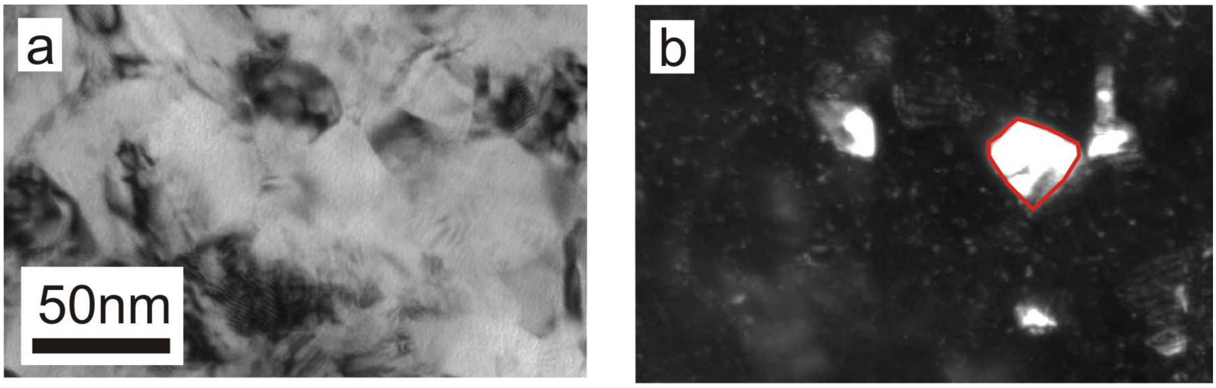

Figure 3: TEM micrograph of as prepared NC-Nickel in bright field (a) and dark field (b) from the same area (same magnification). The red polygon in (b) marks the outer boundary of one grain.

The number averaged grain size of 26nm is derived from 365 grains with a standard deviation of +/- 14nm. The grain size distribution is narrow with only five grains having a grain size between 60 and 80 nm and two grains between 80 and 100 nm. The volume averaged grain size of NC-Nickel is 33.5nm with a standard deviation of 42nm. Details about the calculation of the number averaged and volume averaged grain size can be found in Appendix B. Further microstructural details about this material are presented in several Sections within this thesis.

2.1.2. Ultra fine-grained Nickel

The production of UFG material is possible either by microstructure refinement of bulk material or via grain coarsening of NC materials. The latter method is carried out by the annealing of nano-grained material. When this method is applied to NC-Nickel containing impurities, they will segregate to the GBs resulting in complete loss of ductility [97]. Microstructural refinement by severe plastic deformation is another method to produce full dense UFG materials [98]. The material used in this thesis was provided by Prof. Zehetbauer and produced via HPT. CG Nickel with a purity of 99.9% was deformed by one turn under a pressure of 8GPa. At the outer radius from the 8mm disc, the shear strain was about 95 corresponding with a von Mises strain of about 55.

The grain size distribution presented in Figure 4 is established from the TEM dark field micrographs (shown in the inset). The micrographs are obtained from the same distance from the center of the disk as tensile specimen. The grain sizes of individual grains vary from 20nm up to 400nm and exhibit a number averaged grain size of about 155nm with 80nm standard deviation. The volume averaged grain size of UFG-Nickel is 191nm with a standard deviation of 217nm. X-ray diffraction experiments (see Section 2.3.5) revealed a smaller grain size of ~90 nm using the 111-peak family. The difference between the TEM and X-ray grain size can be explained by sub-GBs, which interrupts the coherent diffraction area from the X-ray measurements and result in a smaller grain size when measured by X-ray diffraction (XRD).

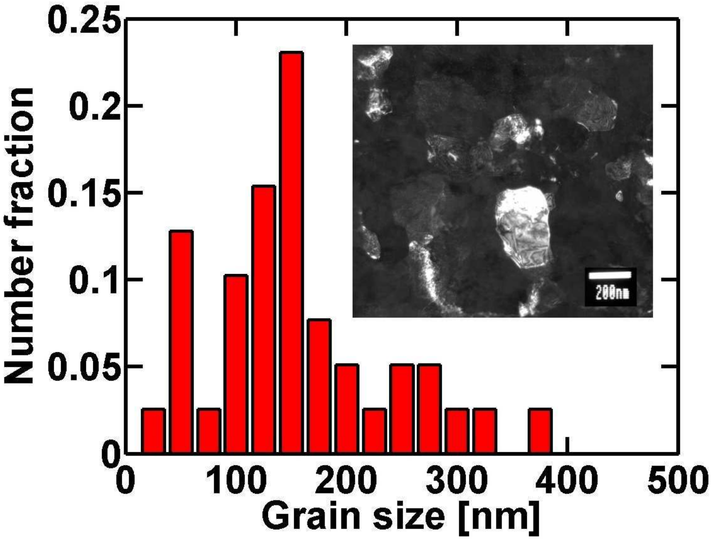

Figure 4: Grain size distribution of HPT Nickel with a number average of about 155nm. The inset shows a typical dark field TEM picture.

Microstructural features of HPT-UFG Nickel are presented in a TEM bright field image in Figure 5. The UFG-Nickel contains, similarly to NC-Nickel, some regions with a lower and some with a higher density of strain fields (compare Figure 5a and Figure 2a). The main difference compared to NC-Nickel is the local distribution. In NC-Nickel the strain fields seem to extend hundreds of micrometers, which is clearly larger than the grain size (see e.g. Figure 2b). In UFG-Nickel, these extensions are from a similar size (few hundred micrometers) but compared to the grain size it changes much faster. In UFG-Nickel, there are clear differences within one grain, which is not the case for NC-Nickel. In Figure 5b, two grains are determined by dark field images and outlined in green and red on the bright field micrograph. These two grains show a distinguishably different defect density between each other, but also within one grain the variations are large.

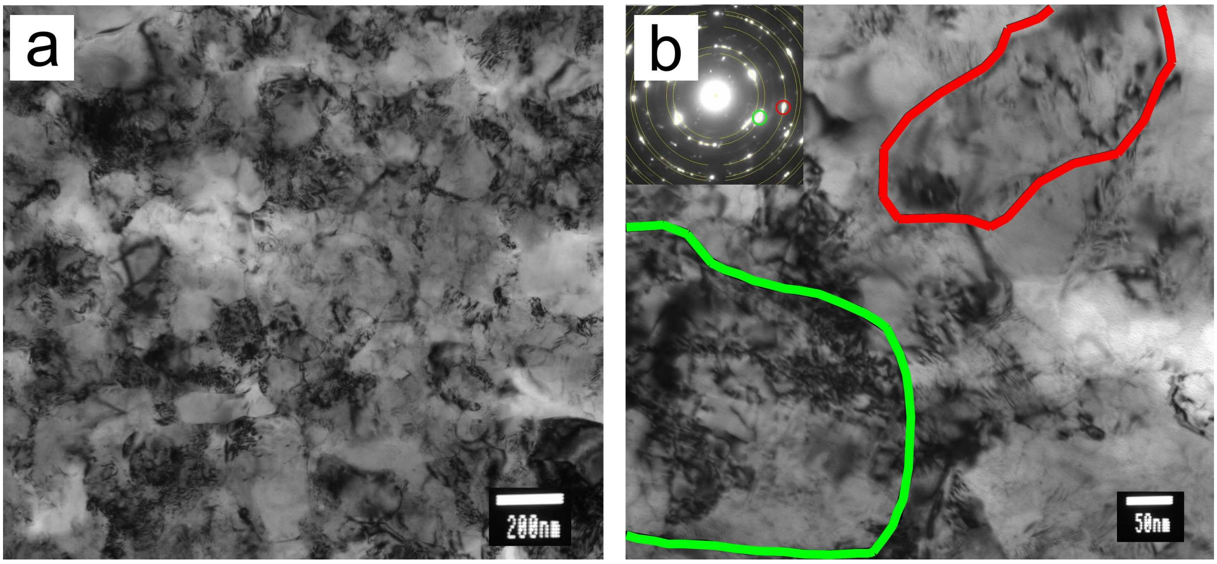

Figure 5: a) TEM brightfield image of HPT material. b). Magnified image where two grains are outlined. Inset: SAD pattern with diffraction spots marked in corresponding colors.

2.1.3. Specimen preparation

The NC-Nickel sheet was purchased in the final thickness of 0.2mm. The UFG disks had an original thickness of 0.8mm. To obtain a similar thickness as that of NC-Nickel the disks are ground carefully down. The HPT process results in a radius dependent shear strain. Therefore, dog bone shaped samples had to be cut equidistant from the central point. The cutting of the tensile and compression samples for NC and UFG material was performed via wire electrical-discharge machining (EDM).

Since the EDM cutting produces a recast-layer, an electro-chemical polishing step was conducted to remove this layer. A polishing time of around one minute at a temperature of -15°C was sufficient to remove approximately 0.015mm within the gauge section of a dog bone using 15V and 0.08A. As electrolyte a standard solution for Nickel consisting of: 3% Perchloric acid (70%) mixed with 30% 2-Butoxyethanol and Methanol served as solvent.

The same solution and temperature was used when TEM specimen were prepared with a TenuPol-5® from 3mm punched disks. To prepare TEM specimen from tensile and compression samples a tripod polishing technique is applied. There the samples are carefully polished to a wedge. At each step, three times the thickness of the expected damaged layer due to the former grinding step was removed. The final "grinding-step" was performed with a suspension containing colloidal silica of 20nm. Afterwards all wedges where glued on a slotted molybdenum ring and ion-milled at cryogenic temperatures until electron transparency. More details about this standard tripod polishing procedure can be found in [85].

2.2. Mechanical testing

2.2.1. Tensile testing

Equipment

Machine

To carry out tensile tests and X-ray diffraction simultaneously at the Swiss light source (SLS) a miniaturized tensile machine is mounted on the goniometer of the materials science (MS) beam line. Such a machine has to fulfill constrains such as lightweight, torque, and size. The “micro tensile-test machine” (MTM) [85, 99] was constructed at the Paul Scherrer Institut (PSI) following a concept of Sharpe W.N. Jr. [100, 101]. A successful implementation of the MTM at the beam line was carried out earlier [85].

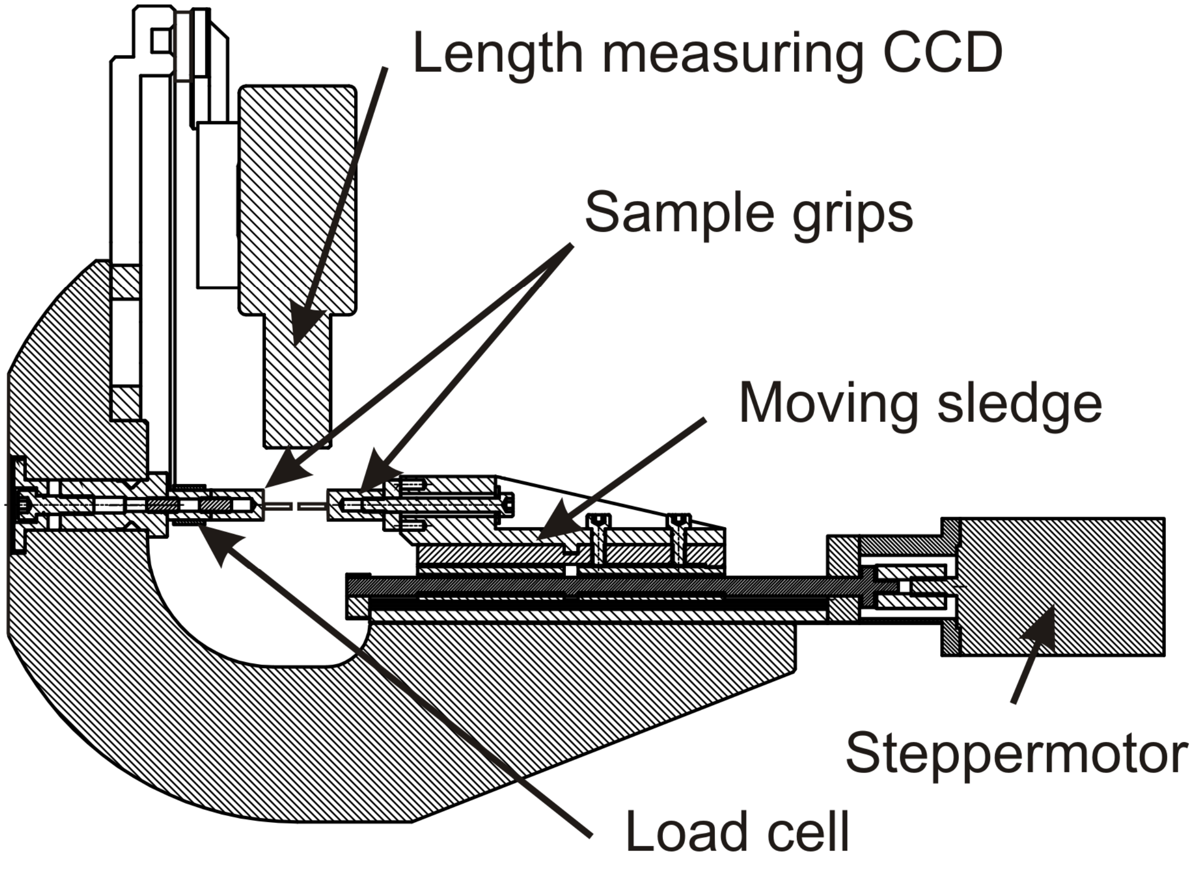
Length measuring CCD
Sample grips
Moving sledge
Steppermotor
Load cell

Figure 6: Technical drawing of the micro tensile machine (MTM).

A technical drawing of the MTM is presented in Figure 6. The base of the tensile machine is an aluminum frame with a guided sledge moved by a stepper motor through a spindle. A stepper motor turns the spindle and applies via a moving sledge a load to the sample. More details about the control can be found below in the *Control unit* Section on Page 22. To measure the response of the sample a load cell for the force and a CCD camera for the elongation are used.

Sample geometry

Figure 7 presents the so-called "dog bone" shaped sample used within this thesis.

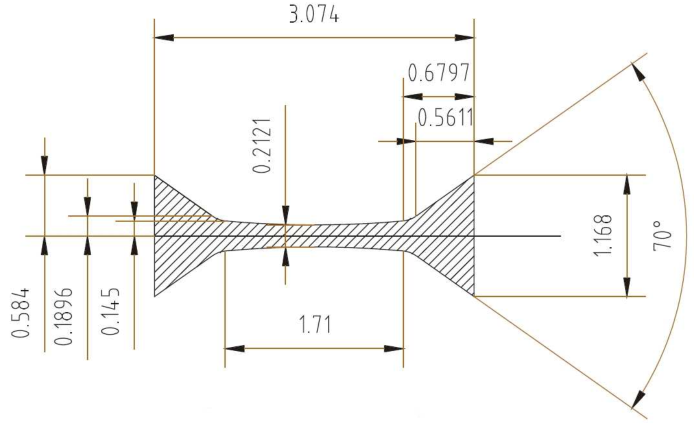

Figure 7: Technical drawing of the miniaturized tensile test specimen.

The sample has a nominal thickness of about 0.2mm depending on the polishing time. The triangular ends – tapers – are part of grip system for the sample fixation. Two opposite triangular shaped counterparts made out of tungsten carbide cobalt (WC-Co) are used at the MTM to apply the force (grips). Figure 8 shows the arrangement with the sample clamped between the grips. This system has the advantage of being self-aligning and allows fast sample exchange compared for instance with gluing. Therefore, such an approach is often used for miniaturized sample testing [101-103].

The gauge section is slightly curved (radius 9.4mm) resulting in an engineering stress which is 1% higher than the nominal stress for an uncurved gauge section [104] (a stress concentration factor of 1.01). This curvature is undesirable for an uni-axial tensile test. However this specimen design was chosen since it assures that the plastic deformation occurs there where the X-rays probe the specimen [85].

An equivalent sample design with a straight gauge section would also cause a stress concentration at the transition region to the taper independent of any possible fillet. In any case, an additional fillet – approximately 0.25mm – between the taper and the gauge section is applied to reduce the stress concentration at this point [101]. Sharpe et al. [103] found 5% lower stress values for dog bone shaped specimen with a stress concentration factor of 1.01 compared with conventional test specimens of A533-B steel.

The MTM allows also the usage of other sample geometries, which are not used within this thesis. Details about such possible samples geometries and corresponding grips can be found in reference [99].

Length measurement

The CCD camera is part of a commercial length measurement system obtained from MESSPHYSIK®. In this method, a black and white contrast of the sample is generated via a parallel illumination through a block LED. Figure 8 shows the picture seen by the CCD camera. The black areas are the grips on the left and the right side and the sample in the center. Since the sample is clamped between the grips and no difference between the pieces is visible, green dashed lines are drawn on top of the picture to outline the single components. The length value *L* is represented by the blue lines. It is obtained from the black white contrast parallel to the yellow line. To increase the precision eight lines above and below the yellow one are averaged. The red lines marks the outer boarder of these 16 lines used to measure the length. This technique features do to interpolation and averaging a statistical error of 43nm (standard deviation).

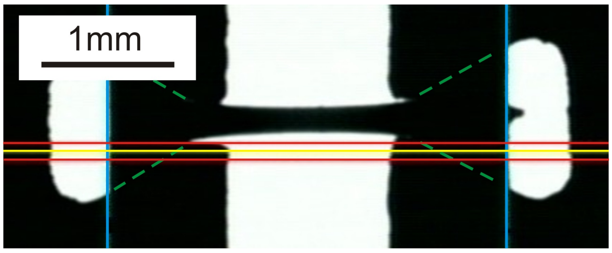

Figure 8: Length measurement of the dog bone with commercial system from Messphysik®.

As shown in Figure 8, the strain is measured at the end of the taper. This method neglects any deformation of the taper and possible transition regions between the taper and the gauge section. A more precise method is the usage of a interferometric strain gauge in the central region of the dog bone [105], which is deselected due to its impracticality to install it at the in-situ set-up. Another method is to follow points or structures at the surface of the sample and calculate the strain through an image recognition method. However, due to the necessary light conditions and the poor resolution of the CCD camera this method is not applied. Budrovic [85] has show that the usage of an initial gauge length L_o of 1.7mm and the measurement of the elongation at the end of the taper is a safe approximation for the strain in the central region of the tensile specimen and therefore used throughout this thesis.

Force measurement

The force F measurement was carried out via a MLP50 load cell from Transducer-Techniques®. The statistical error is 38mN (standard deviation) obtained from a measurement for several minutes without sample (zero load). The load cell was calibrated beforehand with sample weights. This calibration exhibits a systematic error of 185mN. To compare the data with data obtained using other tensile machines the systematic error has to be included via error propagation.

Cross-section measurement

The cross section A_0 is calculated by multiplying the gauge breadth b and height h. Both breadth and height are measured before each test with a micrometer. The statistical error in the cross section arises from the micrometer and is 2μm for each direction. For a single test, this error is systematic and can be ignored. If different samples are compared the error has to be included.

Stress and strain calculations

The elongation of the sample ΔL is calculated by subtracting the actual length l form the initial measured length l_0 according to (1),

$$\Delta L = l - l_0 \,. \tag{1}$$

For initial gauge length L_o a fixed value of 1.7mm is used [85]. The cross section A_o is obtained by the multiplication of the dog bone breadth b and the height/thickness h according to (2),

$$A_0 = b * h \,. \tag{2}$$

These values are then used to calculate the engineering strain ε_{eng} and engineering stress σ_{eng} according to (3),

$$\varepsilon_{eng} = \frac{\Delta L}{L_0} \quad and \quad \sigma_{eng} = \frac{F}{A_0} . \tag{3}$$

The true strain ε_{true} or true stress σ_{true} is calculated via (4),

$$\varepsilon_{true} = \ln\left(1 + \varepsilon_{eng}\right) \quad and \quad \sigma_{true} = \sigma_{eng}\left(1 + \varepsilon_{eng}\right) . \tag{4}$$

However, one has to mention that the calculated true strain and true stress is only valid until necking appears which happens usually at the ultimate tensile strength (UTS). Beyond this point, the analytic approximation of uni-axial stress is not applicable [106]. Despites this fact, the “calculated” true stress is used beyond the UTS for comparison.

Error estimation

Summarizing the statistical errors and assuming that these errors are not correlated with each other allows calculating the standard deviation Δ_ϕ of the system (5) via conventional error propagation [107, 108],

$$\Delta_\phi = \sqrt{\sum_{I=1}^{m} \left(\frac{\partial \phi}{\partial x_i} \right)^2 \Delta x_i^{\,2}} . \tag{5}$$

Empirical covariances such as influences from one to another measuring method of the single variables (e.g. force and cross section) are not expected and a priori neglected.

For a single test the error on the true strain can be calculated by (6),

$$\Delta \varepsilon_{true} = \sqrt{\left(\partial_l \varepsilon_{true}\right)^2 \Delta l^2 + \left(\partial_{l_0} \varepsilon_{true}\right)^2 \Delta l_0^{\,2}} , \tag{6}$$

and the error of the true stress by (7),

$$\Delta \sigma_{true} = \sqrt{\left(\partial_F \sigma_{true}\right)^2 \Delta F^2 + \left(\partial_l \sigma_{true}\right)^2 \Delta l^2 + \left(\partial_{l_0} \sigma_{true}\right)^2 \Delta l_0^{\,2}} . \tag{7}$$

The statistical errors (Δl, Δl_0, ΔF) used in (6) and (7) are the obtained from static measurements described above.

If different tests are compared, the error on σ and ε increases due to the error of the cross section, which has been neglected for a single test due to their systematic character. Therefore, the terms $(\delta_b \sigma_{true})^2 \Delta b^2$ and $(\delta_h \sigma_{true})^2 \Delta h^2$ have to be added under the square root of (7).

To compare the results from different machines the statistical error of the calibration ΔF has to be included via error propagation. The used standard deviations to calculate the error bars are 38mN for the force ΔF, 43nm for the length Δl and Δl_0, 2µm for the cross sectional dimensions Δb and Δh, and 185mN for the force calibration ΔF_2.

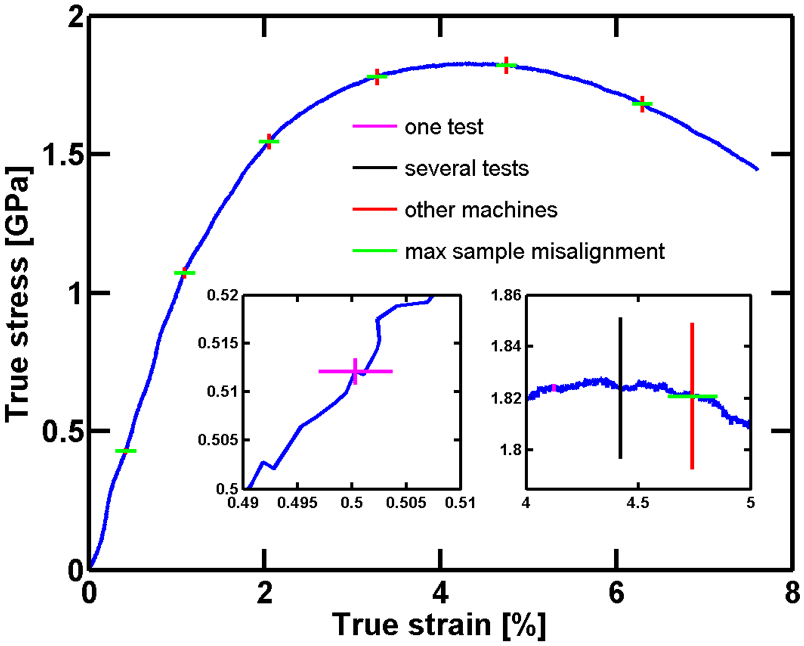

Figure 9: Measurement errors on example deformation. See text for different error bars in insets.

Figure 9 shows a true stress-true strain curve with error bars (+/- standard deviation) for the error calculations. These error bars are presented on top of the data at several points and the insets show two magnifications. The error bars are defined as follows:

- *Magenta* error bars: For a single test, the error in the strain depends only on the two length measurement errors, Δl *and* Δl_0. The error in the force depends on the statistical error ΔF. These errors are rather small, since these three values are measured quite accurately.
- *Black* error bars: If different samples are tested on the same machine, the error in stress increases since cross section measurement, Δb^2 and Δh^2, becomes a statistical error as described in the previous paragraph.
- *Red* error bars: If the measured data are compared with different machines, the force calibration is included as a statistical error increasing the error in stress.

- *Green* error bars: The error in strain depends only on the camera resolution of 43nm. If a horizontal misaligning of maximal 10μm is included, the dog bone looks elongated by ~2μm Δl.

This fragmentation clearly shows that the error on the stress is mainly dependent on the cross sectional measurements. The error on the stain results more likely from a horizontal misalignment because the accuracy of the length measurement is rather exact.

Control unit

The system is controlled via a LabView® program running on a PC. The program has been continuously developed/improved within the timeframe of this thesis. A schematic graphical overview of this system is presented in Figure 10.

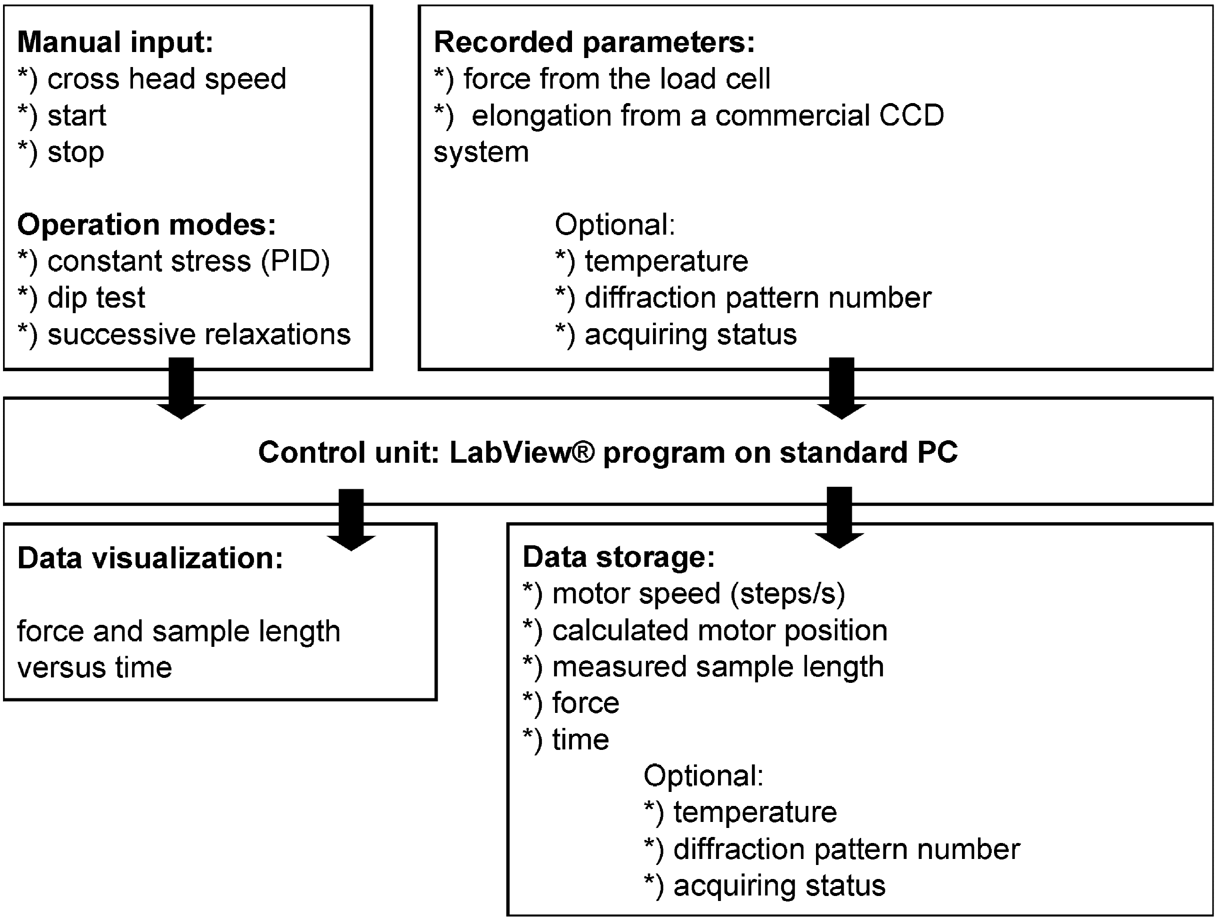
Manual input:
*) cross head speed
*) start
*) stop
Operation modes:
*) constant stress (PID)
*) dip test
*) successive relaxations
Recorded parameters:
*) force from the load cell
*) elongation from a commercial CCD system
Optional:
*) temperature
*) diffraction pattern number
*) acquiring status
Control unit: LabView® program on standard PC
Data visualization:
force and sample length versus time
Data storage:
*) motor speed (steps/s)
*) calculated motor position
*) measured sample length
*) force
*) time
Optional:
*) temperature
*) diffraction pattern number
*) acquiring status

Figure 10: Schematic representation of the MTM control unit.

The input parameters to the program consist of the load cell value for the force, the specimen length from the CCD system and the status of the motor controller. Furthermore, it is possible to record two temperatures (e.g. sample environment and ambient temperature) with an external thermometer. If the test is carried out in-situ at the SLS the number of the diffraction pattern as well as the recording status of the X-ray detector (on/off) could be optional feed into the system. All recorded data are written into a file.

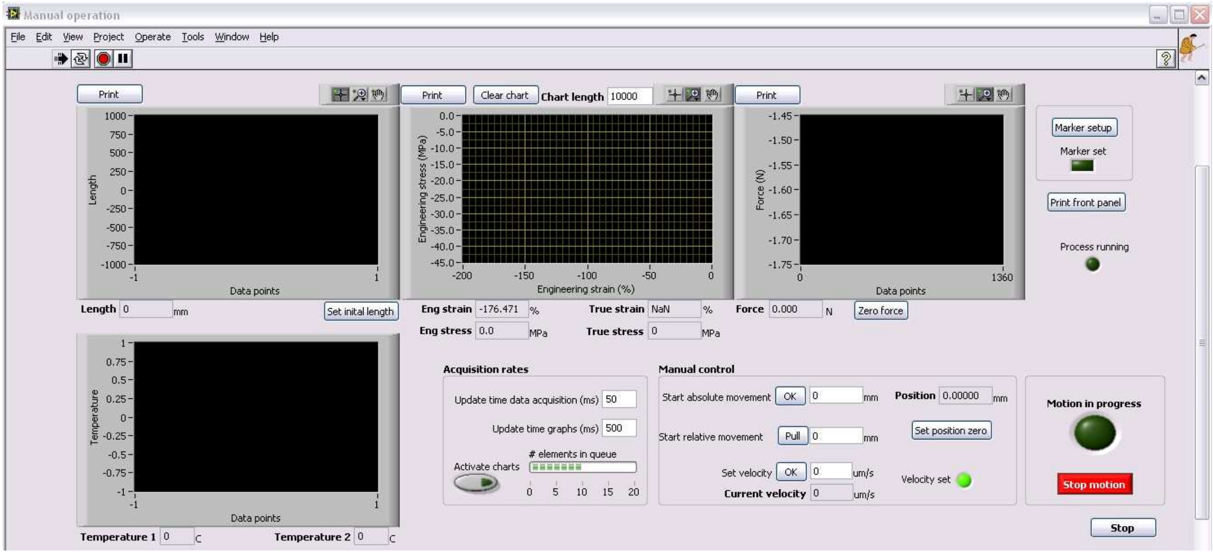
Manual operation
File Edit View Project Operate Tools Window Help
Print
Clear chart
Length
1000
750
500
250
0
-250
-500
-750
-1000
-1
1
Data points
Engineering stress (MPa)
0.0
-5.0
-10.0
-15.0
-20.0
-25.0
-30.0
-35.0
-40.0
-45.0
-200
-150
-100
-50
0
Engineering strain (%)
Force (N)
-1.45
-1.50
-1.55
-1.60
-1.65
-1.70
-1.75
0
1360
Marker setup
Marker set
Print front panel
Process running
Set inital length
Zero force
Temperature
1
0.75
0.5
0.25
0
-0.25
-0.5
-0.75
-1
Acquisition rates
Manual control
Activate charts
# elements in queue
0
5
10
15
20
OK
Pull
Set position zero
Velocity set
Motion in progress
Stop motion
Stop

Chart length 10000

Length 0 mm

Eng strain -176.471 %

True strain NaN %

Force 0.000 N

Eng stress 0.0 MPa

True stress 0 MPa

Update time data acquisition (ms) 50

Update time graphs (ms) 500

Start absolute movement 0 mm

Position 0.00000 mm

Start relative movement 0 mm

Set velocity 0 um/s

Current velocity 0 um/s

Temperature 1 0 C

Temperature 2 0 C

Figure 11: Screen shot from the LabView® program used to control the MTM.

Figure 11, shows the graphical user interface to control the MTM. Four black graphs are visible. The central one shows the calculated engineering stress-strain data. The right one shows the measured force against time and the upper left one the measured length versus time. The lower left graph shows the temperatures versus time. In the central region, input boxes are placed to set the refresh rate of the mentioned graphs. Buttons for manual control are placed to the right of this area (crosshead movement). At the top right, the marker recognition button is placed. This one opens a submenu where the edges for the length measurement for each new sample are identified. At the bottom right corner, a signal light indicates the crosshead movement (on/off).

The system could be run either manually (as mentioned above) or in an automated operation mode. In manual mode, the crosshead can be moved, in absolute or relative values, with a certain speed. The speed has an upper limit of 0.16mm/s (equivalent to a strain rate of $9.4x10^{-2}$ s^{-1} for a dog bone specimen) deduced from the maximum frequency (10kHz) and the step size (16nm) of the stepper motor. However, since the stepper-motor-controller is able to place the motor axis at any radial position there is no lower speed limit.

Operation modes

Constant strain rate

The basic operation mode – the constant strain rate mode – consists of a continuous test where a constant crosshead speed is set (in μm/s). After the process is started, the MTM deforms the specimen, until the machine is stopped or a desired displacement is reached. The duration of a $\sigma-\varepsilon$ curve of a NC-Nickel dog bone (e.g. Figure 9), with a typically used strain rate of approximately $6x10^{-5}$ s^{-1} (crosshead speed of ~0.1μm/s), lasts approximately 20 minutes until failure. With a data acquisition rate of 20Hz, this test produces roughly 24000 data points.

Constant stress

A constant load/engineering-stress mode – regulating the load to a user-defined value – is implemented via a proportional-integral-derivative (PID) controller available in the LabView® program. This mode was used either for creep-experiments or to unload a specimen.

Furthermore, for the low temperature (LT) experiments, this mode was indispensable. During the cooling of the sample, which unavoidable also results in a cooling of some parts of the tensile machine, the thermal contraction resulting from this cooling had to be accommodated to ensure the sample remained unloaded before the actual experiment started.

Dip mode

A dip test is a stress reduction experiment during constant loading. A schematic of such a test is shown in Figure 12. The sample is loaded at a constant strain-rate. At a pre-defined stress, the load is dropped by a certain amount after which the load is kept constant. In other words, the sample is suddenly unloaded followed by a creep experiment. The original idea of such a dip test was first described by Gibbs [109] and used to study internal stresses.

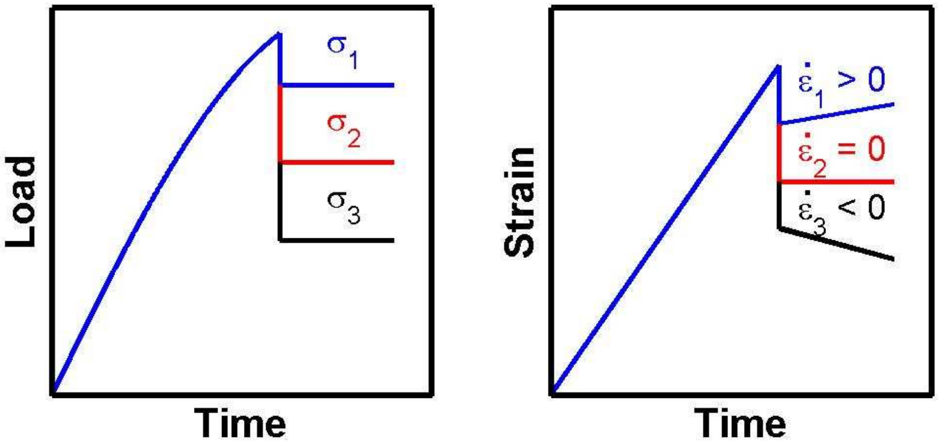
Load
Time
σ_1
σ_2
σ_3
Strain
Time
$\dot{\varepsilon}_1 > 0$
$\dot{\varepsilon}_2 = 0$
$\dot{\varepsilon}_3 < 0$

Figure 12: Schematic representation of a strain-dip test during a constant strain sate test.

Due to machine limitations in response time, it was not possible to control the force precisely during the transition between the unload and the creep part. To avoid machine modifications, a method was applied where at a pre-defined stress, the crosshead is moved a certain distance opposite to the loading direction and then stopped. The average of the stress values is then determined in the first 0.5 seconds. Immediately afterwards this stress is kept constant with the above-mentioned constant stress mode.

Successive stress relaxation mode

Through a simple stress-relaxation measurement, it is possible to extract the apparent activation volume. Therefore, only the crosshead movement has to be stopped. To obtain a physical activation volume, Spätig [75] suggested performing successive relaxations. More details can be found in Section 3.3.

Figure 13 shows three schematic relaxations. The $\Delta\tau$ stands for the stress reduction during one relaxation. The relaxation time t_{rel} is the same for all stress drops. The strain-rate $\dot{\gamma}$ is indexed with *i* and *f* which stand for initial and final respectively.

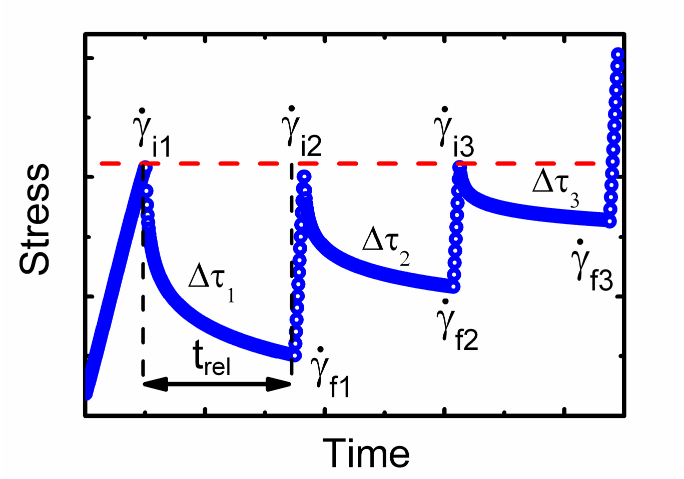

Figure 13: Typical measurement cycles to obtain the physical activation volume.

For such type of tests it is important, that the relaxation time is kept short (~30 seconds) [74], that that the reloading is fast and the reloading stress value is equal to initial stress value. Since it is impossible to perform such a test in manual mode, the complete cycle was implemented as an automated operation mode.

This mode allows entering the number of reloading cycles n and the relaxation time t_{rel} beforehand. At a certain stress level, which can be pre-defined or can be chosen in the course of a constant strain rate test, the control unit performs n-cycles with the relaxation time t_{rel}. In between the relaxation cycles, the machine reloads each time to the initial stress value.

The problematic point was the reloading since it should be as fast as possible and to the same initial stress value. This could be realized by a linear prediction of the force value during the reloading process.

2.2.2. Low Temperature Set-up

The previously described tensile test equipment was originally designed for RT testing only. During the thesis research, it became necessary to perform LT measurements. The method used, mainly driven by financial and time constraints as well as construction constraints defined by the beam line set-up, was able to maintain a stable temperature of 180K during in-situ tensile tests. The chosen solution consisted of two types of cooling simultaneously operating to insure a small temperature gradient within the tested sample over several hours of testing time. The schematic design of this set-up is shown in Figure 14. Figure 15 shows several pictures of the chosen set-up at the MS beam line.

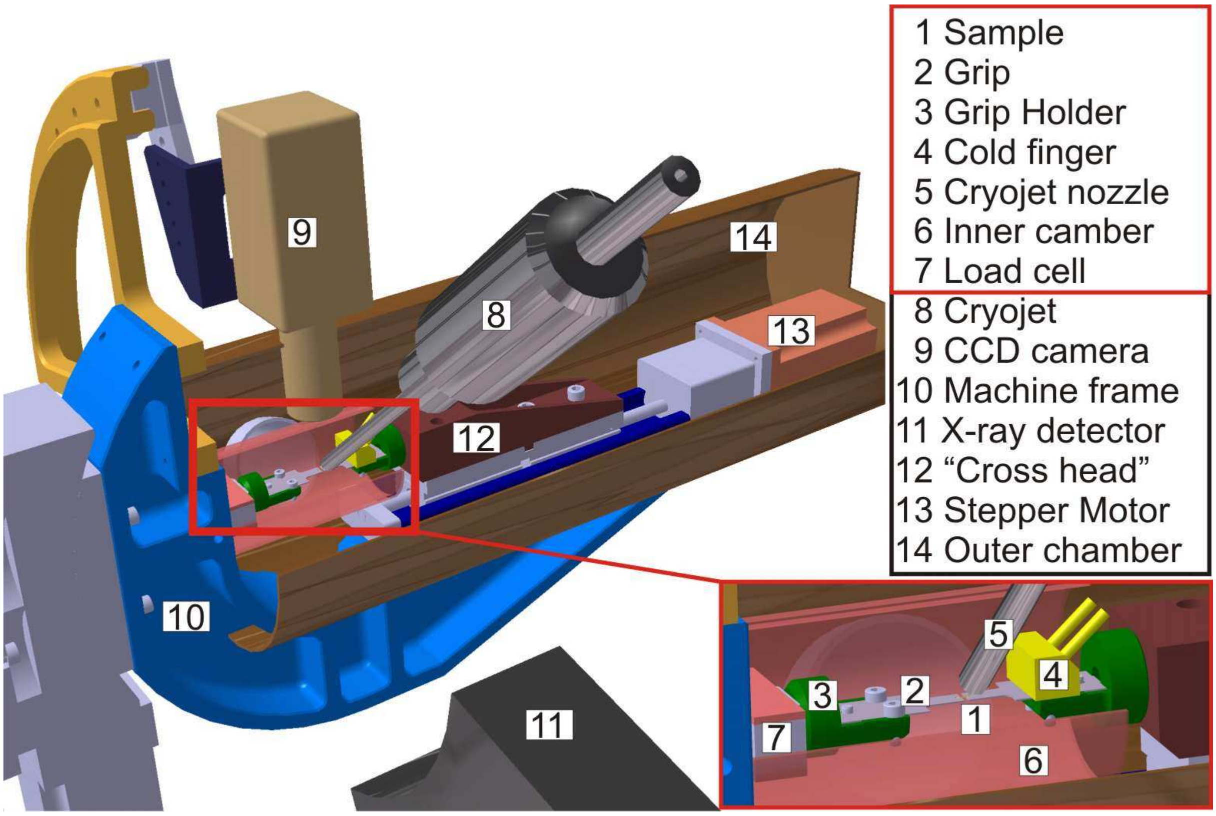
1 Sample
2 Grip
3 Grip Holder
4 Cold finger
5 Cryojet nozzle
6 Inner camber
7 Load cell
8 Cryojet
9 CCD camera
10 Machine frame
11 X-ray detector
12 “Cross head”
13 Stepper Motor
14 Outer chamber
9
14
8
13
12
10
11
5
4
3
2
1
7
6

Figure 14: LT modifications for micro-tensile testing at temperatures down to 180K. Details are explained in the text.

The sample to be tested (Figure 14: Pos. 1) is placed between two tungsten-carbide grips (Figure 14: Pos. 2) which are mounted on grip holders (Figure 14: Pos. 3). These grip holders are made of machineable ceramic (MACOR®), with a very low thermal conductivity to prevent heat flux from the frame to the sample. On the grip opposite the load cell (Figure 14: Pos. 7), a cold finger (Figure 14: Pos. 4) flushed with liquid nitrogen was clamped. Fixing a similar cold finger on the side with the load cell was not possible because the nitrogen-supply-tubes for the cold finger stiffen at liquid nitrogen temperature. A mechanical connection between the load cell and the sample would adversely affect the force measurement. Therefore, a so-called Cryojet from Oxford Instruments® (Figure 14: Pos. 5 and Pos.8) was used to blow N_2 gas with temperatures down to 100K on the sample and partly on the grip mounted on the load cell side. The length measurement was done with the existing CCD camera (Figure 14: Pos. 9) from top. To prevent ice formation on the sample a two-chamber system was used. The inner chamber (Figure 14: Pos. 6) was flushed with dry nitrogen gas from an inlet close to the load cell. This chamber is made of a polymer frame stringed with a Kapton® foil and had one inlet for the Cryojet nozzle (Figure 15c). On the side of the machine crosshead (Figure 14: Pos. 12) the chamber was open. To prevent any further condensation of humidity the whole set-up had to be shielded from the surrounding atmosphere. This was realized by an outer chamber (schematically shown, Figure 14: Pos. 14) flushed with dry nitrogen. The outer chamber consisted of a soft polymer foil loosely tightened around the set-up to allow an exchange of dry N_2. A view of this set-up including this foil and the arrangements at the beam line can be seen in Figure 15.

- Figure 15a shows the whole set-up enclosed in the outer chamber and a PC screen viewing the length measurement of the specimen.
- Figure 15b shows the set-up during the loading of a sample. The outer chamber – polymer foil – and the inner one – Kapton® foil – are removed. The aluminum tube in the lower right corner is a He flushed X-ray beam guide.
- Figure 15c presents the set-up in operating mode where all chambers are closed. The red light in the center origins from the light diode used for the length measurement.

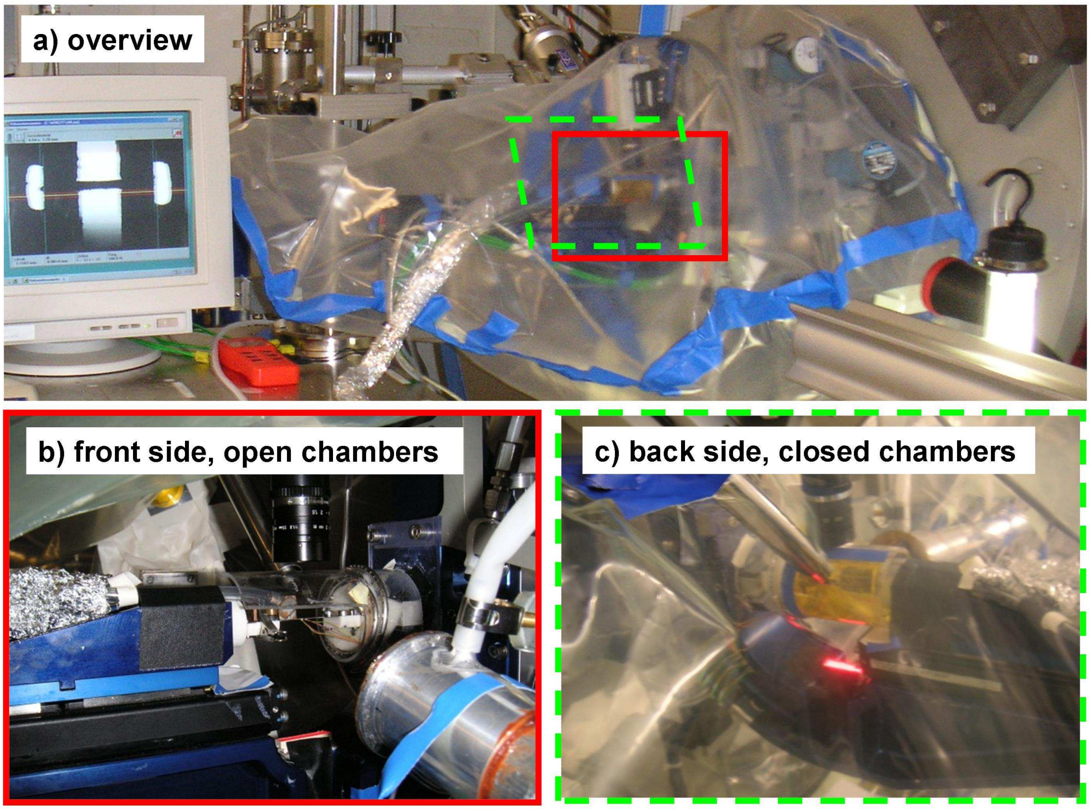

Figure 15: a) Cold temperature set-up at the MS beam line in the SLS. b) Open chambers to load a sample. c) Operating situation where both chambers (outer polymer foil and inner Kapton® tube) are closed.

Temperature measurement

During an in-situ experiment, it was not possible to carry out a temperature measurement on the dog bone. Therefore, a control and calibration measurement had been performed ex-situ previously where three thermocouples (1, 2 and 4) were spot welded on a dog bone and two (3 and 5) glued on the grips (see Figure 16).

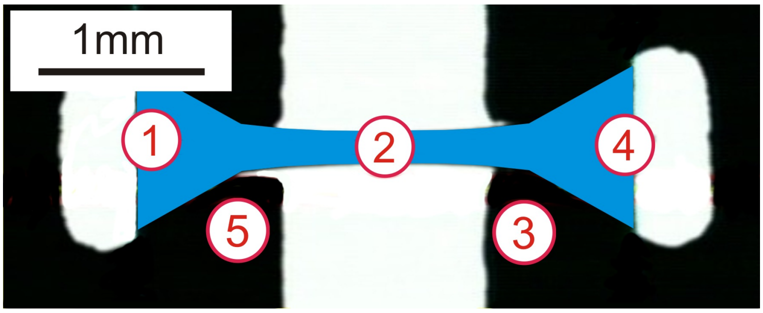

Figure 16: Schematic representation of the thermocouple positions during the temperature calibration measurement.

The five temperatures recorded during the calibration test are shown in Figure 17a. The sample was first cooled with the Cryojet$^{®}$ to a temperature of about 220K (red curve, center of the dog bone). Then the coldfinger was flushed with liquid nitrogen (indicated in Figure 17a) and the dog bone cooled down to the working temperature (indicated with a vertical red line). After the working temperature was achieved, the temperature was stepwise increased by regulating the Crypojet$^{®}$.

Figure 17b shows the temperature differences within the measured points. The maximum gradient within the dog bone at working temperature between points indicated on Figure 16 with (1) and (4) was 14K (cyan). The actual temperature gradient within the gauge section was lower because the measuring points were at the end of the tapers. Nevertheless, it is also clearly visible that adjustable temperatures higher than 180K cause higher temperature gradient in the sample (cyan). For completeness, the differences between points (1) and (2) as well as (2) and (4) are shown in green and black respectively.

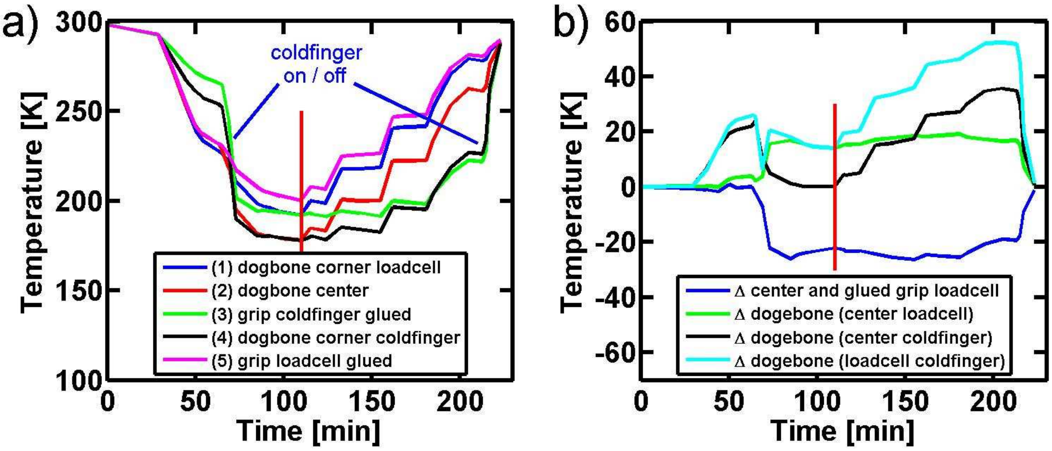

Figure 17: a) Calibration measurement with several thermocouples mounted on the dog bone and the grips. b) Temperature differences emerge during the calibration. The vertical red line marks the usual working temperature (180K).

The temperature difference between the center of the dog bone (2) and the thermocouple glued to the grip on the load cell side (5) is shown in dark blue in Figure 17b. During the time the coldfinger is flushed with liquid nitrogen (temperature below 220K), the difference between these two measuring points is stable with a value around 23K. This correlation allows the measurement of the actual dog bone temperature during a test without physically contacting the sample. Therefore, this thermocouple positioned at point (5) was used in all in-situ LT experiments to determine the sample temperature.

Figure 18 shows an X-ray picture of the grips without the sample. Clearly visible on the left side is the thermocouple (5) glued to the bottom of the grip. The view of this picture is obtained with the X-ray beam position monitor. The high intensity of the synchrotron beam is noticeable by the white band (saturation of the monitor). The rectangular shape reflects the adjusting slits on top and bottom used to narrow the beam.

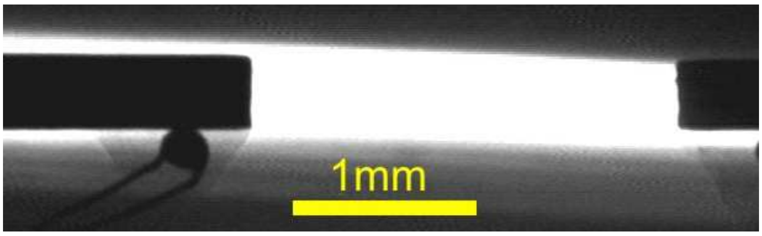

Figure 18: X-ray picture taken at the MS beam line of a thermocouple glued at the bottom of a tensile grip.

2.2.3. Compression testing

The tensile machine as described in the previous Section is also employed to perform compression tests using the same control system, the same machine frame and the same method of moving the crossheads. The transmission of the force from the sample to the frame is carried by the form-fit-connection, which is shown in green in a cross sectional view in Figure 19 for both systems. The machine frame (red streaked), the load cell (black frame), and the grips (gray streaked) are also depicted in Figure 19. The blue line indicates the point of force transmission from the form-fit-connection to the frame in both machines. Figure 19 demonstrates that the form-fit-connection used in the tensile machine would not be able to transfer the force. To account for the differences between the tensile and compression force paths the form-fit-connection was modified for the compression machine.

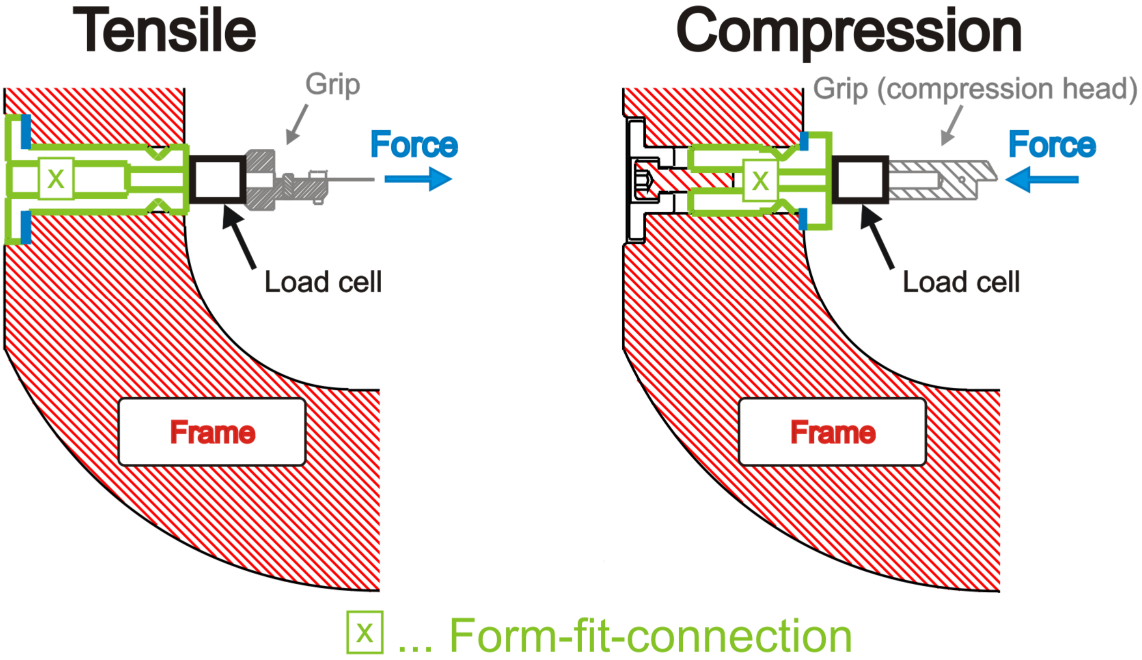

Figure 19: Technical cross sectional drawing of a part of the tensile and compression machine. The different form-fit-connections for tension and compression are drawn in green. The force transfer to the frame is pictured with a blue line.

The compression heads, made out of hardened steel, are shown in Figure 20. They are designed with two types of chamfers: one to reduce the error in the length measurement (Number 1 in Figure 20) and another one to minimize the background noise of the X-rays

(Number 2 in Figure 20). The reductions in width (Number 3 in Figure 20) and height (Number 4 in Figure 20) are made to align the sample with the compression axis.

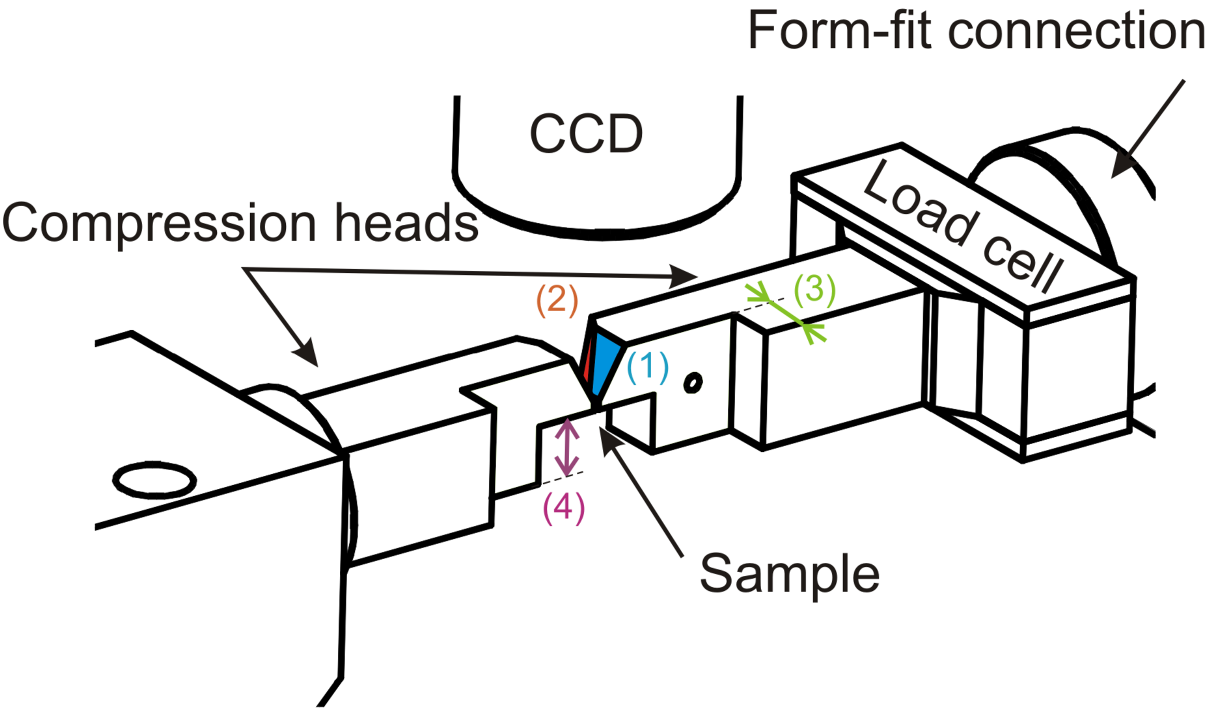

Figure 20: Technical 3D drawing of the compression set-up seen in beam direction. The sample with usual dimensions of 0.2x0.6x0.6mm is not possible to resolve within this resolution. The numbers are described in the text.

Figure 21 shows a compression sample (0.6x0.6mm^2) between the compression heads seen from the length measurement camera (CCD). On top of the figure, one can see part of chamfer (Figure 20, 2) on top of the picture. The red and the blue lines have a function similar as that described in Figure 8 for the length measurement.

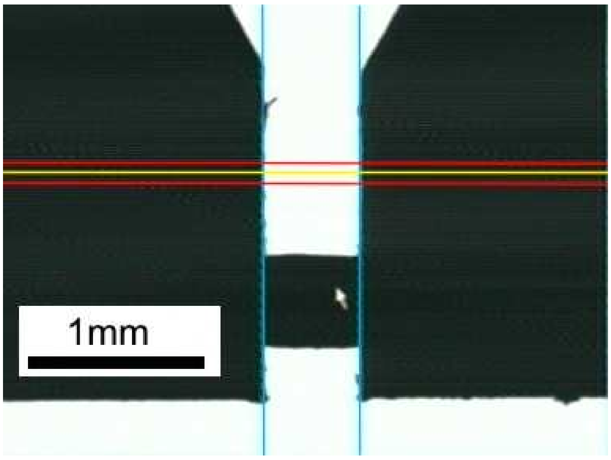

Figure 21: Compression sample seen from the length measuring CCD.

Although the machine is designed to endure at least 1000N in tension, the stiffness in compression is even with the adapted form-fit-connection, relatively low. Several attempts to locate the weak point of the machine failed.

For standard machines a compliance correction is applied assuming the machine behaves as a linear spring. Kalidindi et al. [110] showed that this is not valid and suggested therefore a nonlinear correction, based on a procedure including three different tests. These three tests are known as method I direct technique, method II elastic deformation of known material and method III finite plastic strains. The first method I consists of compressing the crossheads without a sample against each other. Method II is based on the deformation of a material with known elastic modulus and is only valid in the elastic region of the used material. Method III uses the stored plastic deformation of an unloaded deformed sample. It compares the length change measured at the sample with the length change measured with the machine.

In Figure 22, the experimental data of all three methods are summarized. The black data is from method I and the blue data sets originate from using method II at three similar Nickel samples (in the elastic region). The two red data points correspond to measurements based on method III, where the lengths of two plastically deformed Nickel samples are measured afterwards in the scanning electron microscope. For comparison, the load displacement curve (l-d Ref. in Figure 22) from a standard compression machine [110] is shown in green. These results show that there are big differences from one to another sample (method II) and that the MTM is much weaker than a standard test machine.

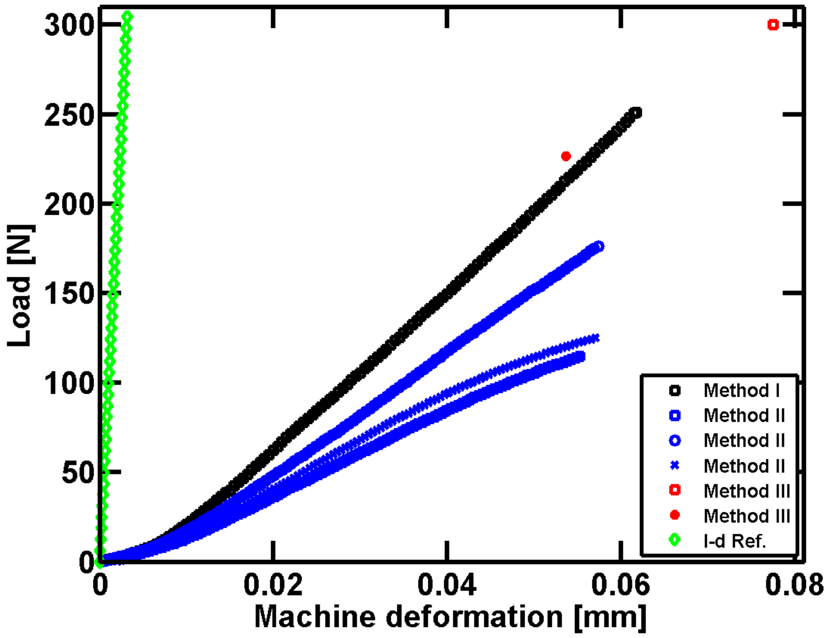

Figure 22: Machine compliance in compression of the MTM. The load-displacement data (l-d Ref.) is the linear part of a standard compression machine [110].

The variations in the measured compliances between the three methods presented above and especial within method II are so big, that one calibration curve – from the average obtained calibration value – would give wrong results if applied to any other sample. Nevertheless, the nonlinearity is weak across the load range and a linear correction with the Young’s modulus of Nickel is the most appropriate and is applied to revise the elongation measurement of the compression tests.

2.3. X-Ray powder diffraction

2.3.1. General

Diffraction of monochromatic X-rays from crystalline structures occurs from constructive interferences according to a simple geometrical relation (Bragg's law),

$$n\lambda = 2 \cdot d \cdot \sin\theta . \tag{8}$$

Here n is the reflection order, λ the X-ray wavelength, d the atomic plane distance, and θ the diffraction angle. The distance d between adjacent planes can be calculated from the lattice cell constant a (3.5239Å for Nickel from reference [111]) and the Miller-indices (*hkl*) of the diffracting plane,

$$d = \frac{a}{\sqrt{h^2 + k^2 + l^2}} . \tag{9}$$

In a perfect single crystal, the diffraction peaks are in principal delta functions and their position can be calculated from (8) & (9). Their integral intensity is influenced by number of factors such as polarization, absorption, multiplicity, temperature, the Lorenz factor, and the structure factor where a detailed description is already given by several authors [111-113]. The diffraction peak widths reflect the coherent scattering length and the local lattice spacing variations (defects) of the tested specimen. More details about the peak width can be found below in Section 2.3.5. The focus within this thesis lies on the changes in the diffraction peak widths and positions during deformation of NC-Nickel.

2.3.2. X-Ray sources

.

Laboratory source

X-ray powder diffraction experiments for pre-characterization of the materials to be studied are performed on a standard machine (Siemens D-500) using a copper cathode (8.047keV) in θ-2θ conditions.

Synchrotron

All in-situ deformation and diffraction measurements are carried out at the MS beam line at the SLS. This beam line operates with a wiggler as primary device to extract the white photon beam from the electron storage ring. To select a specific energy, a double crystal monochromator is used. The focusing of the X-ray beam is obtained by the use of two Rh-coated mirrors. For further minimization of the beam size, several slits are positioned after the focusing mirror. With this set-up, it is possible to change energies from 5keV to 40keV and obtain a good penetration depth (several tens of μm for the highest energies) in most metals. However, the photon flux exhibits a maximum of 10^{13}photons/s around 12keV and decreases with increasing energy. The chosen energy of 17.5keV is a tradeoff between the penetration depth, the fluorescence light from the sample – which would decrease the peak to background ratio – and a reasonable flux. The insertion of 15 filters – different metal films from 100μm to 2mm – allows reducing the beam intensity/flux. The graduation of these filters is energy dependent but the transmission values range roughly from 0.99 to 10^{-6}. More details on the beam line are published in reference [114].

2.3.3. Experimental set-up

Materials science beam line at the SLS

All experiments were carried out at the powder diffraction station at the MS beam line at the SLS, which is placed 36.1m from the X-rays source, the wiggler. A schematic overview of the station is presented in Figure 23. The goniometer (red) placed on top of one lifting table (yellow) allows rotating the sample holder, the Microstrip detector, and a Multicrystal analyzer (not used within this thesis). On the sample holder, the MTM is fixed. The second lifting table provides room for any further set-up equipment.

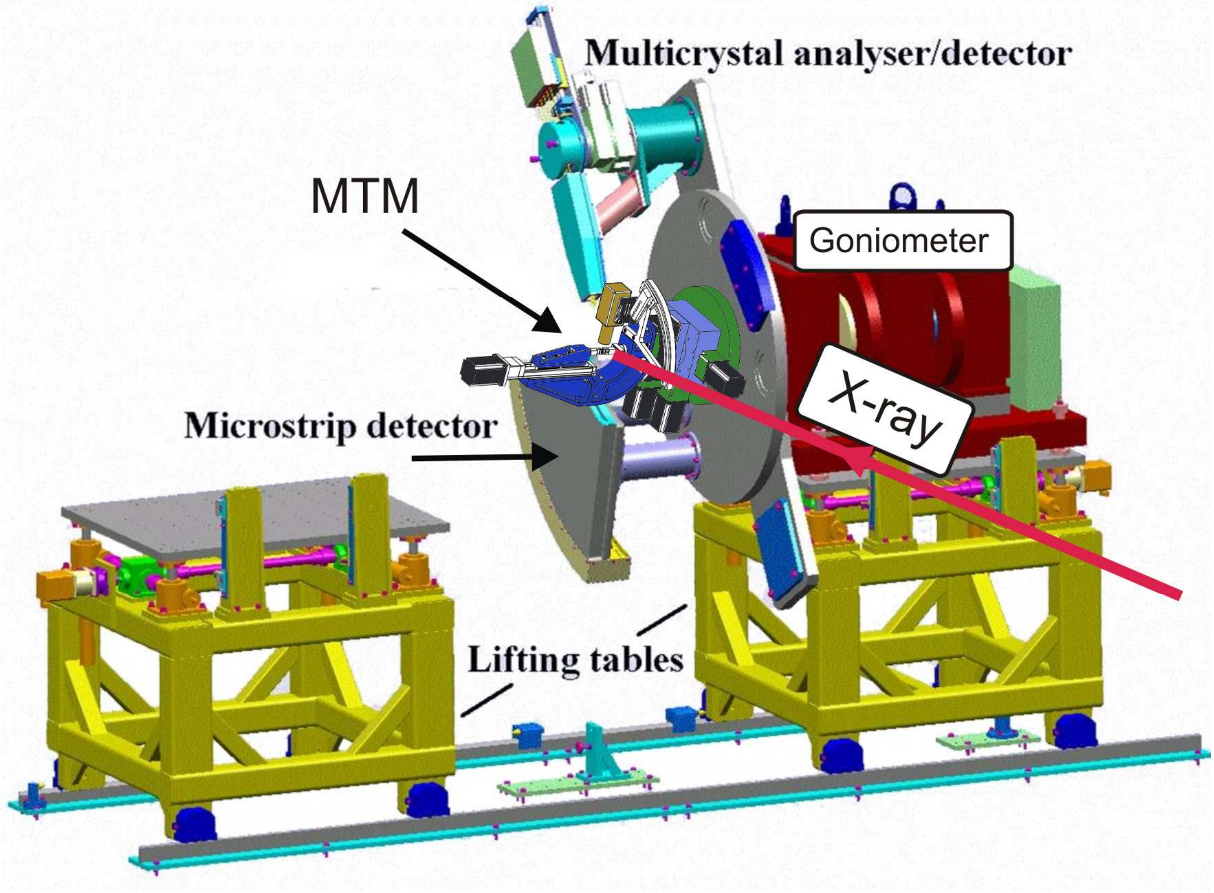
Multicrystal analyser/detector
MTM
Goniometer
X-ray
Microstrip detector
Lifting tables

Figure 23: Schematic drawing of the powder diffraction station at the MS beam line.

Diffraction geometry

For diffraction experiments, the direction of the diffraction vector is essential. Figure 24 shows the geometry of the set-up at the MS beam line. The tensile axis of the sample corresponds with the Y direction. The X-ray beam comes along the X direction and strikes the sample at its lower surface. The Microstrip detector acquires only the component of the diffracted beam cone, which lies in the X-Z plane. Thus, the diffraction vector corresponding with the measured peaks are in the X-Z plane normal to the tensile axis.

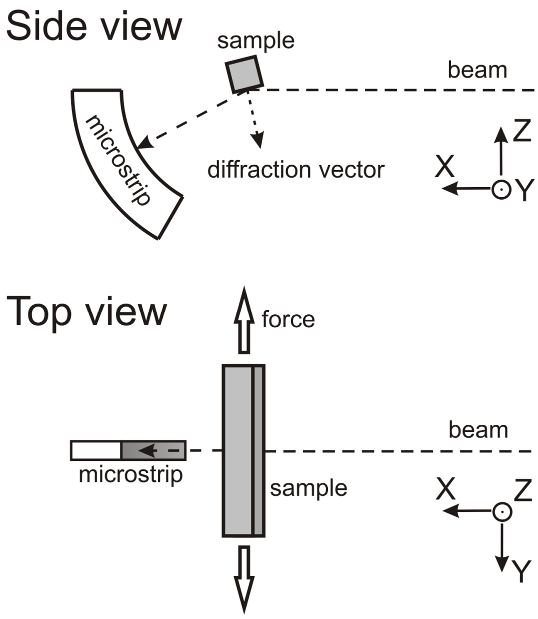

Figure 24: Diffraction geometry at the beam line. The diffraction vector is perpendicular to the tensile direction.

X-ray detection

The goniometer carries the two available detectors (multicrystal and Microstrip) and the MTM (see Figure 23). It also allows that all three components can in principle independently rotated over 360º. From the two possible detector systems, only the Microstrip detector can be used for the in-situ measurements because it allows taking a full pattern of 60º angular range at once. This special system is called MYTHEN detector and described by Schmitt et al. [115]. It operates as a single photon counter and the angular resolution is ~0.004º with a minimum read out time of 250μs. If not specified further, the diffraction patterns are taken every ~16 seconds. The actual exposure time in the order of 10 seconds is a rough optimum between diffracted intensity from the dog bones and the maximum count rate of the detector. The detector itself needs around 6 seconds for a full read out.

Intrinsic to the detector system is that X-ray energy is recorded with a different sensitivity (count rate). Furthermore, at the same X-ray energy differences in the count rate between the cannels can be present. Therefore, each channel has to be calibrated with a homogeneous illumination before a test series (flat field calibration). To obtain such a homogeneous illumination for all channels the fluorescence light of dissolved molybdenum salt with the $K_{\alpha1}$ emission line at 17.5keV is used.

The detector is constructed of 12 separated modules where each of them has 1280 channels. The gaps between these modules cause a missing angular range of approximately 0.2º and can be seen e.g. in Figure 27. Furthermore, there are very few of the total 15360 channels, which are permanently not working (dead channels). Additionally, it can happen that random channels read noise level instead of the actual signal especially if the count rate is over 40k counts (hot channels). A data treatment accounting for such irregular (hot) channels is applied.

One major difference between a standard powder diffraction measurement and the set-up used at the beam line is that the incoming angle and the sample position are fixed whereas in a θ-2θ scan the sample surface follows the center between incoming and outcoming angle. This has important consequences when performed during deformation.

The fixed incoming angle causes that a grain, which initially contributes to a diffraction peak, does not contribute anymore after the lattice spacing has changed e.g. due to elastic loading. Additionally, The MHYTEN system is a line detector and therefore only grains with the diffraction plane orthogonal to the beam-detector plane are in diffraction conditions. The fixed incoming angle and the line detector implies that a large number of grains have to be illuminated by the incoming beam to obtain a decent diffracted signal. A detailed calculation of the fraction of contributing grains with this set-up can be found in the appendix of [99].

Another consequence of the above set-up is that one has to be careful by interpreting peak intensities. For instance, information on the texture can only be obtained if certain assumptions are made about the sample symmetry.

In order to be able to interpret peak profiles from measurements performed in the current set-up one has to evaluate the error coming from the sample geometry. Figure 25 illustrates this broadening schematically.

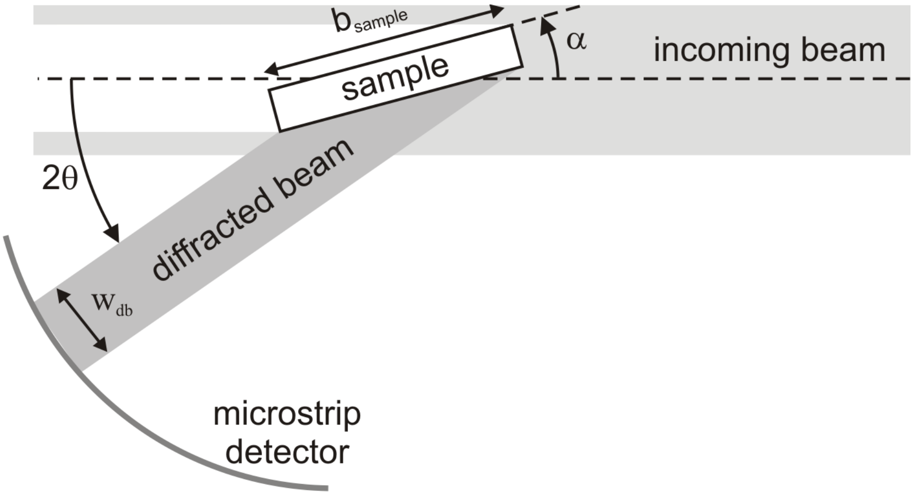

Figure 25: Sample geometry at the MS beam line seen in the tensile direction.

It can be seen that the diffracted beam width (w_{db}) projected onto the detector depends on the breadth of the sample (indicated with b_{sample}) and on the inclination of the sample (α). If the sample is completely illuminated relation (10),

$$w_{db} = b_{sample} \sin(2\theta - \alpha)\,, \qquad \textbf{(10)}$$

can be used to calculate (w_{db}). In case the incoming beam is smaller than the sample, b_{sample} becomes the illuminated size. Figure 26 shows a calculation of (10) for three sample inclinations (α), 10°, 15° and 20°. A nominal sample breadth (b_{sample}) of 200µm is used to calculate w_{db}. The lower limit is the intrinsic detector resolution of 0.004°.

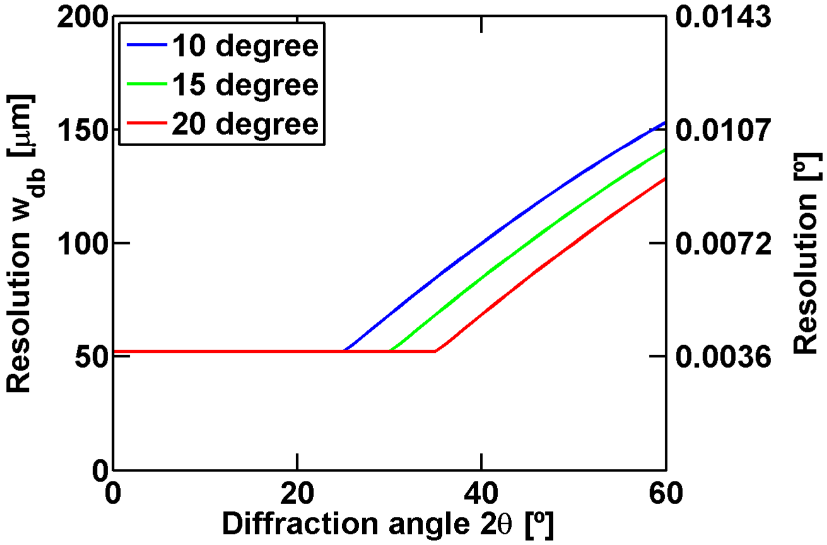

Figure 26: Peak broadening by the sample with a breadth of 200µm. Resolution on the left side corresponds (10) and the right side is recalculated to angular values with the sample to detector distance of 80cm.

In the case of NC- Nickel, the peak broadening due to grain size and strain is at least 0.15° for the narrowest peak (111) at 17.5keV. Figure 26 shows that the broadening due to the sample geometry is at least one order of magnitude smaller than the broadening of the diffraction peaks from NC Nickel. More details of the in-situ set-up are published in [99].

2.3.4. Data treatment

The powder diffraction data recorded from any experiment is available as intensity versus diffraction angle. Each diffraction peak is cut out of the full spectra and fitted separately with a split Pearson-VII (P-VII) function (11) plus a linear function as background.

$$\begin{aligned} P(\theta) &= H\left[1+(2^{1/M_R}-1)(10^{\alpha}+1)^2\left(\frac{\theta-\theta_0}{w}\right)\right]^{-M_R} && \text{if } \theta \geq \theta_0 \\ P(\theta) &= H\left[1+(2^{1/M_L}-1)(10^{-\alpha}+1)^2\left(\frac{\theta-\theta_0}{w}\right)\right]^{-M_L} && \text{if } \theta_0 \leq \theta \end{aligned} \tag{11}$$

θ is the diffraction angle, θ_0 the angle which correspond with the peak maximum, H the peak height, w the full-width at half-maximum (FWHM), α the (logarithmic) asymmetry parameter, and M_R and M_L, respectively, the right and the left decay exponent. The integrated area is calculated over an angular range of eight times the FWHM of the peak. The integrated width is defined as the integrated area divided by the height of the peak.

From the calculated residuals r_i,

$$r_i = I_i - P_i - bg_i, \tag{12}$$

a least-square objective function is constructed,

$$\chi^2 = \sum_i \left(\frac{r_i}{\sqrt{I_i}}\right)^2. \tag{13}$$

Here I_i is the intensity, P_i the P-VII fit and bg_i the background fit where the subscript i correspond to a certain channel recorded from the Microstrip detector. Each channel has a direct relation to its diffraction angle θ_i. The used robust-least-square algorithm [116] is performed iteratively by reweighting the objective function in the following way:

1.) Fit the model by an unweighted least squares (that is, χ^2).

2.) Calculate the standardized residuals $R=r_i/Ks$, where K is a tuning constant (4.685) and s is the robust variance given by MAD/0.6745 (MAD is the median absolute deviation of the residuals).
3.) Compute the robust weights via $w_i=(1-u_i^2)^2$ if $|u_i|<1$ (i.e., if $r_i<Ks$) and $w_i=0$ otherwise.
4.) Redo the fit with weighted minimizer: $\chi^2=\sum_i w_i\left(\frac{r_i}{\sqrt{I_i}}\right)^2$
5.) Repeat the steps 2 to 4 until the MAD changes no more than a selected fractional tolerance.

Figure 27 presents a 111 diffraction peak of NC-Nickel in the as prepared state. The X-ray energy was 17.5keV and the fit was performed with a split P-VII function. The fitted distribution of the diffraction peak exhibits a peak position of 20.049°, a FWHM of 0.17855°, a integrated width of 0.2448°, a height of 9805.5 counts, a M_L value of 1.40, a M_R value of 1.17 and a asymmetry parameter a of $-2.16*10^{-3}$ whereby the background was fitted with a first order polynomial.

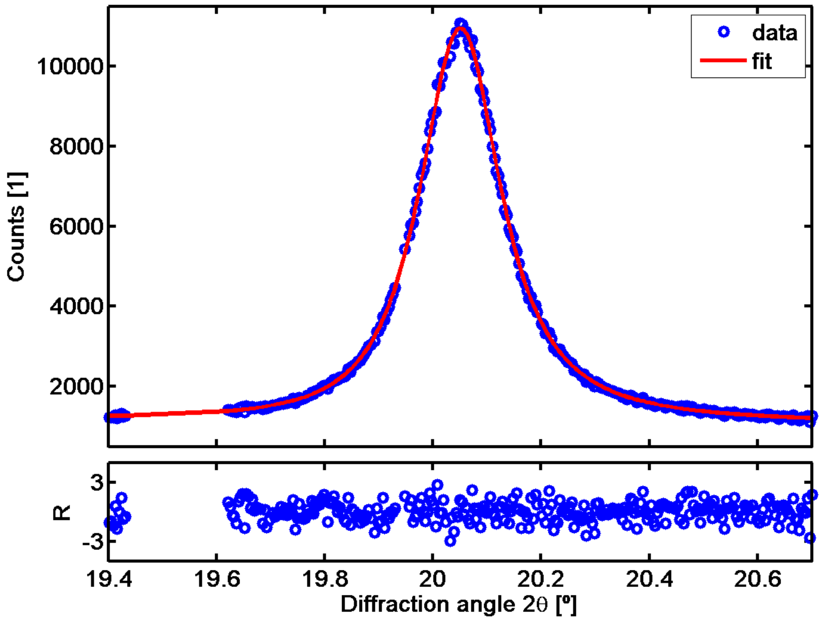

Figure 27: 111 diffraction peak of NC-Nickel and its fit (red). The R-values are the standardized residuals of the fit. The data gap seen around 19.5° originates from the gap between the single modules. The smaller gaps originate from hot channels from the Microstrip detector.

Figure 27 shows as well the standardized residuals *R*. The good quality of the fit is evident through the smooth character of the residuals as well as the fact that none of the standardized residuals is larger than three [99].

2.3.5. Extracting structural parameters

Scherrer derived already in 1918 a formula [117], which allows calculating the crystallite size *c* of a powder spectrum using only the FWHM of a diffracted beam at a certain diffraction angle θ_B,

$$c = \frac{0.9 \cdot \lambda}{FWHM \cdot \cos\theta_B} . \tag{14}$$

The deduction of this formula is based on the coherent scattering length parallel to the diffraction vector. This formula does not consider contributions to the FWHM for variations in the lattice spacing, which for instance arise from dislocations and other defect structures.

Based on the work of Stokes and Wilson [118], Williamson and Hall [119] derived a method which allows the deconvolution of the integrated width δ in two parts. One of these parts originates from the coherent scattering length and the other one from the variations in the lattice spacing – RMS-strain. This method requires analyzing of multiple diffraction peaks from one pattern.

Williamson and Hall method

In the Williamson and Hall (WH) approach, the idea of deconvoluting the size and strain contribution lies in their different angle dependence. In general, the total diffraction peak width, δ_θ^{total}, can be written as a combination of size and strain broadening,

$$\delta_\theta^{total} = \delta_\theta^{size} + \delta_\theta^{strain} . \tag{15}$$

For the size contribution,

$$\delta_\theta^{size} = \frac{\lambda}{L\cos\theta} , \tag{16}$$

a formula similar to the Scherrer formula (14) is used. The crystallite size *c* in (14) is now defined as *L* the average column length seen by the X-rays. The contribution from the strain δ_θ^{strain} [113] is written as,

$$\delta_\theta^{strain} = 4e\tan\theta , \tag{17}$$

where e is an upper limit for the inhomogeneous strain. The commonly used value is the RMS-strain $<\varepsilon^2>^{1/2}$ which is 4/5 of e.

The size and strain contributions described in (16) and (17) depend in a different way on the diffraction angle. However, if a change of variables is performed from the diffraction angle θ to the scattering vector s,

$$s \equiv \frac{2\sin\theta}{\lambda}, \tag{18}$$

the broadening can be written as,

$$\delta_s^{total} = \delta_\theta^{total} \frac{2\cos\theta}{\lambda}. \tag{19}$$

Now the size broadening in can be rewritten as,

$$\delta_s^{size} = \frac{1}{L}, \tag{20}$$

and the strain broadening as,

$$\delta_s^{strain} = 2es. \tag{21}$$

The size broadening as it is written in (20) is independent of the diffraction vector but the strain broadening depends on the diffraction vector (21). This allows now separating the size and strain component of the total diffraction peak broadening.

Here a comment concerning the usage of different definitions for the diffraction peak width is necessary: To be consistent with literature, the experimental peak widths are presented by their FWHM within this thesis. However, if the WH method is carried out to separate size and strain contributions – as described in this section – the integrated width of the peak profile is used.

In order to deconvolute δ_θ^{total} into size and strain contributions one needs for each part a line profile function. The aim is to match the distribution occurring from size and strain to a Gaussian or to a Cauchy type function. In the literature, three different methods are commonly mentioned. Two methods where the same type of function is used for both contribution – the so-called Cauchy-Cauchy or the Gaussian-Gaussian way – is according to Klug [113] not sufficient to describe the separation of the contributions. Therefore, the method of deconvoluting the size and strain contributions by Cauchy-Gaussian way is suggested. This supposes that crystallite size distribution influences the peak in a Cauchy way and the strain in Gaussian way. The total width is given by,

$$\delta_s^{total} = \delta_s^{size}\left(\frac{\exp\left(-\left(\delta_s^{size}/\delta_s^{strain}\right)^2/\pi\right)}{1-erf\left(\sqrt{2/\pi}\left(\delta_s^{size}/\delta_s^{strain}\right)\right)}\right), \tag{22}$$

where the erf(x) is defined by,

$$erf(x) \equiv \frac{1}{\sqrt{2\pi}}\int_0^x e^{-t/2}dt\,. \tag{23}$$

This relation is approximated by,

$$\frac{\delta_s^{size}}{\delta_s^{total}} = 1-\left[\frac{\delta_s^{strain}}{\delta_s^{total}}\right]^2, \tag{24}$$

with an error of at most 10 per cent [120]. By resubstituting (20) and (21) it results in,

$$\left[\frac{\delta_s^{total}}{s}\right]^2 = 4e^2 + \frac{1}{L}\left[\frac{\delta_s^{total}}{s^2}\right]. \tag{25}$$

Now the linear fit through the two defined relations $[\delta_s^{total}/s]^2$ and $[\delta_s^{total}/s^2]$ (25) will lead to the column length L and the RMS-strain $<\varepsilon^2>^{1/2}$.

Defects such as dislocations have a directional strain field. This non-rotational symmetric strain field suggests that only peaks from the same diffraction family should be used for the WH analysis.

Warren-Averbach method

For completeness, another method to extract the size and strain contribution is mentioned. It is based on a Fourier analysis where the peak has to be described by its Fourier coefficients determined from the peak intensity $I(\theta)$ via,

$$A(L) = \int I(\theta)\exp(-2\pi i\theta L)d\theta\,. \tag{26}$$

If the Fourier coefficient are plotted with respect to their harmonic number, Bertaut [121] showed that the initial slope of this correlation gives a measurement of the crystallite thickness. However, he considered only a size effect. Warren and Averbach [112, 122] included lattice distortions, strains, and stated that the cosine coefficient $A(L)$ in (26) is a multiplication of the cosine coefficient from size $A^D(L)$ and strain $A^\varepsilon(L)$,

$$A(L) = A^D(L)A^\varepsilon(L)\,. \tag{27}$$

The strain coefficient A^{ε} can be written as,

$$A^{\varepsilon}(L) = \cos(2\pi L Z_n) . \qquad \textbf{(28)}$$

Z_n is the displacement difference between different coherent diffraction cells along the diffraction vector q. Due to the possible exponential expansion [112] of the strain function (28), the logarithmic coefficient can be established via

$$\ln A(L,q) = \ln A^{D} - 2\pi^{2} L^{2} < \varepsilon^{2}(L) > q^{2} . \qquad \textbf{(29)}$$

More details about this procedure can be found in the book of Warren [112]. The hot channels (see Figure 27) impede the Warren-Averbach method and moreover to keep consistent with earlier performed work [69, 85, 99] only the above presented WH method is used within this thesis.

Modified methods

The above-described methods assume an isotropic broadening of the peaks. If this is not the case, one has to restrict the analysis to the same peak family. To visualize such effects a schematic drawing of the so-called WH plot is shown in Figure 28. There the peak widths are plotted with respect to there peak positions.

The WH-plot of a strain free material is diffraction order independent. It will result in horizontal line (black data). If isotropic strain is present in the material, higher-order diffraction peaks will broaden more and the data presented in the WH-plot of this material will have a constant slope (red data). If the strain in the material is not isotropically distributed, the coherent scattering length is orientation dependent and the different diffraction peak widths will be influenced differently. This is shown schematically with the blue data in Figure 28 and one refers to it as WH anisotropy.

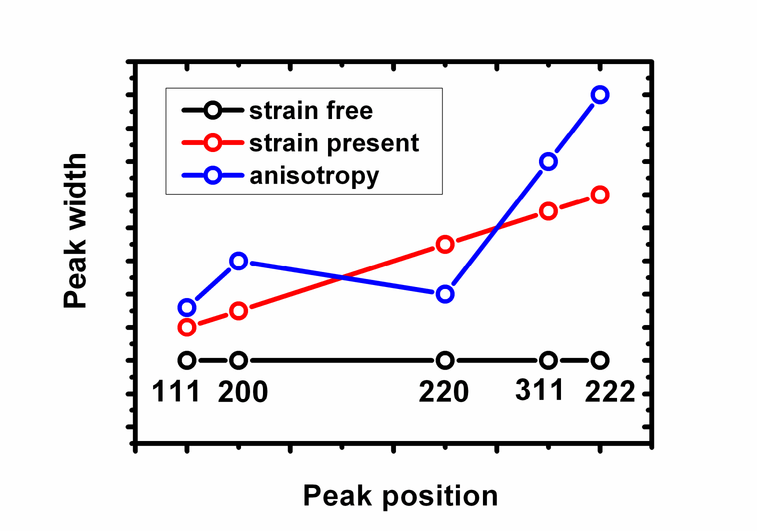

Figure 28: Schematic WH plot for three possible situations.

If one (some) type(s) of defect(s) is(are) present, one can estimate/calculate the contribution to the anisotropy. Warren had for example shown the influence of faulting [112] on the behavior of the different diffraction peaks.

Several models and methods where developed over the time to explain the appearing anisotropy [112, 123-125] and relate them to lattice dislocations, stacking faults and/or twin fault content. Ungar [126], used a concept from Krivoglaz [123] to modify the Warren-Averbach method where they included theoretical calculated dislocation contrast factors in the analysis. With this concept, it is possible to relate the measured peak broadening from several peaks not only to size and strain but also to a dislocation density. However, this approach assumes that all the contributions come from one type of defect and it ignores other possible contributions e.g. triple lines. Furthermore, within bulk NC structures a high density of GBs is present which contribute to diffuse scattering.

In this thesis it could be shown (see Section 3.5), that the presence of dislocations in the grain interior is not a requirement to explain the WH anisotropy when the grain size is in the nm regime. Dislocations that are incompletely absorbed in the GBs or extrinsic to the GBs can cause a similar WH anisotropy. Therefore, a method such as that suggested by Ungar et al. [127] to extract dislocation densities from peak broadening are not very appropriate for bulk NC materials and only simple and very limited types of defects can be assumed and studied.

Another approach performed from Scardi et al. [128] is to introduce all types of defects (e.g. crystallite size, dislocations, stacking faults, twins; and their distribution) into a physical model and simulate the full pattern. It is then possible to model the diffraction data and refine the parameters until experimental obtained data is accurately described. Such an approach is called whole powder pattern modeling (WPPM) but is, due to the lack of reliable models to describe the complex microstructure of NC-Nickel, not carried out within this thesis. A resent and comprehensive overview on used diffraction peak analysis techniques is given by Mittemeijer and Scardi [129].

2.4. 3-dimensional atom probe

In order to address a possible influence of impurities on the deformation behavior of NC-Nickel it is important to know their local distribution. The only method to extract atomic positions is the 3DAP technique. The principle of the 3DAP originates from the field ion microscope (FIM). Therefore, the FIM will be explained first.

2.4.1. FIM

The FIM is based on electric field ionization of gas atoms (Ne, He, Ar …) and the possibility of guiding these ions via an electric field. The gas atoms are usually called image gas because they are generating the magnified picture of the studied sample. A schematic set-up is illustrated in Figure 29.

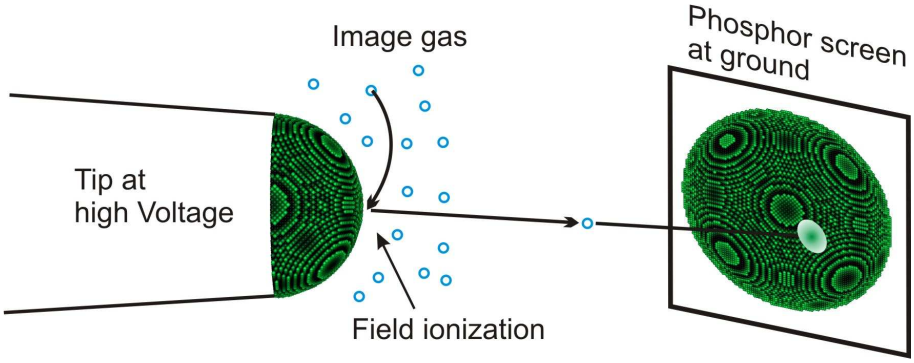

Figure 29: A schematic representation of a field ion microscope. Ionized image gas atoms are projected towards the phosphorus screen. The shown tip is Nickel single crystal half sphere with 17nm diameter.

The basic components of a FIM are a vacuum chamber, a phosphorus screen, image gas, a high voltage source and of course the testing specimen. This specimen has to be in needle shape with a small tip radius. This is necessary because a high electric field *E* is essential for the operation of the microscope and it depends directly from the tip radius r (30),

$$E = \frac{V}{k_f r}. \qquad \textbf{(30)}$$

k_f is a numerical constant in the order of 5 [130]. The image gas atoms eventually collide with the tip. If their kinetic energy is low enough, they can be trapped by the electric field. If the electric field is sufficient high (usual 10 to 50V/nm), it can ionize the image gas atoms by a tunneling process. Such produced ions are then radially repelled in form of a stereographic-like projection and collide into the electrically grounded phosphorus screen.

Atomic steps and structures such as GBs or different chemical compositions cause local variation in the electric field. These variations give finally the image contrast seen on the phosphorus screen. The possible magnification is very high because it is proportional to the inverse tip radius times the sample detector distance.

However, the high electric field may cause as well desorption of atoms by field evaporation. This process of field evaporation guides now to the principal of 3DAP.

2.4.2. 3DAP

In contrast to FIM, which functions with an image gas, the 3DAP uses the specimen atoms to obtain an image. The aim is to evaporate single atoms from the surface and detect these with chemical and positional sensitivity.

- For the evaporation of single atoms, the tip will be imposed a voltage below the evaporation limit of the test specimen. Superimposed short electric pulses are applied. Careful adjustments allow then that every n-th pulse removes only one atom of the specimen.
- A multi-anode system [131] is used for areal detection on the screen.
- The chemical sensitivity is obtained via the time-of-flight principle. There the time is measured between the “start” of one atom, known from the electrical pulse, and its “arrival” on the detector. Knowing the sample detector distance (*L*) and measuring the flight time (*t*) the mass (*m*) per charge (*n*) can be calculated (31).

$$m/n = 2eV(t/L)^2 \tag{31}$$

The presented method allows now chemical and area sensitive determination of each detected atom. If this information is combined with appropriate software, it is possible to reconstruct a 3-dimensional picture of the evaporated specimen [132].

However, several challenges complicate this technique and raise numerous restrictions. First, the tip has to be cooled to temperatures between 20-100K to reduce the atomic movement and increase the spatial resolution of the position detection. In front of the actual detector, a so-called micro channel plate (MCP) [133] is necessary to enhance the signal to a detectable level. This MCP has only 60 percent sensitive surface and therefore not every arriving ion can be counted. However, each ion produces in the MCP ~1000 secondary electrons resulting in an intense signal on the detector. Furthermore, only metals can be studied due to the necessity of imposing an electric field for repelling ionized atoms. Moreover, to be able to use only moderate voltages (below 20keV) the sample tip has to be in the order of 100nm.

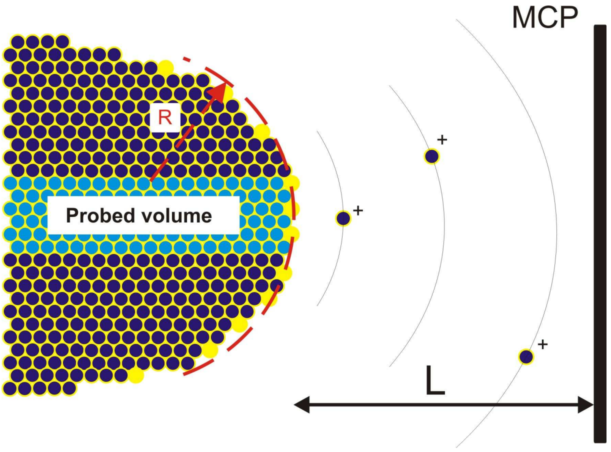

Figure 30: A schematic sample tip in a 3DAP configuration.

If the sample of interest is metallic and it is possible to get a tip radius smaller than 100nm it can be studied with 3DAP. However, the probed volume will be rather small (see Figure 30). The radial projection and the detector area (only the primal MCP is shown) limit the studied volume to a few nm in diameter. The length of the probed volume is limited to the stability of the tip and the maximum evaporation field e.g. the maximum applicable voltage. With ongoing evaporation, the tip will blunt and the evaporation field (*E*) decreases (30).

To obtain a reasonable amount of atoms the above-mentioned electric pulses have to be applied at very frequently (~2kHz). These fast changes of high electrical field can destroy the specimen, especially those which are not homogeneous, such as multilayers and NC systems. The NC material studied within this thesis is very sensitive to mechanical failure caused by the electric pulses. Therefore, pulses from a femto-second laser shot on the tip served as short-term field enhancer to evaporate surface atoms.

The 3DAP measurements are carried out in collaboration with M. X. Sauvage from the department *Groupe de physique des matériaux* of the *Université de Rouen*.

2.5. Simulated diffraction pattern

2.5.1. Molecular dynamics (general)

MD simulations calculate the trajectory of N particles according to Newton's law where the interaction of these particles is described by an atomic potential. The initial conditions of a simulation contain the number and positions of the atoms and the temperature, whereby the latter is described by the mean velocity of the atoms. The boundary conditions describe the boarders of the arrangement – fixed or free surfaces – as well as a possible periodicity. The atomic potential describes the interaction of the atoms by a multi atom energy function,

$$V(r_1,...,r_N)\,. \tag{32}$$

Here, $r_1,..,r_N$ are the $3N$ coordinates of the atomic configurations. The basic numerical task is to solve then the Newtown equation of motion,

$$m_i\ddot{r}_i(t) = F(r_1,...,r_N) = -\nabla_i V(r_1,...,r_N) \tag{33}$$

whereby the index i represents all atoms/atom positions r from 1 to N. Since one is interested in the trajectory of the atomic position, one has to integrate numerically Newton's equation (33). For this purpose a predictor-corrector scheme is used which is also called Gear algorithm. Details on integration method can be found in the appendix of reference [134].

2.5.2. Sample construction

The sample construction includes the buildup of the atomic structure, the relaxation (according to the atomic potential function) and the equilibration (choice of temperature) of the atomic configuration.

Samples used in this thesis are NC arrangements of Aluminum atoms. To construct these samples the Voronoi technique is used [135]. Therefore, a number of crystallite center points (seeds) are chosen randomly within a box. In each center, a randomly rotated FCC structure is placed. According to the Voronoi construction, each crystallite extends until half of the distance to the closest neighboring grain center. The construction can cause that, on the border between two crystallites, the atoms are placed much closer than the nearest neighbor distance. To avoid such configurations atoms that are close then 80% of the nearest neighbor distance are removed.

After geometrical construction, the sample contains atomic positions e.g. GB atoms, which are far from a local energy minimum. Therefore, the structure has to be relaxed by molecular static runs. Afterwards, the sample is heated to testing temperatures (applying a distribution of random velocities) and thermally equilibrated during several MD runs in order to get a Boltzmann distribution of the velocities. In this way, a cell structure is constructed as it can be seen in Figure 31. The coloring of the atoms is according to local crystallinity where gray atoms represent FCC, red hexagonal close-packed (HCP), blue other 12-coordinated and green non 12-coordinated atoms [136].

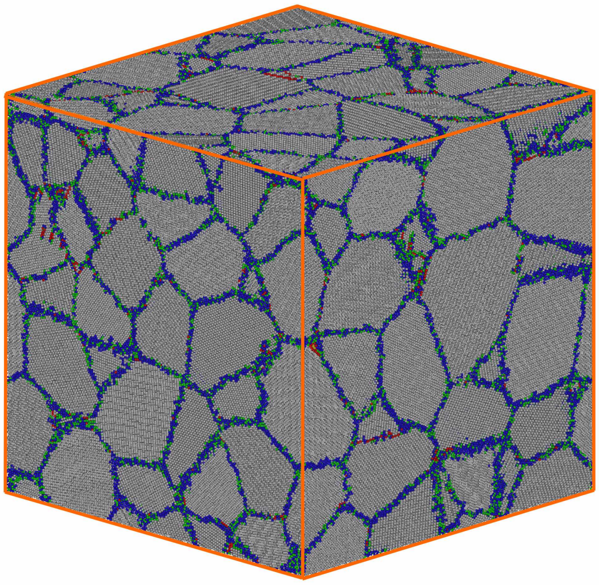

Figure 31: NC arrangement of FCC lattice. The orange lines show an edge of periodicity. For atom coloring, see text.

2.5.3. moldyPSI

The program used to perform the simulations is called moldyPSI. It is a parallelized FORTRAN code based on the program moldy [137]. It can handle multimillion atom structures and computes several thousand time-steps in a reasonable time. The code is capable of performing molecular statics and MD simulation and has on-the-fly analysis tools. The potential used to calculated Aluminum interactions is an embedded atom potential developed by Mishin [138].

2.5.4. Deforming computational samples

The relaxed and equilibrated structure is then deformed by applying a uni-axial constant stress under full three-dimensional periodicity via the Parrinello-Rahman technique [139]. The temperature is kept constant via rescaling the atomic velocities every 50 MD steps by a factor $\sqrt{T_{actuall} / T_{desired}}$.

2.5.5. Calculating XRD diffraction pattern

Derlet et al. [14] derived a method to calculate the XRD spectra from the atomic positions of a simulation cell. The diffraction intensity I can be calculated (34) for a certain scattering vector $k=2\pi\sin(\theta/\lambda)$ for a given wavelength λ,

$$\begin{aligned} I(k) &= 1+\int_0^{r_c} dr\, l(r)\frac{\sin kr}{kr} + 4\pi\rho\left(\frac{r_c \cos kr_c}{k^2} - \frac{\sin kr_c}{k^3}\right) \\ &\approx 1+\int_0^{r_c} dr\, l(r)\frac{\sin kr}{kr} + 4\pi\rho\frac{r_c \cos kr_c}{k^2}\,. \end{aligned} \tag{34}$$

For computational time reasons the inter-atomic pair correlation function $l(r)$ is computed only until a certain cut-off radius r_c, which is typically slightly bigger than the grain size. Above the cut-off radius, a bulk density ρ is used to describe the pair correlation function. This approximation is valid if the cut-off radius is much bigger than the wavelength, which is the case in the studied samples (r_c ~ tens of nm, $\lambda < Å$).

2.5.6. Calculating internal stress

Atomistic simulations essentially contain information on the atomic position and allow calculating the internal stress distribution within the sample. Cormier et al. [140] accomplished with (35) an improvement over the usual Virial expression for local stress in that it rigorously satisfies conservation of linear momentum for the chosen volume element.

$$\sigma_{\mu\nu}^{\Omega} = \frac{1}{\Omega}\left\langle \sum_{i\in\Omega} m v_{i,\mu} v_{i,\nu} + \frac{1}{2}\sum_{i\in\Omega,j} F(r_{ij})\frac{r_{ij,\mu} r_{ij,\nu}}{r_{ij}} l_{ij} \right\rangle \tag{35}$$

In (35), $F(r_{ij}) = F(|\vec{r}_i - \vec{r}_j|)$ represents the force magnitude between atoms i and j, at positions r_i and r_j with corresponding velocities $\vec{v}_i$ and $\vec{v}_j$ .Thus for each chosen volume element, the stress is determined by the individual atomic Virial stress contributions only within the volume element (l_{ij} representing the fraction of the bond between atoms i and j within the volume Ω). The $\langle \cdots \rangle$ represents a time average taken during a MD simulation. The volume element is chosen to be a sphere centered at each atom with a radius that is approximately half way between the first and second nearest neighbor shell (~4Å). More details can be find in reference [14].

3. Results

3.1. Plastic deformation of nanocrystalline Nickel

Plastic deformation of NC-Nickel at RT studied in-situ with X-ray diffraction was for the first time carried out by Budrovic [85]. Since then, the set-up at the beam line has been improved in terms of detector quality and pattern recording speed, resulting in an increase in the resolution in measured peak broadening. Therefore, the research was started by carrying out the same test as performed by Budrovic with the goal to explore what can be learned from the increased resolution. Figure 32 shows the stress strain and stress time data of this test. The sample was loaded two times to the plastic region with a long waiting time of 130 minutes before reloading.

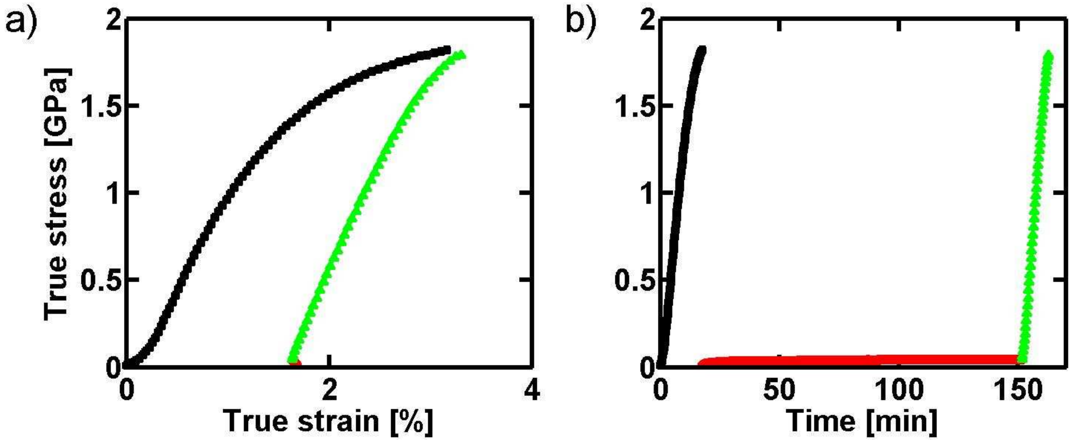

Figure 32: a) Stress strain data of NC-ED Nickel and b) corresponding stress time data.

Figure 33 shows the FWHM of six peaks during the first and second loading cycle.

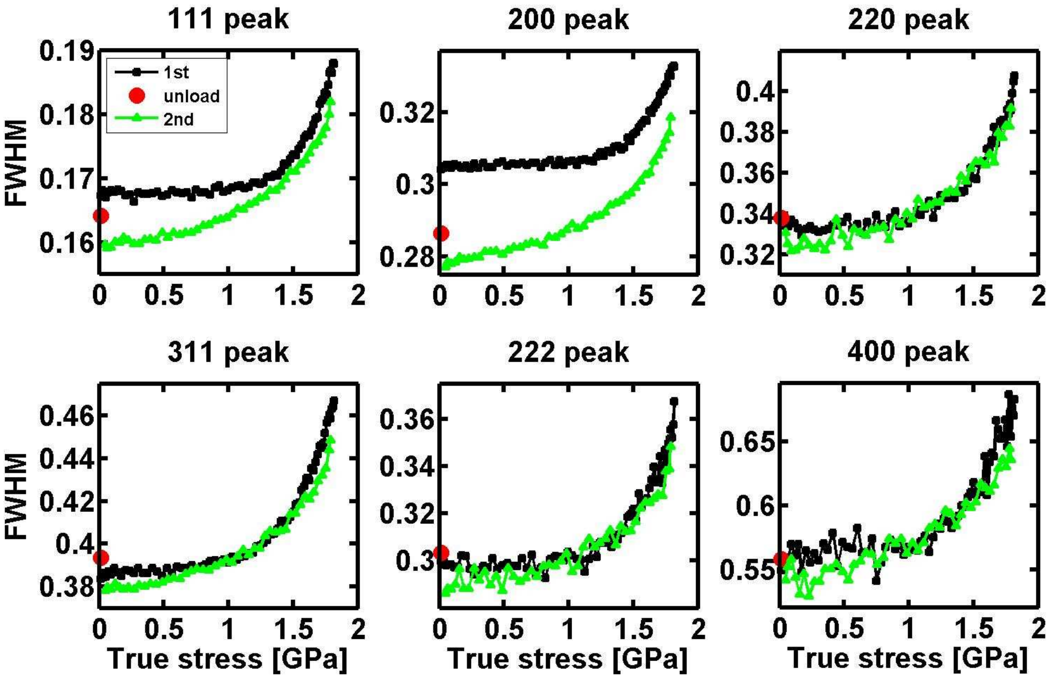

Figure 33: FWHM behavior during the first (black) and second (green) loading data. The blue dot is the first value upon unloading.

During initial loading until ~1GPa, the FWHM (black data) stays unchanged or shows a very slight increase. Around ~1.3GPa, the FWHM starts increasing drastically as a function of stress for all peaks. Immediately after unloading, the FWHM recovers to a value indicated by the red dots. These values differ sometimes from the values prior to loading, with a clear decrease in FWHM recorded for the 200 peak and slight increase in FWHM recorded for the 311 peak. During a waiting time of 130 minutes, a time dependent reduction in the FWHM is observed for all peaks and after 130 minutes all FWHM values are smaller then those of measured prior to loading. In the second loading cycle (green data), the FWHM increases for all peaks even below 1GPa, which is remarkably different when compared to the behavior during the first loading cycle. Furthermore, the change in slope is more gradual during the second loading as the sudden change observed during the first loading. Once ~1.5GPa is reached, the behavior of the FWHM is similar to that of the first loading cycle.

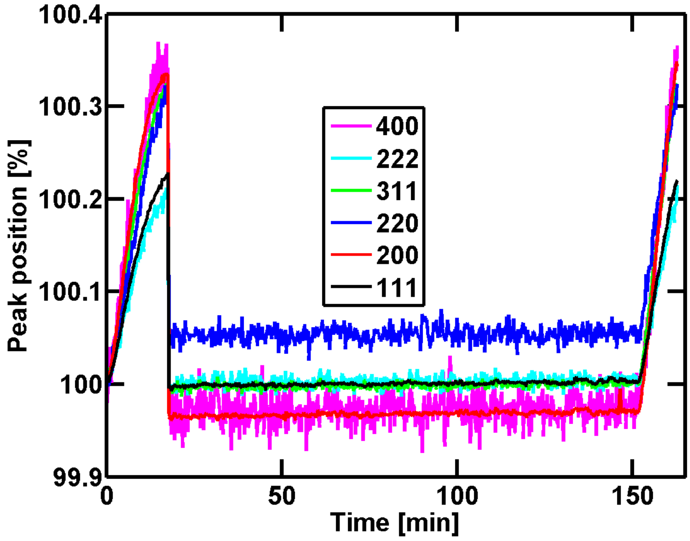

Figure 34: Relative peak positions plotted versus time.

Figure 34 shows the peak positions as a percent of their initial value. The 111, 222 and 311 peaks are complete reversible upon unloading. The 220 peak position increases and the peak position of the 200 peak family decreases after plastic deformation causing a relative change to the initial peak position.

Main findings:

Load-unload experiments show a change in peak broadening behavior during successive deformations and peak dependent FWHM reduction upon unloading from the fully plastic regime. To address the change in broadening and the onset of reduction the transition from the elastic to the plastic regime – the microplastic regime – more detailed load-unload cycles have been performed and are presented in the following.

3.1.1. Load-unload cycles in the microplastic regime

Stress strain data

In Figure 35A, and Figure 35C, the mechanical data of the tests performed to investigate the transition from the elastic to the plastic regime – microplastic regime – in NC-Nickel is presented. Additionally, the comparison with UFG-Nickel is given (see Figure 35B and D). In detail, there are two series of five loading cycles performed, where in one series each loading stress level was higher than the one before. In each cycle, the specimen was unloaded as fast as possible at the pre-defined force. Then the sample was kept for 20 minutes around 10MPa, which is less than a ~500th of the ultimate tensile strength. This stress was necessary to keep the sample in the sample holder. The samples were loaded up to respectively 25%, 40%, 60%, 75% and 95% of the UTS.

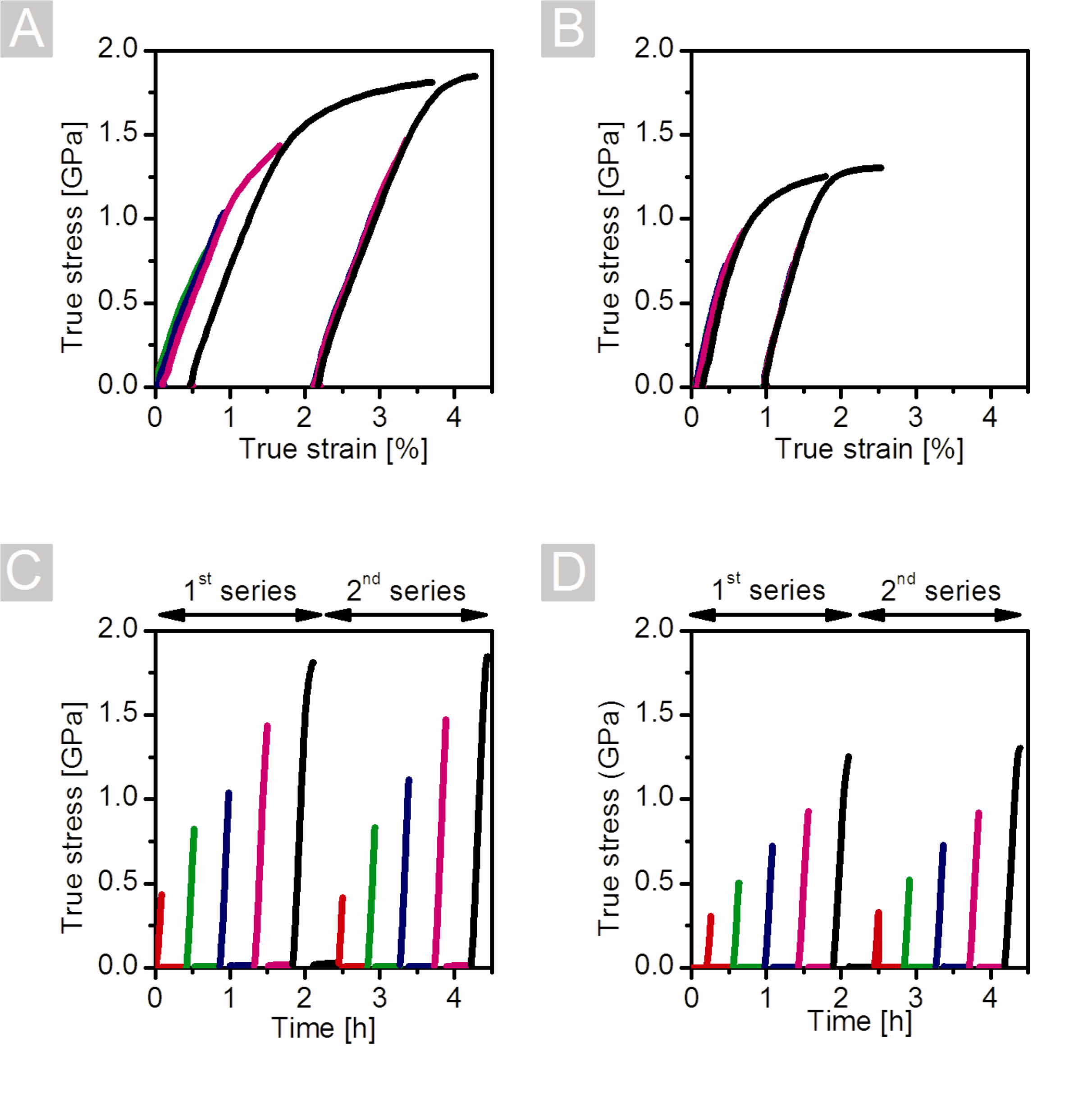

Figure 35: Load-unload cycles performed at NC Nickel (A, C) and UFG-Nickel (B, D) are shown in terms of stress strain (A, B) and as stress time (C, D). The latter emphasis the waiting time between the loading cycles.

FWHM data

Figure 36 presents now the FWHM for selected diffraction peaks of both materials. To ease comparison the FWHM values of the undeformed samples are plotted through the whole test period with dashed lines.

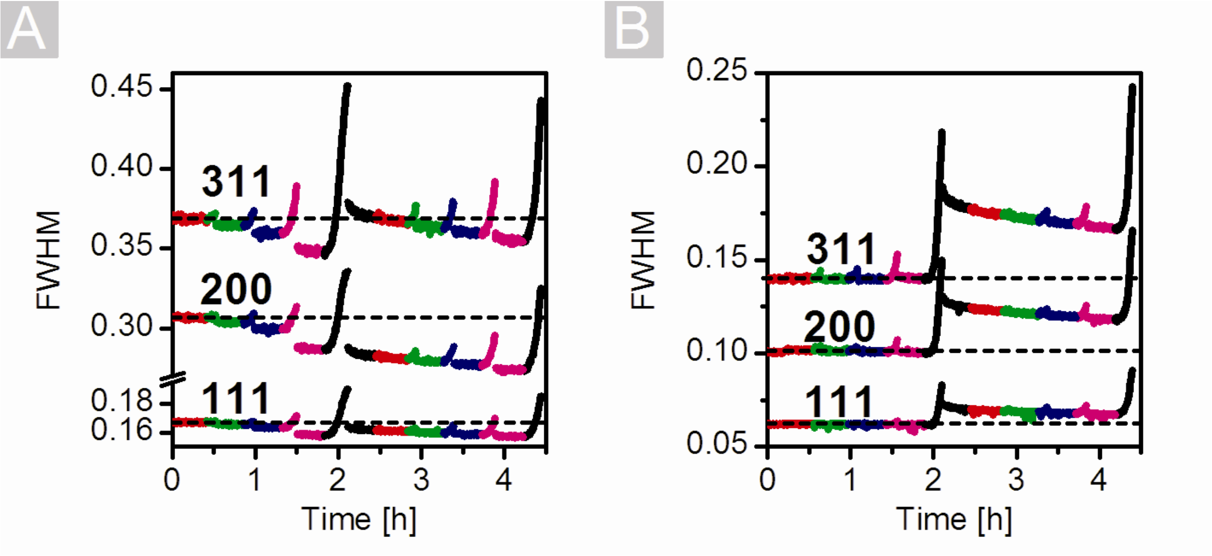

Figure 36: FWHM of NC Nickel (A) and ultra fine grained Nickel (B) for three diffraction Peaks during the loading cycles presented in Figure 35.

In the first loading series, there is a similar behavior for all the diffraction peak widths of NC-Nickel. Upon unloading from the first stress level (400MPa), no changes in the FWHM can be recognized. Upon unloading from the second step (800MPa), a reduction of the peak width occurs. More pronounced reductions are observed upon unloading from the higher stress levels. Additionally, a time depended recovery of the FWHM is observed once the sample is unloaded from 1.4GPa (magenta curve). This feature is better visible in Figure 37 where only the 311 peak is presented.

Once the sample has been loaded to the full plastic regime (black curve), the recovery of the peak widths are different for the 311, 200 and 111 peaks and the behaviors are similar to what was observed by deforming the sample without interruption to 3% strain (see Section 3.1). Additionally, a time-dependence is observed for all peaks upon unloading from the full plastic regime. The 311 peak experiences a reversibility of the broadening compared to the as prepared value after 10 minutes unloading, whereas the 111 peak is immediately reversible to the as prepared state. Both of these peaks exhibit broadening in respect to the value upon unloading from 1.4GPa (magenta curve). The 200 peak however shows full reversibility to the lowest FWHM value achieved upon unloading from 1.4GPa (magenta curve). The extra reductions in the FWHM upon unloading at 40%, 60% and 75% seen in the first series of load cycles are no longer visible in the second series for the 311, 111 and 200 peaks. The time-dependence is ongoing and no significant interruptions due to the loading cycles occur (see Figure 36).

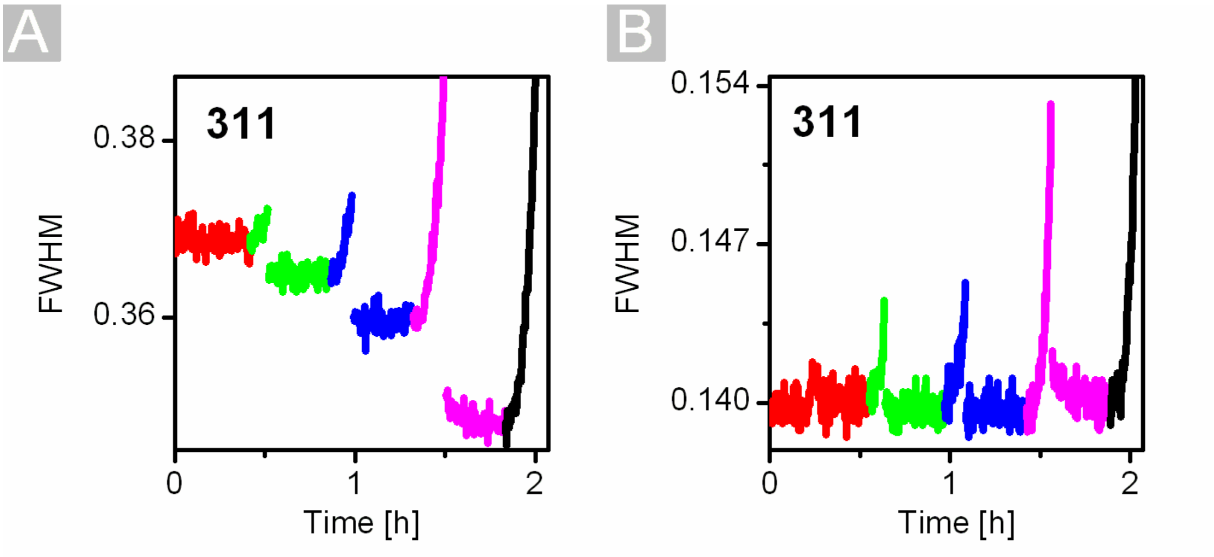

Figure 37: A zoom of the FWHM of the 311 peak from the first series for NC and UFG-Nickel of the previous figure.

The same loading cycles were carried out on UFG-Nickel. The stress strain curve is presented in Figure 35B and the stress time curve in Figure 35D. Figure 36B shows the corresponding FWHM of the 111, 200, and 311 peaks during the test. In the first series, the FWHM upon unloading is the same as the as prepared value. This is very clear in Figure 37 where the FWHM of the 311 peak is shown for both the NC and UFG-Nickel. Upon unloading from 75% of the UTS (950MPa), to be compared with the 1.4GPa cycle for NC-Nickel (magenta curve), time dependent recovery starts to be visible in UFG-Nickel (see magenta data in Figure 37B). Once the material is deformed in the full plastic regime, a clear irreversibility in FWHM is observed for all diffraction peaks. Similar to the NC-Nickel, for all peaks a time dependent recovery in FWHM is observed upon unloading. However in UFG-Nickel after more than two hours unloading all diffraction peaks are still considerable broader compared to the initial values before loading –111 peak 8.5% broader, 200 peak 17.5% broader and the 311 peak is 20% broader.

Peak position data

Figure 38, shows the peak positions – in percentage of their initial value – for NC- a) and UFG-Nickel b). During the first test series of load cycles, the 111, 222 and 311 peaks stay within their scatter at the same position after each unloading. As long as the sample is not loaded in the full plastic regime, the peak position comes back to the same value. The peak position is very sensitive to sample position. This demonstrates that the sample did not change its position during the load-unload cycles. Once the sample was loaded into the full plastic region, the peak positions differ from their original value upon unloading. The behavior of this relative deviation between the positions of the peaks in UFG-Nickel is somewhat different from the NC behavior. The decrease of the 200 and 400 peaks in UFG-Nickel is 0.06% instead of 0.04% in NC-Nickel. The 111 and 222 peaks increase in UFG-Nickel by 0.015% whereas in NC-Nickel they do not change. The 311 peak position of the UFG-Nickel decreases by 0.02% whereas in NC-Nickel no change occurs. Bigger differences between the two types of Nickel occur in the 220 peaks. There the peak position of UFG-Nickel increases only by 0.005% whereas in NC-Nickel it increases by about 0.07%.

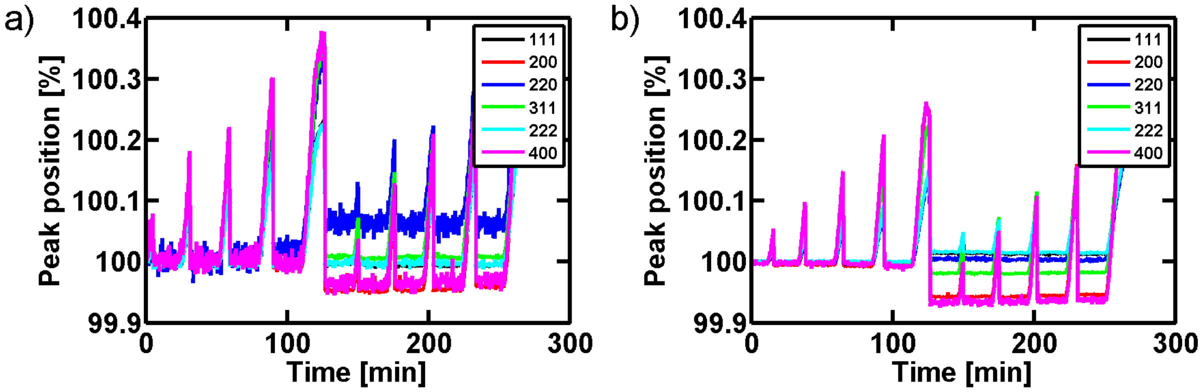

Figure 38: Relative peak position of a) the NC-Nickel and of b) the UFG-Nickel.

Main findings:

Load-unload cycles starting in the elastic region show a reduction in the FWHM upon unloading for all peaks in NC-Nickel if unloading is performed before the full plastic regime. The amount of reduction is hkl dependent. This is not the case for the UFG-material where the initial FWHM value is reached upon each unloading. Once the NC-Nickel specimen is loaded to the full plastic regime, no further reduction in the FWHM upon unloading is observed when further loading cycles are applied. Additionally, time dependent recovery of *the FWHM is observed for both the NC- and UFG-Nickel. Allowing time to recover, the FWHM of all diffraction peaks are equal or smaller compared to the values prior to loading in NC-Nickel; on the contrary, in UFG-Nickel they are all broader. Furthermore, the relative change in peak position upon unloading from the full plastic regime is different for the two tested materials.*

To address the extra recovery in the FWHM and their dependency on the loading history and the waiting time between the cycles, further tests have been performed.

- To study the influence of the waiting periods between the loading cycles, tests with unequal waiting times were performed (Page 64).
- To address the behavior of the FWHM between 1.4GPa (75% UTS) and the UTS which we will call in the following the "transient" region (Page 67), load-unload tests were performed in between.
- To address the effect of reduced initial RMS-strain load-unload cycles were performed on pre-annealed samples. The influence of the annealing on the microstructure has been studied by in-situ annealing experiments (Page 72).
- To examine the time-dependence, load-unload tests were performed at RT on pre-annealed specimens (Page 76) and at 180K (Section 3.2 on Page 87).

3.1.2. Influence of waiting time between two loading cycles

Previous results for NC-Nickel showed a stepwise reduction in the FWHM upon unloading from loads that were smaller then the UTS. This reduction appeared after 40%, 60% and 75% of the UTS. To investigate if this reduction depends on the waiting periods during unloading and/or on the previous load level, load-unload cycles were carried out where both parameters – waiting times and load levels – were varied.

Stress strain data

The mechanical data of two different tests are presented in Figure 39.

- Test sample number one (green data) was first twice loaded to 1.4GPa and then twice to 1.8GPa, followed each time by an unloading period of 2 hours. The sample broke as it got loaded the second time to 1.8GPa.

- Test sample number two (blue data) was four times loaded to 800MPa with each time 20 minutes waiting period in-between. Then it was loaded to 1.4GPa followed by 60 minutes unloading. Afterwards the sample was loaded five times around the UTS. The unloaded waiting times between the cycles 6, 7, 8, 9 and 10 were respectively 90, 80, 50 and 5 minutes.

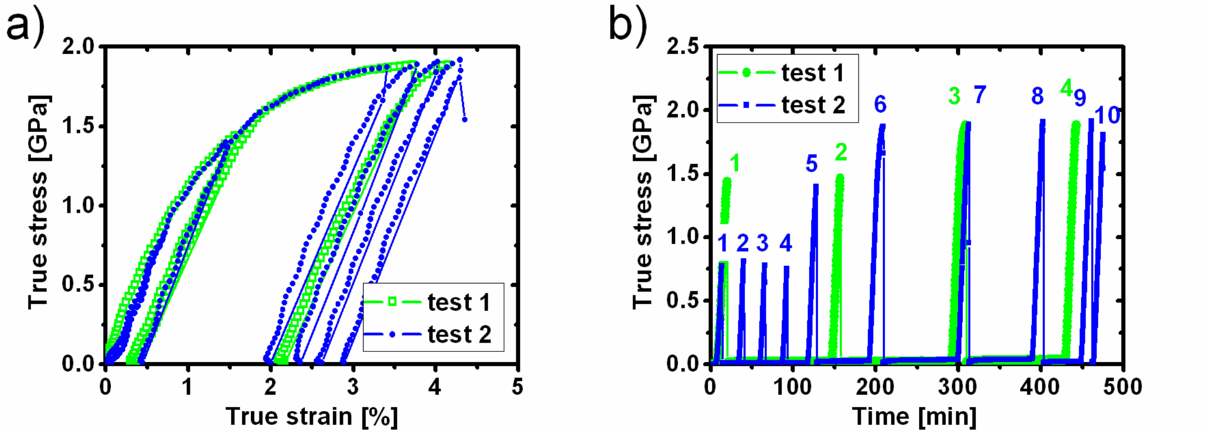

Figure 39: Stress strain a) and stress time b) data from two load-unload cycles. In the stress time date the loading cycles are marked with numbers.

Figure 40 presents now the diffraction data of these tests for the a) 200 and b) the 311 peak. It is particular interesting to look at the 200 and the 311 peaks. The peak broadening of the 200 peak exhibit full reversibility upon unloading from the full plastic regime in the former test (Section 3.1.1) and the 311 peak is interesting because it has the highest initial permanent broadening upon unloading – this “permanent” broadening vanishes with time: see as well Section 3.1.1.

FWHM behavior of the 200 peak

In Figure 40a, it is clear visible that the FWHM of the 200 peak experiences a strong reduction in the FWHM upon unloading from 1.4GPa (green 1). The second load-unload cycle at 1.4GPa reduces only slightly the FWHM (green 2). Sample number two was four times loaded to 800MPa (blue 1 - 4). After the first loading cycle (blue 1), an expected small reduction occurs. As it can be noticed, no important reductions in the loading cycles 2, 3 and 4 are observed. However, if this specimen is afterwards loaded for the first time to 1.4GPa (blue 5), a stronger decrease in FWHM is measured and the value reached is similar to the one in the first unloading cycle of sample 1 (indicated by a red arrow). If the samples are then loaded to the full plastic regime, no important further changes in the FWHM are observed in the initial value upon unloading. A horizontal red line is plotted in the graph to indicate that this value is for both tests the same. However, clear time-dependence – best visible in test number two – in the FWHM is visible for both samples after unloading from the full plastic regime.

FWHM behavior of the 311 peak

In Figure 40b, the FWHM data of the 311 peak is shown. The behavior is qualitatively the same as that of the 200 peak: i.e. the strongest recovery in FWHM is observed after an unload at 1.4GPa. The red arrow in Figure 40b indicates this value (test 2: blue 5 and test 1: green 1). However, when the sample was loaded to the full plastic regime the situation is different: the FWHM is irreversible relative to the lowest obtained value. The irreversibility is similar for both tests and indicated in the figure with a red line. Time-dependence is present for both tests (after green 3 and blue 6) and during this time dependent recovery, the FWHMs reach values that are similar to those of undeformed NC-Nickel.

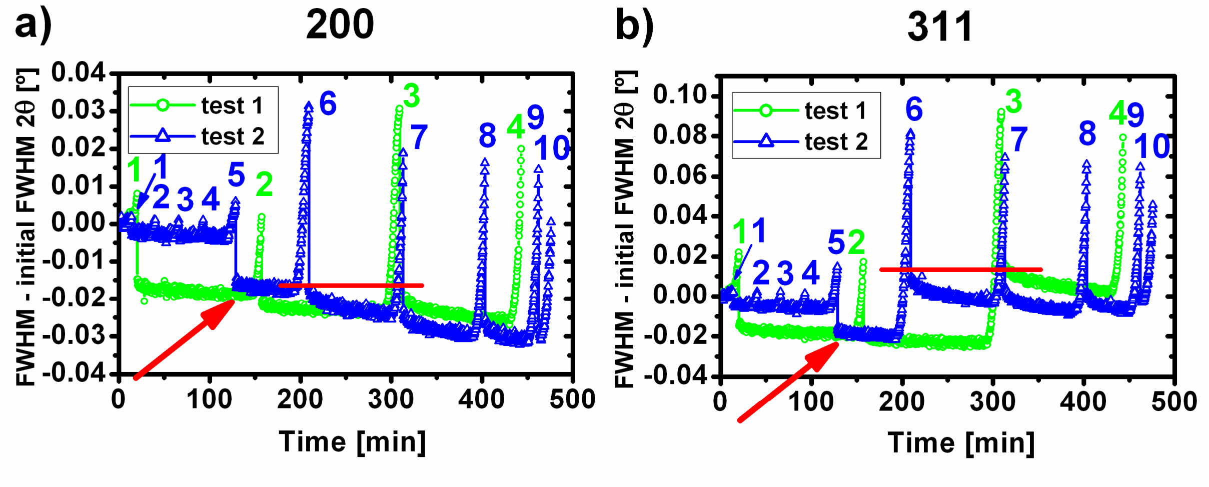

Figure 40: Evolution of two different peaks during different series of loading cycles.

Behavior of the peak positions

The peak positions – in percentage of their initial value – are presented in Figure 41. After the specimen was loaded the first time to the full plastic regime, a clear change in the peak positions is evident for the 220, 200 and the 400 peak. The 200 and 400 peaks are reducing their peak position of 0.05%, whereas the 220 peak increases his value about 0.07% of the diffraction angle. The rest of the peaks (111, 222 and 311) are stable upon all unloading cycles. A small difference between the two tests can be noted. Test sample number 1, which was immediately loaded to 1.4GPa, shows a slight increase for the 220 peak upon unloading for the first time. The general behavior presented here is the same as it has been observed in the test before (Section 3.1.1) shown in Figure 38.

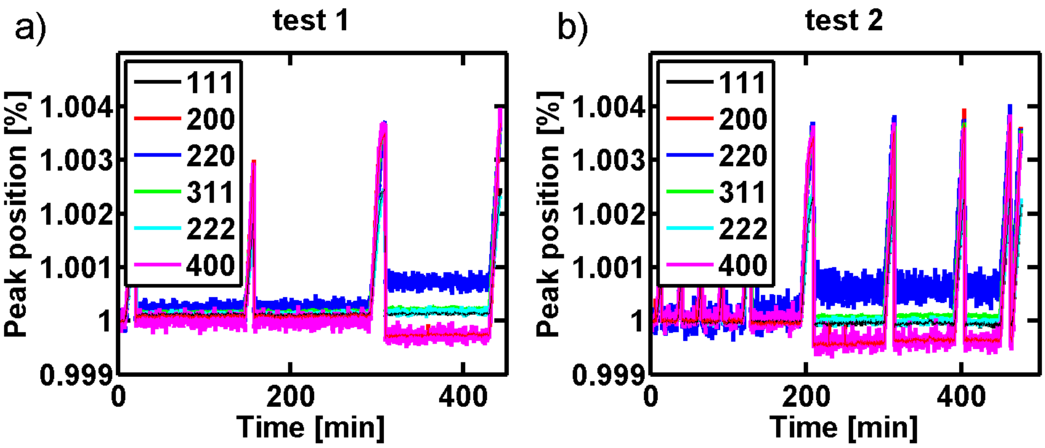

Figure 41: Peak positions of two different loading cycles.

Main findings:

The history of loading cycles performed at stresses below the UTS in terms of waiting time and loading sequences/maximum-stress does not influence the peak width and peak position obtained in the full plastic regime. Upon unloading from 1.4GPa, the strongest reduction in FWHM is observed and changes in the peak position appear.

3.1.3. Load-unload cycles in the transient region

The biggest reduction in the FWHM for any peak occurs upon unloading from 1.4GPa. The test discussed here examines load-unload cycles performed in the region between 1.4GPa and UTS.

Stress strain data

The true stress in the test cycle probing the transient region between 75% and 100% of the UTS is presented in Figure 42 versus a) strain and b) time.

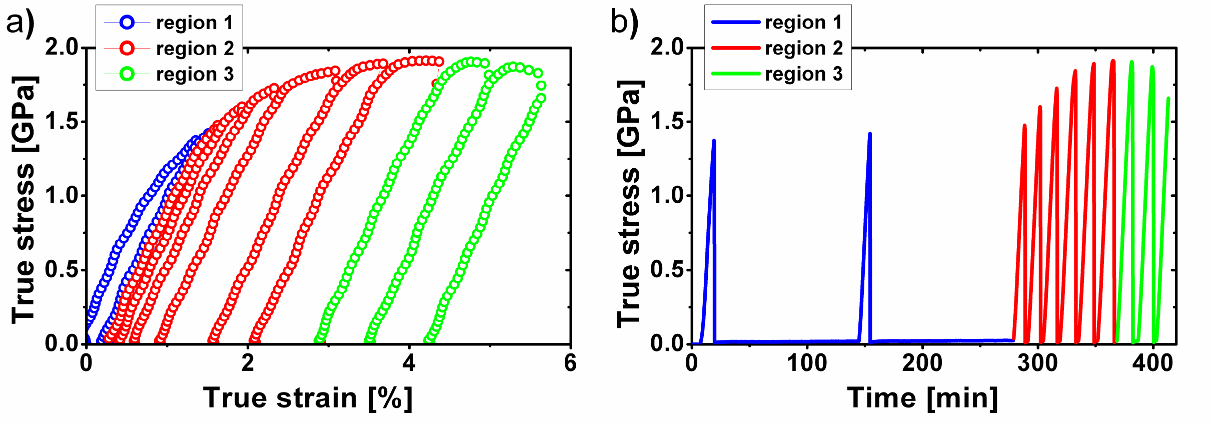

Figure 42: Stress strain a) and stress time b) evaluation a test cycle probing between 75% and 100% of the UTS. For details about the regions, see text.

The presented results are spit in to three regions as indicated with colors in Figure 42.

- First region: load values lower then 1.4GPA (blue)

The sample was in the beginning twice loaded to 1.4GPa and every time kept unloaded for two hours. The aim was to reduce the FWHM, by preloading in the microplastic regime, to the lowest possible value.

- Second region: load values between 1.4GPa and UTS (red)

After these two primary cycles, six additional load-unload cycles are carried out before the UTS is reached. The loading values of the first five cycles are respectively 1500MPa, 1635MPa, 1740MPa, 1860MPa and 1893MPa. The sixth loading cycle reached a UTS of 1912MPa and was unloaded at 1902MPa.

- Third region: loading beyond the UTS (green)

The following three loading cycles were performed after the UTS was reached; i.e. in a region where necking starts to be observed. The sample was loaded in the first two cycles to 1875MPa and 1807MPa respectively. The third loading reached 1680MPa around 5.7% of total strain where the sample failed.

Note that in the second and third region the sample was kept approximately 3 minutes in the unloaded condition. This is different from all earlier experiments, where the sample was kept usually 20 minutes in the unloaded stage. However, in the previous Section 3.1.2, it could be shown that the waiting time and loading sequence have no influence on the peak width and peak position upon unloading and is only dependent on the maximum load.

Behavior of the peak widths

In Figure 43 the FWHM versus time of the three peaks 111, 200 and 311 are shown in percent (normalized) of their starting values 0.167°, 0.307° and 0.371° respectively. The inset shows the details of the first two loading cycles.

First region: The first loading cycle to 1.4GPa reduced the FWHM between 4.5% and 6% depending on the peak. Keeping the sample unloaded for 100 minutes, an additional reduction of about 1% is observed.

The second load-unload cycle to 1.4GPa causes an additional reduction in the FWHM of about 1% for all peaks. This is clearly visible in the inset of Figure 43. Keeping the sample again unloaded for 100 minutes, an additional reduction of 0.5% is present. It can be noticed that the reduction in the FWHM after the second loading to 1.4GPa levels off faster than in the first cycle.

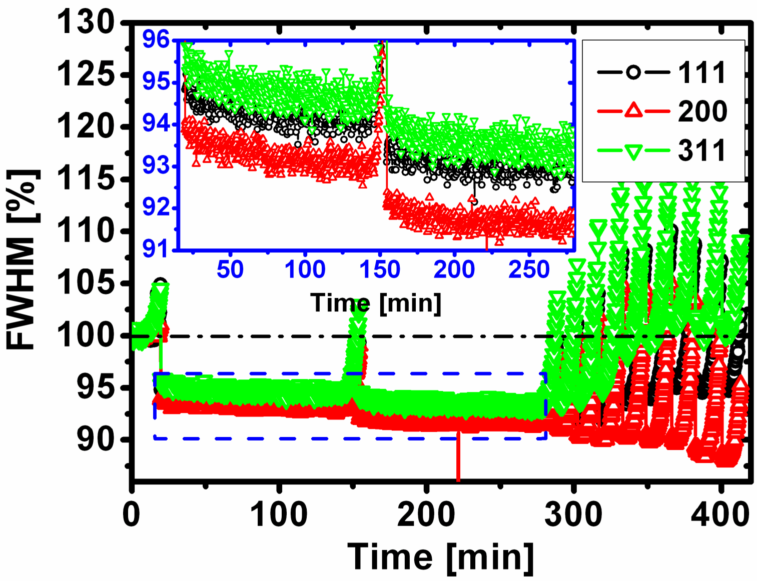

Figure 43: Time evolution of the normalized FWHM during the test presented in the previous figure. The inset shows the two long unloading periods after loading to 1.4GPa.

Second region: After the first two cycles were finished, load-unload cycles with 3 minutes waiting time were conducted. A clear difference in the FWHM between the presented peaks can be observed during this fast load-unload cycles (Figure 43). In the unloaded stage, the FWHM of the 111 and the 311 peaks increases, whereas the 200 peak keeps on decreasing its FWHM value.

To enhance the different behavior of the FWHM of the different peaks, only the unloaded values of the FWHM (applied stress below 30MPa) are shown in Figure 44. To improve the clarity of these tendencies arrows are shown on top. Now it is visible that all analyzed peaks except the 200, keep on increasing their FWHM values once the stress level of about 1.4GPa is exceeded in the load cycle beforehand. It was already observed in previous experiments, that the 200 peak tends to lower his FWHM at most compared to the other analyzed diffraction peaks. The 111 (black) and 400 (magenta) peaks show a moderated increase whereas the 220 (blue) and 222 (cyan) peaks exhibit a stronger increase. The 311 peak (green) is the only peak, which increases his FWHM upon unloading to a level that exceeds the initial starting value.

The peak broadening of the observed peaks upon unloading from the UTS (last loading in region 2) exhibits the same values as if the sample would have been directly loaded to UTS. This strengthens the findings from the previous Section (3.1.2) that the history of the loading – number of loading cycles and waiting time in the unloaded phase – does not influence the peak broadening upon unloading.

Third region: The FWHM from all peaks reduces slightly upon unloading once the sample has exceeded the ultimate strength. This trend is clear visible in Figure 44.

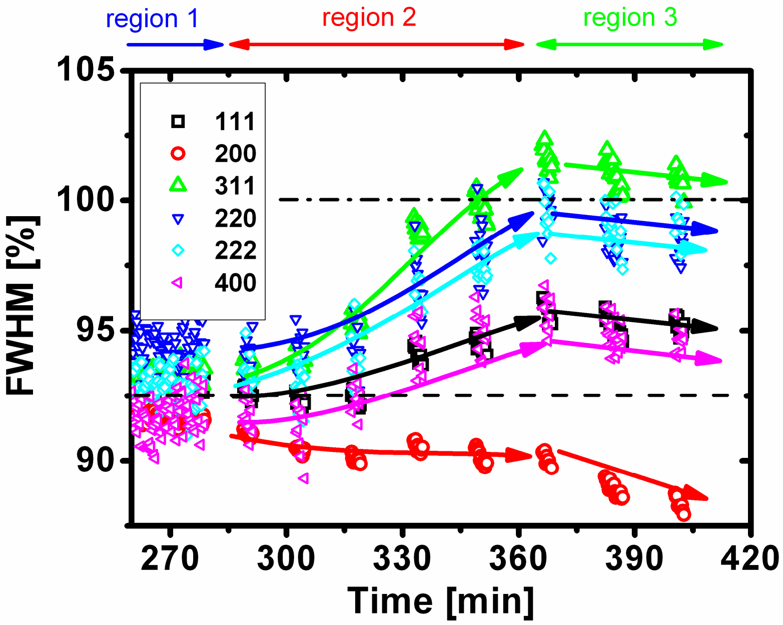

Figure 44: FWHM data of the unloaded sample. The dashed dotted line indicates as prepared FWHM value. The dashed line marks the lowest FWHM value: upon unloading from 1.4GPa.

Behavior of the peak positions

Figure 45 shows the peak position upon unloading. There are only marginal changes in the FWHM values upon unloading from 1.4GPa (first region). Therefore, the presented data starts at the end of the first region. In the diagram, the peak position values in region two and three are indicated by overlaid eye guide arrow indicating the trend.

In the second region, the peak positions of the 111, 222 and 311 peaks stay constant, confirm with former presented experiments. The 200 and 400 peak position gradually decreases when the stress from which unloading is performed increases whereas the 220 peak increases. The peak position values exhibit a 0.04% reduction for the 200 peak family and an increase of roughly 0.07% for the 220 peak. These changes are of the same magnitude as those observed when no additional unloadings are performed.

In the third region, the trends of the peak position behavior change. The most remarkable changes occur from the 200 and 400 peaks, for which the peak position starts increasing again. However, there the sample possibly necks and no clear stress state can be defined. Therefore, no particular attention will be paid to these results.

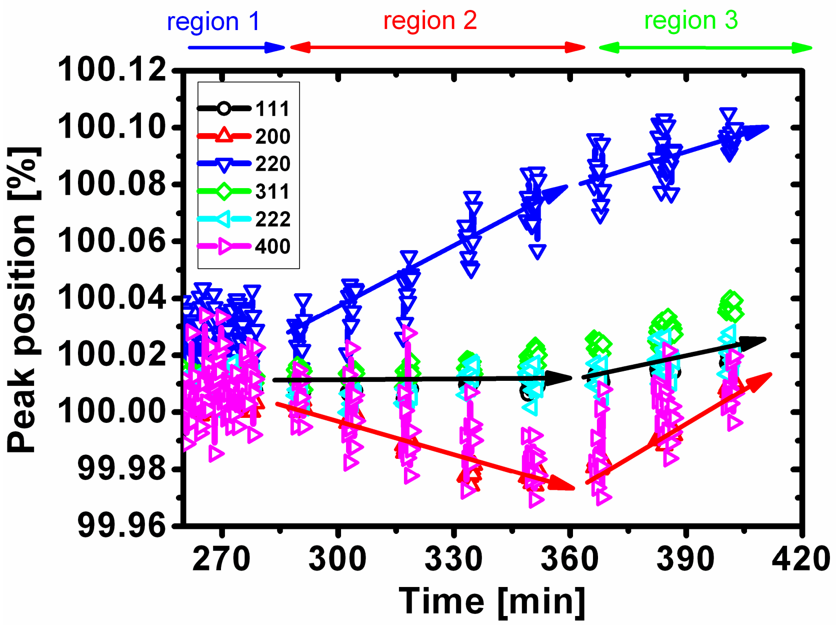

Figure 45: Peak positions of the diffraction peaks if the load is less than 30MPa on the sample.

Main findings:

The FWHM values for all peaks except the 200 peak reach their minimum upon unloading from 1.4GPa. Then they monotonically increase with increasing stress in the loading cycle *beforehand. The change in peak position for the 220, 200 and 400 peaks is as well monotonic upon unloading after the loading values exceed 1.4GPa. The values reached once unloaded from the UTS are similar as observed for a one-time loading.*

3.1.4. Effect of pre-annealing

It is known that the RMS-strain in NC-Nickel can be reduced by annealing [45, 141]. To examine the effect of reduced RMS-strain, load-unload cycles were performed on pre-annealed specimens. Beforehand, the influence of the annealing temperature was studied in-situ during X-ray diffraction and this in a relatively large temperature range.

In-situ annealing

The oven at the MS beam line of the SLS is designed to hold quartz capillaries. To be able to test the NC-Nickel sample in the same position as during a deformation experiment, the gauge section ($0.2x0.2x{\sim}1mm^3$) of a polished dog bone was cut out and placed inside such a capillary.

Starting from RT the temperature was increased in steps of 10ºC from RT to 250ºC. Each step in temperature was held constant for 15 minutes. During the heating process, the X-ray diffraction patterns were recorded continuously with an exposure time of 10 seconds. Figure 46 shows the (220) diffraction peak measured at four different temperatures. For temperatures below 200°C, the peaks can be fitted with a single P-VII function as is shown in Figure 46 for the data obtained at 120°C. From 200ºC on, the use of two P-VII functions is necessary in order to obtain a good fit. This is demonstrated in the three other graphs of Figure 46, displaying the data of the diffraction peaks and the fits for 200ºC, 220ºC and 250ºC.

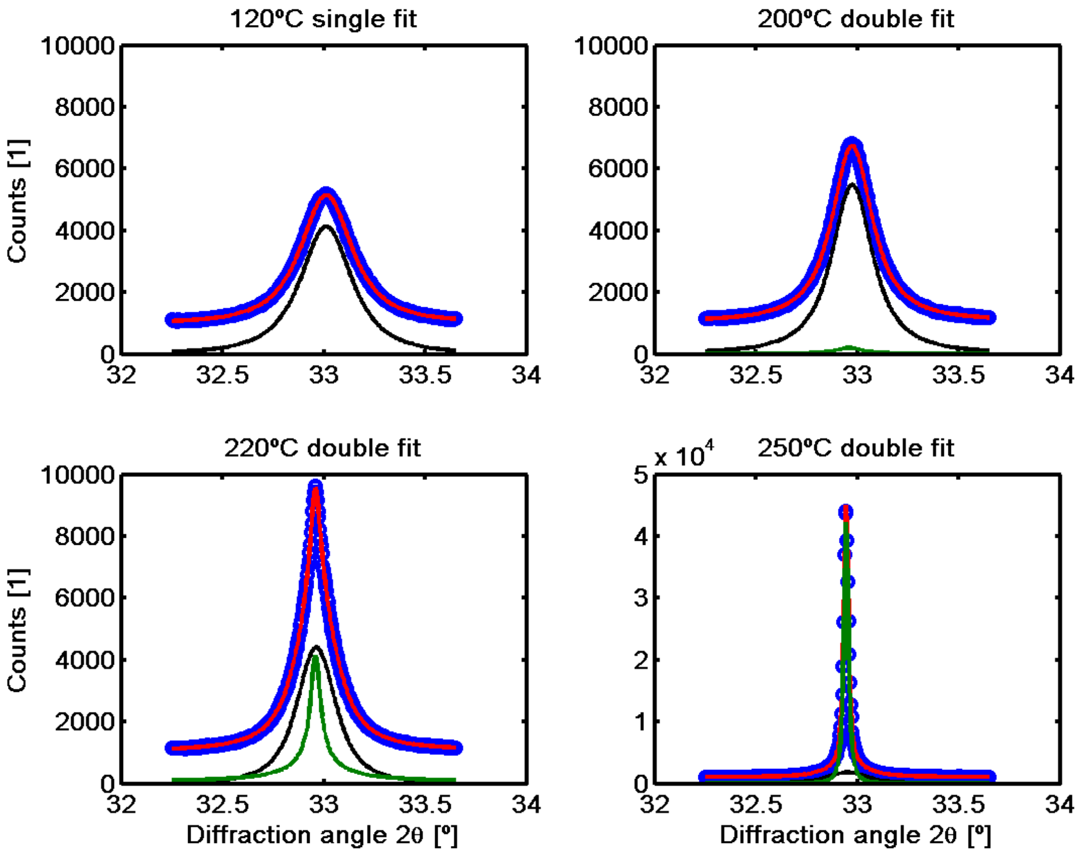

Figure 46: Diffraction peak (220) during the in-situ annealing at four different temperatures. The measured data is presented in blue. Black and green curves are the P-VII peak fittings without background and magenta the summation of the two fitted P-VII peaks plus the background.

Below 200°C

Figure 47 presents the FWHM in percent of their initial value of all measured diffraction peaks as a function of temperature. In this plot, each value represents an average of 45 consecutive diffraction patterns. Minor changes in the FWHM occur until a temperature of about 100°C. The 400 peak deviates more but this peak exhibit the highest scatter due to the small intensity. Above 100ºC, the FWHM start to reduce for all peaks. At 140°C – shown with a green dashed line – all the FWHM values reduce to 95% of their original value. At 180°C, the peak widths have reduced to about 84%. Around this temperature, the deviations between the different peaks start to become more important. The 220 and 222 peaks exhibit the largest reduction whereas the 400 peak shows the smallest reduction.

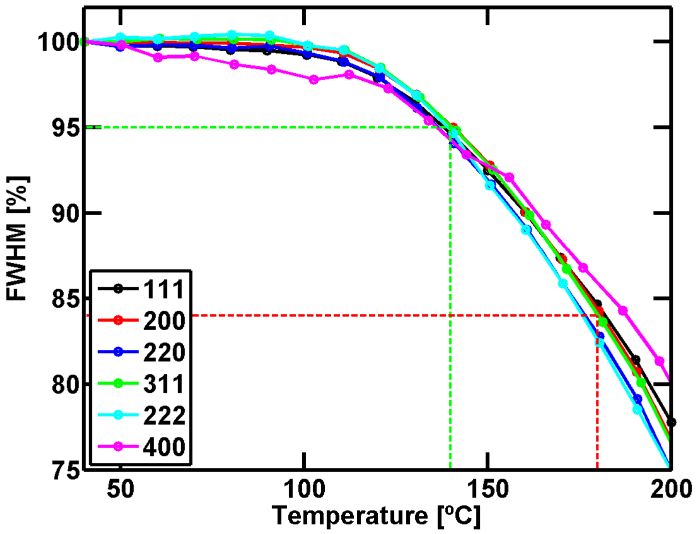

Figure 47: In-situ annealing of NC-Nickel. The FWHM of six diffraction peaks is plotted as a percentage of the as prepared value versus the temperature.

Figure 48 shows TEM pictures of NC-Nickel in the as prepared state and annealed at 180°C, both pictures were taken with the same magnification. The micrograph from the annealed specimen (Figure 48a) exhibits a larger fraction of grains which do not contain gray scale variations within a grain (Figure 48b). Furthermore, it can be noticed that in the annealed material, the GBs can be more easily distinguished, but this is of course a non-quantifiable observation. The grain size distribution obtained using dark field imaging is presented in Figure 49 and a comparison with Figure 2b suggests that no measureable changes in grain size can be observed until 180°C.

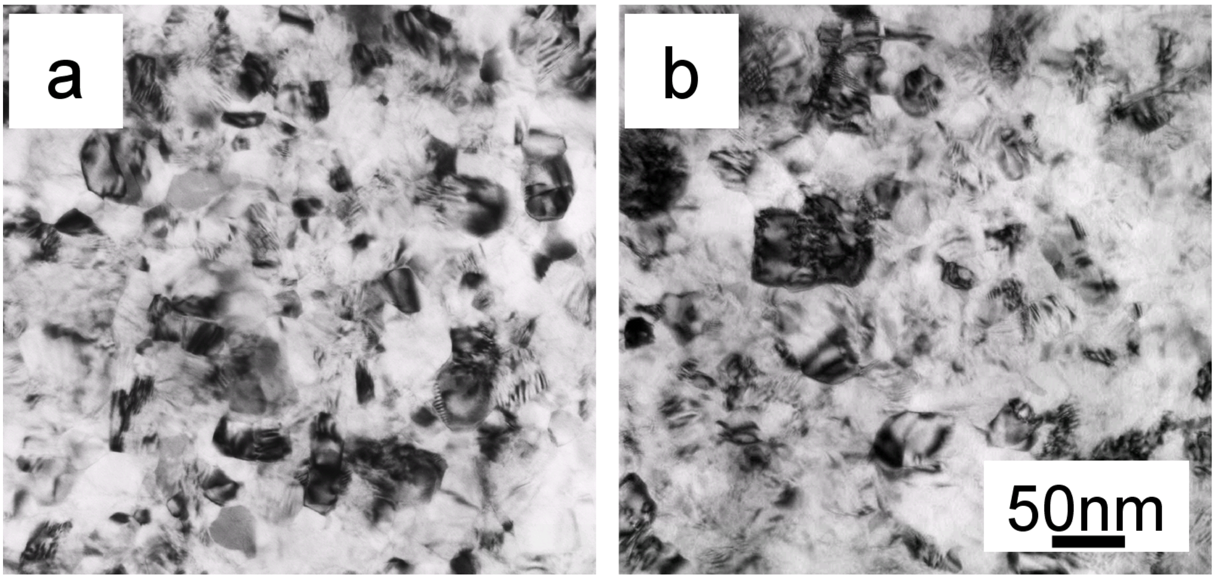

Figure 48: TEM micrographs of (a) NC-Nickel annealed at 180C and (b) as prepared.

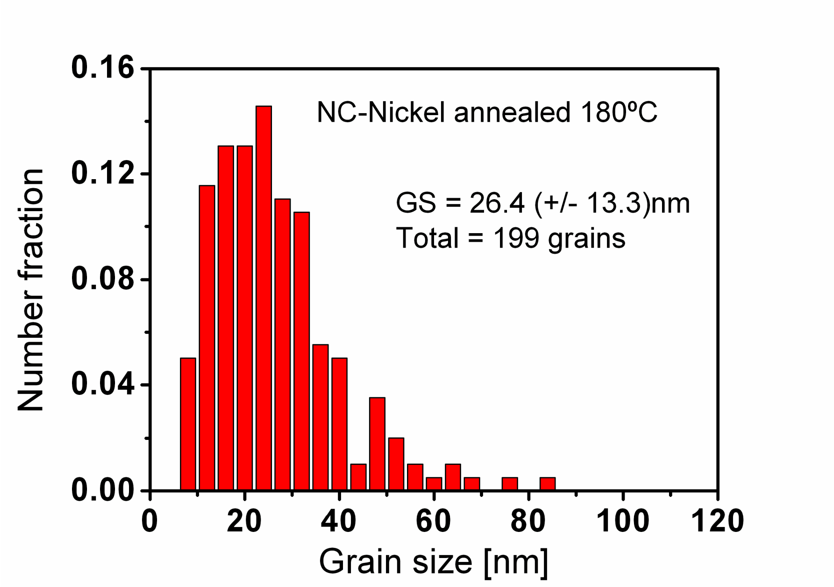

Figure 49: Grain size distribution corresponding to the TEM micrograph shown in Figure 48a.

Above 200°C

Abnormal grain growth in NC-Nickel has been observed at temperatures between 190ºC and 320ºC [142, 143]. During this abnormal growth, a bi-modal grain size distribution is expected which results in diffraction peaks that consist of two convoluted X-ray signals. One broad peak related to the nano-grains and one narrower peak related to the already grown “bigger” grains. Therefore, the use of two P-VII functions as shown in Figure 46 is justified above 200ºC.

Figure 50 compares the integrated intensities of the two contributions. The intensity of the narrow peak gradually increases from 200ºC on. Around 230ºC the contributions of these two peak intensities are roughly equal. The scatter on the data below 210°C is due to the low intensity of the narrow peak.

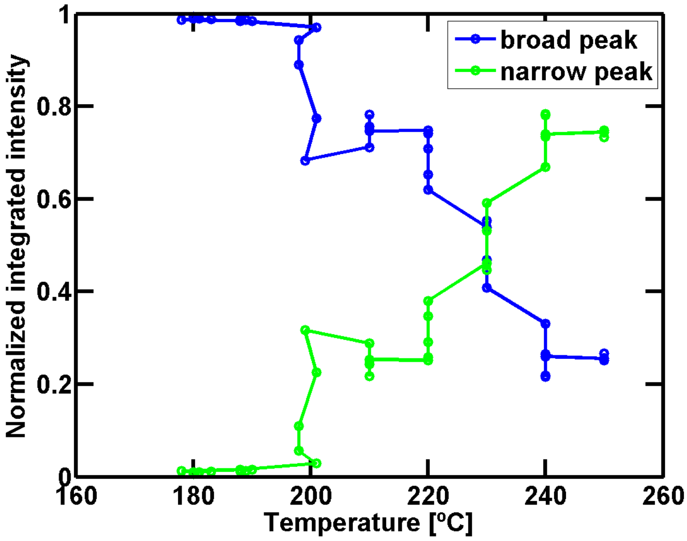

Figure 50: Relative contribution of the total integrated intensity of the 220 peak during in-situ annealing.

Main findings:

In-situ annealing experiments showed that a reduction in the FWHM starts to occur just above 100°C. Furthermore, if the temperature exceeds 200°C XRD suggests a bimodal grain size distribution indicating abnormal grain growth.

Load-unload experiment on pre-annealed specimens

To study the effect of pre-annealing on the recovering of the FWHM in the microplastic regime, load-unload cycles were carried out as presented in Section 3.1.1. The samples were annealed prior to loading during 30 minutes at 140°C and 180°C. These temperatures have been chosen on the basis of former experiments, evidencing a clear reduction in the initial FWHM but no measurable grain growth.

Stress strain data

Figure 51 shows the stress strain and stress time data of the three samples. Two series of loading cycles were performed where the samples were loaded to 25%, 40%, 60%, 75% and 95% of the UTS. Between each cycle, the samples were kept unloaded for 20 minutes. The stress strain data shows that the as prepared NC-Nickel deviates much faster from a linear behavior than the annealed material. In other words, the annealed NC-Nickel exhibits an extended linear behavior and a shorter strain-hardening region if compared to the as prepared material. It is also evident that the samples failed much earlier if they where annealed.

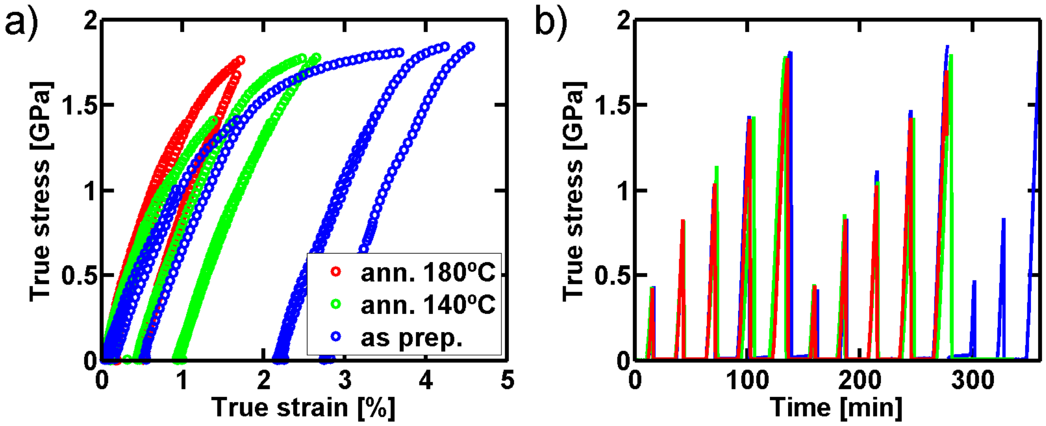

Figure 51: Stress strain a) and stress time data b) during load-unload tests on as prepared material (blue) and pre-annealed at 140°C (green) and 180°C (red).

FWHM data

Figure 52 shows the comparison of the FWHM for three tested samples: the as prepared material is shown in blue and the annealed samples are presented in green (140C°) and red (180°C).

The as prepared material (blue curve) shows in the first series a reduction, until the sample was loaded for the first time into the fully plastic regime. Once the sample was loaded to the fully plastic regime, a time dependent recovery of the FWHM is observed after unloading (Section 3.1.1).

If the sample was pre-annealed at 140°C (green curves), the initial value of the FWHM is lower then that of the as prepared sample. The reductions upon unloading in the first series are smaller but still existent. Furthermore, the lowest value for the FWHM that is reached upon unloading from 1.4GPa is below that reached in the as prepared material. The time-dependence appearing after loading to the flow stress is still existent but less pronounced than in the as prepared material.

If the sample was pre-annealed at 180°C, both the time-dependence and the extra recovery vanish (red curve). Note that the value of the FWHM in the 180°C pre-annealed sample is well below the lowest value of the FWHM that can be reached by load-unloading cycles in the as prepared sample. The FWHM is however clearly irreversible after unloading from the full plastic regime. This is not easily visible in the 111 diffraction peak, however very pronounced for the 220, 311, 222 and 400 peaks.

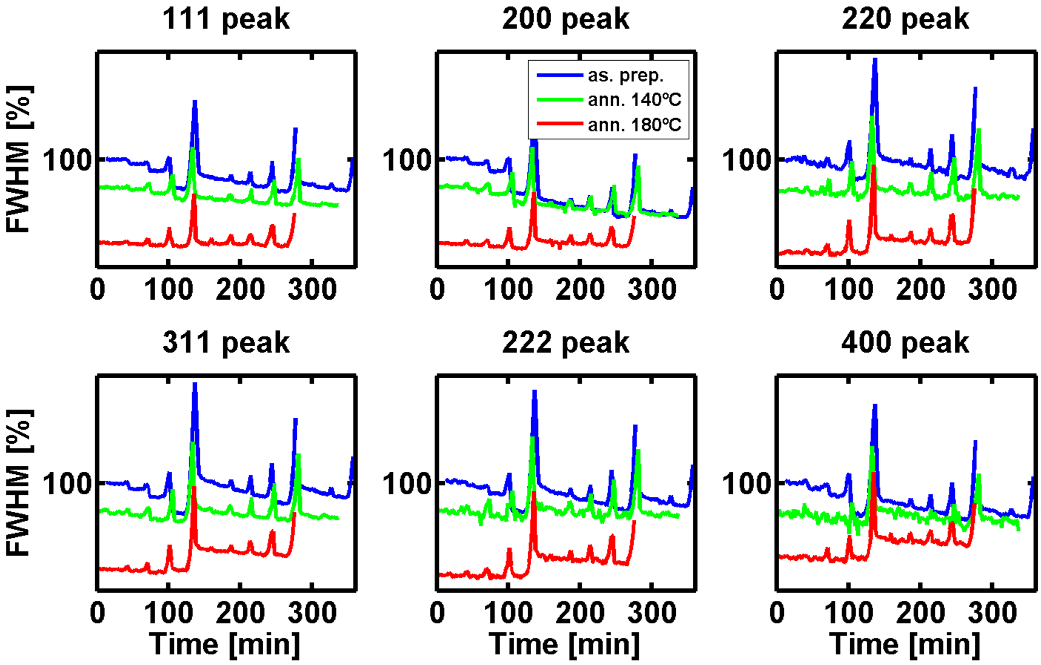

Figure 52: Comparison of FWHM during load-unload cycles from NC-material. The blue curves represent the as prepared material. The green and the red curves are obtained from samples that were pre-annealed at 140°C and 180°C respectively.

Peak position data

Figure 53 shows the influence on the peak position during load-unload cycles at three different temperatures. The peak position of the 220 peak increases and that of the 200 and 400 peaks decreases (see Figure 53a). In Figure 53b and c, it is clearly visible that the relative change of peak position upon unloading from fully plastic deformation exhibits the same trend but the amount of the change is reduced by pre-annealing the sample.

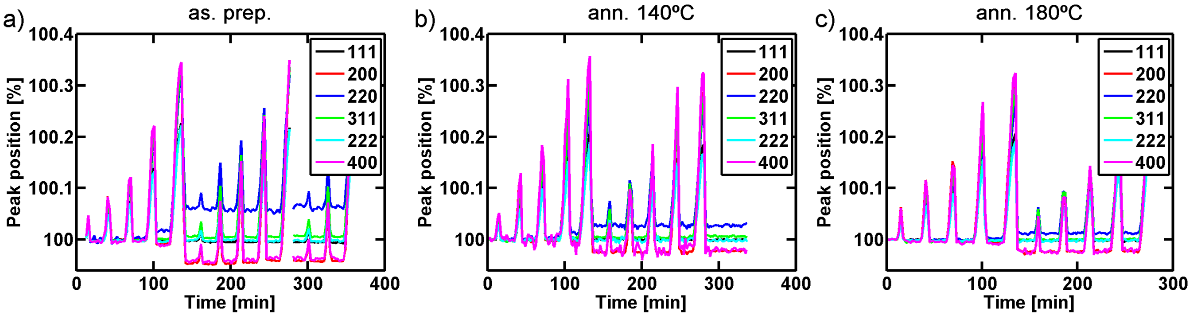

Figure 53: Relative peak positions of the as prepared a), 140°C b) and 180°C c) annealed specimen.

Main findings:

Load-unload experiments have demonstrated that a part of the RMS-strain present in the as prepared NC structure can be relieved by load-unload cycles in the microplastic regime before the maximum flow stress is reached. When the RMS-strain is reduced by means of pre-annealing at 140°C, the reduction in the FWHM upon unloading in the microplastic regime is reduced. No extra recovery can be observed anymore when the sample is pre-annealed at 180ºC. Also the time dependent recovery of the FWHM upon unloading can be reduced by pre-annealing however this effect does not vanish completely. The relative changes occurring in peak position in the as prepared material are less pronounced in pre-annealed samples.

3.1.5. Summary

In-situ deformation experiments revealed a reversibility of all peak widths for NC-Nickel at least to the value of the as prepared state as was already shown by Budrovic [85, 89]. Moreover, it could be shown that

a) the loading sequence and waiting time between the loading cycles does not influence the peak broadening value reached upon unloading,

b) the lowest reachable possible peak broadening is upon unloading from 1.4GPa,

c) and a reduction of the intrinsic stored RMS-strain by annealing reduces the FWHM upon unloading till stress levels of 1.4GPa.

Furthermore, upon unloading the peak positions of the 200, 400 and 220 peaks change gradually from 1.4GPa until the UTS whereas the 111, 222 and 311 peaks do not change.

3.2. Temperature influence on the deformation behavior

Plastic deformation of NC-materials is governed by dislocation processes that can be thermally activated [144]. Moreover, it is known [142] and shown (3.1.4) that temperatures higher than RT can change the RMS-strain structure of NC-materials.

In the previous Section (3.1), all tests on NC-Nickel were performed at RT. To study the influence of temperature without changing the microstructure and internal strain similar experiment as presented in the previous Sections were performed at temperatures well below the RT.

3.2.1. Multiple load-unload cycles at 180K

Figure 54a shows the stress strain response of a NC-Nickel specimen tested at 180K (colored data). The experiments were carried out with the set-up described in Section 2.2.2. To ease the comparison, RT stress strain data are added in grey. The ultimate tensile strength at 180K is higher then its value at RT.

Figure 54b shows the FWHM of the 311 peak using the same colors for the different loading cycles. In contrast to the reversibility peak broadening observed at RT, at 180K the FWHM does not recover upon unloading.

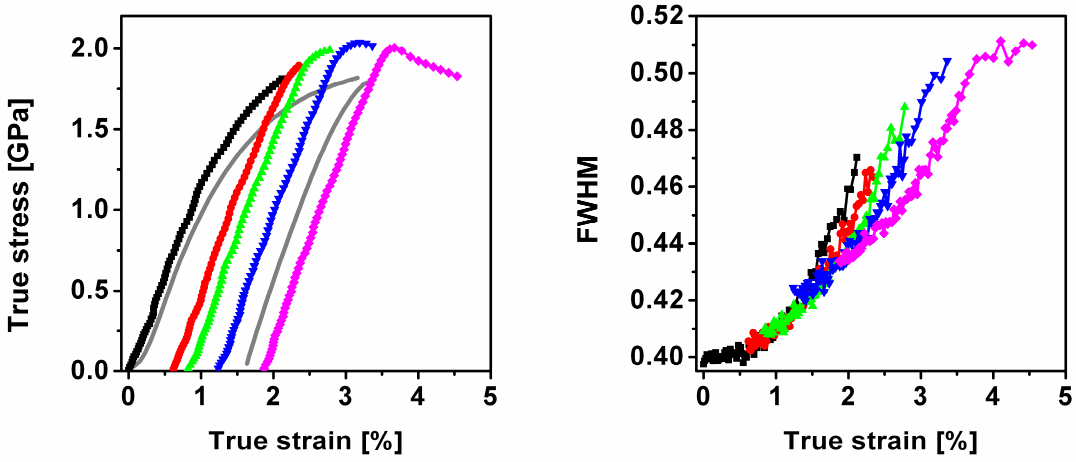

Figure 54: Stress strain data a) from load-unload experiment at RT (gray) and 180K (colors), b) corresponding FWHM (311) data.

This difference in the FWHM between RT and 180K is more visible when plotting the FWHM versus the true stress. Figure 55 shows a direct comparison between a deformation at RT and at 180K for the 311 peak.

The RT data in Figure 55a, is already discussed in Section 3.1. The LT data shown in Figure 55b, exhibit one clear difference. The starting point of the FWHM is for each successive loading cycle higher compared to the starting point of the previous loading cycle.

The FWHM behavior during loading at LT is similar as the behavior at RT. In the first loading cycle (black data), only little change of broadening in the 311 peak width can be observed until ~1GPa. Then a change in slope (FWHM versus stress) is clear visible and most pronounced around ~1.2GPa. In the following loading cycles at LT (2nd, 3rd, 4th and 5th), the FWHM increases for all peaks from the beginning of the loading and the change of slope between the beginning and the end of the deformation is lower when compared to the first loading cycle (black data).

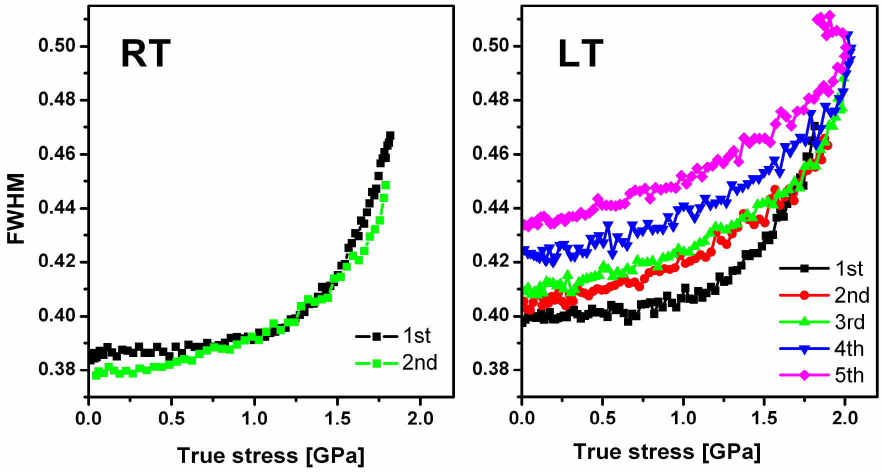

Figure 55: a) FWHM of the 311 reflection of different load cycles plotted against their true stress for RT deformation and b) at 180K (LT)

Details about other diffraction peaks are presented in Figure 56. Overall, one can see that there is a similar behavior for all diffraction peaks. The starting point of each loading cycle is higher than the starting point of the previous cycle. Small differences in the slope of the FWHM versus stress behavior between the successive loading cycles are present.

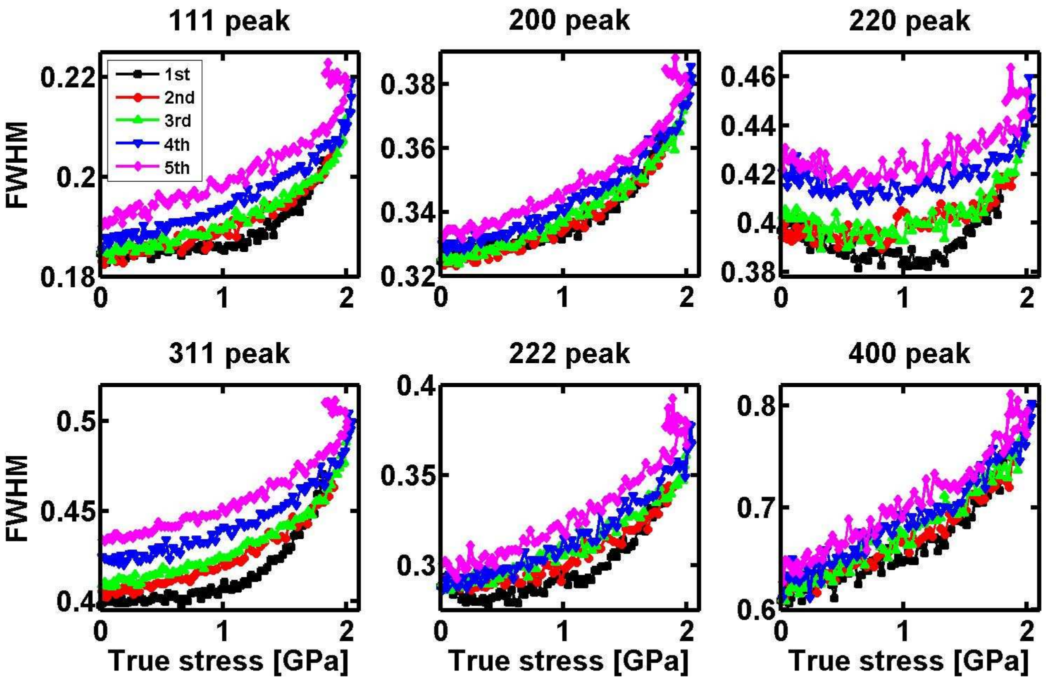

Figure 56: FWHM of six analyzed diffraction peaks. The initial FWHM values are 0.185 (111), 0.325 (200), 0.400 (220), 0.398 (311), 0.290 (222), 0.612 (400).

An exception is the 220 peak where in the beginning of the deformation a reduction in FWHM is observed, as demonstrated in Figure 57. The FWHM reduces in the first loading cycle up to roughly 1.1GPa indicated with a black arrow. After reaching this load, the FWHM increases with further increasing stress. In each of the following loading cycles, the FWHM reduces first till a certain load value and then starts increasing again. The stress at which the FWHM starts increasing gets always lower with increasing cycle number. At the fifth loading cycle, the FWHM starts already increasing at 600MPa (indicated with a magenta arrow).

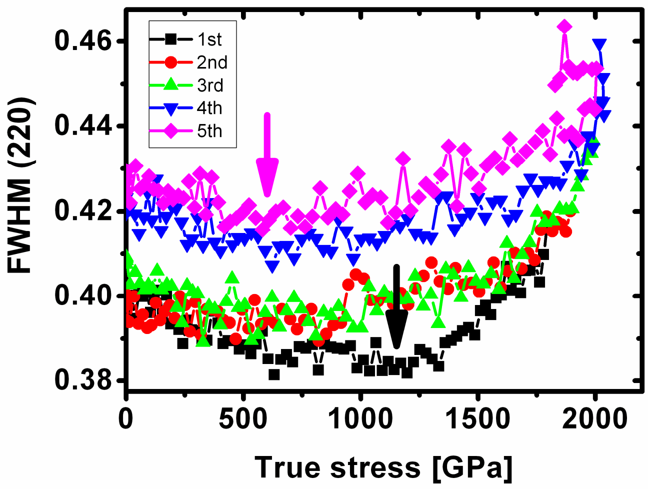

Figure 57: FWHM of the 220 reflection during deformation at 180K.

Figure 58 shows the temperature-time data (blue) during the experiment plotted on top of the true stress-time data (red). Even though the stepwise unloading was performed reasonably fast, it took several seconds. Once the sample was unloaded to a low force, five X-ray patterns were recorded before reloading. The low force, which was clearly less than 1N (~10MPa), was necessary to keep the sample within the grips. The whole procedure of unloading and static measurement plus starting the new loading cycle took at least two minutes. Figure 58 shows that all loading cycles took more than one and a half hour during which the temperature changed by seven degrees.

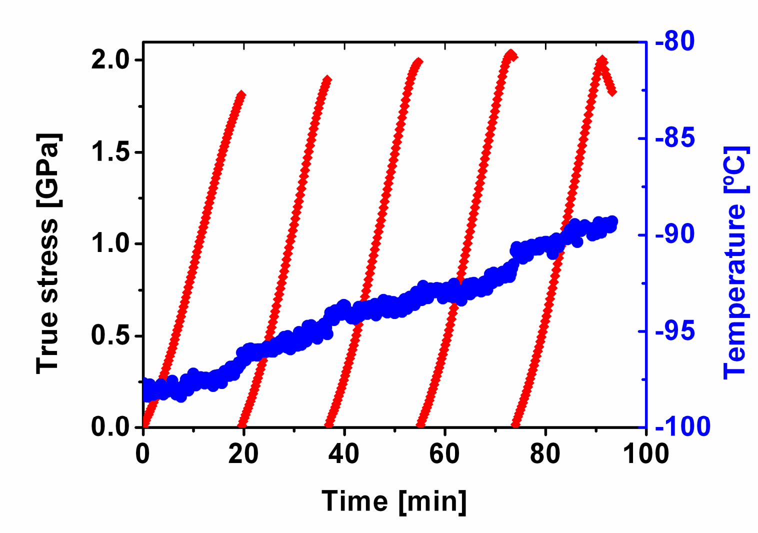

Figure 58: The temperature during the load-unload experiment in terms of time

Microstructural characterization with SEM and TEM

Figure 59a shows a SEM micrograph of one side of the fractured sample and a magnification of the fractured surface taken from the other side of the sample (Figure 59b). The geometry of the fractured surface suggests that fracture is triggered by a flaw. The discontinuity in the fracture surface starts at the lower left and extends to the central region (see Figure 59a). Investigating the fractured surface at a higher magnification, a dimple-like structure can be seen (Figure 59b). The size of the dimples is much larger than the grain size.

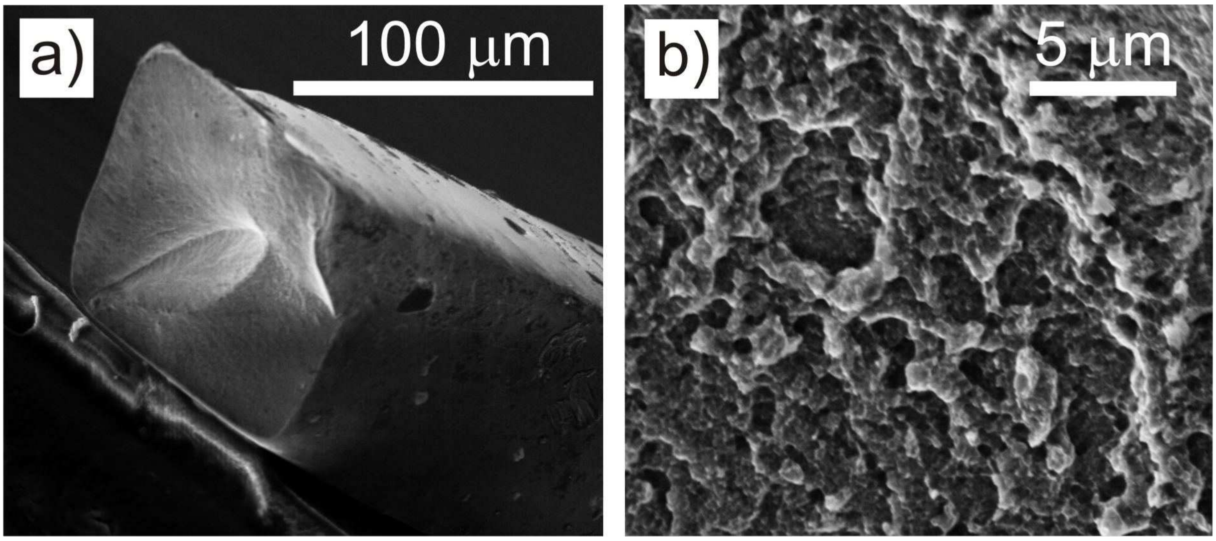

Figure 59: a) SEM picture of fractured LT deformed sample. b) Magnified picture from the opposite side fractured piece. Booth pictures where recorded with an acceleration voltage of 20keV.

Figure 60a, presents a brightfield TEM micrograph taken close to the fracture surface. Some strain fields in grain interiors are visible but compared to the as prepared material (Figure 2a) these seems to be less pronounced and localized which is probably is a result from the reduced amount of strain fields. In the same area, a set of dark field TEM images were made. From these data, a grain size distribution is extracted and presented in Figure 60b. The average grain size derived from 182 counted grains is 35.1nm and shows a standard deviation of 19nm. This is a small increase compared to the as prepared value of about 28nm.

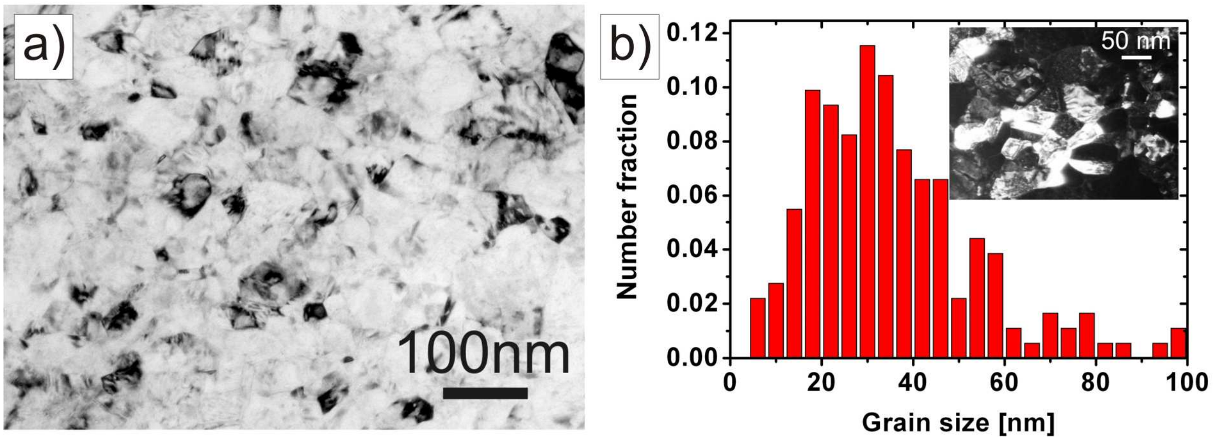

Figure 60: a) TEM bright field image of the LT deformed sample. b) Grain size distribution taken from dark tilt images close to the fracture surface. The insert shows a small area of such a TEM micrograph

Main findings:

The load-unload cycles at LT exhibit irreversible peak broadening upon unloading which is not the case at RT. Furthermore, similar to RT observations a change in slope (FWHM versus stress) is present which reduces with increasing deformation cycle. During LT deformation, the grain size increases slightly.

To tackle the stored irreversibility in the FWHM upon unloading at LT the following tests have been performed.

- After plastic deformation at 180K, the peak profile was followed during re-warming the sample to RT. Then the sample was subjected to another loading cycle at RT (Section 3.2.2).
- Load-unload cycles were performed in the microplastic regime at LT (Section 3.2.3).
- LT deformation tests on UFG-Nickel were performed to investigate the temperature influence on grain sizes bigger than the NC regime (Section 3.2.4).

3.2.2. Single load-unload cycles at LT with subsequent load-unload at RT

Figure 61a shows the stress-strain data of the load-unload cycle at LT (blue) with a subsequent one at RT (red data) where it can be seen that the flow stress during the deformation at LT is clearly higher than the flow stress at RT. Between the loading cycles the sample was reheated to RT. Such heating should extend the sample through thermal expansion, however, a reduction in plastic strain from 2% to 1% is observed. This “reduction” can be explained through ice formation as follows: Although the LT deformation setup was designed to prevent ice formation, it is possible that a small layer of ice (~20μm) formed on the sample during the cooling phase. This would increase the length of the dog bone measured with the CCD at LT and reduce it through melting during the heating phase.

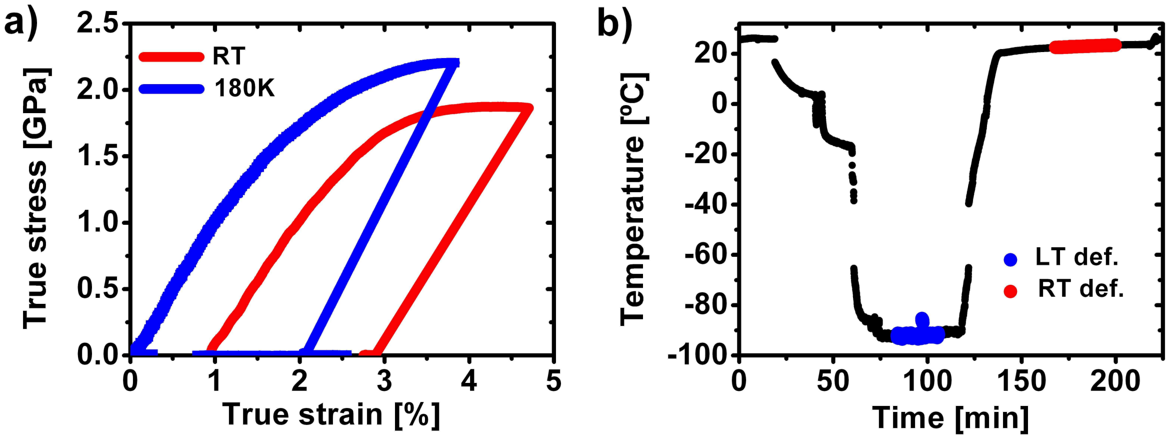

Figure 61: a) Stress-strain data from load-unload cycles performed at LT and RT. b) Temperature-time data during the whole test. The period where the sample was deformed is correspondingly marked in blue (LT) and red (RT).

Figure 61b shows the temperature during these tests. In the beginning, the sample was cooled only by the Cryojet®. Once a temperature of -20 ° C was reached, the cold finger was flushed with liquid nitrogen. A fast drop in temperature occurred and stabilized after 15 minutes at -93°C. A small increase in temperature by 6.5K was observed around 100 minutes and lasted for 30 seconds. This increase in temperature occurred probably due to a short problem in the liquid nitrogen flow, since no other change, e.g. in the force or strain measurement, was recorded. To reheat the sample to RT first the Cryojet® was switched off. At a sample temperature of about -40°C the liquid nitrogen flow was stopped and the temperature continued to rise. The gap in the temperature between -40°C and -60°C is due to measuring method explained on Page 29.

In Figure 62, the FWHM during this test is shown for four peaks. All peak widths stay at their initial value during cooling to 180K. Upon unloading this width is irreversible as already demonstrated in Figure 55. The striking part is that during heating until RT the FWHM reduces gradually back to their initial value. An exception is the 311 peak where 11% of the total broadening does not recover. All other peaks show complete reversibility of their FWHM within the resolution limits. During the following deformation carried out at RT the FWHM values are entirely reversible upon unloading relative to the condition before RT deformation.

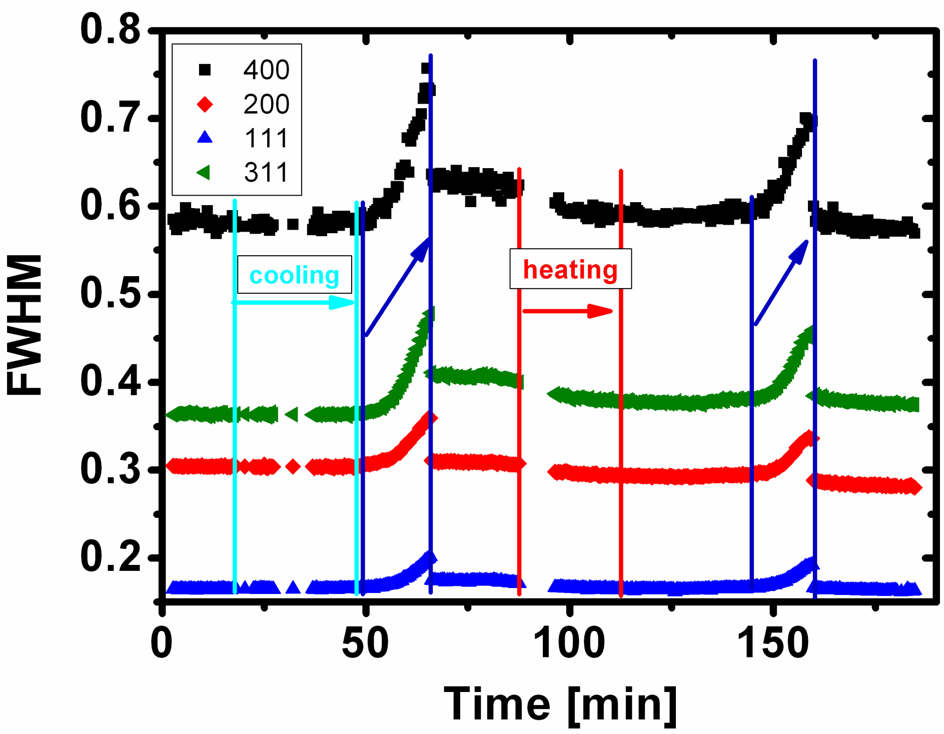

Figure 62: FWHM during loading at 180K followed by a loading at 300K.

Main findings:

The LT deformation exhibits an irreversible broadening upon unloading. However, the thermal energy applied to the sample through re-heating to RT causes a reduction of all peak widths and the FWHM of most peaks return to their initial value. During the following loading cycle at RT, the FWHM is again reversible which demonstrates that the – deformation and temperature – history of the sample is of no importance.

3.2.3. Load-unload cycles in the microplastic regime at low temperature

Similar load-unload cycles as presented beforehand (Section 3.1.1) with waiting times of 20 minutes in the unloaded state were performed at 180K. During this experiment, slight ice formation on the sample occurred which caused an irregular increase of the length measured from the CCD (see Figure 8). Therefore, the strain measurement of this test was not possible. The stress-time and temperature-time cycles are presented in Figure 63. The temperature changed about 10K during a test period of 2.5 hours. Around 160 minutes after the test started (see Figure 63), a constant increase in the temperature is visible. This was caused by a loss off cooling power on the cold finger (see Section 2.2.2). The stress time data (blue in Figure 63) show spikes during cooling of the sample. This is caused by the operating PID controller, which tries to retain an “unloaded” sample.

Stress strain data

Once the temperature stabilized, the sample was submitted to two series of loading cycles. The first series had loading values of 400MPa, 800MPa, 1250MPa and 2070MPa separated by an unloaded time of 20 minutes. The second series had only three loading cycles with slightly different stress values (860MPa, 1600MPa and 2150MPa).

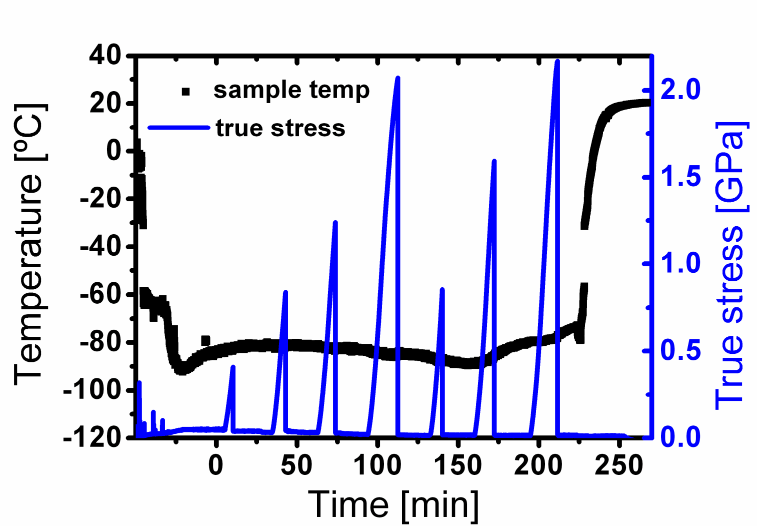

Figure 63: Load-unload cycles performed around -90°C. The zero point in time is set when the X-ray diffraction recording started.

Analyzing the FWHM of the low temperature measurements

To analyze the LT measurements it is best to compare them to a similar RT test. Therefore, in Figure 64, the FWHM values during LT deformation of a) the 200 and b) the 311 peak are presented together with a RT experiment “test 2” already shown in Section 3.1.2. There the initial FWHM values of the different peaks are subtracted from the values during load to ease comparison. This was necessary as it is explained in Appendix C.

During cooling, the FWHM does not change, as it is shown in Figure 64, because the first 10 data points were measured at RT just before cooling started. This also shows that the stress spikes occurring during cooling did not affect the peak broadening.

The green arrows shown in Figure 64 indicate the time-dependence in the FWHM. They all have the same slope of 0.025degree (2θ) per hour and start after the first unload from the fully plastic regime.

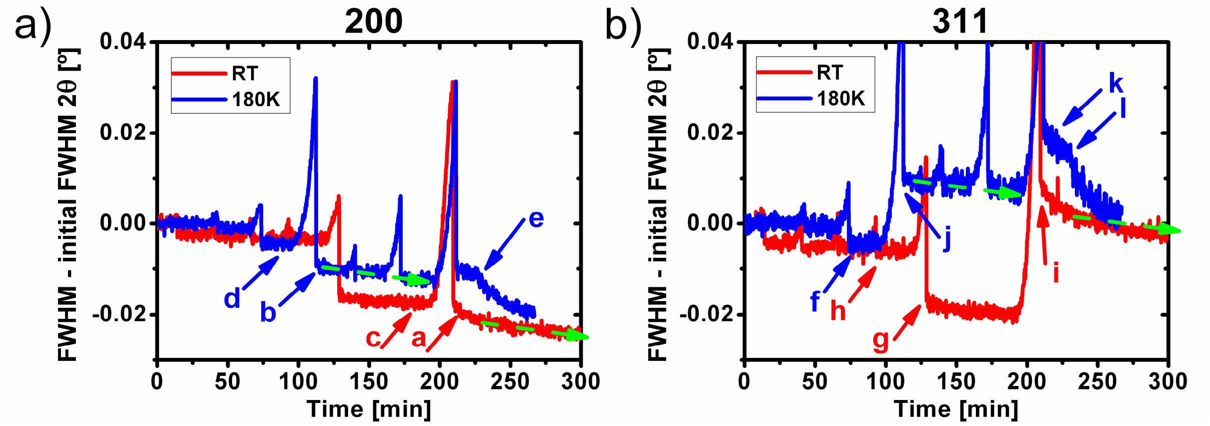

Figure 64: FWHM of a) the 200 peak and b) the 311 peak during the test series at 180K compared to a loading series at RT. The initial values are subtracted. For details, see text.

FWHM behavior of the 200 peak

Figure 64a compares the FWHM of the 200 peak during RT and 180K.

FWHM reduction

The reduction in the FWHM after the fully plastic loading is larger at RT (marked with an (a)) than at LT (b). It has been shown before, that the 200 peak exhibits additional reduction upon unloading from the full plastic regime (a) compared to the value upon unloading from 1.4GPa (c). This is also the case for the experiment at 180K. However, it has to be mentioned that the stress level in the unloaded region before loading to the UTS (b) at 180K was only 1.25GPa compared to the 1.4GPa at RT (c).

FWHM time-dependence

The time dependence after full plastic deformation at LT is marked with the green arrow. At RT, this slope is the same within the scatter (green arrows exhibit the same slope for RT and LT), but the constant slope is reached after a fast reduction immediately after unloading (a). During a test at 180K, such initial fast reduction is not present after unloading (b).

Heading to RT

An expected feature occurs during the heating to RT (see previous Section 3.2.2). During the heating (start marked with e), the FWHM value reduces and reaches a value comparable with the values obtained after deformation at RT.

FWHM behavior of the 311 peak

Figure 64b compares the FWHM of the 311 peak during RT and 180K.

FWHM reduction

The reduction in the FWHM after loading to 1.4GPa at 180K (f) is less compared to the RT reduction (g) and is similar to the reduction occurring at RT if the sample was unloaded from 800MPa (h). However, also here it has to be mentioned that the stress level in the unloaded region before loading to the UTS (f) at 180K was only 1.25GPa compared to the 1.4GPa at RT (g).

Upon unloading from the fully plastic regime, the FWHM at RT (i) is only slightly lower than that at LT (j); however, both FWHM values are higher than the as prepared value. This irreversibility in the FWHM at LT increases once it is loaded to the second time to the full plastic regime (k).

FWHM time-dependence

The time-dependence in the 311 peak upon unloading from the full plastic regime seems to be more pronounced at RT (starting at i) than at 180K (starting at j). The green arrows are again with the same slope printed on top of the data.

Heating to RT

During heating, the FWHM value of the 311 peak reduces strongly until the end of the test (starts marked with (l). Similar as for the 200 peak the FWHM reaches a value comparable with the values obtained after deformation at RT.

Behavior of the peak positions

The evolution of the peak positions during the loading cycles at LT are shown in Figure 65. In general, the behavior at LT is similar as that at RT (e.g. Figure 41). The first 10 data points were measured before the sample was cooled to testing temperature and an average of these values are used for the starting point (100%). When cooling the sample the peaks shift of about 0.1% compared to the RT peak position, which corresponds to the thermal expansion/contraction.

Before the maximum stress is reached, the peak positions return upon unloading to the initial (LT) values, which is the same as at RT (see Figure 41). After deforming the sample the first time into the full plastic region, the relative change in peak position is the same as observed at RT. The 220 peak position changes to larger values (~0.07%) and the 400 and 200 peaks positions reduced their value by approximately 0.05%. The relative changes at LT are similar as at RT.

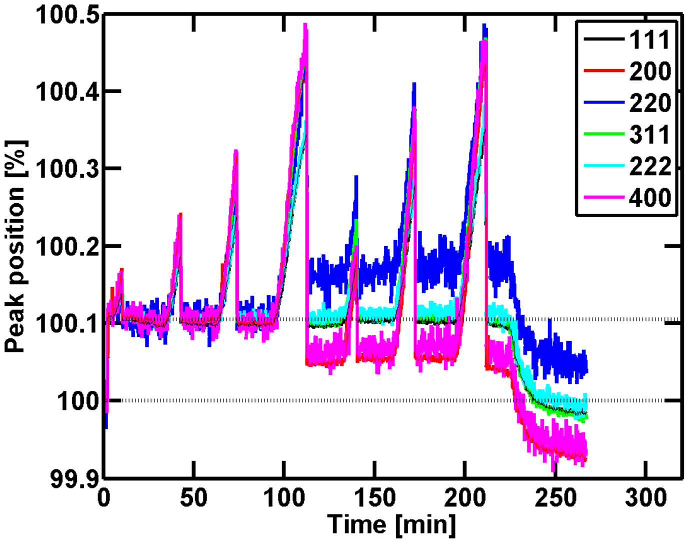

Figure 65: Relative peak position compared to the RT value during several load-unload cycles performed at 180K.

After the two series of loading cycles, the sample was warmed up to RT in the unloaded state. During this heating process, all peaks change in a similar way according to the thermal expansion and reached the expected RT values after plastic deformation. The 111, 222 and 311 peak positions return basically to their initial RT position but a slight reduction of 0.01% is present. The 220 peak position exhibits an increase of 0.07% and the 200 and 400 peak positions a reduction of 0.05%.

Main findings:

The comparison between LT and RT deformation reveals that the reduction in the FWHM of the 200 and 311 peak upon unloading from the full plastic regime is less when carried out at 180K. It shows as well that these effects are removed once the specimen is heated to RT. The time-dependence upon unloading is roughly the same at both deformation temperatures. The peak positions behavior at 180K is equivalent to the behavior at RT except that the absolute position changes according to the thermal lattice contraction.

3.2.4. Loading cycles on UFG-Nickel

In order to demonstrate the differences in the deformation behavior between NC and coarser grained Nickel all key experiments were also performed on UFG-Nickel. For these experiments, the same set-up and sample shape was used.

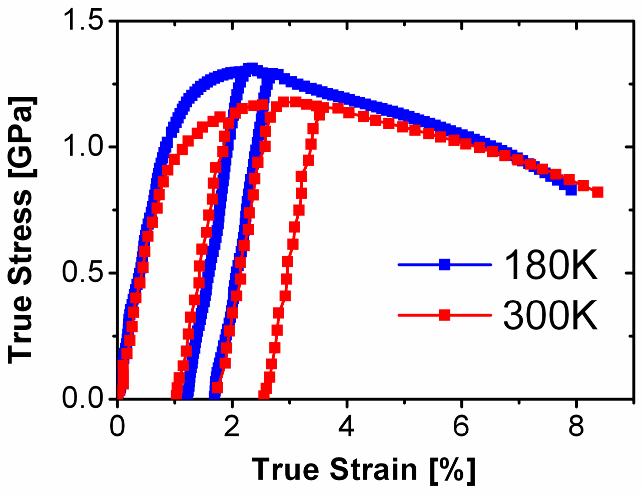

Figure 66: Stress strain data from HPT-Nickel tested at different temperatures.

On HPT-Nickel several load-unload cycles were performed at RT as well as at 180K. Figure 66 shows the stress strain data from these experiments. The maximum load and maximum elongation reached at RT is in agreement with previous published results [69]. Similar to NC-Nickel a higher strength at lower temperature can be observed, 1.17GPa at RT and 1.30GPa at 180K. The elongation to failure is almost the same for both temperatures with a value of around 8%.

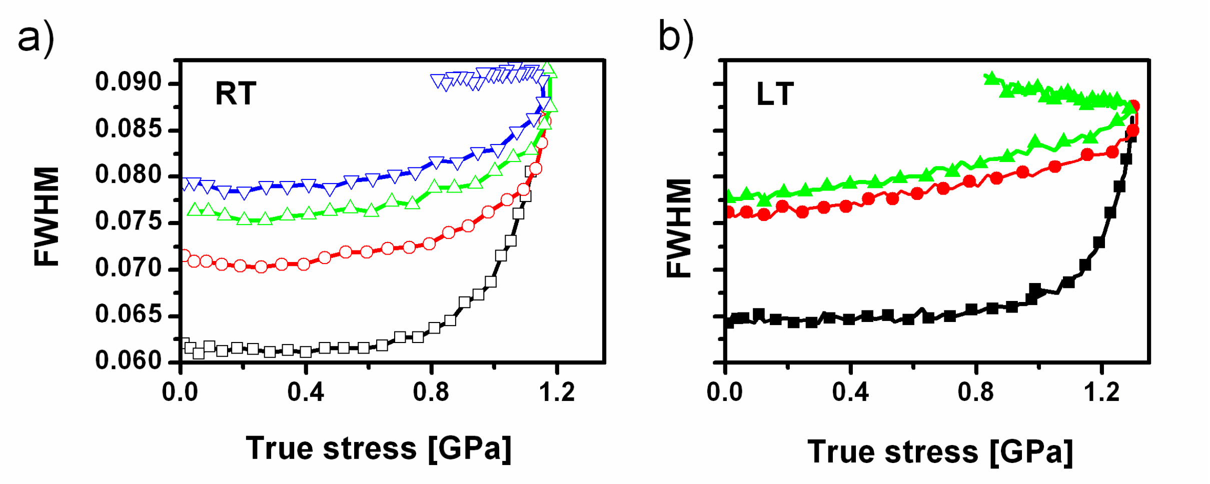

Figure 67: FWHM of the 111 peak during deformed via several load-unload cycles at a) RT and b) LT

In Figure 67 shows the FWHM of the 111 peak during deformation of UFG-Nickel at RT a) and at LT b). There is a clear irreversibility in the FWHM upon unloading from the plastic region for both the RT and LT deformation. During loading the sample for the first time, the FWHM stays constant until 0.7GPa for RT and 0.9GPa for LT. At higher loads a strong increase in peak width occurs. However, during the following loading cycles the FWHM behaves differently. During RT deformation, the FWHM is first slightly decreasing until 300MPa before increasing. At LT, the FWHM immediately increases even at the early stage of loading.

In the last loading cycle both samples were deformed to ~8% true strain (see Figure 66). The FWHM behavior at RT after the UTS (Figure 67a, last loading cycle in blue) consists of a stable broadening or even a small reduction. In contrast to the RT deformation, the UFG-Nickel sample deformed at 180K increase its FWHM after the UTS (Figure 67b, last loading cycle in green). However, this difference has to be taken with care due to the fact that the sample exhibit necking and no defined stress state is present.

Grain size distribution: HPT Nickel

TEM investigations were carried out to characterize the evolution of the microstructure in the deformations zone after deformation at 180K. A bright field micrograph from the deformation zone of the HPT Nickel specimen deformed at 180K is presented in Figure 68a. Some grains show clear GBs, however, the majority of the GBs are not clear enough to distinguish between the grains in a bright field image. The dislocation defect structure is pronounced in some areas but no homogeneous pattern is recognizable across the observed area.

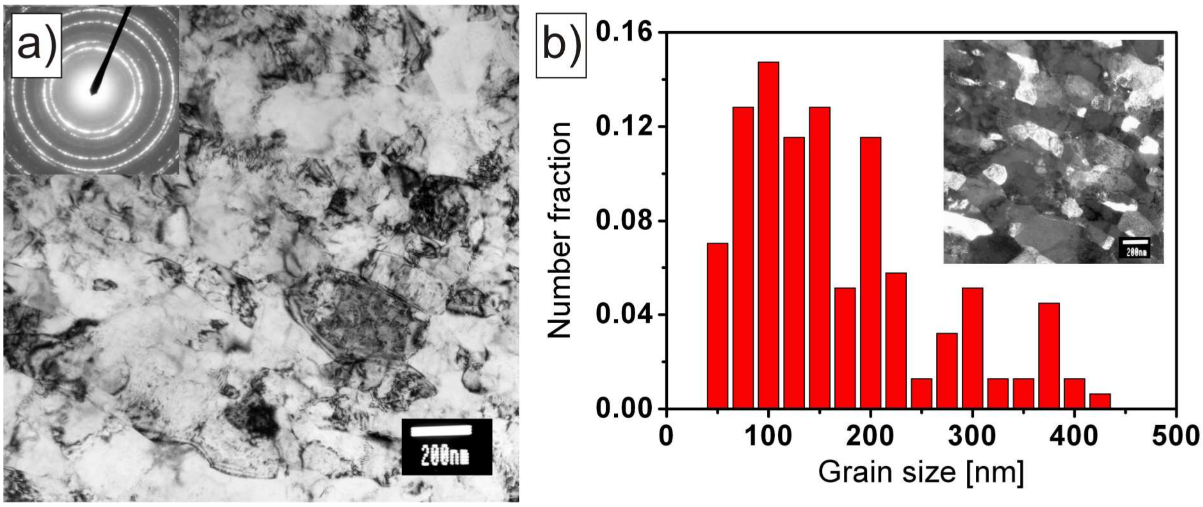

Figure 68: a) Bright field TEM picture of HPT nickel after LT. The inset shows a selected-area diffraction form the whole region. b) Grain size distribution from several dark field images (inset).

Figure 68b shows the grain size distribution from 156 grains obtained from dark field images. The average grain size after deformation at 180K given is 167nm with a standard deviation of 92nm. This value is very similar compared with the as prepared value of 155nm (see Section 2.1.2).

Main findings:

The FWHM behavior of UFG-Nickel is similar at RT and at LT. However, if the FWHM behavior of UFG-Nickel during deformation is compared with NC-Nickel it is distinctively different. The peak broadening in UFG-Nickel increases permanently upon unloading from a plastic deformation compared to the as prepared value. Hence, this FWHM behavior is equivalent what is expected for CG material [89, 145].

3.2.5. Tensile failure of nanocrystalline Nickel

The failure of many NC-Nickel samples is usually caused by a flaw like defect (Figure 69a). Some samples deformed at 180K exhibit elongations to failure of about 7 percent (Figure 69b) and some samples deformed at RT fail at 4.5 percent. Due to the low significant statistics, it is difficult to derive general rules if the temperature influences the elongation to failure. However, what can be said with certainty is that all samples observed within this thesis, which do not exhibit an elongation to failure of 7 percent, contained a flaw like feature within their fracture surface.

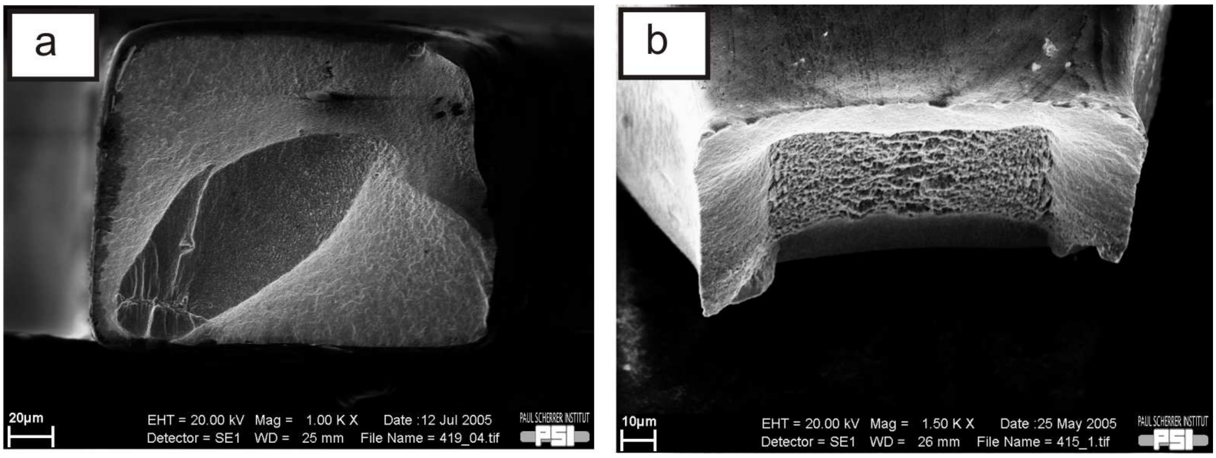
a
20µm
EHT = 20.00 kV Mag = 1.00 K X Date :12 Jul 2005
Detector = SE1 WD = 25 mm File Name = 419_04.tif
PAUL SCHERRER INSTITUT
PSI
b
10µm
EHT = 20.00 kV Mag = 1.50 K X Date :25 May 2005
Detector = SE1 WD = 26 mm File Name = 415_1.tif
PAUL SCHERRER INSTITUT
PSI

Figure 69: SEM micrograph from a fracture surface from a sample deformed at (a) RT (4.5% elongation to failure) and (b) 180K (7% elongation to failure)

3.2.6. Summary

LT experiments reveal a change of peak width behavior during deformation for NC-Nickel whereas the peak position only changes with thermal contraction. The reversibility of peak width by loading the sample in the full plastic regime disappears and upon unloading a slight irreversible peak broadening is present. However, this broadening can be removed by bringing the tested specimen back to RT.

Experiments on UFG-Nickel reveal a clear irreversible peak broadening upon unloading compared to NC-Nickel, however, for UFG-Nickel no noteworthy difference could be observed between RT and LT behavior.

3.3. Transient mechanical test

To gather more information on the underlying deformation mechanism occurring in NC-Nickel so-called transition tests were performed in collaboration with J.L. Martin who is an expert in this field [74]. The general idea of transition tests is to alter one imposed condition such as strain rate, stress or temperature and study the response of the material. In this frame work, strain-dip tests at RT (3.3.1) as well as successive stress relaxations at different temperatures (3.3.2) were carried out. A detailed essay about the materials response and the mathematical description can be found in Appendix A.

3.3.1. Separation of internal and effective stresses

Strain-dip tests were carried out at RT during constant strain rate test ($10^{-4}s^{-1}$) at three strain levels (2%, 3% and 4% true strain). The stress drops $\Delta\tau$ were performed with a strain rate > $10^{-2}s^{-1}$ followed by a short period of creep during which the plastic strain γ_p is measured as function of time. This is shown schematically in Figure 12 on Page 25. It is assumed that the internal stress does not change during the stress drop, i.e., there is no significant change in the microstructure. The initial creep rate is determined by a linear fit of the first 10s of creep. For each different stress drop $\Delta\tau$, a different sample is used. All tensile test samples originating from the same batch and are prepared in the same way. The Taylor factor (3.06) is used for extracting the shear stress τ from the applied normal stress [146].

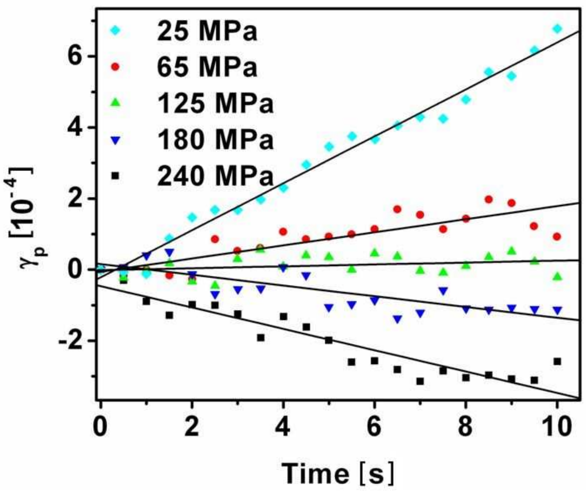

Figure 70: Creep measurements after a stress reduction at 3% true strain. The true stress before the drop was 1.8GPa.

Figure 70 shows the plastic strain as function of time for the five different stress drops all performed at a true strain of 3%. It can be seen that if the stress drop is small a positive creep rate is present, however if it exceeds ~125MPa shear stress a negative creep is observed. The corresponding creep rates as a function of $\Delta\tau$ are shown in Figure 71 where the dashed line represents the best-fit obtained using equation (40) on page 173. The fit reveals now a thermal (effective) stress component of ~140MPa shear stress (420MPa normal stress).

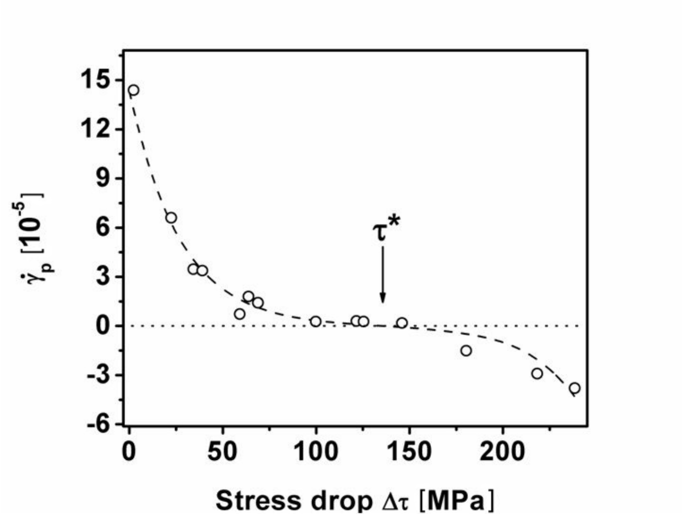

Figure 71: Creep rate as function of stress drop performed at 3% strain. The dashed line represents the best-fit obtained using (40).

Figure 72 shows the effective and internal normal stress for three different strain levels (2%, 3% and 4% true strain) as a function of strain.

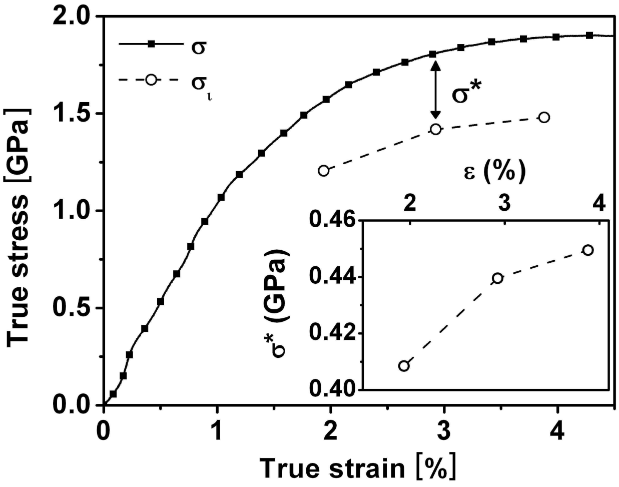

Figure 72: Macroscopic stress/strain curve together with the internal stress. The inset shows the effective stress as a function of strain.

The measurements revealed that both internal stresses (420MPa normal stress at 3% true strain) as well as their ratio between τ^*/τ_i in the order of 0.3, are large as compared to what is measured in single crystal FCC metals [147]. Furthermore, by using equation (41) on page 173 an activation volume of $10b^3$ can be derived for NC-Nickel tested at RT.

3.3.2. Activation volume measurements

Successive stress relaxations were carried out at three different temperatures (180K, 230K and 300K) over the whole range of the stress strain curve (see e.g. Figure 73). Details of the stress-time data during relaxation in the elastic and in the plastic region are shown in the insets of Figure 73. In the elastic region, the reduction in stress was found to be zero after three relaxations. In the plastic region, at maximum five relaxations were performed.

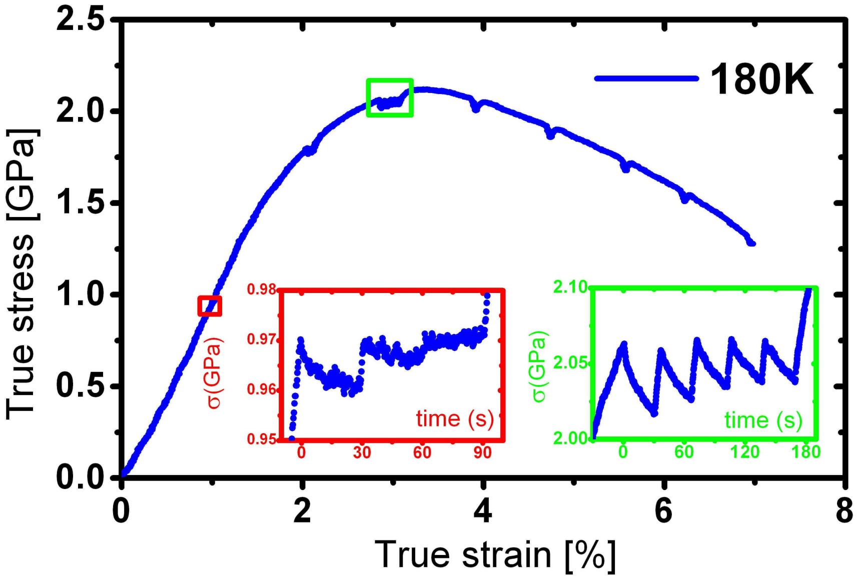

Figure 73: Stress strain data during successive relaxations performed at several positions during deformation at 180K. The inset shows two examples of such successive relaxations at different stress levels.

In Figure 74, the activation volumes calculated from successive relaxations via equation (52), (54) and (55) at several different samples are plotted against the true stress and true strain. The activation volume is expressed in b^3, where b is the shortest Burgers vector of a dislocation. This Burgers vector is the half lattice constant in [110] direction, which is 0.249nm for Nickel. In the elastic region, an activation volume in the order of $100b^3$ is measured at RT. If the sample is tested at 180K the activation volume increases to approximately double the RT value.

The activation volume measured at higher strains/stresses decrease for all three tested temperatures. At RT, the reduction moderates around 0.5% true strain (1GPa) and continue to reduce. Around 3% true strain the activation volume reaches its minimum of $15b^3$. At lower temperatures, this change seems to happen at higher strains/stresses. However, tests performed at 180K also reach the lowest activation volume around 3% true strain but the value of $35b^3$ is distinct higher than at RT.

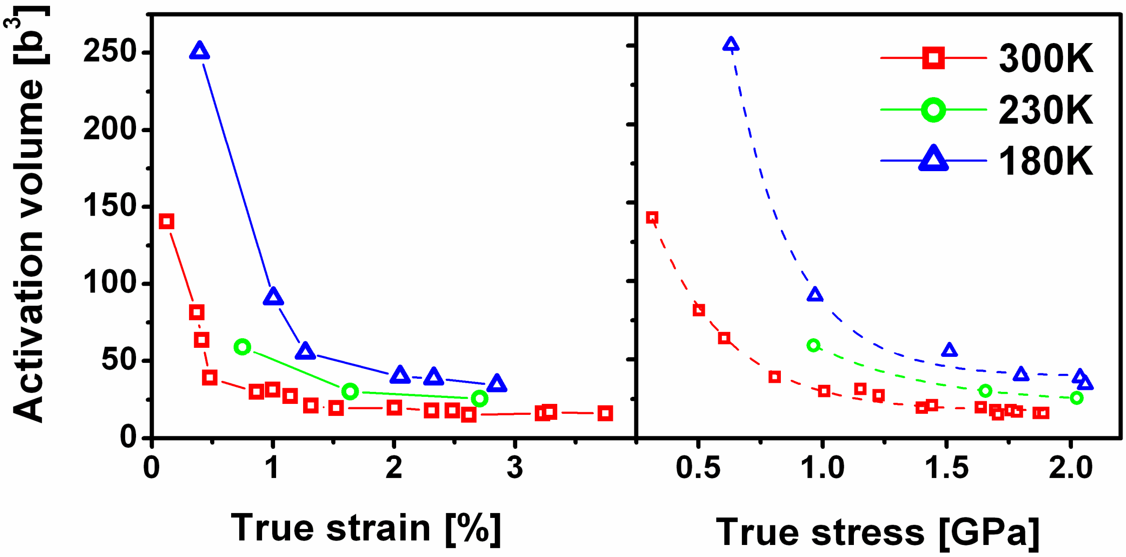

Figure 74: Activation volume data points plotted versus the strain and stress they are measured at three different temperatures.

Activation volumes measured after the UTS was reached, are not presented in this data because the real stress state in the necking region is undefined (see Figure 73 and equation (51)).

3.3.3. Summary

The internal stress as well as the ratio between the internal and effective stress is very high in NC-Nickel. Successive relaxation at RT revealed an activation volume in the order of $15b^{3,}$ which is approximately the same value as found with strain-dip test. The measured activation volume in NC-Nickel is at least one order of magnitude smaller than typical activation volumes found for CG Nickel [45]. When NC-Nickel is tested at 180K the activation volume increases to ~$35b^3$.

3.4. Compression results

The limited tensile ductility of NC-Nickel does not allow to obtain large deformation levels. Therefore, compression tests were carried out to study the material at large plastic strains. Furthermore, the grain size stability in NC metals has been of concern since the large energy associated with the high density of GBs represents a driving force for grain growth. To investigate the stability of NC-Nickel long-time stress relaxation experiments and long-time creep tests were carried out at stresses close to the UTS.

3.4.1. Load-unload cycles

Mechanical data

Figure 75 shows the stress strain data from six load-unload cycles performed on NC-Nickel in compression. The sample was loaded with an initial strain rate of $1.6*10^{-4}s^{-1}$. In order to follow the behavior of the peak broadening the sample was unloaded at different stresses/strains (0.8GPa/2.3%, 1.5GPa/4%, 1.88GPa/6.5%, 2GPa/10%, 2.02GPa/15% and 2.04GPa/19.7%). Between each unloading and the next loading cycle, the sample was kept 10 min in an unloaded state, allowing detection of an eventual time dependent recovery of the FWHM. The characteristic of the stress strain curve is that after a short strain-hardening regime NC-Nickel plastifies with an almost constant flow stress.

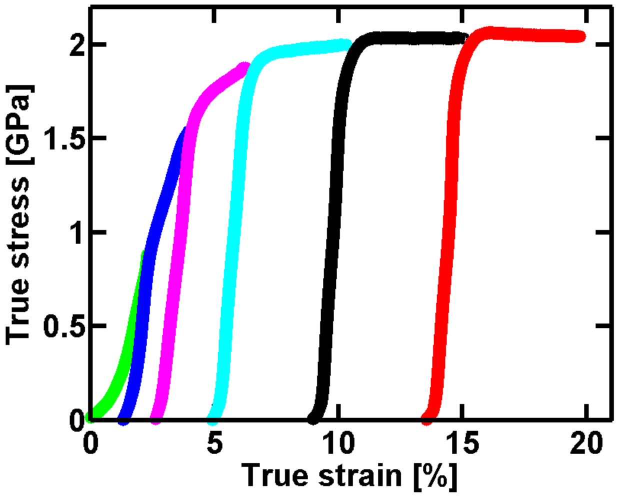

Figure 75: Stress strain data of a load-unload cycle in compression.

Figure 76 presents a SEM picture after compressive deformation. The post-mortem investigation revealed a plastic deformation of 19.3% engineering strain. It has to be mentioned that the deformation mode applied here does not correspond with an ideal uni-axial compressive mode. The deformed sample was slightly barreled after deformation (as is shown in Figure 76), which has to be ascribed to friction between the sample surface and the crossheads.

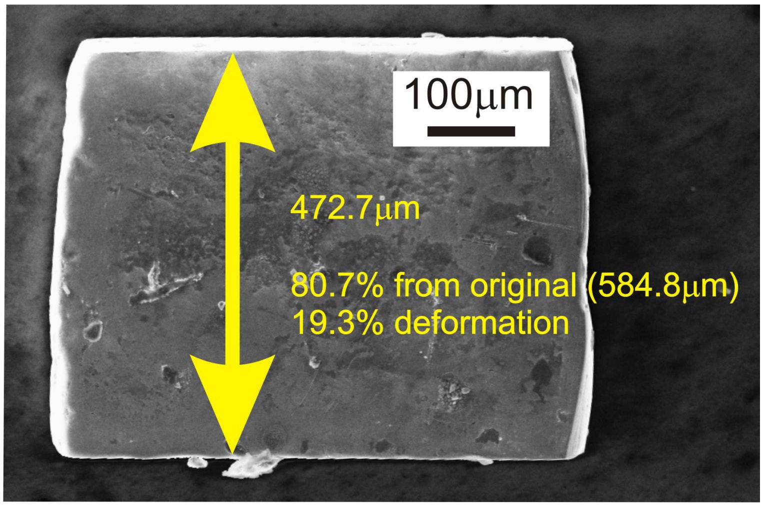

Figure 76: SEM picture of the deformation sample after the loading cycle.

Diffraction data

Figure 77 shows the FWHM of the (111), (200), (220), (311), (222) and (400) diffraction peaks as a function of time. Upon each unloading, there were 10 min waiting time before the sample is reloaded. In the first two unloading cycles (green and blue), an extra recovery of the FWHM for all peaks is present. At higher stresses, the (111) and (200) continue to reduce upon unloading whereas all other peaks have a tendency to demonstrate a slight increase. After the third time loading (magenta), a time dependent recovery of the FWHM sets in upon unloading. The maximal amount of peak broadening during compression testing is of the same order as during tensile tests. For example, the broadening of 311 peak during tensile testing is around 0.1° (2θ). This is visible in Figure 36 if the value upon unloading from the microplastic regime is compared with the FWHM value at the UTS. The broadening of the 311 peak reached during compression testing in the fourth loading cycle (cyan in Figure 77) is as well around 0.1°.

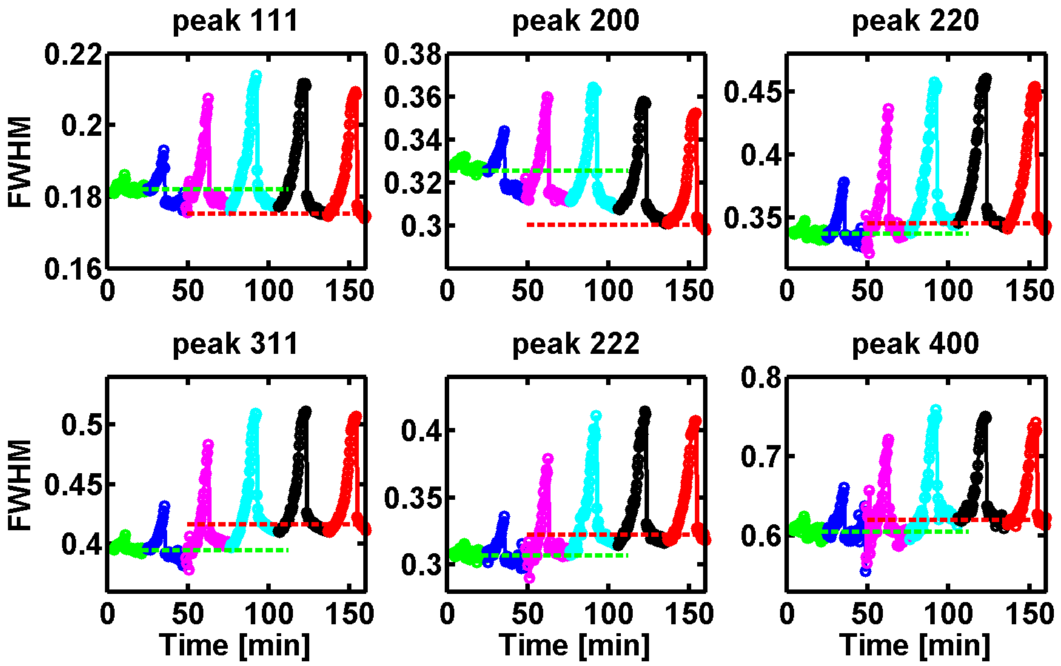

Figure 77: FWHM (in ° of 2θ) of six peaks during six load-unload cycles. Each color corresponds to one load cycle and the following 10minutes unloading period.

The peak positions of all six peaks are displayed against time in Figure 78. A red and green dotted line indicates the initial and the last value in the unloading state respectively. For the 220 peak, little is changing in all unloading states. For all other peaks, a small increase upon each unloading is visible. The effect is most pronounced in the 200 peak. A comparison with tensile test results is presented in the discussion (Section 4.2.2).

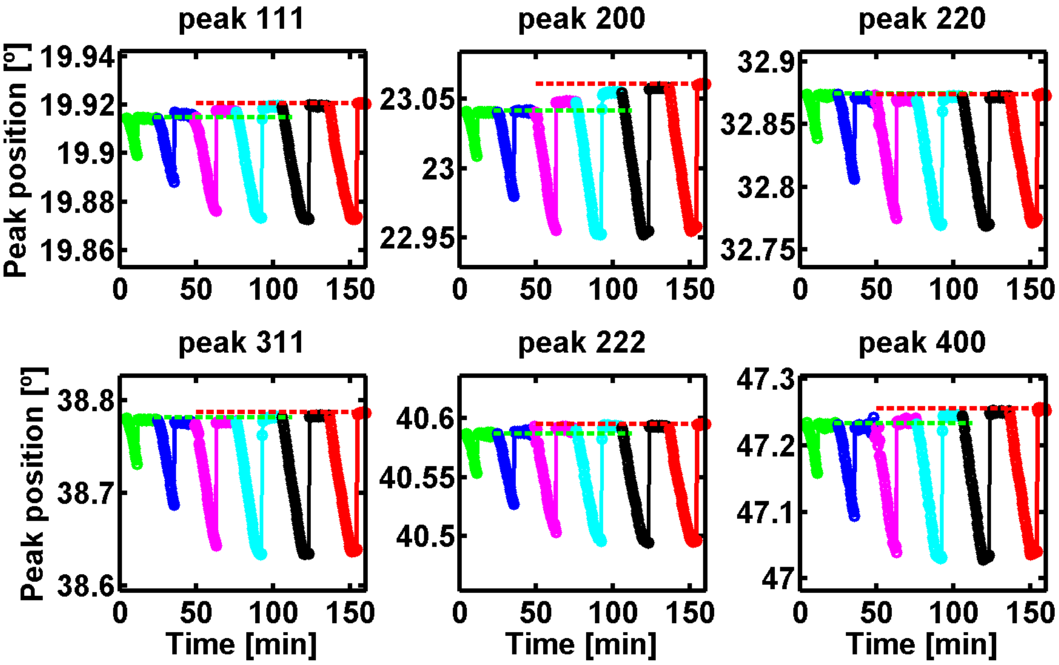

Figure 78: Peak positions versus time during six load-unload cycles.

TEM analysis

Figure 79a shows a brightfield TEM micrograph of a TEM lamella from a central region of the deformed sample. Compared to as prepared material the polygonal shape of the NC grains are better visible in the micrograph. In some areas, there are contrast variations within the size of one grain. A few possible twins could be observed indicated by red arrows in Figure 79a.

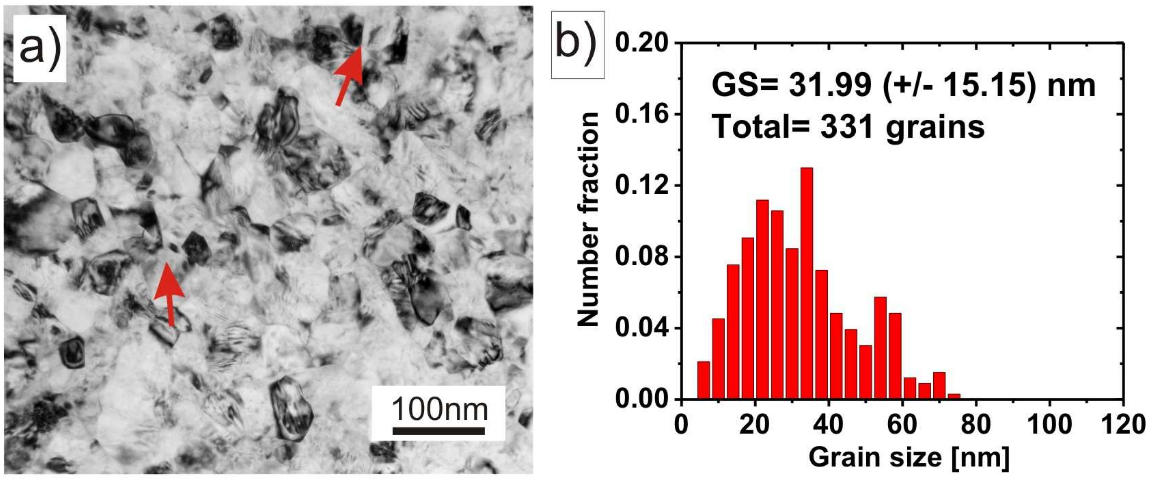
a)
100nm
b)
GS= 31.99 (+/- 15.15) nm
Total= 331 grains
Number fraction
0.20
0.16
0.12
0.08
0.04
0.00
0
20
40
60
80
100
120
Grain size [nm]

Figure 79: a) TEM brightfield picture from the compression sample after deformation and b) the corresponding grain size distribution from several darkfield images.

The grain size distribution shown in Figure 79b, exhibit a mean value of 32nm and a narrow distribution affirmed by the standard deviation of 15nm.

Main findings:

The load-unload cycles in compression exhibit a maximum elongation of 19.7% true strain at a stress of 2.04GPa. The FWHM of the 111 and 200 peak reduce upon each unloading whereas the FWHM of the other peaks slightly increase. Furthermore, a time dependent decrease in the FWHM upon unloading is visible for all peaks after deformation to 6% true strain. TEM micrographs reveal a mean grain size of 32nm after deformation. Furthermore, the TEM micrograph show more clear and distinct grains if compared to the undeformed material.

3.4.2. Stress relaxation test

Mechanical data

Figure 80a shows the stress strain data and the stress time data of a continuous compression test. The sample was loaded with constant crosshead speed of 0.1mm/s equivalent with an initial strain rate of ~1.65*10^{-4}s^{-1}.

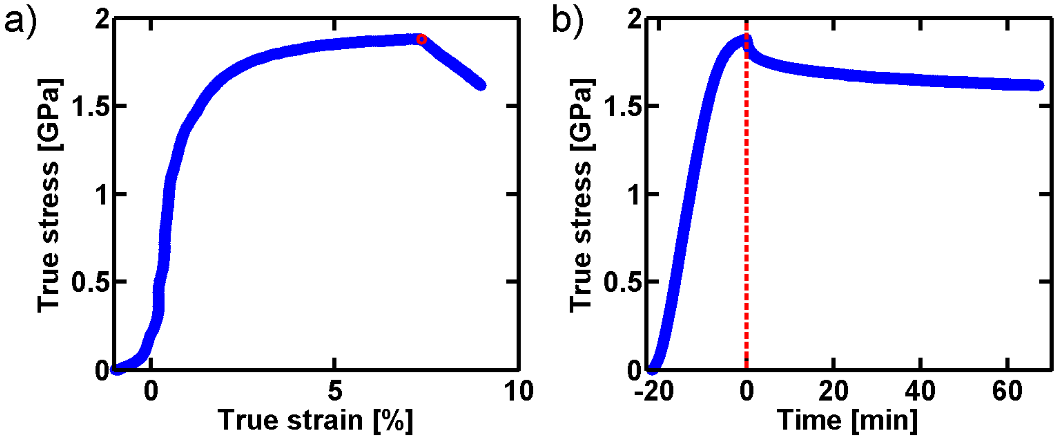

Figure 80: Stress strain and stress time data for a relaxation experiment in compression. The dashed red line/red dot mark the point from when on the crosshead where stopped. The increase in strain after the crossheads are stopped is due to the MTM.

The true-stress true-strain curve can be characterized by a linear loading until ~1.2GPa followed by a transient region. At a strain of 7.3% corresponding with a load of 1.88GPa, the crosshead was stopped (indicated in Figure 80a with a red dot and in b with a red dashed line) and the stress reduction was followed over time (Figure 80b). After 65 minutes, the stress level dropped 14% to 1.62GPa. However, due to low stiffness of the MTM (see also Section 2.2.3 at Page 31) the sample gained 1.6% additional strain.

TEM analysis

The micrograph in Figure 81a shows a typical area. Only a few grains are clearly visible. The TEM brightfield image is characterized by strong contrast variations well below the grain size. From several dark field images, a mean grain size of 28nm was established.

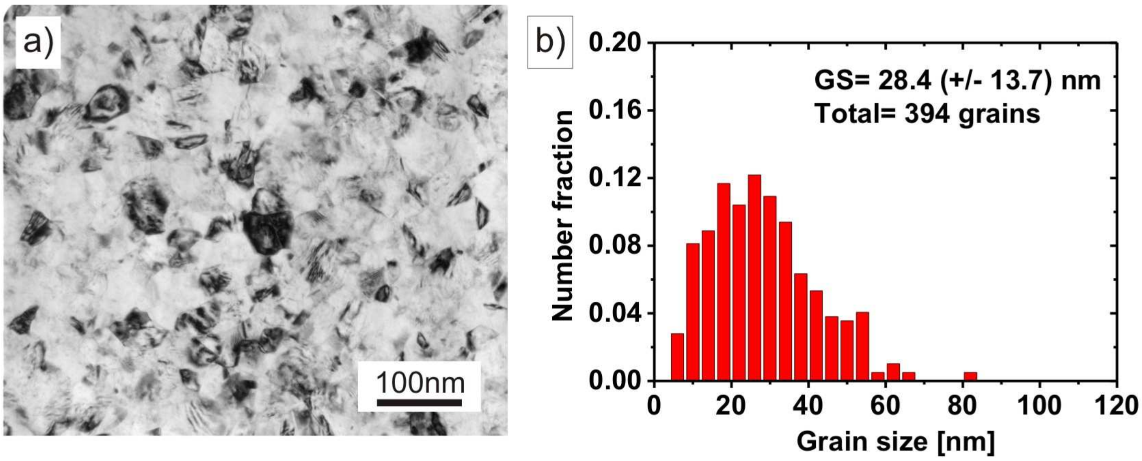

Figure 81: a) TEM micrograph and b) grain size distribution of a strain controlled compression experiment.

3.4.3. Creep test

Mechanical data

In Figure 82a, the stress strain data and the stress time data of a creep/load controlled test is shown. The sample was first loaded with a constant crosshead speed of 0.1mm/s equivalent with an initial strain rate of ~$1.75*10^{-4}s^{-1}$. As the engineering stresses reached 2.0GPa (5.8% engineering strain, marked with a red dot), the sample was kept at constant load until 15% strain. This creep period lasted for 240 minutes and was followed by an unload.

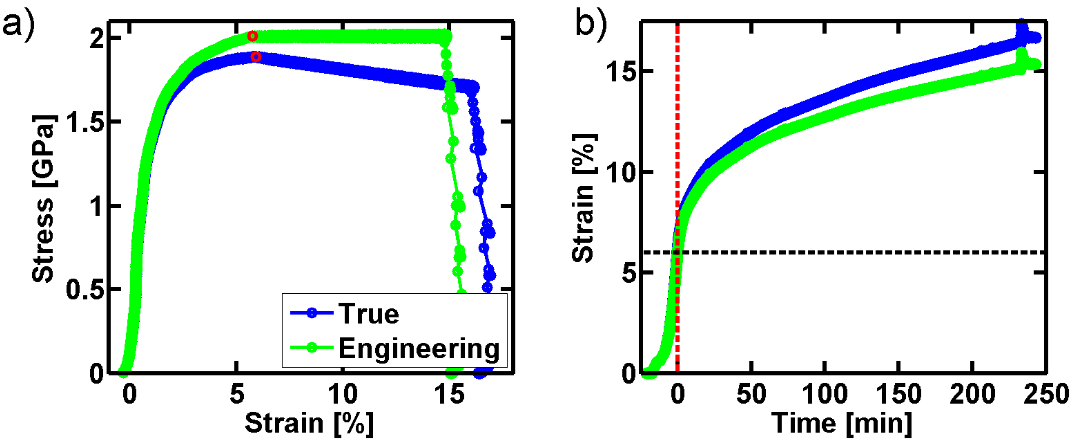

Figure 82: Stress strain and strain time data for a constant load experiment in compression. The dashed red line/red dots mark the point from when on constant load was applied.

The strain (engineering and true) time data is shown in Figure 82b. The point where constant load was started is indicated with a red dashed line on the time axis and a black dashed line on the strain axis. After a rapid increase in the first 50 minutes (primary creep) the increase in strain stabilizes at a creep rate of about $4*10^{-6}s^{-1}$ (secondary creep). This creep rate data is shown in Figure 83.

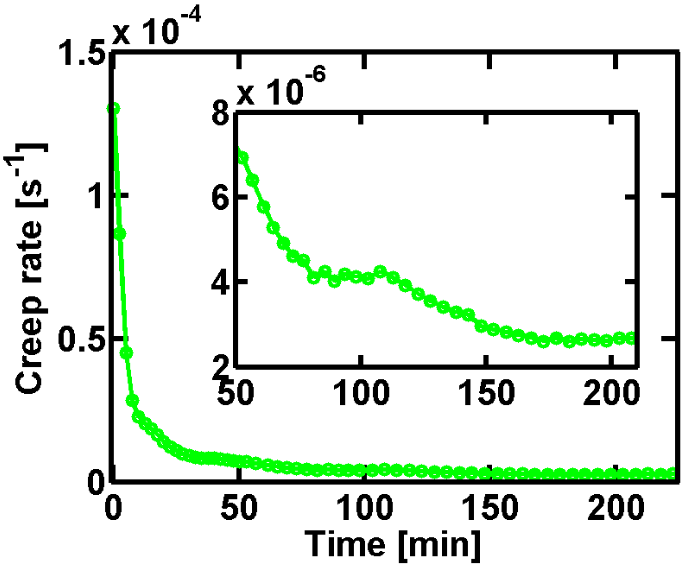

Figure 83: Creep data during constant load experiment in compression. The inset shows details above 50minutes creep.

TEM analysis

Figure 84a shows a TEM micrograph from the sample after the creep test. Compared with the as prepared material (see Figure 2a) it can be recognized that the shape of the grains are better defined in the TEM picture. There are low contrast regions but only few areas show short/fast variations in contrast indicating a clear grain structure. The deformed sample exhibit a mean grain size of 27nm established from 270 grains counted from dark field images.

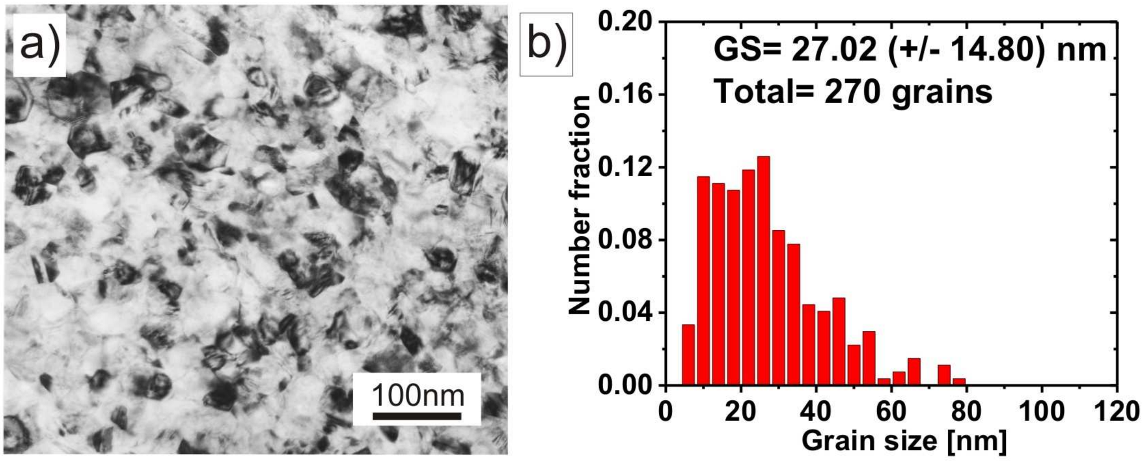

Figure 84: a) TEM micrograph and b) grain size distribution of a load controlled compression experiment.

3.4.4. Summary

The load-unload compression experiments revealed that the peak broadening behavior upon unloading after 20% deformation is comparable as what has been observed in a tensile test. Pronounced is the reduction in the broadening of the 200 peak and the increase in the 311 peak width. The peak positions change slightly upon unloading. A comparison with the tensile data is given in the discussion Chapter.

During the relaxation test started at 1.88GPa, the stress level dropped after 65 minutes by 14% to 1.62GPa and reached a final deformation of ~9% strain. The creep test started at 2GPa and lasted for 240 minutes where a strain of 15% was reached. This test exhibited a primary and secondary creep region where in the latter one a creep rate of $\sim 4*10^{-6}s^{-1}$ was reached.

Table 1 summarizes qualitatively the analyzed TEM bright field micrographs from NC-Nickel compression samples listed according to their governed strain. In general, there is a trend that the grain shapes become more distinct if the sample was deformed to higher strains.

Test	Strain (%)	Grain size (nm)	Observed features	Figure
as prepared	0	26.2	Only few clear grain structures	Figure 2
relaxation	9	28.4	Some clear grain structures	Figure 81
creep	15	27.0	More clear grain structures	Figure 84
load-unload	20	31.9	Several clear grains with a well defined polygonal shape	Figure 79

Table 1: TEM analysis of compression samples compared with the as prepared material.

An important outcome from the compressed NC-Nickel samples is that grain coarsening seems to be minor even at these large strains during compression. In NC-Aluminum, stress driven grain growth was observed for freestanding films during uni-axial tensile experiments [68]. Furthermore, inert gas condensed NC-Copper with an initial grain size (32nm) shows an increase of more than double (77nm) after compressive deformation [148]. This can be seen in Figure 85 where the results from Copper and Nickel are compared. These results form other NC FCC metals highlights the stable grain size in NC-Nickel.

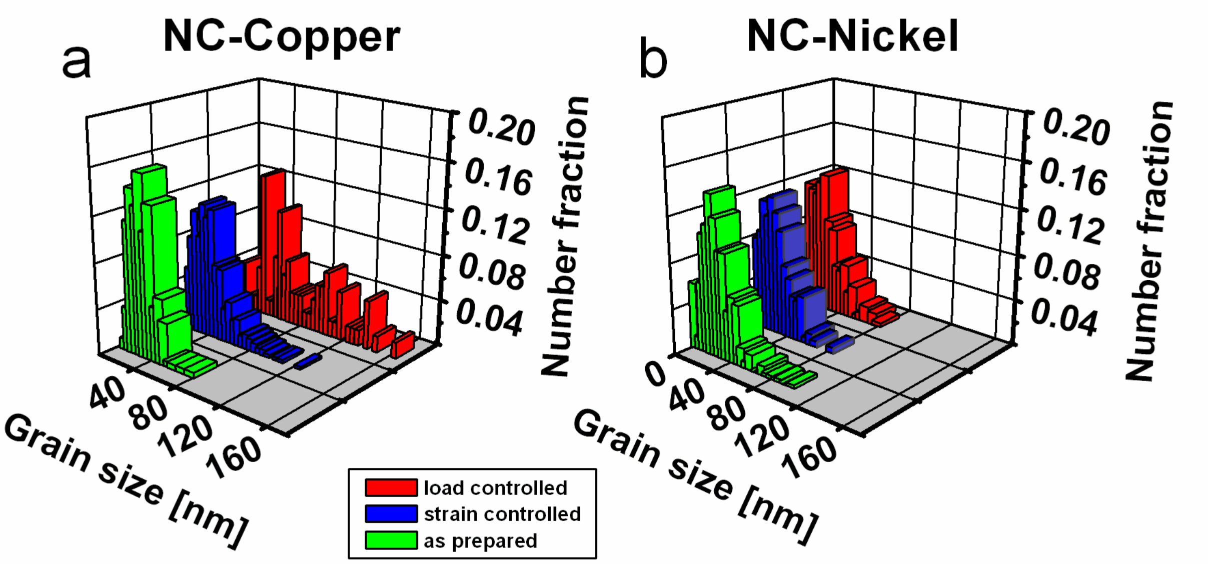

Figure 85: Grain size distributions of the as prepared, strain-controlled and load-controlled Copper a) and Nickel b) samples. Details on the deformation parameters of NC-Nickel can be found in Section 3.4.2 and Section 3.4.3 and from NC-Copper in reference [148].

3.5. XRD calculation plus Williamson-Hall analysis

It is known that dislocations and twins can change the peak widths and therefore the shape of the WH plot. To study separately their influence, two different types of MD samples were constructed where one contains only dislocations and the other one only twins. From each MD cell type, an initial configuration without defects and three other ones with different defect quantities were studied using methods described in Section 2.5. From all eight MD configurations isotropic X-ray diffraction pattern were calculated (Section 2.5.5). Furthermore, it has to be mentioned that Aluminum was chosen, rather than Nickel or Copper, because the empirical potential used [138] allows the nucleation of both leading and trailing partial dislocations at the GB during tensile deformation due to the ratio of the unstable to stable stacking fault being close to unity [55].

3.5.1. Introducing dislocation defects

A NC-Aluminum configuration, DIS-0 that contains 100 defect-free grains (in total ~ 5 million atoms) with a mean grain size of 10nm was constructed (see Section 2.5.2.). To obtain a relaxed structure the sample was flash annealed during 100ps of MD at 800K followed by 10ps of equilibration at 300K. By applying a constant uni-axial tensile stress of 1.6GPa to this sample, an initial strain rate of ~ 7×10^8 was obtained during the first 60ps, increasing to a value of ~ 1.7×10^9 at 80ps of deformation as shown in Figure 86. Such a rapid increase in strain rate beyond 80ps is related to the activation of different slip systems within one grain, together with the observation of some mechanical twinning close to triple junction regions by means of sequential partial dislocation activity from GBs [149]. It should be noted that the activation of multiple slip systems and the observation of different slip mechanisms originate from the high strain rates of simulations [55]. At the largest strain in Figure 86, a total of 180 lattice full-dislocations were observed. The goal was to obtain samples with considerable dislocation content, justifying the use of the high strain rates. Such configurations were unloaded by instantaneously reducing the applied load to zero followed by RT MD for 20ps. Figure 86 also displays the corresponding unloading curves (blue) starting from three different plastic strains, resulting in the unloaded configurations DIS-1, DIS-2 and DIS-3. The unloading of the sample was necessary to be able to calculate the X-ray diffraction pattern because the calculation involves an orientation average where the bulk stress state must be isotropic.

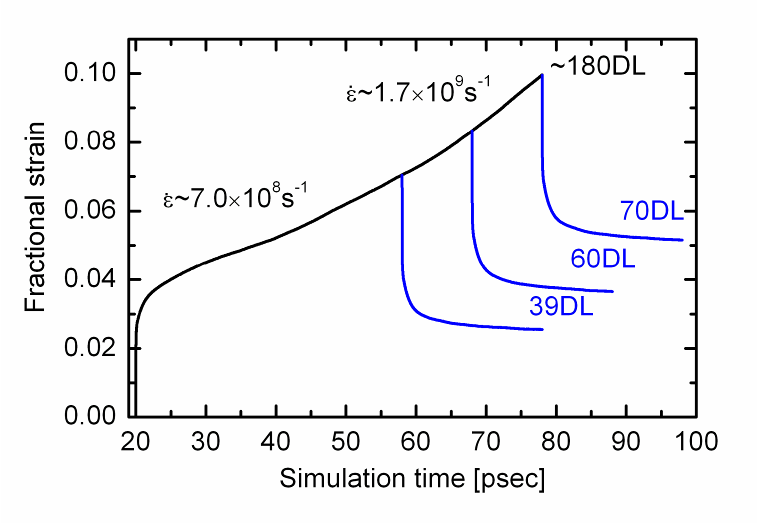

Figure 86: Deformation curve in strain versus simulation time to construct samples with certain dislocation (DL) content. Black is the deformation of the initial sample by constant stress of 1.6GPa. The three blue data sets are the unloading curves.

The remaining dislocations were categorized into four classes as displayed in Figure 87 using the visualization software (AMIRA®). Figure 87a and Figure 87b display two classes of full lattice dislocations where the first represent dislocations well within the grain interior and the second perfect dislocations close to the GB. Figure 87c and Figure 87d represent both partial dislocations. They are sub-classified as clearly visible partial dislocation close to the GB (Figure 87c), and the leftover core segments of a dislocation that is not fully absorbed (Figure 87d). Note that the class represented in Figure 87d can be identified with either nucleation of a partial dislocation or absorption of the trailing partial; in both cases, a “lattice Burger’s vector” content can be identified. Finally, note that the percentage of multiple slip in grains increases in the order DIS-1, DIS-2 and DIS-3 (10%, 15% and 17%, respectively).

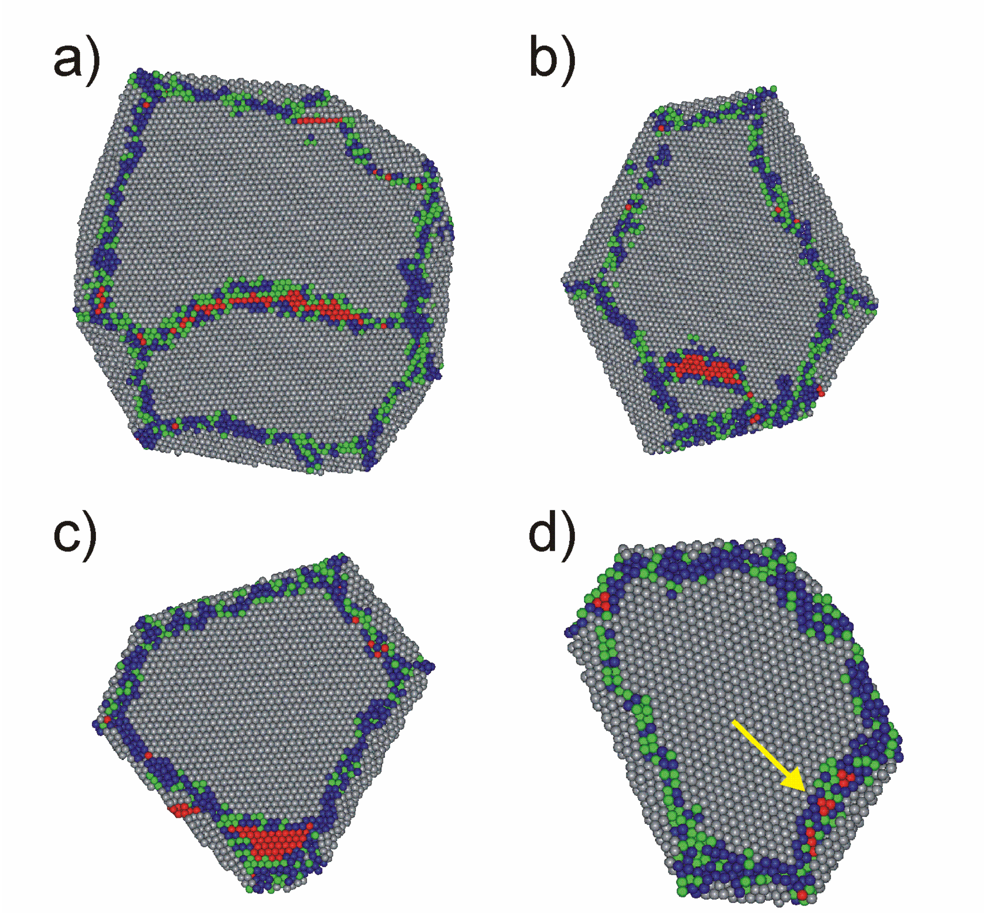

Figure 87: Classes of dislocation used for the analyze: a) perfect dislocation well within the grain; b) perfect dislocation close to GB; c) partial dislocation attached with its stacking fault to the GB; d) partial core segment in the GB. For color code, see section 2.5.2.

Table 2 presents a detailed atomic scale investigation of the dislocation structures of the three unloaded samples in terms of the total number of remaining full and partial dislocations, and their proximity to the GB. It is important to note that in spite of the short unloading times, a large percentage of lattice dislocations are absorbed in the GB: in DIS-3 110 of the 180 lattice dislocations present before unloading are absorbed in the GBs during unloading.

Sample	DIS-1	DIS-2	DIS-3
Number of dislocations	39	60	70
Number of perfect dislocations	18	36	42
% in grain interior	78	58	52
% close to GB	22	42	48
Number of partial dislocations	31	24	28
% clearly visible	81	79	79
% where core segment is only visible	19	21	21

Table 2: Number of dislocations within the different samples, classified according to Figure 87.

3.5.2. Introducing twin defects

The twin defects transecting the whole grain are geometrically introduced in a sample with ~1.2 million atoms and 15 grains [150] with an average grain diameter of the order of 12nm. Three samples are constructed where the sample with the lowest twin density (TWIN-1) contains one twin in seven of the 15 grains. The sample called TWIN-2 contains one twin per grain. The highest twin density is present in sample TWIN-3. There in average every 10th plane is a twin plane, which corresponds with a twin-probability-factor α of 0.1 as defined in the Warren twin analysis theory [112].

3.5.3. X-ray calculations from MD simulation cells

The calculated diffraction patterns/peaks from the different samples (DIS-0 [as prepared and flash annealed], DIS-1, DIS-2, DIS-3, and TWIN-0, TWIN-1, TWIN-2, TWIN-3) were fitted with the same function as the experimental data, i.e. a P-VII (see Section 2.3.4). Figure 88 shows now the 111 and 200 diffraction peaks from a) two dislocation and b) two twin samples. The black data was calculated from the defect free samples and the red data from the samples with the highest defect densities. The MD samples with the highest defect density of each type are shown above the diffraction peaks.

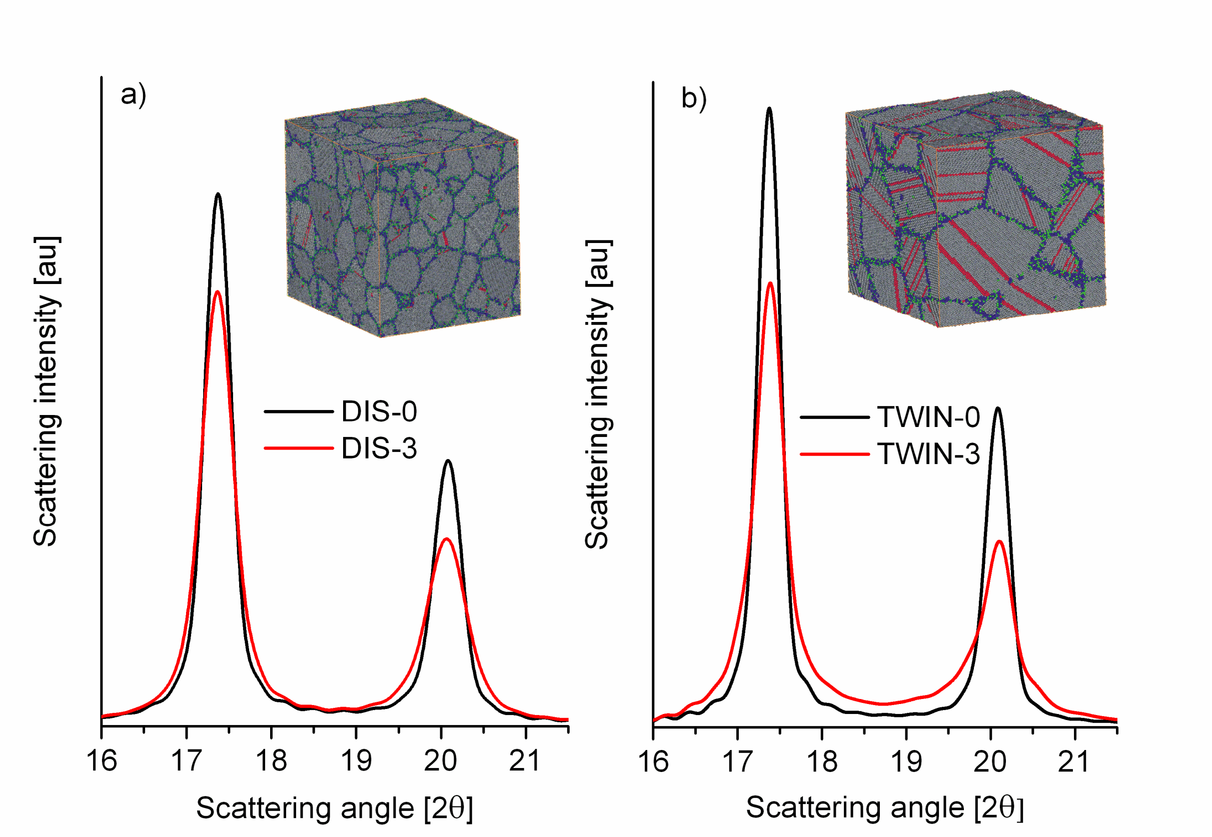

Figure 88: Results on the dislocation (left) and twin (twin) samples. Diffraction pattern from the as constructed (black) and defect samples (red) are shown with their corresponding MD sample (corresponds to the red data).

Close inspections of the calculated diffraction pattern reveal oscillations at the background level originating from the relatively discrete and narrow grain size distribution of the tested samples: sharp changes in misorientation in real space introduce long-range oscillatory behavior in reciprocal space. If a truly continuous grain size distribution is present, this effect is averaged over. Figure 89 displays in detail the 220 peak and the corresponding fit for samples DIS-00 (blue) and DIS-3 (green) with their residuals. The residuals clearly show now the weak oscillatory behavior. Interestingly, the magnitude is somewhat reduced for the dislocated sample. However, due to the same grain shape and misorientation distribution of the compared samples, such errors were systematic, making it possible to identify trends over different dislocation and twin densities. Despite all deficiency, each peak could be fitted to a P-VII function with a relative error of at most 10% in the peak widths.

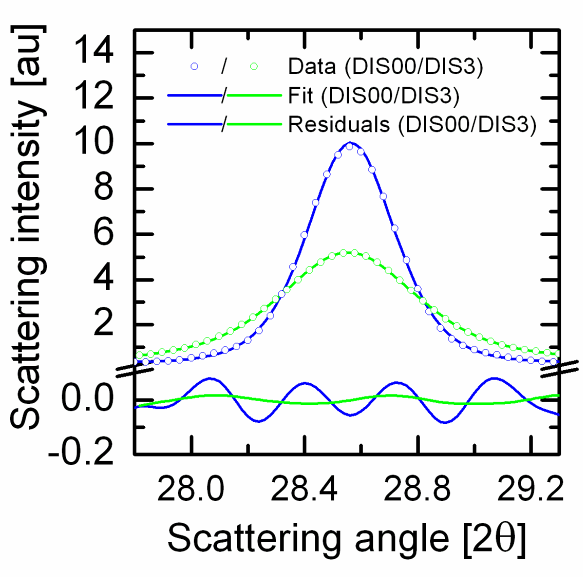

Figure 89: Peak fit quality displayed on the 220 peak with the residuals of an as prepared sample (blue) and one with introduced dislocations (green).

3.5.4. WH anisotropy from calculated spectra

The results obtained from the simulations and calculations are now the diffraction pattern from samples with a known defect structure. The different signatures of the dislocation and twins on the WH plot are shown in Figure 90 where the peak widths are plotted as a function of peak position in terms of scattering vector (18) for the diffraction peaks 111, 200, 220, 311, 222 and 400.

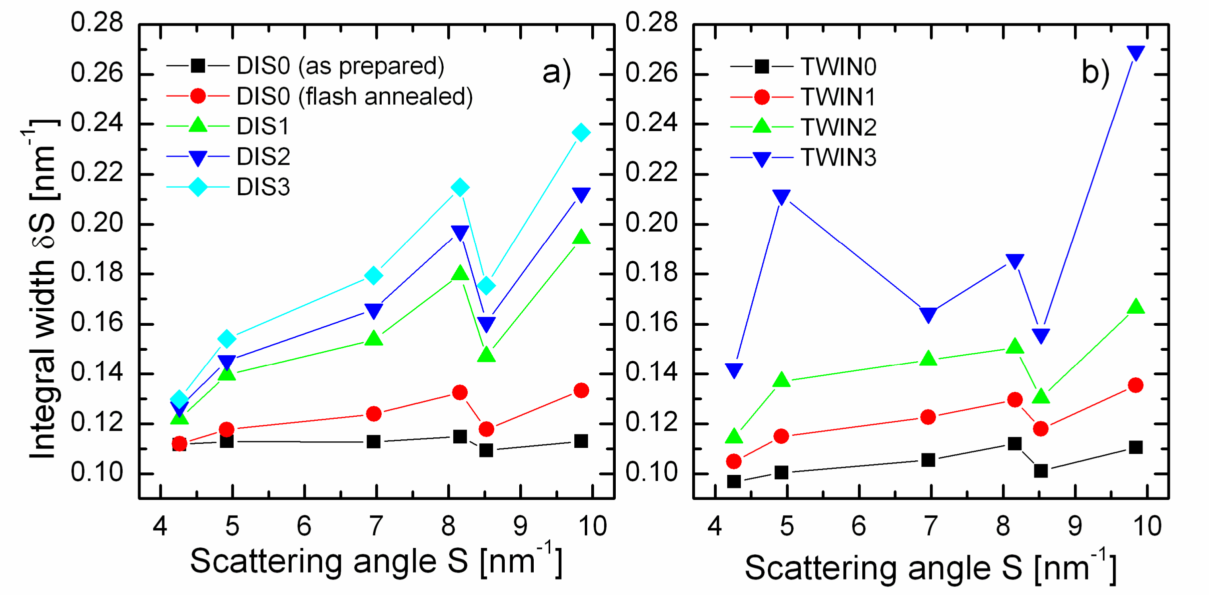

Figure 90: WH plot for all dislocations and twin samples. For details, see text.

Changes in the WH anisotropy through dislocations

DIS-0 produces a WH plot that exhibits little anisotropy (Figure 90a), confirming the weak strain fields of the intrinsic GB dislocations within the as constructed dense NC GB network [14]. For the deformed samples DIS-1 to DIS-3, an increase in anisotropy is observed with a pronounced increase in the integrated width of the (311) peak as the dislocation content increases. Also shown in Figure 90a is the WH data of the sample prior to the 800 K relaxation procedure. It demonstrates that the computational annealing procedure, which results in a GB structure consisting of better-defined extrinsic GB dislocations in general high-angle GBs [151], also results in an increase of the WH anisotropy similar to the type obtained from dislocations.

Sample	111/222 Grain size (nm)	111/222 RMS-strain (%)	200/400 Grain size (nm)	200/400 RMS-strain (%)
DIS-0	10.4	0.16	10.9	0.14
DIS-1	10.3	0.27	11.2	0.24
DIS-2	10.2	0.34	11.5	0.57
DIS-3	10.6	0.42	12.3	0.67

Table 3: Mean grain size and RMS-strain derived via the Cauchy-Gaussian deconvolution of size and strain from the 111/222 and 200/400 family of the calculated diffraction peaks.

Table 3 displays the mean grain size as well as the RMS-strain of the 111/222 and 200/400 family of peaks using a Cauchy-Gaussian deconvolution of the integrated width. The grain size is approximately constant for all samples, which can be expected from the short MD simulation times used to introduce the dislocations. The RMS-strain increases roughly linear with increasing lattice dislocation content as shown in Figure 91. The fluctuation for grain size and RMS-strain are slightly bigger for the 200/400 family.

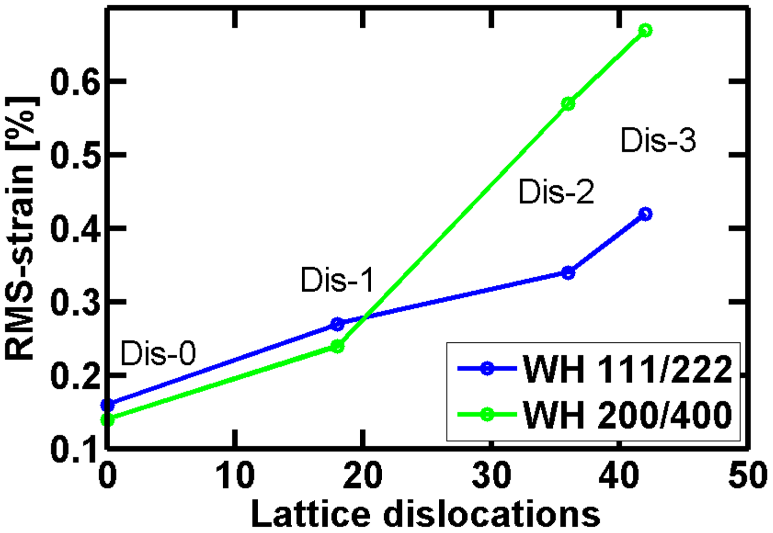

Figure 91: Relation between RMS-stain and lattice dislocations. The data is taken from Table 2 and Table 3.

The RMS values extracted for the DIS-3 sample are high, but not unreasonable high. RMS values of NC-Nickel extracted from the 111/222 peak family are around 0.36% (see Figure 129). It has to be noted however, that the grain size differs quite a bit and for other materials with the similar grain size, e.g. inert gas condensed Copper, much lower values are obtained. Furthermore, NC-Nickel differs in other microstructural details, such as incorporated impurities.

To ascertain the contribution of lattice dislocations to the increase in anisotropy seen in Figure 90a, sample DIS-2 was separated into its constituent grains and an XRD spectrum of each grain was calculated. An average XRD spectrum was constructed from the XRD spectra of those grains that do not belong to the classification contained in Table 2, i.e. those grains containing no observable lattice dislocations.

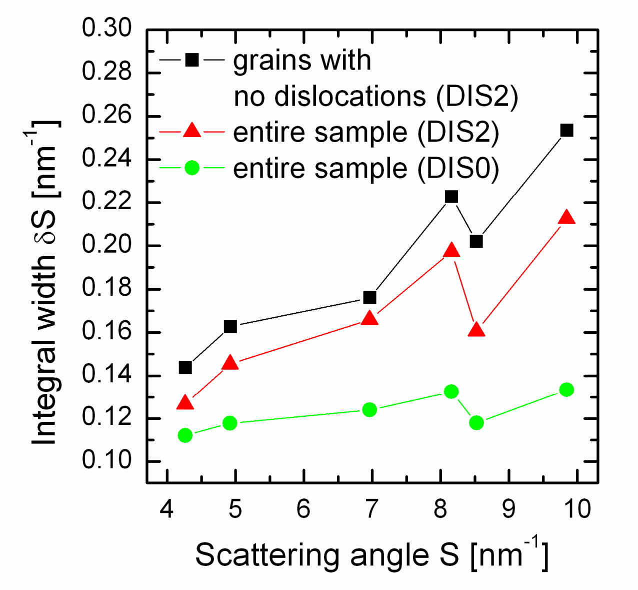

Figure 92: WH plots of sample DIS-0 and DIS-2 as well of all grains from sample DIS-2 containing no easily observable dislocation content.

Figure 92 displays the resulting WH plot compared to the full spectra of DIS-2 and DIS-0 and demonstrates that the grains that contain no observable dislocations produce a similar WH anisotropy as that seen for the entire sample DIS-2. In other words, the increase in anisotropy seen in DIS-2 compared to DIS-1 arises not just from those grains containing easily observable lattice dislocations. That peak widths of DIS-2 without dislocations shifted to higher values than those of the entire DIS-2 sample arises from the algorithm used to extract the individual grains where only FCC atoms are extracted with no nearest neighbors close to the GB. Thereby the coherent scattering volume is slightly reduced.

Changes in the WH anisotropy through twins

The WH plots from the samples containing twin defects are presented in Figure 90b. The samples with relative low twin densities (TWIN-1 and TWIN-2) change only slightly the anisotropy when compared to the as prepared state (TWIN-0). The integrated width shifts in general to higher values reflecting the smaller coherent scattering volumes resulting from the introduction of the twins. In contrast, the TWIN-3 sample with a twin probability factor of 0.1 shows a strong anisotropy compared to the other ones. It is clearly visible that the peak widths of the 200 family (200 and 400 peak) have increased compared to the other peaks. This is explained by Warren’s twin analysis [112]. Qualitatively this is due to the fact that for the 111 family there is always one 111 direction that is not affected by the twins, whereas all 100 planes have the same geometrical relationship with the 111 plane.

That samples TWIN-1 and TWIN-2 do not follow this trend can be understood qualitatively from the realization that the probabilistic Warren analysis cannot be applied to samples TWIN-1 and TWIN-2, since such an analysis considers the peak index-dependent coherent scattering volume length scale as the average distance between neighboring twin planes: TWIN-1 and TWIN-2 contain at most one twin per grain and therefore the coherent scattering volume length scale is defined by the average distance between the twin and neighboring GB.

Internal stress

Figure 93 displays a section of atoms showing a central grain and its neighbors. The left column (a, c and e) is the configuration for sample DIS-0 and the right column (b, d and f) is the same configuration for sample DIS-2. The coloring is in a and b according to the local crystallinity, in c and d according to the local hydrostatic pressure where blue represents -1.5GPa or lower and red 1.5GPa or higher and in e and f according to their local deviatoric stress (35) where blue represents 0GPa and red 1.5GPa or higher. Intermediate stress levels can be resolved with the presented color bar. It has to be noted that negative hydrostatic stress represents tension and positive stress compressions. The deviatoric stress can be considered as the magnitude of the maximal resolved shear stress. The yellow arrows in some sub pictures indicate stress concentrations, which resulted in the case of DIS-2 (d and f) from the absorption of a lattice dislocation in the GB. Since no slip occurred in the as prepared sample (DIS-0), the stress intensities in c are related to GB dislocations.

In Figure 93b, the core structure of the dislocation (circled in yellow) is clearly visible by means of the red stacking fault connecting the leading and the trailing partials. The viewing direction of the atomic section shown in Figure 93 is along the (111) slip plane (indicated by the yellow lines intersecting the yellow circle) and nearly perpendicular to the (110) slip vector of the dislocation. Detailed analysis has shown that this perfect dislocation has a predominant edge character with a Burgers vector directed towards the right hand side of the figure. The edge character is reflected in the hydrostatic stress distribution around the dislocation (Figure 93d): above the slip plane, the pressure shows a tensile region (blue) whereas below the slip plane (due to the extra 110 half plane) a compression region (red) is present.

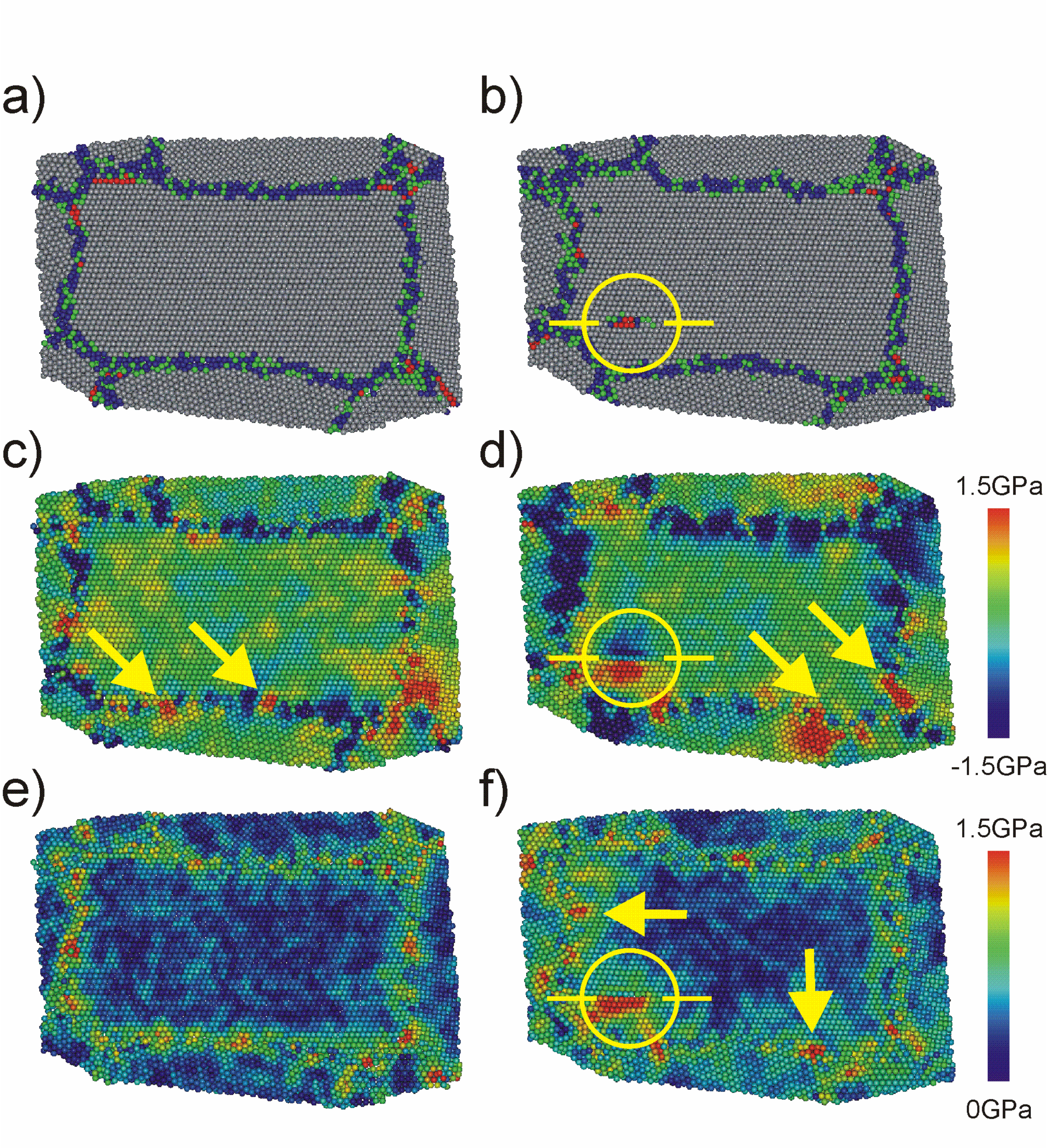

Figure 93: The a) local crystallinity, c) local hydrostatic pressure and e) local maximum shear of a section of the sample prior to loading (DIS-0). b), d), and f) are the same sections of the loaded/unloaded sample (DIS-2).

The deviatoric shear signature around the observed dislocation (Figure 93f) consists of a high shear region below the dislocation (red). This is not the expected signature from an edge dislocation according to elasticity. The long-range stress fields associated with a perfect dislocation should create shear lobes ahead and behind a perfect dislocation [4]. The reason for the suppressed shear lobes lies probably in the image stresses occurring from the nearby GBs and/or the 250fs time average, which does not remove all variations in stress arising from thermal activity.

The WH analysis above could show that additional anisotropy does not necessary origin from lattice dislocation. Therefore, it is worth investigating the development of stress intensities. Figure 94 presents the same section as shown in Figure 93 although with the resulting displacement vector between the configurations DIS-0 and DIS-2. The color code represents the magnitude of the displacement where blue represents 0Å and red 5Å or more.

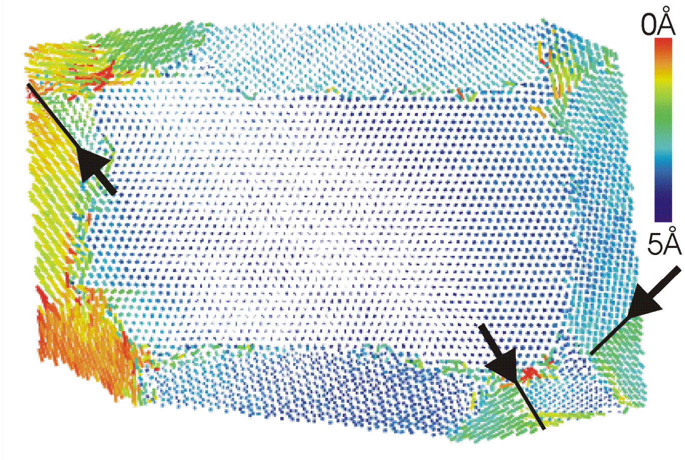

Figure 94: Atomic displacement vectors between configuration a and b shown in Figure 93.

The black arrows indicate slip activity in adjoining grains depositing a dislocation in the GB. This regions correlate well with the stress intensities observed in the pressure pictures in Figure 93d and f (indicated with a yellow arrow). Such deposited dislocations are not counted in the dislocation content listed in Table 2. In other words, the stress fields creating the anisotropy in the WH plot not only origins from “easy” identifiable lattice dislocations content defined by the four categories in Figure 87 but also from absorbed dislocation in the GB without core signature.

3.5.5. Summary

It is found that by introducing a lattice dislocation or twin content into computer generated NC samples and calculating the corresponding two-theta X-ray diffraction spectra, the peak integral-width anisotropy shows a clear difference between this two types of defects. However, the twin content has to be in average more than one twin per grain to exhibit clear “twin” anisotropy. Furthermore, the simulations also demonstrate that a similar anisotropy in the WH plot as that induced by lattice dislocations can be obtained by the presence of highly localized stress intensities in GBs induced by “absorbed” lattice dislocations. This might be only valid for small enough grains.

3.6. 3D atom probe investigations

It is know that impurities and their distributions strongly influence the properties of materials. Moreover, it is believed that the grain size of NC-Nickel is stabilized by impurities introduced during the electrodeposition – the fabrication of the material. However, their distribution is not known. The only technique to localize impurities atom by atom is 3DAP. Consequently, it is used to study the distribution of impurities in NC-Nickel.

It is still a challenge to measure very small amounts of impurities. Therefore, a NC-Nickel foil from the same company with slightly higher impurity content (Table 4 and [85]) is used for this study. This foil exhibits the same grain size and very similar mechanical behavior (90% of the maximum flow stress).

B	Co	Cu	Fe	Mo	P	S	Si	Zn
296	805	76	761	123	190	382	1533	95

Table 4: Impurity concentration established via chemical analysis in ppm.

Concerning the detection of impurities, one has to mention that Co, Mo and Zn were not detected because the proportion of each isotope is below the detection limit of the 3DAP used in this study (50ppm). The boron concentration is about 300ppm (chemical analysis), which should be high enough to be detected on the mass spectra at 5.5a.m.u (atomic mass unit). However, it never appears. One should also note that P does not clearly appear in the background because its concentration is low, while Co is located just between two Nickel isotopes where the background is high. In the following results, only impurities are presented where the signal clearly exceed the background noise.

The principal aim was to study the material in the as prepared state. Furthermore, the influence of temperature is investigated related to annealing experiments in Section 3.1.4. Therefore, samples annealed at 140ºC and 180ºC were probed. A possible influence of deformation on the impurity distribution was addressed by investigating a sample which was beforehand plastically deformed in tension to the UTS (~3% deformation).

3.6.1. Impurities in as prepared material

Figure 95 presents a cut out of a reconstructed part of as prepared NC-Nickel specimen (A1). The sample was cut by EDM from the sheet (0.2mm thickness) in the dimensions 0.2x~5mm followed by electro polishing. Impurity concentrations were measured in this volume containing 10^5 atoms. The results for Si, P, S, Fe and Co are summarized together with the standard deviation of the 3DAP measurements and the wet chemical analysis in Table 5. It seems that the 3DAP measurements are consistent with the chemical analysis. Only the results obtained for Co and S are out of the 3DAP standard deviation. One should note that a volume of 10^5 atoms ($10x10x8nm^3$) is quite small, corresponding only to about half a grain of 20nm grain size (including the detector efficiency of 50%).

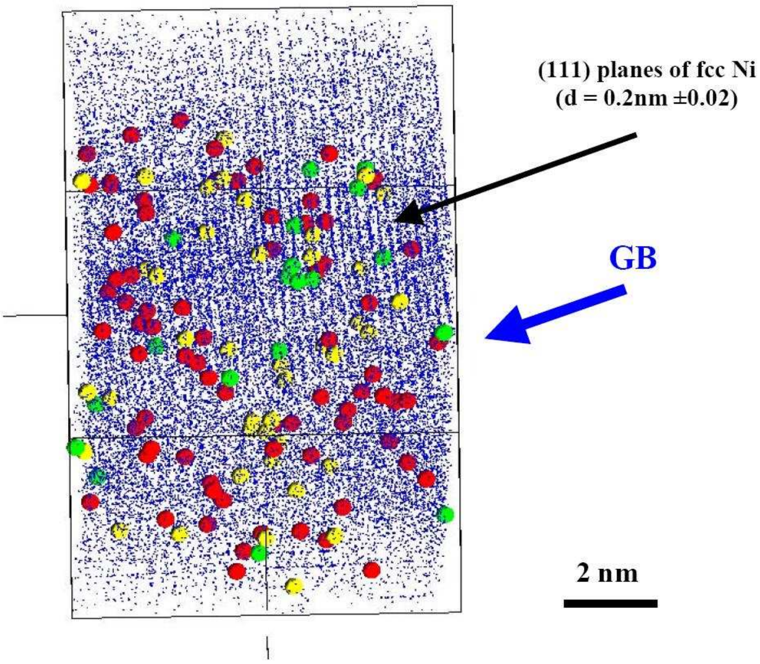

Figure 95: 3D reconstruction of as prepared NC Nickel ($10x10x8nm^3$-A1). Nickel: blue, Fe: yellow, Si: red, S: green.

The sample presented in Figure 95, contains a GB indicated by a blue arrow. This is identifiable, since the top area exhibits visible regular atomic planes ending in the middle of the analyzed sample. Impurity atoms clearly detected above the background noise are shown with bigger dots.

ppm	Fe	P	S	Si	Co
3DAP (A1)	758	137	315	1377	588
Std. 3DAP	172	73	11	231	151
chem. anal.	761	190	382	1533	805

Table 5: Impurity concentration measured with 3DAP their standard deviation (Std.) and the results from a chemical analysis.

In the presented dataset, the impurity atoms are uniformly distributed within the material and no higher concentrations of any detected impurities occur on the GB. From the same specimen a second data set (A2) was obtained. This was considerable bigger ($8x8x33nm^3$) and two grains could be separated by the strength of the evaporation field indicating a different crystal orientation. Also here the detected impurities (Si, S and P) did not show any particular segregation across the analyzed volume.

However, two more data sets (P1, P2) where analyzed from different specimens prepared in the same way for which the impurity concentrations obtained via 3DAP differ from those obtained by chemical analysis (see Table 6). The Si concentration is very low and carbon is now detected. However, S, P and Fe are similar to the chemical analysis.

ppm	Fe	P	S	Si	C
chem. anal.	761	190	382	1533	-
data set P1	750	150	400	300	200
data set P2	800	<100	1000	300	100

Table 6: Impurity concentration from two data sets. Standard deviation is +/-100ppm.

Furthermore, there are some clear localized concentrations of impurities. Figure 96 shows a 3D reconstruction of data set P1 with a sample volume of $8x8x55nm^3$. The nickel atoms are excluded to enhance the visibility. Two regions, separated by ~20nm and indicated with a black arrow, are visible which have a higher concentration of impurities.

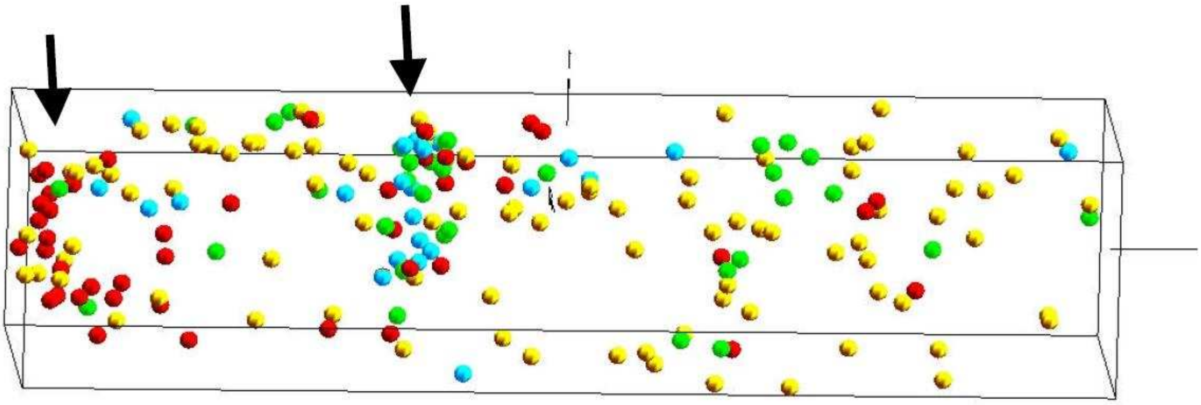

Figure 96: Analyzed volume of as prepared NC-Nickel (8x8x55nm^3). The Fe atoms are plotted in yellow, Si in red, S in green and C in blue. Impurities concentration sites are indicated by black arrows.

The concentration of impurities is computed across the segregation area indicated with a black arrow more central of Figure 96 and shown in Figure 97. For the analysis, a sampling volume of 3nm thickness was used. An obvious concentration of Si, S and C can be observed while the detected Fe is homogenously distributed over the analyzed volume.

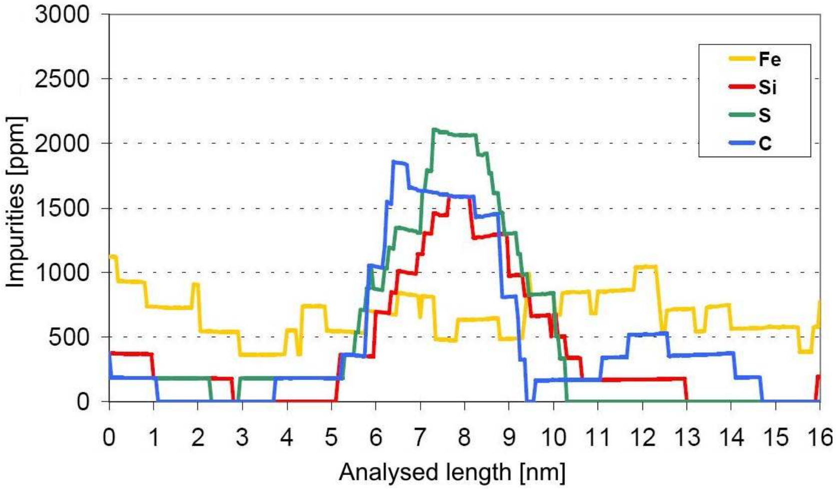

Figure 97: Composition profile across the arrowed segregation in Figure 96.

Two more data sets (D1, D2) were obtained from the central region of a dog bone (0.2x0.2x~1.7mm). The detected amount of impurities is very low (Table 7). There was no Si detected and the P and S levels were very low. Furthermore, a significant amount of C was detected.

ppm	Fe	P	S	Si	C
chem. anal.	761	190	382	1533	-
data set D1	600	100	200	<100	200
data set D2	700	<100	<100	<100	150

Table 7: Impurity concentration from two data sets obtained from the central region of a dog bone. Standard deviation: +/-100ppm.

Figure 98 shows a 3D reconstruction of data set D1. The sample volume of 13x13x21nm^3 shows Nickel atoms with small blue dots as well as Fe (yellow) and C (light blue) atoms. In this sample, a homogeneous distribution for Fe and C can be observed. Atomic planes can be observed in the upper part of the image but no significant segregation was found.

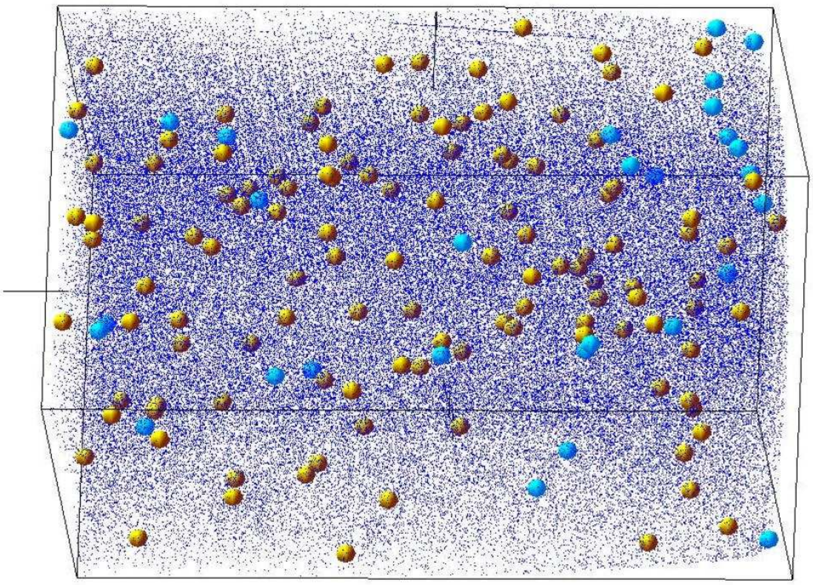

Figure 98: As prepared sample volume extracted from the central region of a dog bone. The Ni atoms are shown in blue, while Fe in yellow and C in light blue.

Summarizing the as prepared state, a few analyzed samples show a heterogeneous distribution of a number of impurities, especially Si, from one to another examined volume. Moreover, some impurities exhibit significant segregation, which seems to correspond when in the probed volume a low amount of Si is observed.

The data sets P1, P2, D1 and D2 exhibit a significant amount of carbon. This can be explained due to the better experimental conditions since P1, P2, D1 and D2 are obtained later than A1 and A2 when the background noise level was reduced especially in the range of 5 till 15a.m.u.

The results do not provide a clear picture on the distribution of impurities in the as prepared state. To gather a clear statement from 3DAP much higher statistics would be needed to quantify a heterogeneous distribution on the macroscopic level.

3.6.2. Impurities in deformed material

Overall, six successful data sets could be obtained from deformed samples. In most of the analyzed volumes, the only impurity element detected was iron (~800ppm), which was homogeneously distributed over all samples, also the GBs. Most surprisingly is that the nominal Si concentration of 1500ppm was almost everywhere below 100ppm. Figure 99 shows a relative large volume of 11x11x47nm^3 where two GBs are detected and indicated by black arrows. No obvious segregation of any impurities could be observed. In the middle and on the right side clear lattice planes can be observed.

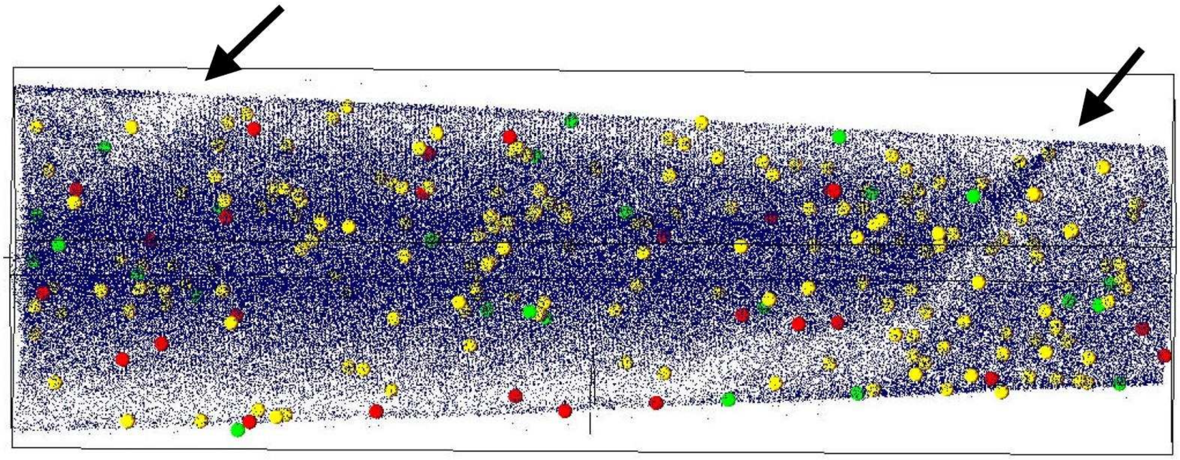

Figure 99: Reconstruction of an analyzed volume (11x11x47nm^3) from a deformed sample. Nickel atoms are in dark blue, Fe in yellow, Si in red and S in green. The black arrows indicate GBs.

However, it has to be mentioned that in one GB – detected by a lower evaporation field and an increase in single charged detected nickel ions – some evidence of Si segregation was observed. The Si reached a composition of up to 5000ppm while the detected Fe and S did not segregate.

3.6.3. Impurities in material annealed at 140°C

Only one quantitative data set was obtained in which segregation could be observed. However, this observed concentration of impurities started immediately at the beginning of the evaporation as has therefore taken with care. In Figure 100, a 3D reconstruction of the dataset and concentration profile of the detected impurities can be seen.

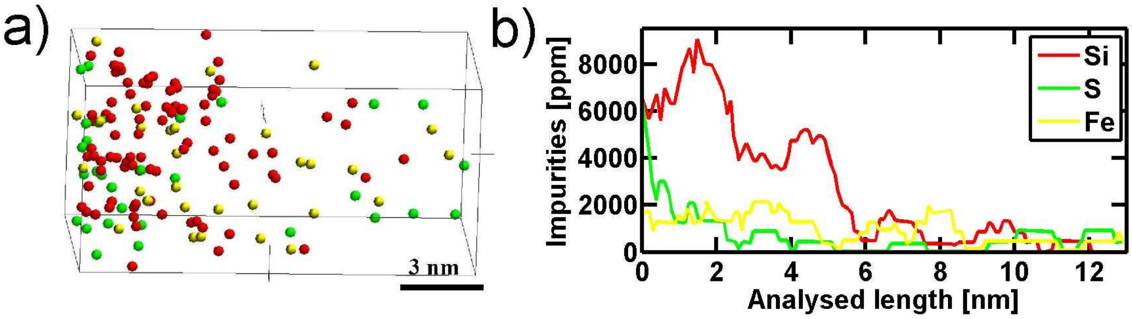

Figure 100: 3D reconstruction (7x7x13nm^3) and concentration profile from left to right of a 140°C annealed specimen.

The nominal iron concentration is high but no pronounced segregation can be found compared to the detected S and Si one.

3.6.4. Impurities material annealed at 180°C

In total only two quantitative data sets were obtained from the sample annealed at 180°C. One obtained volume contained only iron impurities and a clear visible GB (see Figure 101) indicated with a black arrow. The right side of the presented volume shows clear the observed atomic planes. The distribution of the iron atoms is very homogeneous over the whole volume.

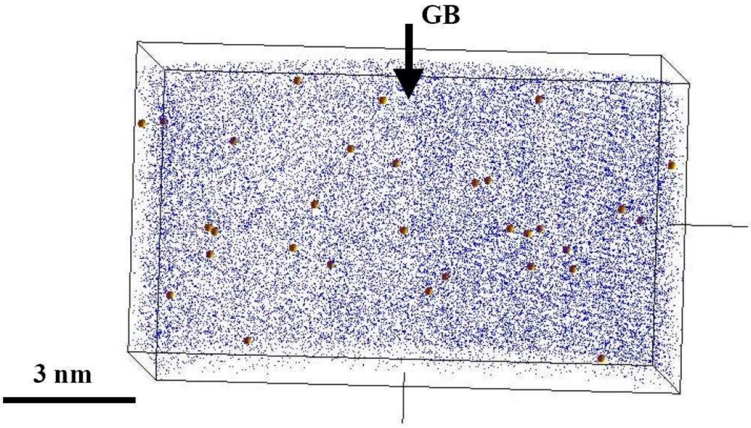

Figure 101: Data set with 12x12x7nm3 from a 180°C annealed specimen. The GB is indicated.

The second observed volume (10x10x30nm3) is presented in Figure 102a. Two probable GBs are indicated with a black arrow. It shows some segregation of Si and S along one GB. It is worth noting that P was not detected in this volume.

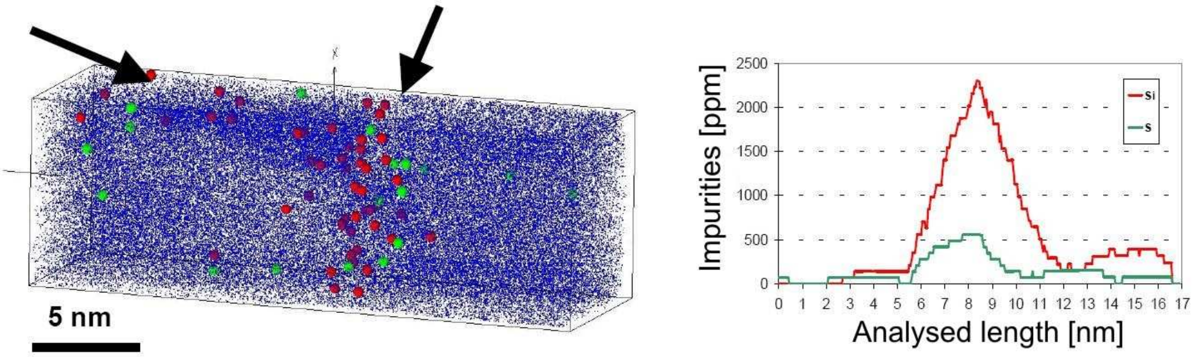

(a) (b)

Figure 102: (a) 3D reconstruction of an analyzed volume (10x10x30nm^3) in the NC-Nickel annealed at 180°C. b) Composition profile of enhanced concentration in the center of the analyzed volume.

Figure 102b, shows the composition profile along the mentioned GB. For the analysis, a sampling volume of 3nm thickness was used. It clearly shows a segregation of Si and an enhanced concentration of S.

3.6.5. Summary

A macroscopically heterogeneous distribution of silicon is found in the as prepared state of NC-Nickel. Furthermore, a non-uniform distribution of some impurities (Si, S and C) indicates segregation. However, the low statistics does not allow a clear and conclusive picture. Analysis of the deformed sample revealed mostly a homogeneous distribution. The annealed samples show some evidence for the presence of impurity segregation at some GBs but not all.

4. Discussion

The aim of this thesis was to investigate the deformation mechanisms in NC-Nickel using different experimental techniques with a focus on X-ray diffraction. The discussion starts with an explanation of stresses within polycrystalline materials and shows how they can be related to the measured X-ray parameters. The obtained data are discussed in terms of different deformation regimes of NC-Nickel. For a greater understanding of the deformation mechanism the outcome of transient tests are included in the discussion. The comprehensive conclusions are summarized by an interpretation of the data at the end of the discussion.

4.1. Stresses in polycrystalline materials

The classification of internal stresses and strains in polycrystalline materials is done typically by relating them to the length scales of grain size, and three different types of stress are distinguished:

- σ_I, Type I stress is homogeneous over a very large number of crystal domains (macrostress).
- σ_{II}, Type II stress is the homogeneous stress within one grain (intergranular stress).
- σ_{III}, Type III stress is homogeneous only over small parts of a crystalline grain and therefore reflects the inhomogeneous stress within a grain (intragranular stress).

Type II and III stresses are also called microstresses. A graphical representation of the different types of stresses is presented in Figure 103.

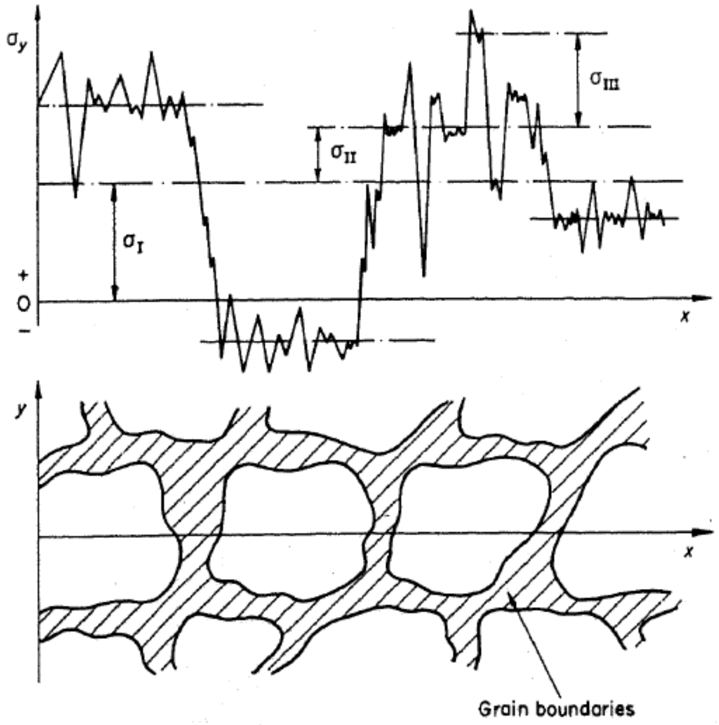

Figure 103: Three types of stresses present in a polycrystalline material (from Maeder [152]).

It is important to note that the internal stresses are not directly related to the applied stress plotted in a stress strain curve. The applied stress may however be separated into a component that represents the internal stress variations within the material plus an effective stress, which can be seen as the stress that a dislocation needs to overcome an obstacle. The actual separation of these stresses is carried out by the use of strain-dip tests presented in Section 3.3.1. Details of this separation follow in Section 4.3.1 and Appendix A. The X-ray diffraction measurements, give information on the internal stress landscape and when performed in-situ, allows one to follow the evolution of the internal stresses during deformation. The relation between the internal stress and the obtained X-ray diffraction peak parameters is described in the following Sections. Section 4.1.1 shows what can be learnt from X-ray diffraction peaks in an unloaded sample and Section 4.1.2 describes what happens to the diffraction peaks during the loading of the sample.

It should be mentioned that diffraction probes the lattice spacing and during loading the change in lattice spacing – in other words the lattice strain. In engineering terms, however, it is more common to use the term stress, which is related to the strain via elasticity. Within this discussion both terms will be used interchangeably. Moreover, a deviation from the theoretical position of a hkl diffraction can be related directly to lattice strain of the material along that particular hkl direction. With the current set-up and the uncertainties in the sample positioning and energy calibration, only the changes in the lattice strain are measured.

4.1.1. Relation between internal stresses and X-ray peak parameters: unloaded sample

In a NC material all three types of internal stresses can be present. In the following Sections it will be described how the different types of stresses can influence the measured peak parameters, peak position and peak width.

Type I stresses represent the mean macro stresses and will influence the peak positions.

Type II stresses are homogeneous within one grain. Since the X-ray measurements performed within this thesis illuminate the whole gauge length, billions of grains with a slightly different stress/strain state will be probed. Each grain will then scatter with a slightly different diffraction angle, which will result in a distribution causing a diffraction peak to broaden. Furthermore, if for example in a material more grains are under compressive stresses than under tensile stresses, the mean peak position will be shifted compared to a material where they are balanced.

Such variations of strains from one grain to another, and their influence on the diffraction pattern are schematically represented in Figure 104. On the left side, three different grain-to-grain variations are shown where the gray level and the number indicate the actual stress state. The diffraction peaks on the right side corresponds to the different scenarios. The peak width associated with the upper most grain agglomeration is broader than the peak associated with the central agglomeration, whereas the peak associated with the lower grain agglomeration has the same peak width but a different mean (peak position) when compared to the upper peak. These two observations emphasize that type II stresses can contribute to both peak broadening and to a peak shift.

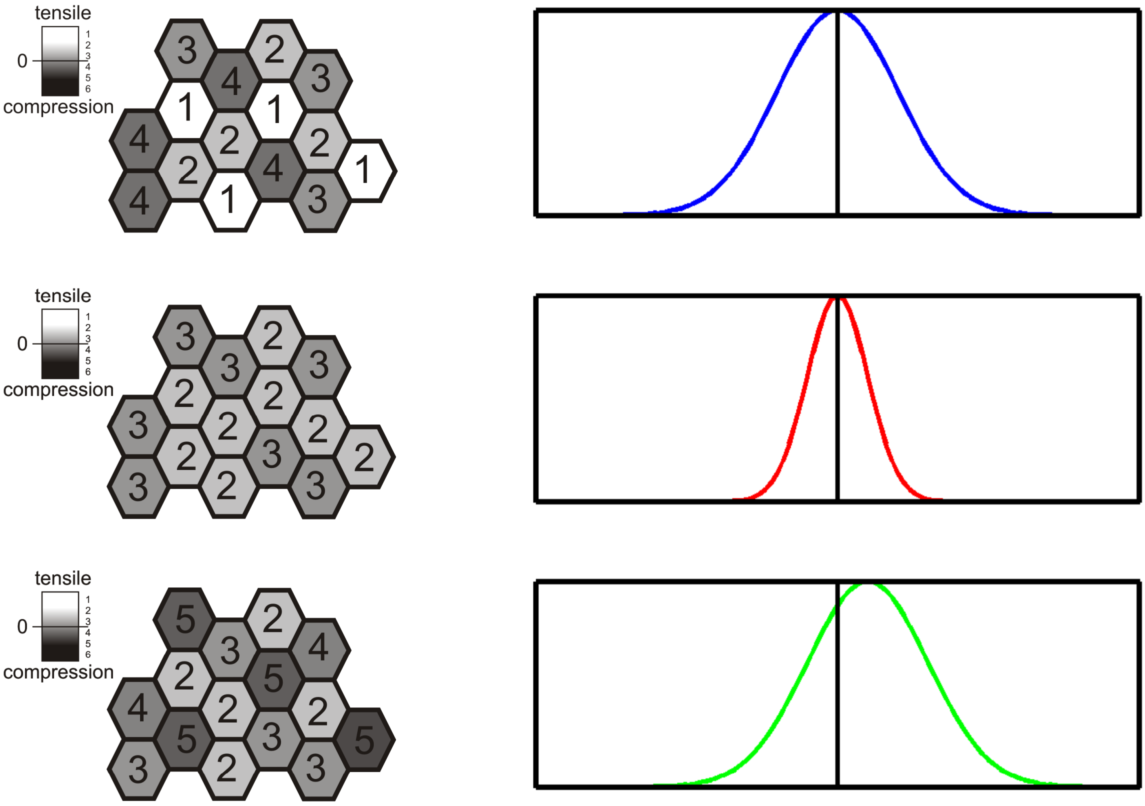
tensile
0
1
2
3
4
5
6
compression
3 2 4 3 1 1 4 2 2 2 4 1 4 1 3
tensile
0
1
2
3
4
5
6
compression
3 2 3 3 2 2 3 2 2 3 2 2 3 2 3
tensile
0
1
2
3
4
5
6
compression
5 2 3 4 2 5 4 2 2 5 3 5 3 2 3

Figure 104: Schematic model showing the influence of type II stresses on the diffraction peak profile. The upper and the middle grain-stress-arrangements show different variations among the grains (visible by the gray values) but have the same mean stress and therefore influence only the peak width. The upper and the lower grain-stress-arrangement have the same distribution but a different mean and therefore influence the peak position.

Type III stresses are inhomogeneous stresses within the grains (see Figure 103) which will contribute to the peak broadening. These types of stresses are related to the stress signature of defects such as dislocations, interstitial and substitution impurities, and voids. The amount of type III stresses will therefore influence the amount of diffraction peak broadening. The actual contribution to the peak broadening from dislocations is elaborated with calculations in Section 3.5, and will be discussed in a Section 4.1.3.

The effects of the different classified types of stresses and strains on the diffraction peak parameters can be summarized as follows. Type I and II stresses will influence the peak position and type II and III stresses will influence the peak broadening.

4.1.2. Relation between internal stresses and X-ray peak parameters: during loading

In a first approximation, the mechanical response of one crystallite during elastic loading can be described without the interaction with its surrounding grains. This means that the build up of type II stresses due to materials anisotropy is neglected. Then the peak positions during loading are only influenced by type I stresses. Such a simplification allows that each grain can be treated as a single crystal whose response follows linear elasticity. In other words, if a crystallite is loaded in, e.g. the 111 direction, the strain will follow Hooke's law with the Young's modulus of the 111 direction.

Within this thesis, the peak positions have been presented as angular values or relative changes from the position in the as prepared material. By differentiating (8) one obtains,

$$\varepsilon_{hkl} = \frac{\Delta d_{hkl}}{d_{hkl}} = -\cot(\theta)\Delta\theta \,. \qquad \textbf{(36)}$$

The above formula allows the calculation of the change in lattice strain for different diffraction peaks. If a tensile stress is applied on the sample, the utilized scattering geometry (see Figure 24) causes a Poisson contraction of the lattice planes that are probed by the X-rays. Due to the single crystal elastic anisotropy, the lattice contraction will depend on the direction of the applied stress.

A schematic graph illustrates this in Figure 105. If the stress is applied in the *[l,m,n]* direction, the Poisson contraction along the *[u,v,w]* direction can be calculated as follows:

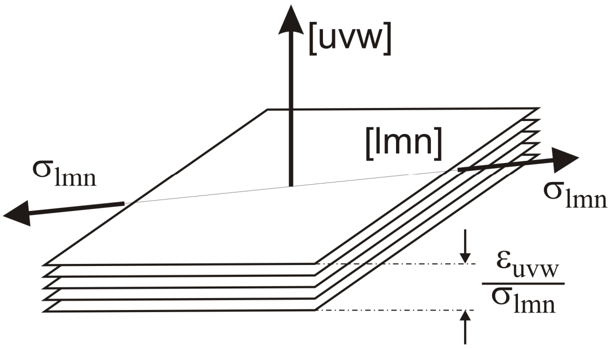

Figure 105: Schematic showing the contraction of lattice planes according to the applied stress in a single crystal. For details, see text.

If a uni-axial stress σ_{lmn} is applied to a cubic crystal along the unit vector *[l,m,n]*, then the perpendicular elastic strain ε_{uvw} is given by,

$$\frac{\varepsilon_{uvw}}{\sigma} = S_{12} + \left[S_{11} - S_{12} - \frac{1}{2} S_{44} \right] F \,, \tag{37}$$

where S_{ij} is the elastic compliance tensor in contracted matrix notation (Voigt) [153]. The factor F is calculated from the engaged vector components given by,

$$F = \left(l^2 u^2 + m^2 v^2 + n^2 w^2 \right). \tag{38}$$

In the present configuration the directions *[l,m,n]* and *[u,v,w]* are perpendicular to each other. If *[u,v,w]* is equal to *[1,0,0]* and *[1,1,1]*, the factor F will be equal 0 and 1/3 respectively for all possible *[l,m,n]* [154, 155]. Thus, the transverse strains developing along a <100> and <111> directions are independent of the perpendicular applied uni-axial loading direction. For Nickel the relations ($\varepsilon_{per<100>}/\sigma$) and ($\varepsilon_{per<111>}/\sigma$) are according to (37) and (38) -2.744MPa^{-1} (-2744με/GPa) and -0.720MPa^{-1} (-720με/GPa) respectively.

As already mentioned, the analytical description of the *u00* and *uuu* peak does not take into account that the probed crystals are embedded in a matrix of surrounding grains of the polycrystalline aggregate. Therefore, it can be expected that the measured peak position during elastic loading deviate from the simple prediction given above. Due to anisotropy of the stiffness in Nickel (see Table 8), differently oriented grains will respond in different ways. The overall elastic behavior of a polycrystalline material can be treated by a strain continuation condition according to Voigt [156] or by a stress continuation condition according to Reuss [157]. However, both approaches violate the corresponding equilibrium – Voigt the stress and Reuss the strain – and therefore an appropriate sum is often employed. In the present work, this aspect will not be considered.

Direction	111	200	220	311
Young’s modulus (GPa)	304	136	232	184

Table 8: Young’s moduli of Nickel in different crystallographic directions. Note that these stiffnesses are only valid if the stress is applied parallel to the normal vector of the crystallographic plane.

The above description of the peak position behavior treated only the elastic single crystal behavior in the transverse direction and indicated the difficulties arising within a polycrystalline material. Furthermore, the treatment ignores the possible contribution of a distribution of type II stresses where the mean value changes upon unloading.

Figure 106 presents the theoretical calculated single crystal lattice strain of Nickel for the 111 and 200 peaks. Moreover, the figure contains as well the experimentally measured change of lattice strain of NC-Nickel during loading for the same peaks. The experimental data correspond to the test presented in Figure 32.

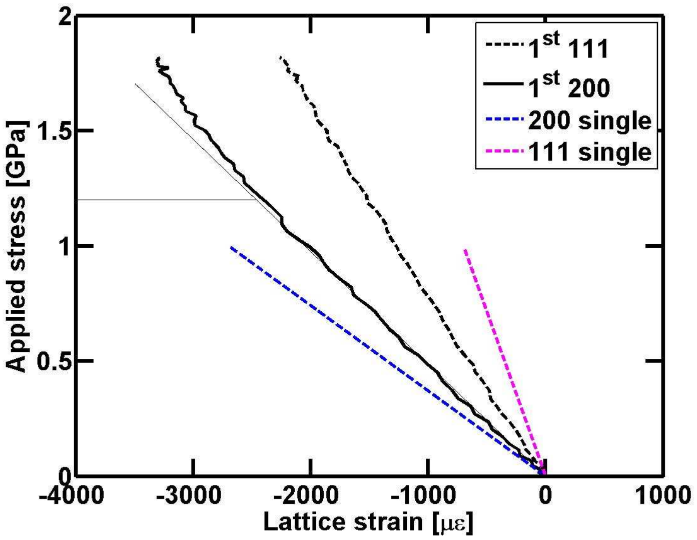

Figure 106: Lattice strains versus applied stress for the first loading cycle of the 111 and 200 peaks (correspond to the test in Figure 32). The blue and magenta lines are the theoretical single crystal behaviors for the 200 and 111 peaks respectively calculated via (37) and (38).

The 111 peak exhibits a linear loading until the maximum stress. The 200 peak in contrast exhibits a deviation from linearity, which starts around 1.2GPa (indicated in Figure 106 with thin black lines). First, this result clearly shows that neither peak follows their single crystal prediction. Second it is evident that the strongest elastic crystallographic direction (111, see Table 8) remains linear during loading, whereas the weakest direction (200) appears to deviate from linearity indicating intergranular interactions.

The broadening of the diffraction peak is influenced by the grain size and the RMS-strain inside the material (see Section 2.3.5). In the as prepared NC-Nickel sheet, the RMS-strain will be a combination of type II and type III stresses. During elastic loading, the type II stresses will change because the material anisotropy will cause elastic strain heterogeneity [145]. In other words, due to the grain-to-grain interactions, grains with similar orientation compared to the loading axis can have a different stress states depending on the adjacent grains. Consequently, the variations of strains will increase causing a broadening of the diffraction peak. Once the materials starts to deform plastically a complex interplay between type II and type III stresses will be present.

Within this discussion a plastic event in a NC materials stands for a dislocation which is nucleated at the GB, propagated through the NC grain and absorbed at the opposite GB as described in [34]. It is evident that such a plastic event in a NC structure will change the built-up stress state in the grain and its neighbors, causing a change in the type II stress variations. Furthermore, during the dislocation propagation the dislocation itself exhibits an inhomogeneous stress field, a type III stress. The possible interaction of the type II and type III stresses as well as the role of potential GB accommodation processes will be discussed later on.

Figure 33 shows the peak broadening behavior during the loading of NC-Nickel. In the beginning of the deformation, only a very small increase in FWHM can be observed. Once the material is loaded to higher values this changes dramatically and the broadening increases rapidly. For UFG-Nickel (Figure 67a) the general loading characteristic is quantitatively similar except that the actual FWHM values are different (different grain size). The greatest difference between the NC and UFG-Nickel is seen in the peak broadening behavior upon unloading. It is known that in CG material and in UFG-Nickel the strain-hardening regime increases the dislocation density through forest hardening causing permanent increases of dislocation density (type III stresses) that remain upon unloading. This permanent increase upon unloading is absent in NC-Nickel (see Figure 33).

In CG polycrystalline materials peak broadening has also been measured during deformation [145, 158] and was related to a combination of type II and type III stresses. With the help of elastic-plastic simulations it was possible to estimate that the elastic strain heterogeneity in CG austenitic steel represents one third of the total measured peak width [158]. In another experiment the evolution of type II and type III stresses in CG materials had been elaborated with microbeam diffraction experiments during fatigue. They revealed a different behavior in intra- and intergrain microstrains during increasing load-unload cycles, which are far from being understood [159-162]. Due to the micron sized resolution with today’s techniques this distinction is impossible and only a combined behavior, the peak broadening, can be analyzed in NC-Nickel.

4.1.3. Influence of dislocations and twins on the X-ray profile: Calculations from atomistic configurations

The description above dealt with internal stresses and their development and contribution to the diffraction peak parameters. The peak broadening has been treated as having a grain size and a strain component (see Section 2.3.5) where the latter has been split in different categories but no distinct relation to a specific defect has been found. Different types of defects such as twins and dislocations have a characteristic contribution to the peak broadening depending on the hkl orientation. For example, one type of dislocation (e.g. an edge dislocation on a 111 slip plane) will have, for different crystallographic directions a different contribution to the peak broadening which can be calculated using dislocation contrast factors [163]. These variations between the different diffraction peaks are characterized through the WH anisotropy as described in Section 2.3.5.

Within this thesis, it could be shown that, in a computer-generated NC system constructed from defect-free grains of random orientation with an average grain size of 12 nm, the integral width versus peak position exhibits a minor WH anisotropy despite the high interface density and the local stress intensities observed in the GBs (see Figure 90). By introducing dislocations or twins, the WH plot develops an anisotropy that is characteristic for each type of defect. Comparison of the WH anisotropy arising from the introduction of twins Figure 90b with that of experimental NC-Copper (Figure 107b) suggests that the closest resemblance between experiment and simulation can be found in the heavily twinned computer-generated sample, TWIN-3.

Although the experimental twin faulting probability α is 8 times smaller then that of TWIN-3, both WH plots exhibit the expected strong 111/200 anisotropy predicted by the Warren analysis procedure. This can be understood by recalling that the grain size for the simulated sample is ~10 nm, whereas for the experimental NC-Copper sample it is ~22 nm, resulting in approximately the same number of twins per grain. Furthermore, the WH plot shifts to higher absolute values of the peak widths, reflecting the reduction in coherent scattering volume due to the presence of the twins. On the other hand, the simulations show that when the microstructure of the sample is dominated by dislocations, the slope of the WH plot increases and develops an anisotropy that is dominated by a broadening of the (311) diffraction peak, which exhibits the greatest increase in peak width. Experimentally this type of anisotropy is also developed during compression of the NC-Nickel to large plastic strains.

Inspection of the experimental WH plot after 6% tensile deformation shows the same trend though to a lesser degree: only very small changes in peak width are observed (see Figure 119). When comparing the WH of the simulated and the experimental samples, one also notices a difference. The ratio of the peak width of the (111) to the (200) peak is much smaller for NC-Nickel than for computational Aluminum. This can be understood through the difference in elastic anisotropy between Aluminum and Nickel, which affects the dislocation contrast factors [163]. Despite the differences in elastic anisotropy, the calculated WH plots compare well to the experimental NC-Copper and NC-Nickel data. Figure 107 shows that the experimental data from NC-Copper corresponds best with a NC the system that contains twins and the NC-Nickel data with the one that contains dislocations.

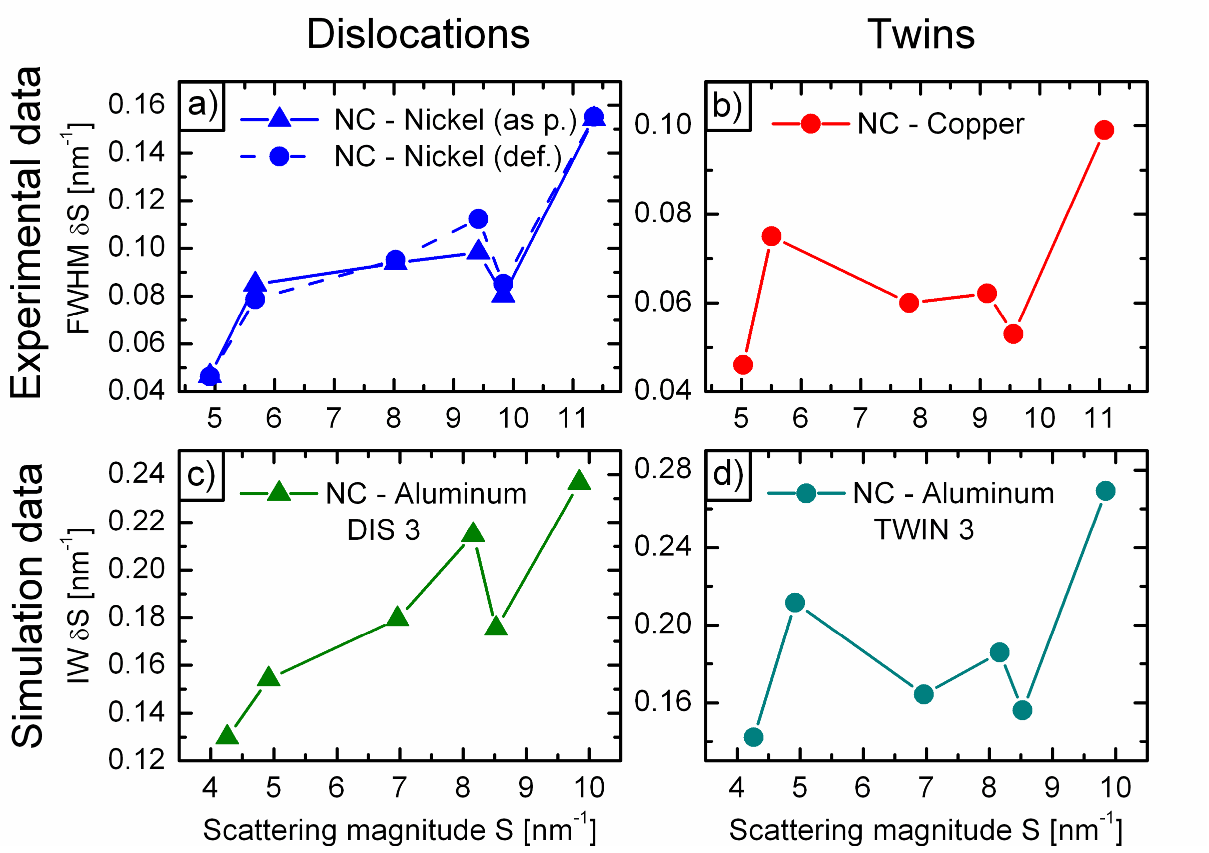

Figure 107: WH plots from experimental data, a) Nickel (▲ as prepared; ● unloaded from compression deformation) and b) Copper (from reference [127]), compared with calculations from Aluminum samples containing c) dislocations and d) twins.

Careful analysis of the computational samples has demonstrated that a ‘‘dislocation’’ type WH anisotropy is not only obtained when lattice dislocations are present in the grain interior, but also can be induced by local stress intensities in the GB resulting from the absorption of lattice dislocations [164]. These stress intensities also have long-range stress fields and therefore contribute to the RMS-strain of the sample, whereas the intrinsic GB dislocations that result from sample relaxation in a Voronoi construction, do not contribute to the RMS-strain at least not at a grain size of ~10nm [14]. It is interesting to notice that when the computational sample is annealed after the Voronoi construction, a weak WH anisotropy becomes apparent. The TEM ‘‘visible’’ lattice dislocation densities (dislocations of the type seen in Figure 87a and b) of DIS-2 amount to ~8x10^{15} m^2, and are somewhat higher than the dislocation density calculated for an as prepared NC-Nickel using profile analysis procedures that employ dislocation contrast factors [165]. The fact, however, that the anisotropy changes very little when omitting the grains containing lattice dislocations suggests that at these small grain sizes the simple approach of the WH analysis with its particular assumptions for lattice dislocation geometries (regular distributed straight dislocations) does not capture qualitatively the peak broadening in NC GB networks. Moreover the simulations demonstrate that there is no need for an easily ‘‘visible’’ lattice dislocation content to explain the experimentally measured WH anisotropy in as prepared and deformed samples.

It has to be mentioned that none of these models consider the effect of impurities within the NC structure as it is experimental observed (Section 3.6 and [86, 141]).

4.2. The XRD view on deformation regimes

In NC-Nickel, the diffraction peak widths experience a reduction upon unloading until load levels of 1.4GPa (see Figure 37 and Figure 44). This distinctly different behavior of the internal stress state measured through the peak profile motivates the division of the deformation of NC-Nickel into a micro- and a macroplastic regime. As long as the peak broadening reduces upon unloading, the deformation regimes will be referred to as the microplastic regime. However, once the FWHM increases for the majority of diffraction peaks (see Figure 44), the deformation regime will be referred to as the macroplastic regime.

4.2.1. Microplastic regime

The microplastic regime in polycrystalline materials does not have a unique definition. The lower limit of the transition from elastic to plastic deformation is usually related to short-range dislocation motion: for example the irreversible bowing out of a dislocation segment [166]. The upper limit of microplasticity is usually defined as the stress at which the majority of grains are plastically deforming [167].

However, what do these definitions mean for a NC system? If NC-Nickel with a grain size of 30nm is deformed to 0.2% plastic strain [168] only 25% of the grains have to slip [82] if one assumes that the deformation is entirely governed by dislocations sweeping the whole grain. This indicates a strongly heterogeneous deformation of NC systems compared to the CG counterpart. A considerable amount of plastic strain is produced in the microplastic regime, i.e. between the lower and the upper limit as defined previously.

Load-unload experiments have shown that the FWHM present in the as prepared material can be reduced when the maximum load on the sample exceeds 400MPa, i.e. in the microplastic regime (Figure 36 and Figure 37). This is not observed in similar load-unload cycles performed on UFG-Nickel (Figure 36). A similar trend is also observed in (cryo) ball milled Copper with a grain size of ~23nm [169] during a load-unload cycles at 1% plastic strain, as shown in Figure 108b (red data).

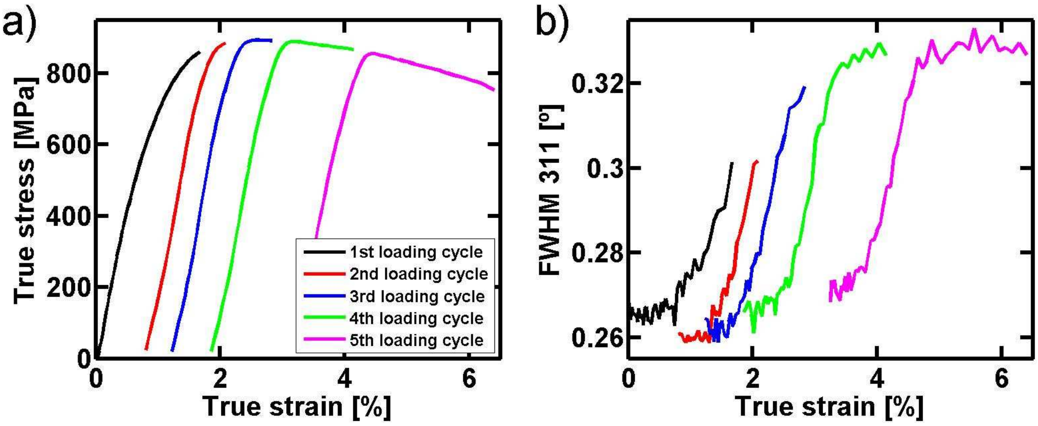

Figure 108: a) Stress strain data of ball-milled NC Copper during load-unload cycles. b) Evolution of the 311 peak width during the deformation.

For NC-Nickel, the deformation history and the waiting time between two load cycles do not influence the maximum amount of reduction in FWHM that can be obtained for the different diffraction peaks (Section 3.1.2). The FWHM upon unloading from 1.4GPa reaches the lowest possible value for most diffraction peaks (see Figure 44). Once the material is deformed to the maximum flow stress and unloaded, the subsequent application of further load-unload cycles below 1.4GPa do not evidence a further reduction of the FWHM. Moreover, when a NC sample is annealed at low temperatures, which do not cause grain growth, load-unload cycles below 1.4GPa cannot further reduce the FWHM. As already mentioned, such a change in the peak width can indicate a change in grain size and/or in the RMS-strain.

Origin of FWHM reduction

The TEM grain size analysis throughout the thesis revealed no major changes in the grain size of NC-Nickel during deformation (see Section 3.4). Figure 109 shows two grain size histograms for an as prepared and a deformed sample. The mean value for both distributions is of the order of about 28nm with a standard deviation of 14nm, which is 50% of the mean value. If for example the diffraction peak broadening is only influenced by the grain size effect, the Scherrer formula (14) provides an inverse but linear relation between the crystallite size and the peak broadening. This means that a 5 percent increase in grain size would cause a 5 percent reduction in the peak broadening, which is about the value obtained after unloading from 1.4GPa. Such an increase of 5 percent in grain size is not observable in the TEM statistics and therefore it cannot be excluded as a possible origin for the observed reduction in the FWHM.

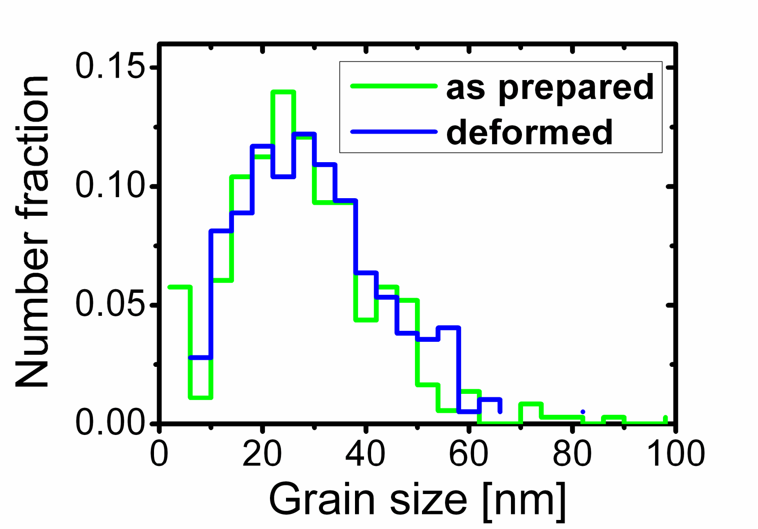

Figure 109: Grain size distribution of as prepared material and deformed sample (until 9% in compression, see 3.4.2).

A better approach to investigate the changes in FWHM is to use the WH-method, in which the contributions of grain size and RMS-strain can be separated. In Figure 110 the total broadening of the 111 peak is separated (see (19)) via the Cauchy-Gaussian method into its size and strain component (see (15)-(25)). It is clearly visible that for loading cycles up to 1.4GPa the reduction in FWHM is related to the strain contribution. However, once the load exceeds 1.4GPa, a change in the size contribution occurs. This analysis suggests that the FWHM reduction in the microplastic regime is solely related to a reduction in RMS-strain, i.e. microstrain. The effect of changing the size contribution after loading to the plastic region will be discussed in the following Section.

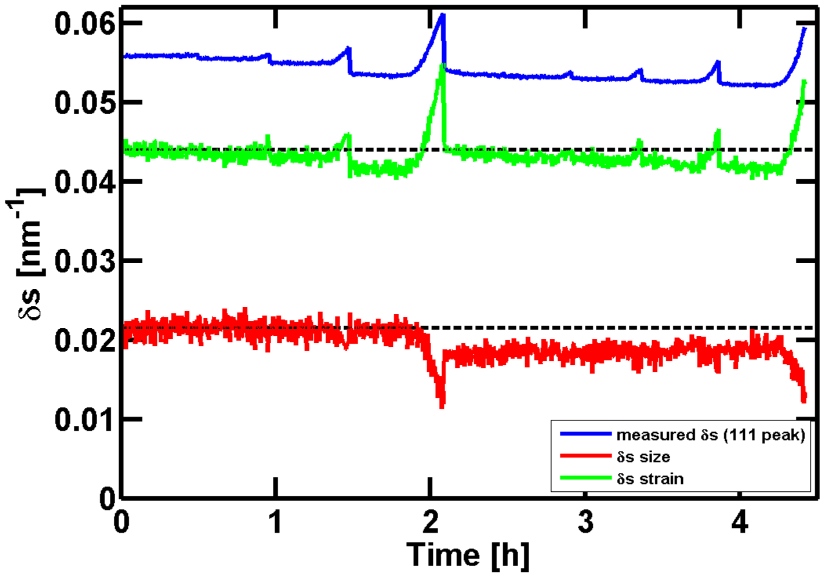

Figure 110: Deconvolution of peak broadening (blue) through the WH analysis in size (red) and strain (green) contributions for the 111 diffraction peak during load-unload cycles. The dashed lines represent the initial values. The corresponding mechanical data from NC-Nickel is shown in Figure 35.

Model systems that could explain the FWHM reduction

In the previous paragraphs, possible reasons of the observed changes in peak broadening were discussed in terms of grain size and RMS-strain. In the microplastic regime, the influence of the grain size seems to be marginal. Below, several possibilities are presented that attempt to explain the reduction in FWHM in the microplastic regime in terms of RMS-strain. These changes in RMS-strain/stress will be related to materials properties (microstrains), i.e. the possible contribution of type II (intergrain) and type III (intragrain) stress.

Structural relaxation processes

In the as prepared NC structure, X-ray diffraction and TEM revealed that elastic strains are stored. These strains can originate from stress concentrations within the GB as well as extrinsic GB dislocations arising from the manufacturing of the material. Processes that are able to cause a structural relaxation can originate from plastic events or from GB relaxation processes. Both processes will change the pre-strained configuration. Moreover, they will interact with each other through accommodation processes: e.g. a dislocation that deposits itself into the GB will be accommodated through changes in the GB structure.

As already mentioned a central observation has been a lowering of RMS-strain upon unloading in the microplastic regime when probed with XRD and analyzed with the WH method. This can be explained by a simplified picture shown in Figure 111.

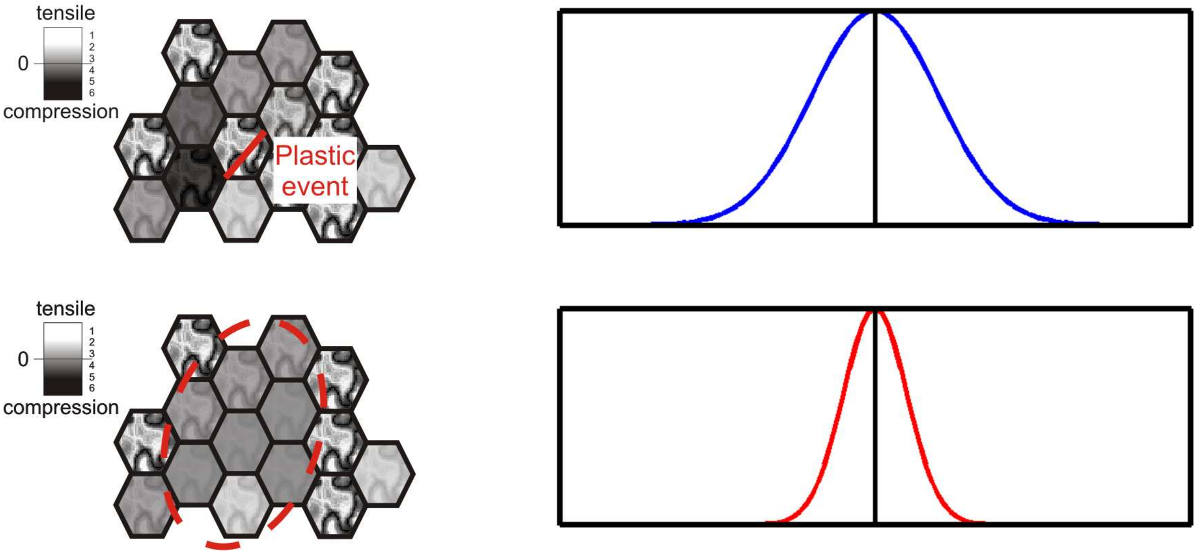

Figure 111: Schematic of a scenario where one plastic event relaxes the RMS-strain in a grain and its surrounding. The grains with their stress fields on the left side correspond with the X-ray diffraction data on the right side.

In the honeycomb structure of this figure, the gray levels represent schematically the stresses in the NC grains. The top configuration shows the as prepared situation. Type II stresses are symbolized by the variations between the grains and the type III stresses are symbolized by the variations within a NC grain. A plastic event is schematically represented as a red line in the center of the upper agglomeration. As a consequence of this plastic event, the central grain and the surrounding neighbors reduce both, their type III and their type II stress, resulting in a local reduction of the RMS-stress - represented by the gray levels in the lower honeycomb in Figure 111. This relaxed area is circled with a dashed red line where both the variations within one grain and the variations between the grains, are reduced compared to the as prepared configuration. This simple example demonstrates how a plastic event can locally reduce stress fluctuations. If such a process is representative of all discrete plastic events, then a reduction in the RMS-strain will lead to a narrowing of the peak as visualized in Figure 111.

An equivalent possible source for a reduction in the RMS-strain without a plastic event is a global relaxation of the GB network through atomic shuffling stimulated by the applied mechanical energy. This could cause the same reduction of the RMS-strain without a distinct plastic event beforehand. With these model systems, no change in grain size is necessary to explain the peak behavior in the microplastic regime.

Cleaning up of extrinsic GB dislocations

A plastic event, which can be related to the nucleation, propagation, absorption and dissociation of a dislocation into the GB, reduces the strain fluctuations. Additionally, it could also be imagined that such processes would effectively increase the grain size. Simply speaking, the coherent scattering area grows if pre-existing extrinsic GB dislocations disappear. From a WH analysis of a load-unload cycle shown in Figure 110, the contribution to the FWHM from grain size is constant and therefore does not suggest such a change in grain size in the microplastic regime. However, the simple WH analysis assumes certain distributions for different contributions that might not reflect the actual microstructural configuration in NC-Nickel. Moreover, if one would attribute the magnitude of the observed total peak broadening reduction just to a grain size increase, the above scenario would quantitatively explain the reduction in FWHM.

Influence of impurities

Impurities cause inhomogeneous stress fields, type III stresses, if they are present in the bulk of a NC grain. These inhomogeneous stresses will be enhanced if these impurities are interstitials compared to substitutional atoms. In any case, these stresses can be reduced if the impurities diffuse to favorable positions such as free volume within a GB where the atomic structure can relax more easily causing a reduction of the RMS-strain. This process can be stimulated by propagating dislocations [170] or through pipe diffusion along the dislocation core, which can acts as a channel for rapid diffusion [171-174].

The results obtained by 3DAP results are not conclusive but do not indicate such behavior during deformation (Section 3.6.2). Moreover, the amount of necessary dislocations is expected to be low in the micoplastic regime [82] and RT is normally not sufficient for any type of non-negligible diffusion.

The presented mechanisms can explain the observed reduction within the RMS-strain in the transition from the elastic to the plastic regime, the microplastic regime. However, which process is ultimately the dominant one that causes the observed reduction in the FWHM in the microplastic regime remains unclear. In any case, such a reduction is incompatible with a classical hardening regime where activation of multiple slip systems in the GB region and/or an increased presence of geometrical dislocations, because such processes would have the tendency to increase RMS-strains or at least keep the values constant, as it has been observed for UFG-Nickel (Figure 36). These results challenge the validity of the 0.2% definition for macroscopic yield stress when the grain sizes reaches the sub 50 nanometer range, as schematically represented in Figure 112. For UFG-Nickel with a 155 nm grain size, the assumptions related to the definition are still justified when analyzed by X-rays. The change from micro- to macroplasticity occurs in the NC metal at 1400MPa, i.e., at a strain that deviates 0.7% from Hooke's Law, which is well beyond the 0.2% definition of the yield stress. Using the suggested transition from micro- to macro-plasticity to study grain-size-dependent strengthening will not only reduce the scattering in the experimental yield stress data but also provide a different view on the validity of current plasticity laws [24].

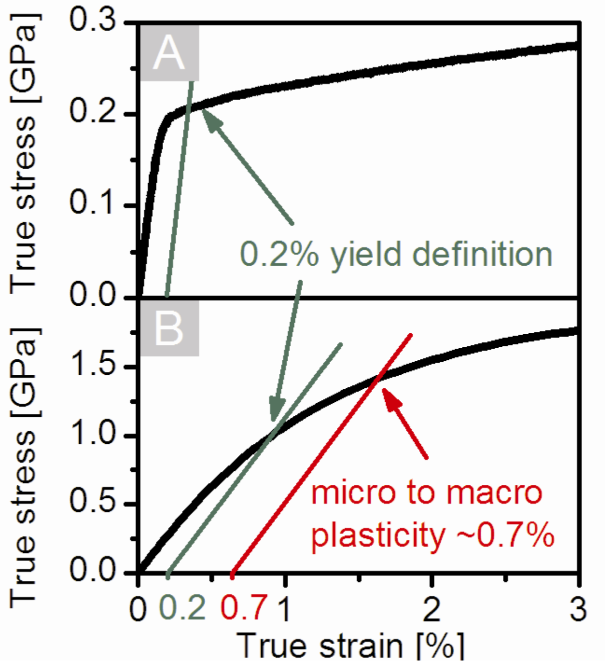

Figure 112: Change from micro to macroplasticity in CG material (A) and in nanograined materials (B) as suggested from the governed results (see text).

The effect of pre-annealing on the microplastic regime

NC-Nickel shows that after annealing at 180ºC NC-Nickel exhibits less contrast in the TEM micrographs signalizing a decrease in local strain fields (Figure 48) when compared to the as prepared NC-Nickel (Figure 2a). Moreover, annealing does not change the grain size distribution (Figure 49) but reduces the peak width by ~15%, which can be interpreted as a reduction in the RMS-strain (see Section 3.1.4). Jang et al. [96] have observed changes at or near the GB in NC-Iron through low temperature annealing by high resolution transmission electron microscopy (HREM). Figure 113a shows a typical Fourier-filtered HREM image of an as-milled NC Iron GB. The circled area marks the GB where lattice fringes are disconnected. After annealing the NC Iron sample for 24 hours at 100ºC, a significant amount of lattice fringes are continuous (see Figure 113b), and the misfit of lattice planes is accommodated by a regularly spaced GB dislocation (circled). Jang et al. proposed from their extensive observations that the GBs evolve gradually from a discontinuous to a more ordered structure through annealing.

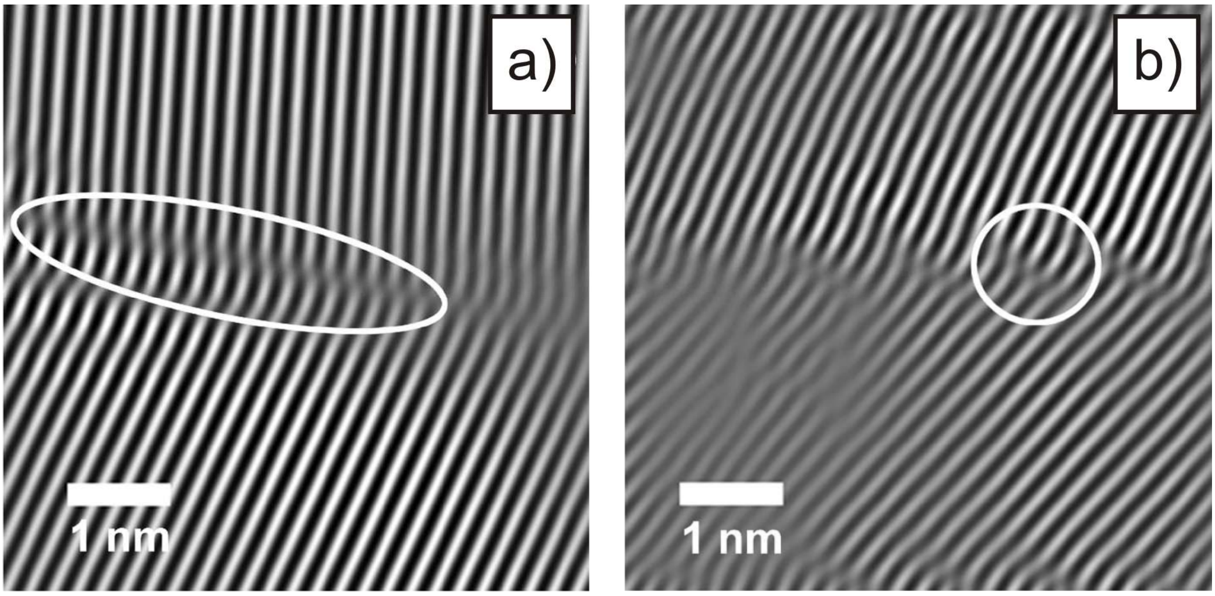

Figure 113: Fourier-filtered HREM images of a GB from as-milled a) and annealed b) NC Iron. Figure adapted from [96].

This observation in NC materials suggests that raising the temperature or applying a mechanical load in the microplastic regime has a similar effect on the material – both result in a relaxation of the GB structure. It is also observed that low temperature annealing extends the elastic regime (Figure 51a) and increases the strength of the subsequently loaded NC-Nickel (Section 3.1.4 and [44, 175]).

In a CG material, annealing reduces the amount of mobile dislocations, which results in a higher stress level being needed in the early stage of deformation to generate plastic strain. On the other hand, it is possible to imagine that a reduction in stress fluctuations through annealing increases the overall pinning strength of GB ledges thus hindering dislocation propagation. This is much more important in NC materials due to the high interface area. A further scenario is connected to the nucleation of dislocations. However, the contribution of short-range and long-range stress fields on the nucleation of dislocations is unclear. If the long-range stress fields contribute to the nucleation, their influence is evident from the observed reduction in contrast variations in TEM pictures when the as prepared material is compared to the annealed material. This in turn suggests that the observed deformation effects in NC-Nickel are strongly connected to the initial stored RMS-strain and that through low temperature annealing the previously defined microplastic regime in NC-Nickel can be reduced.

4.2.2. Macroplastic regime

Once the load of 1.4GPa (0.7% plastic strain) is exceeded, upon unloading the residual peak broadening increases with strain (see Section 3.1.3 and Figure 44) for most diffraction peaks. To demonstrate this feature Figure 114 shows the FWHM of the 111, 200 and 311 peaks plotted against the strain.

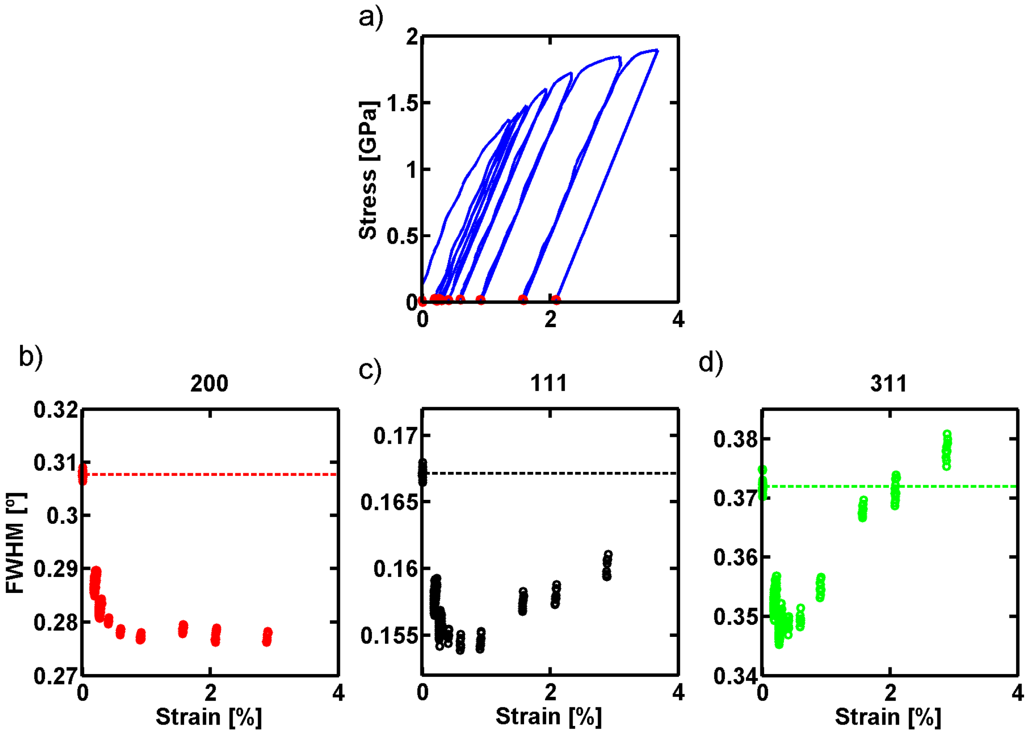

Figure 114: a) Stress strain data from Section 3.1.3. FWHM values of the 200 b), 111 c) and 311 d) peak upon unloading versus the strain.

The 200 peak shown in Figure 114 is the only peak, which does not increase its FWHM in the macroplastic regime. All other peaks increase their FWHM where the 311 peak actually becomes slightly broader than its as prepared value at a strain of greater than 2%. This suggests that once the majority of the grains start deforming plastically, dislocations are still accommodated in the GBs but there is no room for network accommodation to facilitate an extra relief of RMS-strain.

NC-Nickel deformed at RT well into the macroplastic regime exhibits reversibility for most peaks when compared to the as prepared value of the peak width (see Figure 33, Figure 36 and Figure 44). If the FWHM values upon unloading from 1.4GPa (microplastic regime) are compared, all peak broadening – except the 200 – increases. Experiments carried out at 180K show that the peak broadening is not reversible upon unloading compared to their initial FWHM value (Figure 54b, Figure 55 and Figure 56). The deformation at 180K leaves inhomogeneous strain inside the material and causes an increase in strength (Figure 54a). However, this footprint of the LT deformation can be removed simply by heating the sample to RT. A follow-up macroplastic deformation at RT exhibits the same FWHM behavior, as if the sample would have no thermal and/or deformation history [176]. In terms of the dislocation picture, the additional inhomogeneous strains that remain upon unloading at 180K can be understood by a "freezing-in" of dislocations due to a restriction in the atomic activity within the surrounding GB.

If one summarizes the evolution of the peak broadening during continuous (Figure 33) and load-unload tests (Figure 36) one can conclude the following points:

- Until ~ 800MPa, the material responds elastically.
- From ~ 800MPa to ~1.4GPa, the material begins to plastify heterogeneously, which is visible by the reduction in peak width upon unloading.
- Around 1.4GPa, the material exhibits its lowest possible RMS-strain state. If the material is loaded to higher stresses, RMS-strain is built up again. This is an indication that the material starts to deform more homogeneously because the possibility of network accommodations is exhausted.

In Section 3.1.3, it is shown that the peak positions upon unloading start to change after a loading stress of 1.4GPa (~0.7% plastic strain) is exceeded. This change is peak dependent and increases monotonically with increasing stress. By calculating the change in lattice strain from the peak positions and plotting it versus the applied stress, it is also possible to see at which stress this change starts occurring (see Figure 106). The data in Figure 106 originates from a load-unload cycle (Figure 32, Section 3.1) but only the first loading is shown.

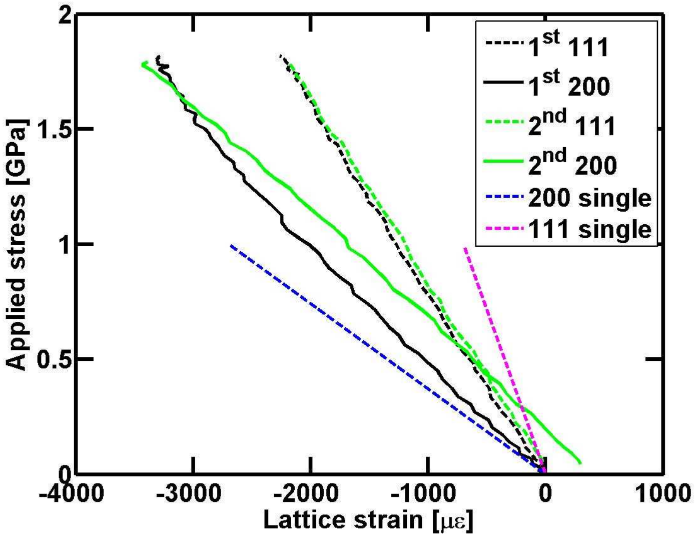

Figure 115: Lattice strains versus applied stress for the first and the second loading cycle of the 111 and 200 peaks (correspond to the test in Figure 32). Continuation of Figure 106.

Figure 115 shows now both loading cycles. The 111 peak exhibits a linear relation in the first and in the second loading cycle. For the 200 peak, it is evident that in the first loading cycle a deviation from linearity is present. The unloading exhibits a linear relation resulting in a relative change of lattice parameter for the 200 direction. The second loading cycle of the 200 peak shows a linear relation, however, the observed slope seems to move towards the slope of the 200 single crystal behavior. The relative change in the unloaded sample after plastic deformation for the 200 peak suggests changes in residual strain. It is known that residual strains can depend strongly on the crystallographic direction especially in such an elastically anisotropic material as Nickel (see Table 8).

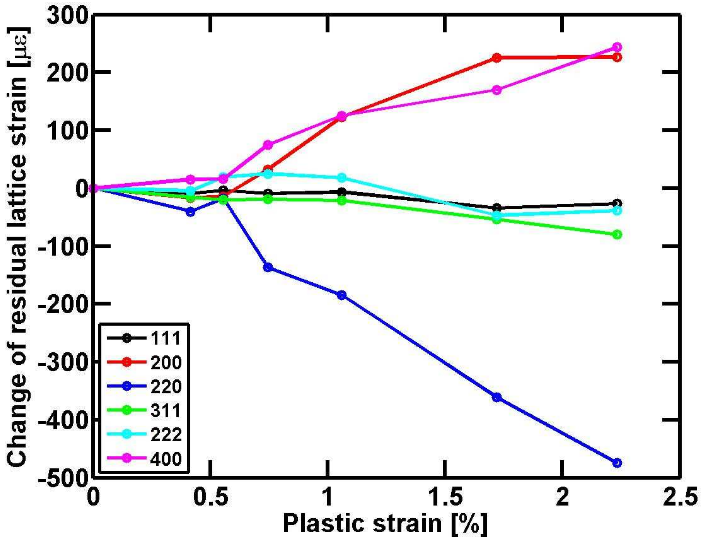

Figure 116: Residual lattice strain values versus plastic strain load-unload tests of NC-Nickel (data corresponds to Section 3.1.3).

Figure 116 shows changes in the residual lattice strain plotted versus the plastic strain. In the microplastic regime, only small changes can be observed. Once the NC-Nickel specimen is deformed above the microplastic regime (~0.7% plastic strain), the residual lattice strain of the 200 peak family becomes gradually positive with increasing plastic strain. The residual lattice strain of the 111 peak family and the 311 peak is rather stable. On the other hand the 220 peak changes to negative values. A similar behavior in the change of residual lattice strain for the different peaks was observed by Clausen using neutron diffraction on Copper [177] as shown in Figure 117. Note that the amount of the observed changes in the residual lattice strain in NC-Nickel is significantly bigger. In his Copper data, the change in residual strain saturates after the initial change. Due to the limited tensile ductility of NC-Nickel, it is only possible to investigate plastic strains until ~2.5 percent and no clear saturation can be observed.

Clausen used a self-consistent model to calculate this behavior and established that his model predictions of peak behavior are in general good agreement, but have the largest problems with residual strains perpendicular to the tensile axis, which is precisely what is measured in our experiments.

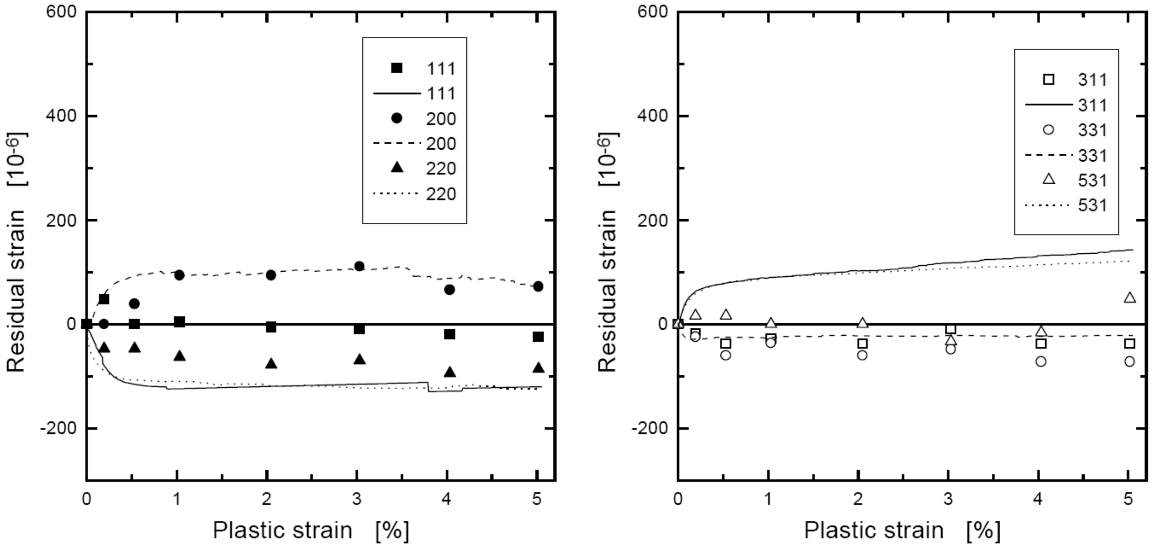

Figure 117: Residual strain values measured with neutron diffraction on polycrystalline Copper in transverse direction. The lines originate from self-consistent model prediction. Data from [177].

From these results, two trends can be established. Firstly, upon unloading in every test on NC-Nickel, the changes in peak positions occur after plastic deformation, and they are of the same relative amount (Figure 38 and Figure 41) even if the test is carried out at 180K (Figure 65). Secondly, the load-unload test in the transient region shows that this change is monotonic until the UTS (Figure 45). In general, the evolution of residual lattice strains in NC-Nickel is qualitatively equivalent with conventional CG FCC metals obtained by Clausen [177].

The observed time-dependence in the FWHM upon unloading (see Figure 36) is present in all tests once the material is deformed to the full plastic regime. It is slightly less pronounced for LT deformation (Figure 64) and it reduces monotonically with the pre-annealing temperature (Figure 52), but it never entirely vanishes – even at 180°C annealing temperature. Hand in hand with the time dependent reduction in the FWHM is a reduction in the bulk strain, e.g. the sample shrinks. This is obvious by the observed negative strain rate after the dip in a strain reduction tests (see Section 3.3.1). Unloading the sample is the same as a dip test but with a drop to zero stress. That the sample also shrinks after complete unloading can be seen in Figure 118. Figure 118a, shows the true strain versus time from the test presented in Figure 32. The black data represents the first loading. Then the sample is unloaded and kept at 10MPa (red data). The green data is the second loading cycle. Since the changes in the unloaded phase (red data) are difficult to see in the scale of this figure, the unloaded data is shown in Figure 118b. Here sample shrinkage is clearly visible.

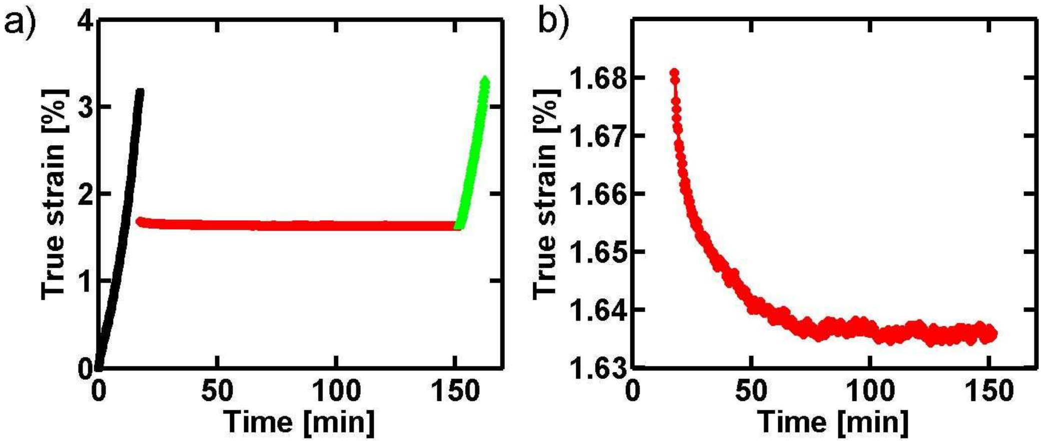

Figure 118: a) Strain versus time from Figure 32. b) Strain upon unloading from the full plastic regime.

In CG materials, sample shrinkage can be explained by relaxation of dislocation networks [178]. However, in NC materials, no such dislocation networks are observed. Rajagopalan et al. [179] studied freestanding NC Aluminum and Gold films and explains a recovery of plastic strain through thermally assisted dislocation depinning from grain boundary ledges or impurities with different local energy barriers. He argues that the temperature dependent recovery is ongoing until all internal residual strains are eliminated. This could be in agreement with the observed time dependent reduction in FWHM and associated with the running back and final full absorption of dislocation in GBs after overcoming the last pinning point. The process described by Rajagopalan et al. is only one possible explanation. It is also possible that slow – diffusion assisted – GB accommodation processes such as sliding or grain rotation are present.

Very large plastic strains in NC-Nickel

Characteristic for the compressive deformation is that after a short strain-hardening regime, the NC-Nickel plastifies with an almost constant flow stress. During tensile experiments, it could be shown that the 311 peak increases the most compared to its value upon unloading in the microplastic regime (see Figure 44 and Section 3.1). It is therefore not surprising that this effect is enhanced during a compression experiment in which 20% strain is achieved. This aspect is best shown in the considerable difference in the anisotropy presented in Figure 119. Also the calculation of the XRD pattern from MD samples containing dislocations showed that the WH plot increases and develops an anisotropy that is dominated by a broadening of the (311) diffraction peak. Why the 311 peak width does not recover is at this stage not known.

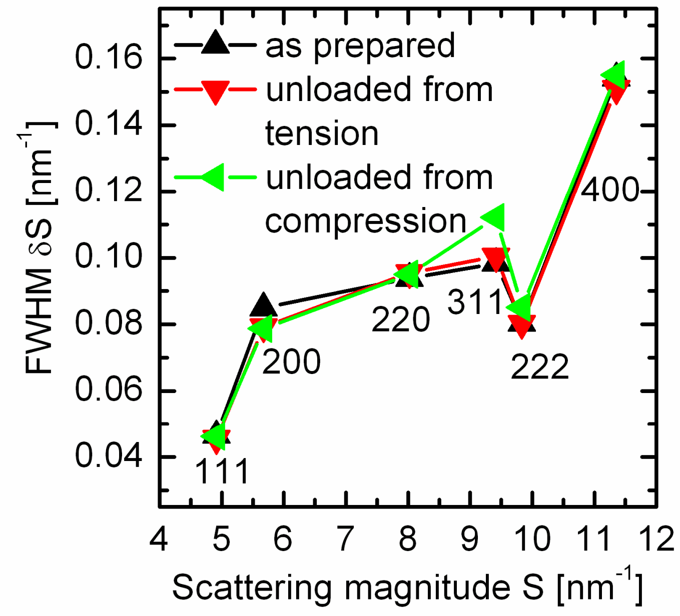

Figure 119: Williamson–Hall plots for experimental NC-Nickel (black) as prepared, (red) unloaded from tensile deformation and (green) unloaded from compression deformation.

The measured changes in the residual lattice strain during compression and the corresponding tension values are presented in Figure 120. Here one can see that the simple linear increase in peak width seen for some peaks in the tension data is not present to the same degree in the compression data. For the compression data, some peaks exhibit first a positive residual strain that changes to a negative value at higher strains, which cannot be explained until now. What becomes apparent is that at the larger strains of the compression data, the change in lattice parameter tends to saturate for all peaks. This was not possible to see within the plastic strain reached within tension experiments.

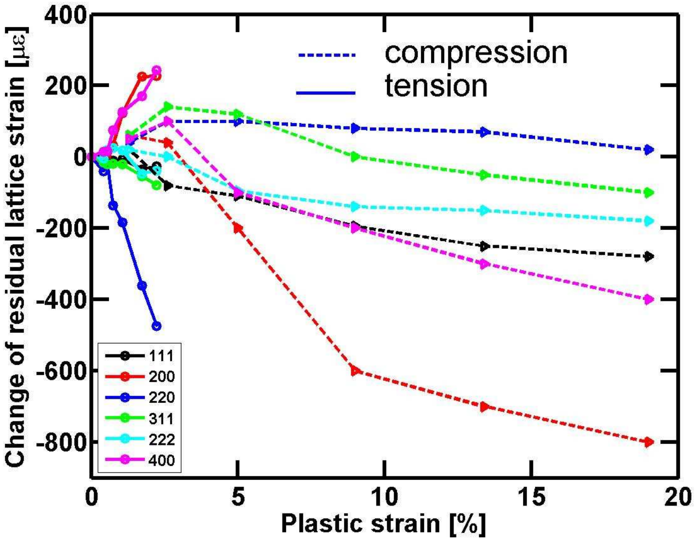

Figure 120: Residual lattice strain values during compression of NC-Nickel. The tensile data from Figure 116 is added.

Compared to NC-Copper, NC-Nickel deformed to the large compressive strains showed very little change in grain size [148]. The lack of grain coarsening in NC-Nickel might be related to the presence of impurity atoms. However, atom probe microscopy did not provide evidence for GB segregation (see Section 3.6 and [143]). Grain growth has been observed in NC-Nickel [67, 180] under conditions of high-pressure torsion, i.e. in the presence of large hydrostatic and shear stresses as well as large strains. However, under constant load (Section 3.4.3) there seems to be only a slight increase in the population of grains with a diameter between 60 and 80 nm [148].

4.2.3. Summary

In-situ X-ray diffraction experiments gave insights on the deformation behavior of NC materials. The time resolved XRD technique allowed to pinpoint a transition region in NC materials where the mechanical data shows only a gradual change from the elastic to the plastic regime when compared to their CG counterparts. Through the in-situ diffraction data, it is now possible to observe a structural relaxation by loading the material into the microplastic region or annealing. None of deformation models presented in the introduction (Section 1.1.3) can be excluded but it is important to realize that NC materials deform very heterogeneously in the early stage of plasticity. Through the presented X-ray data, it is suggested that the initially stored RMS-strain level is reduced through loading the NC material.

The grain size stability in NC-Nickel is superior compared to other NC materials with a similar grain size and it is assumed that this is due to the presence of impurities. Despite there being no significant grain growth in NC-Nickel, a small increase is possible especially if the deformation level is high.

4.3. Deformation mechanisms: a view provided by transient test

A thermally activated deformation mechanisms is an atomic scale process that is characterized by an activation energy and an activation volume, defining the probability that such an atomic mechanism can occur.

The macroscopic applied stress can be considered as a sum of a temperature dependent effective stress plus a temperature independent internal stress. The assumption that the latter is temperature independent corresponds to the assumption that there exists no structural relaxation upon changing the temperature. The effective stress corresponds to local energy barrier which can be influenced by thermal activation and usually decreases with increasing temperature for a given strain rate. Due to their temperature dependence, the effective and internal stresses are also called thermal and athermal stress respectively.

To investigate thermally activated mechanisms and to separate the thermal and athermal stress components in NC-Nickel, the activation volume is measured via transient tests and the separation of the athermal and thermal stress components is carried out via dip tests. These experiments will be discussed in the following two paragraphs. For more details, see Appendix A.

4.3.1. Separation of athermal and thermal stress component with Dip tests

The samples are loaded up to a certain applied stress level using a constant strain rate. Then the stress is dropped very rapidly by a certain amount followed by a short period of creep during which the plastic strain is measured as a function of time (Appendix A). It is assumed that the internal stress does not change during the stress drop, i.e., there is no significant change in the microstructure. At the moment of the stress drop, it can be assumed that several dislocations have been nucleated and are propagating. As suggested by MD simulations, a dislocation will be hindered on its way across the grain interior by the presence of GB ledges, acting as pinning points that have to be overcome by thermal activation [34]. These pinning points represent localized obstacles with characteristically short-range interactions – it is the associated short-range stress field of such structure that constitutes the effective stress. Thus total stress acting on the dislocation is given by the sum of long-range (temperature independent) and short-range (temperature dependent) stress fields [84], as shown in Figure 121.

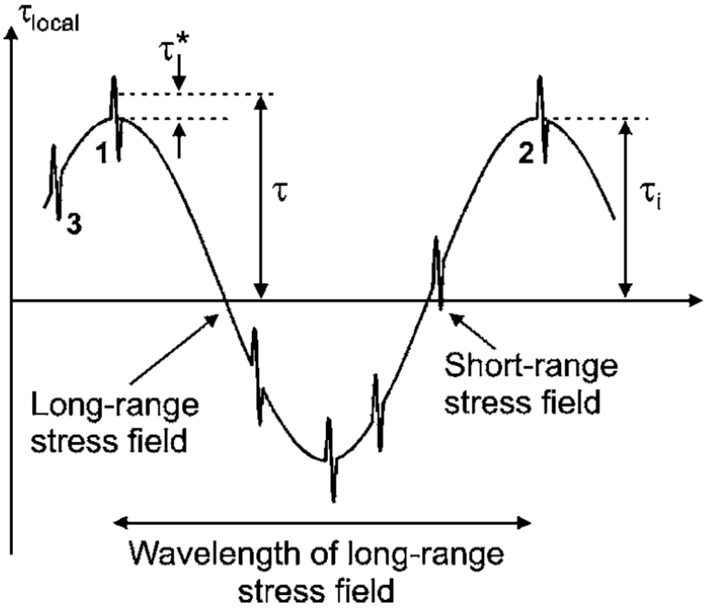
τ_{local}
τ^*
1
2
3
τ
τ_i
Long-range stress field
Short-range stress field
Wavelength of long-range stress field

Figure 121: Schematic representation of stress fields experienced by a dislocation along the slip path. The applied shear stress, τ, is separated in an effective stress, τ^* and an internal stress τ_i. The numbers correspond to Figure 122.

The dislocations are pinned most effectively when the internal stress opposes the applied stress. Consider a dislocation bypassing an obstacle (pinning point) as shown in Figure 122 (corresponding schematic stress fields see Figure 121).

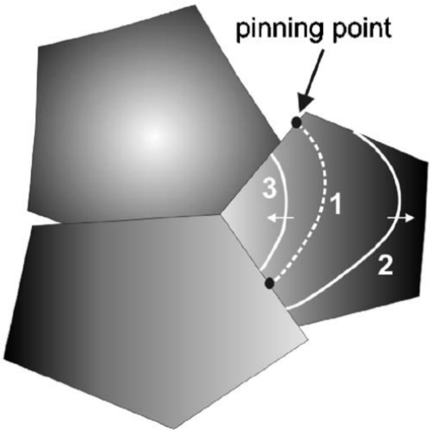
pinning point
3
1
2

Figure 122: Schematic representation of dislocation propagating in a grain during a stress dip test. The gray values represent fluctuations of the internal stress.

When the stress drop is less than the effective stress, τ^*, it will still propagate forward till position (2), producing a positive creep. However, when the stress drop exceeds τ^* the dislocations will run back and eventually stop at the pinning point (3), producing a negative creep. In this picture, τ^* represents an average stress needed to get over a pinning point at constant strain rate. The fact that for NC-Nickel significant negative creep rates are observed together with the reversibility in the peak broadening during in situ X-ray diffraction upon unloading [89] indicates that dislocations can easily run back into the GBs. The increase in τ^* with strain above 1.4GPa applied stress (see inset in Figure 72, τ^* is multiplied by the Taylor factor to get σ^*) points towards an increase of the pinning point density in the GBs, and the increase of the internal stress, τ_i, towards changes in microstructure that are related with an increase in long-range stress fields. Such a picture is compatible with MD simulations results; however, it cannot be confirmed due to restrictions in simulation time: indeed simulations demonstrate continuously changing GB structures and therefore ledge densities during dislocation nucleation and propagation, where extrinsic GB dislocations can be the signature of incomplete absorption, as such contributing to long-range stress fields [34].

In summary, strain-dip tests evidence high values for the effective and the internal stress when compared to CG structures and the existence of a negative creep. The results can be interpreted in terms of a thermally activated dislocation mechanism in which propagation is hindered by pinning at the GB.

4.3.2. Elaborating the activation volume with successive relaxations

The activation volume from successive relaxation at RT (see Section 3.3.2) agrees well with the value calculated from dip tests of around 10-15b^3. However, at 180K the activation volume increases to around 35b^3, which is distinctly higher than the RT value. This is somehow opposed to the observed behavior for CG Nickel at this temperature range [181]. A temperature dependent change of activation volume has been observed for different materials in different temperature ranges towards lower but also towards higher activation volume if the temperature decreases [74]. In general, changes of the activation volume are related to changes of deformation mechanisms. For NC materials very little data are available on the temperature dependent activation volume but the same trend – lower temperature, higher activation volume – has been observed in NC-Nickel down to 77K [44]. This rather smooth change from over a wide temperature range is, however, not typical for observed mechanism changes in CG materials [74]. A common explanation on the increasing activation volume with decreasing temperature in NC-Nickel does not exist at present.

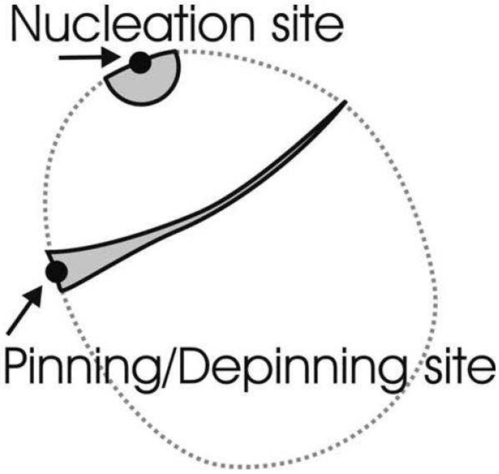

Figure 123: Schematic of slip areas shaded in grey that are involved in the nucleation of a dislocation and the depinning of a dislocation of the GB (indicated by the dotted line). From [34].

Figure 123 shows a schematic for the characteristic slip area shaded in gray for the nucleation. The slip area associated with the pinning-depinning process is also shown in Figure 123. One can easily imagine that both processes have a similar activation volume and none of them can be excluded as dominant effect if only this characteristic is compared. For a loop nucleated of a boundary facet Asaro et al. [46] calculated a activation volume of order of 5-10b^3. However, according to Evan and Rawlings [182] and Conrad [144] there are other possible deformation mechanisms exhibiting an activation volume of between 10^1-10^2b^3. In particular, there is point defect drag, point defect interaction conservative and non-conservative jog motion and cross slip. It has to be noted that such a thermally activated pinning-unpinning process is not taken into account in the model presented by Asaro and Suresh [46], where after nucleation the dislocation motion is considered to be predominantly an athermal event. However, a thermally activated pinning-unpinning mechanism is supported by recent simulations, which suggest a strong temperature depended unpinning of dislocations [34].

4.4. Deformation behavior: a combined view

The in-situ XRD experiments have shown that deformation of NC-Nickel in the initial stage is dominated by the heterogeneous deformation intrinsic to the NC GB network. This is evident in a NC material because the initial strain-hardening regime results in a mechanism that upon unloading lowers the RMS-strain. Such behavior is incompatible with the activation of multiple slip systems within the nanograins and/or the increased presence of geometrical dislocations, since this would have the tendency to increase RMS-strains or at least keep the values constant, as observed for HPT-Nickel. Therefore, it is inadequate to define a yield strength at a particular strain, e.g. 0.2%, and compare these values with CG material. Above 1.4GPa, or a plastic strain of ~0.7%, a transition occurs to a more homogeneous deformation evident by the evolution of the peak broadening because the peak broadening increases for most diffraction peaks once the material is strained further. These results demonstrate the presence of two distinctly different hardening regimes in NC-Nickel that can be related to the microplastic and macroplastic regime.

Figure 124 presents a model to relate the XRD peak positions and peak widths to the microstructure. The as prepared NC structure and a corresponding X-ray diffraction peak are shown in Figure 124a. In the microplastic regime, as long as plastic events are scarce (Figure 124b), incompatibility stresses are accommodated by the GB structure/network, reducing the RMS-strain and consequently causing a reduction in the peak width (Figure 124c). Once the majority of the grains start to deform plastically (Figure 124d), the residual Burgers vector content of these propagating dislocations are still accommodated in the GBs but there is no room for network accommodation. It can be expected that dislocation absorption would become more and more difficult when the number of dislocations involved in the plastic deformation process increases [4]. This would increase the number of stress intensities in GBs resulting in long-range stress fields in grain interiors, i.e. a build up of RMS-strain and contributing to the WH anisotropy. Such an effect explains why a fully reversible peak broadening is observed after unloading of a tensile deformed NC-Nickel, whereas after 20% strain a non-reversible broadening of the 311 peak is observed, and still no dislocations in the grain interiors can be observed by TEM. This picture is compatible with the X-ray diffraction calculations presented in Section 3.5.4, which show that those dislocations that are not fully absorbed (TEM invisible) can also contribute to an order dependent peak broadening. Figure

124e shows a grain structure similar to the as prepared structure. The permanent peak shift can be explained by the change of type II stresses for a certain diffraction direction. This change is a result from the intergranular interactions during loading of the NC-Nickel sample.

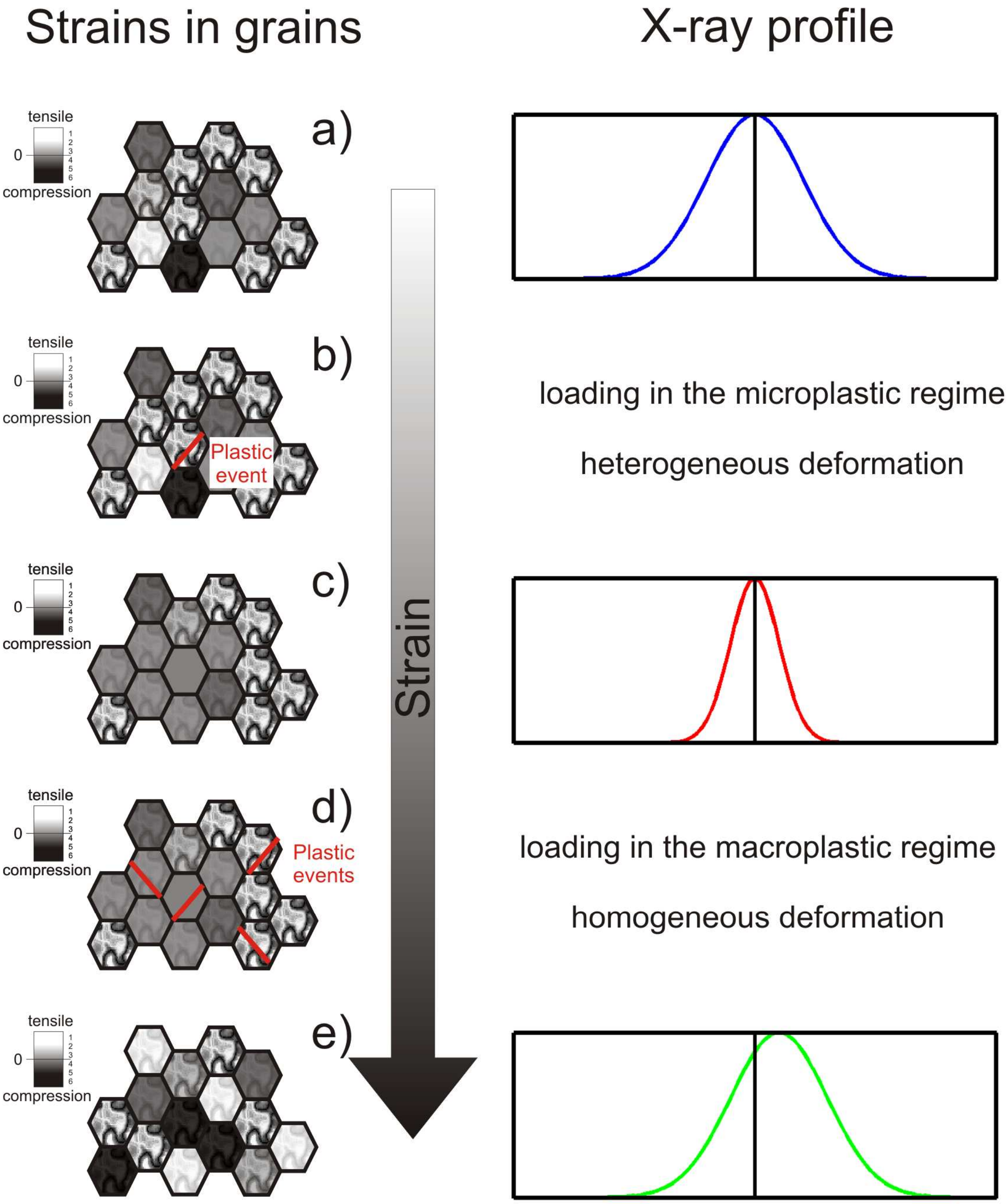
Strains in grains
X-ray profile
tensile
0
compression
1
2
3
4
5
6
a)
b)
Plastic event
c)
d)
Plastic events
e)
Strain
loading in the microplastic regime
heterogeneous deformation
loading in the macroplastic regime
homogeneous deformation

Figure 124: Schematic drawing of NC grain arrangements, their internal stress fields (in gray shades) and the corresponding X-ray diffraction peaks. Following Figure 111 and extending the strain into the macroplastic regime where plastic events introduce strain fields.

In this picture, the FWHM behavior for deformations performed at 180K can be understood by a “freezing-in” of dislocations. In other words, the propagation of dislocations is hindered by pinning points causing an increase in peak broadening upon unloading. If the material is heated to RT, the increased thermal assistance is high enough to overcome the pinning points and the dislocations can propagate further, finally becoming absorbed and resulting in a reduction of the RMS-strain and therefore the peak broadening. Such a picture evidences that the rate limiting process is indeed thermally activated. These outcomes strengthen the above conclusion where the propagation of a dislocation is hindered by its pinning at GB ledges, controlling the thermally activated dislocation mobility. Moreover, the negative creep observed in strain-dip tests substantiates a propagation process hindered by pinning points at GB ledges. Thus the experiments suggest that not only nucleation [46] but also propagation should be considered as a possible rate limiting mechanism in NC metals.

5. Summary

This thesis could greatly extend the knowledge on the deformation behavior of NC Nickel by combining classical mechanical testing and in-situ experiments. In detail, this thesis revealed that:

Within the “hardening” regime of NC-Nickel, two deformation mechanisms are present, where one mechanism reduces the peak broadening, the other one increases it. Since no grain growth is observed during deformation, even under (compressive) deformation up to about 20% strain, the reduction in the peak broadening is interpreted in terms of strain fluctuations in the material.

In the early stage of “hardening” regime – the microplastic regime – it is conceivable that localized plastic events can be accommodated by the grain boundary network resulting in a reduction in the existing strain fluctuations. Beyond a plastic deformation of about 0.7%, the strain fluctuations increase with ongoing deformation. This change from decrease to increase suggests that dislocations cannot get sufficiently absorbed in the grain boundary network anymore and therefore contribute to strain fluctuations resolved by the increasing diffraction peak broadening.

The beginning of plastic deformation in NC-Materials is very inhomogeneous. Therefore, the generally used 0.2% yield criteria does not correspond to the onset of macroscopic plasticity.

If plastic deformation of nanocrystalline Nickel is carried out around 180K, an irreversible peak broadening is observed upon unloading. This result can be understood by a freezing in of dislocations within the grain interior or by suppressing grain boundary accommodation processes. Reheating to room temperature supplies enough thermal mobility to unfreeze the dislocations evident by the recovery of the peak width to its as prepared value.

By introducing a lattice dislocation or twin content into computer-generated NC samples and calculating the corresponding two-theta X-ray diffraction spectra, the peak integral-width anisotropy as a function of scattering angle is found to reflect the experimental anisotropies observed in as prepared NC-Nickel and NC-Copper. Such simulations also demonstrate that a similar anisotropy in the WH plot usually explained by the presence of lattice dislocations can be obtained by the presence of highly localized stress intensities in GBs induced by ‘‘absorbed’’ – TEM invisible – lattice dislocations.

Strain dip tests evidence high values for the effective and the internal stress when compared to coarse grained structures and the existence of a negative creep. These results can be interpreted in terms of a dislocation mechanism where propagation is hindered by pinning at grain boundary ledges controlling the thermally activated dislocation mobility.

A non-uniform distribution of some impurities indicates segregation in NC Nickel, which seems to increase through annealing. However, the few samples studied did not allow a clear and conclusive picture.

These results are graphically summarized in Figure 125 where an update on the knowledge base – as presented in the introduction – is given.

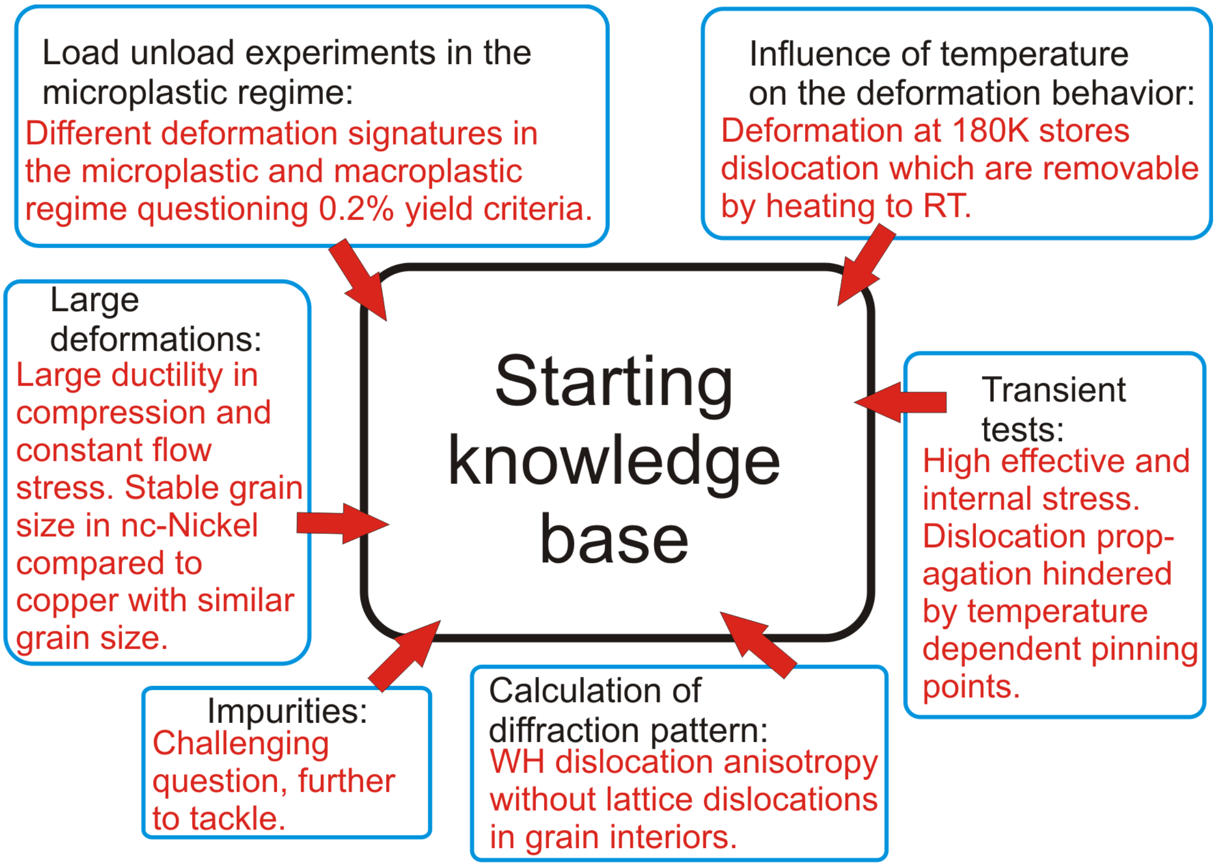
Load unload experiments in the microplastic regime:
Different deformation signatures in the microplastic and macroplastic regime questioning 0.2% yield criteria.
Influence of temperature on the deformation behavior:
Deformation at 180K stores dislocation which are removable by heating to RT.
Large deformations:
Large ductility in compression and constant flow stress. Stable grain size in nc-Nickel compared to copper with similar grain size.
Starting knowledge base
Transient tests:
High effective and internal stress. Dislocation propagation hindered by temperature dependent pinning points.
Impurities:
Challenging question, further to tackle.
Calculation of diffraction pattern:
WH dislocation anisotropy without lattice dislocations in grain interiors.

Figure 125: Short summary of thesis highlights, pointing out the contribution to the knowledge base gained within this thesis.

6. Outlook

The presented investigations extend the knowledge of the deformation mechanisms in NC-Nickel. Further research should be performed to cover the wide class of NC materials that exist and their different synthesis pathways.

In NC materials, a key issue is the content and distribution of impurities and more quantitative information would be of great help. Over the past few years, MD simulation have provided a unique and complimentary viewpoint in classifying the atomic scale processes that may contribute to the experimentally observed plastic deformation properties of NC materials. However, until now only few MD investigations of NC plasticity have considered impurities. The incorporation e.g. of Oxygen [183] in MD simulations would be an important step towards achieving this. Although the grain sizes of the simulated samples are already similar to experimental conditions, the Voronoi construction employed in most MD simulations to construct the NC network exhibits some disadvantages such as unrelaxed triple junction geometries and GBs. These limitations are at present difficult to overcome due to the time scale restriction of simulations, where typically only a few nanoseconds of physical time are simulated.

The developments in focused X-ray diffraction techniques already allow the study of regions as small as several 100nm. With further progress, it could be possible to study a single nano grain and gain local information, as is already done for their CG counterparts.

In the special case of NC-Nickel, deeper insights into the time dependent processes as well as the temperature dependence of the activation volume are of great interest. The calculations of the diffraction peaks are a start in explaining the unloaded WH anisotropy. The dynamic behavior of the diffraction peaks during loading opens new fields of research.

In general, the work entailed in this thesis could show that NC-Nickel exhibits an extended microplastic regime that can easily be modified through small external changes, like low temperature annealing or by load-unload cycles in the micoplastic regime. This finding is an important contribution to the possible applicability of NC bulk structures in future MEMS devices.

Appendix A

Dislocation response to thermal and athermal stresses

If a high enough stress is applied to a crystalline material, it will deform plastically or fracture. In a classical picture, the mechanisms to deform a material plastically can be based on dislocation activity and/or involve diffusional processes. The diffusion-based mechanisms usually operate at high homologous temperatures. Around RT, the plastic deformation of most metals is governed by dislocations. In that case, the average dislocation mobility controls the flow rate of the material. Furthermore, the speed of a single dislocation without any barriers is considered as infinite and the average speed of all dislocations is then controlled by the obstacles, where the dislocations arrests or is being delayed/pinned.

Seeger et al. [184] proposed to decompose the applied shear stress τ which is needed to deform a material plastically, mathematically in two components (39).

$$\tau = \tau_i + \tau^* \qquad \textbf{(39)}$$

The first component τ_i, is related to long-range stress fields that originate from the internal structure and dislocation patterning in the material. This component depends on the temperature only through the temperature dependence of the shear modulus. Therefore, it is called the athermal or internal stress. The second component τ^* is called effective stress. It is related to local energy barriers originating from small obstacles, intrinsic lattice resistance or unpropitious dislocation core configurations. This type of barrier involves a small volume/energy that can be strongly influenced by thermal activation. In other words, the thermal energy helps dislocations to overcome these barriers and results in a reduction in stress when the temperature rises. This stress is therefore also named as the thermal stress component.

In the following two methods will be presented 1) to decompose the athermal and the thermal/effective stress (Determination of long-range stress fields) and 2) to investigate the origin of the short-range obstacles (Investigating the origins of the short-range obstacles).

Determination of long-range stress fields

Four different tests are discussed which allow the determination of long-range stress fields.

- The athermal stress can be determined by measuring the temperature dependence of the stress. The athermal stress is found at temperatures where no influence on the stress is present [182]. Apart from some extrapolation needed to extract the stresses at LT, this method requires that the material is stable over a large range of temperatures and is therefore not considered for NC-Nickel.
- A method where no changes in temperature are necessary is to perform strain rate jump test [185]. However, this test requires a stable structure and has several assumptions (stable flow stress), which can be questioned in NC materials (for details see [185]). Furthermore, it "consumes" a relatively large part of the stress strain curve. Therefore, it is questionable whether the microstructure remains constant throughout the jump test.
- Another similar test revealing the athermal component is a simple stress relaxation. After the crossheads are stopped, the material will transform elastic strain into plastic strain (relax) and finally reach an asymptotic stress which can be ascribed to the athermal stress [186]. Such a simple test suffers from several problems. A relaxation test takes by its principal (long) time to reach an asymptotic value during which the microstructure can change. Furthermore, the possibility of creep especially at high stresses can influence the results.
- A test where the fewest changes in microstructure can be expected is a so-called strain-dip test. This test is often also referred to as stress reduction test. A recent review from Krumel et al. [187] states that this test should be favored compared to other methods. Therefore, stress reduction tests [109, 147, 188-190] are used to perform the separation of the internal τ_i and the effective τ^* stress.

The strain-dip test is carried out as follows: during a continuous deformation – at any point of the stress strain curve – a stress drop $\Delta\tau$ followed by a short creep period is conducted. During this initial creep, the creep rate $\dot{\gamma}_p$ is recorded as a function of time (see description in Section Operation modes at Page 24). This test can be repeated on another sample at the same point of the stress strain curve, but with a different stress drop. The creep rate will be different. At the stress drop where the creep rate is zero, the stresses on the dislocations are in equilibrium with the applied stress i.e. the average dislocation flux is zero. The thermal energy, which normally helps to overcome barriers, is not anymore effective and the material bears the applied stress through its internal stress. In other words, the stress drop $\Delta\tau$ where zero creep follows can be assigned to the effective stress τ^*.

To examine τ^* – from several measurements with different stress drops – Miličkla [189] suggested a hyperbolic sine function (40) to correlate the creep rate dependence of the stress drops.

$$\dot{\gamma}_p = A_t \sinh\left[V\left(\tau^* - \Delta\tau\right)/kT\right] \tag{40}$$

Where A_t is a temperature dependent coefficient including the mobile dislocation density, V the activation volume, T the absolute temperature and k the Boltzmann constant. The above route for the determination of the effective stress also allows calculation of the activation volume. However, for small stress reductions the activation volume can also be derived using relation (41), which considers two distinct data points [74].

$$\dot{\gamma}_{p1} / \dot{\gamma}_{p2} = \exp\left[V\left(\Delta\tau_2 - \Delta\tau_1\right)/kT\right] \tag{41}$$

Equation (41) has the advantage over (40) that τ^* does not need to be known explicitly and no shape function (*sinh*) is needed.

Investigating the origins of the short-range obstacles

In the previous Section, the athermal component of the stress is described as well as a sensible method to measure it. The second part of the applied stress is called the thermal component because the dislocation motion is often controlled only by a couple hundreds of atoms. This corresponds to an energy barrier of one electron volt or less and can be favored to overcome by thermal energy [74]. In other words, the stress needed to deform a crystalline structure at a given strain rate decreases as the temperature increase.

Theoretical assumptions

The Orowan equation (42) describes the deformation rate $\dot{\gamma}$, as a function of mobile dislocation density ρ_m, average dislocation velocity v, the Burger's vector b and a geometrical factor A [191],

$$\dot{\gamma} = A\rho_m bv\,. \qquad \textbf{(42)}$$

The average dislocation velocity v, is controlled by the successful attempt rate of a dislocation to overcome a barrier. To describe these successful attempts a Boltzmann statistic is used with the barrier energy ΔG and the thermal energy kT.

$$v = \frac{A'}{l} \nu_{id} \exp\left(\frac{-\Delta G}{kT}\right) \qquad \textbf{(43)}$$

Here A' is the area swept by a dislocation segment of length l between two successive obstacles and ν_{id} is related to the Debye frequency ν_D via $\nu_{id}=b\nu_D/l$. For the sake of simplicity all constants are summarized in,

$$\dot{\gamma}_0 = A\rho_m b\left(A'/l\right)\nu_{id}\,. \qquad \textbf{(44)}$$

Equation (45) describes the strain rate dependence on the local energy barrier ΔG,

$$\dot{\gamma} = \dot{\gamma}_0 \exp\left(-\Delta G/kT\right). \qquad \textbf{(45)}$$

Through thermodynamic laws and the assumption that the rate limiting process has a constant activation volume V, ΔG can be described by,

$$\Delta G = \Delta G_0 - \tau V\,. \qquad \textbf{(46)}$$

Here ΔG_o is the barrier activation energy at zero stress and τ the shear stress. The activation volume V is defined as,

$$V = -\left(\frac{\partial G}{\partial \tau}\right)_T. \qquad \textbf{(47)}$$

To establish ΔG, the thermodynamic relation,

$$\Delta H = \Delta G - T\Delta S\,, \qquad \textbf{(48)}$$

is useful. Under the assumption that the entropy ΔS is dominated by the temperature influence on the shear modulus ($d\mu/dT$) which can be found in literature [192, 193], Schoeck [194] derived a relation to calculate ΔG,

$$\Delta G = \frac{\Delta H + \frac{T}{\mu}\frac{d\mu}{dT}\tau V}{1 - \frac{T}{\mu}\frac{d\mu}{dT}}\,. \qquad \textbf{(49)}$$

However, to calculate ΔG, it is necessary to first get the activation enthalpy ΔH, which is experimentally accessible. The Maxwell relations allow to write,

$$TV\left(d\tau/dT\right) + \Delta H = 0\,. \qquad \textbf{(50)}$$

ΔH can now be calculated if the temperature dependence of the stress ($d\tau/dT$) and activation volume V are measured.

The temperature dependence of the shear stress can be established by temperature jump experiments either in creep or during constant strain rate tests. An easier way is to derive the dependence from constant strain rate experiments at different temperatures. However, there the stress has to be measured at the same structure for what often the yield point is used. This assumption has to be treated with care especially if the tested material has no clear yield point, e.g. ED-NC Nickel. In a dislocation picture, the same density of mobile dislocation has to be present at different temperatures and only then is it possible to compare their temperature sensitivity.

If the temperature dependence of the stress and the activation volume is measured, ΔH can be calculated via (50). With ΔH and ($d\mu/dT$) from the literature, it is also possible to derive ΔG with Schoeck's formula (51). Then the barrier activation energy at zero stress ΔG_o can be calculated and a full description of the deformation rate $\dot{\gamma}$ is given within the used model.

However, by rewriting (45) to $\Delta G = \alpha kT$ where α is the logarithmic strain rate ratio it can be seen that the equation yields to a linear relation with temperature going through zero. Under some assumptions for realistic values of $\dot{\gamma}_o$ (see equation (44)) and possible applicable strain rates Cagnon [195] established a value for $\alpha \approx 21$. With this assumption, the ΔG_o can be established only through the knowledge of the activation volume (46).

The paragraphs above show that the deformation rate $\dot{\gamma}$ of a material can be fully described if the barrier activation energy at zero stress ΔG_o and the activation volume is known. However, with a few assumptions it could also be indicated that the most important value is the activation volume V. Moreover, the measurement of the temperature dependence of the stress ($d\tau/dT$) in NC-Nickel is vague. Therefore, only the activation volume of NC-Nickel is measured within this thesis. Another factor is that the activation volume is the key parameter most used to compare and discuss the actual deformation mechanism in literature.

Measurement of activation volume

As can be seen in the paragraph above, the activation volume V gives an important insight into the underlying deformation mechanism. To determine it, a transient test has to be applied. It is possible to use strain rate jump tests or stress jumps/changes during creep [182].

Probably the easiest test to perform is stress relaxation, a simple stop of the crossheads and a recording of the stress drop with time. However, if the stress drop does not follow a logarithmic relaxation, several different activation volumes are present and the result will not be conclusive. Another consequence of a simple relaxation is that the measured volume is an apparent activation volume because the mobile dislocation density changes during the relaxation.

In any case, the apparent activation volume can now be calculated using:

$$V_a = 3.06kT\frac{\partial \ln\left(-\dot{\tau}/M\right)}{\partial \tau}. \tag{51}$$

The pre-factor 3.06 (Taylor) is used to convert the resolved shear stress to uni-axial stress [146]. The stored elastic strain, $-\dot{\tau}/M$, is transferred to plastic strain $\dot{\gamma}_p$ where M is the combined elastic modulus of machine and sample. This method is rather complicated because the combined modulus of the machine sample arrangement M has to be known exactly. A simpler method to determine the activation volume is to fit the measured relaxation data to (52),

$$\Delta\tau = -\frac{kT}{V_a}\ln\left(1+\frac{t}{c_r}\right). \tag{52}$$

Here t is the time and c_r is a time constant.

Both presented ways provide only the apparent activation volume. However, by the use of successive relaxations, it is possible to establish also the physical activation volume V. These successive stress relaxations are carried out at the same stress level as it is schematically shown in Figure 13. The reloading has to be quasi-elastic where no change in structure and mobile dislocation density occurs. The physical activation volume V can then be calculated via (53) (for indices see Figure 13),

$$V = kT\frac{\ln\left(\dot{\gamma}_{f1}/\dot{\gamma}_{i2}\right)}{\Delta\tau_1}. \tag{53}$$

The exact determination of the strain rate at the end of the first relaxation and the beginning of the second is with nowadays measurement devices possible, but still tricky. A better way which is currently most commonly used is described by Spätig [75]. There, the apparent activation volume is calculated from one relaxation and then corrected by Ω,

$$V = \frac{V_a}{\Omega}. \tag{54}$$

This correction factor Ω can then be deduced from successive relaxations,

$$\Omega^{-1} = 1 - \left(\frac{kT}{V_a \sum_{1}^{n-1} \Delta\tau_j} \right) \ln\left(\frac{\exp(-V_a \Delta\tau_j / kT) - 1}{\exp(-V_a \Delta\tau_1 / kT) - 1} \right). \tag{55}$$

For more details, especially in how the formulas are derived and which further assumptions are taken, the author refers to [74].

Appendix B

Grain size distributions

The number averaged grain size $\overline{d}$ is an arithmetic mean value calculated via,

$$\overline{d} = \frac{1}{n}\sum d_i \ . \tag{56}$$

There n is the number of counted grains and d_i the individual grain diameter calculated from each measured area, e.g. Figure 3b, assuming a circular grain. The corresponding standard deviation SD_d can be established via,

$$SD_d = \left(\frac{1}{n-1}\sum_{i=1}^{n}(d_i - \overline{d})^2\right)^{\frac{1}{2}} . \tag{57}$$

The volume averaged grain size can be calculated by assuming e.g. a spherical shape. The volume of each grain v_i is then calculated by,

$$v_i = \frac{4*\pi}{3}\left(\frac{d_i}{2}\right)^3 . \tag{58}$$

The average volume $\overline{v}$ is obtained from,

$$\overline{v} = \frac{1}{n}\sum v_i \ , \tag{59}$$

wherefrom the volume averaged grain size $\overline{d}_V$ can be calculated via,

$$\overline{d}_v = 2*\sqrt[3]{\frac{3*\overline{v}}{4*\pi}} . \tag{60}$$

The standard deviation for the volume average grain size SDd_v can be calculated via,

$$SD_v = \left(\frac{1}{n-1}\sum_{i=1}^{n}(v_i - \overline{v})^2\right)^{\frac{1}{2}} , \tag{61}$$

and

$$SD_{d_v} = 2*\sqrt[3]{\frac{3*SD_v}{4*\pi}} . \tag{62}$$

Appendix C

Different surfaces of nanocrystalline Nickel

Throughout the thesis different peak widths for the same peak occurred from different samples, although they were all cut from the same sheet of NC-Nickel. To relate these differences to one or the other side of the metal sheet, several techniques are applied.

The NC-Nickel sheet metal is made via the ED whereby ions are deposited on a substrate material. It is possible that the substrate side and the one which is opposite from it have different structure [30]. Additionally, there was no detailed information available which production parameters were used and how the handling of the purchased sheets was done.

To investigate systematically this difference, a number of samples are compared. Therefore, the peaks widths are plotted with respect to their peak position (see Figure 126) – the so-called WH plot. For visibility of the difference and further determination, the tests are colored in either green or blue according to the FHWM value of the 111 peak. Samples with a FWHM value smaller than 0.17° (measured at 17.5keV) are colored green and samples where this value was larger with blue. Now it is visible that two types of signatures are present.

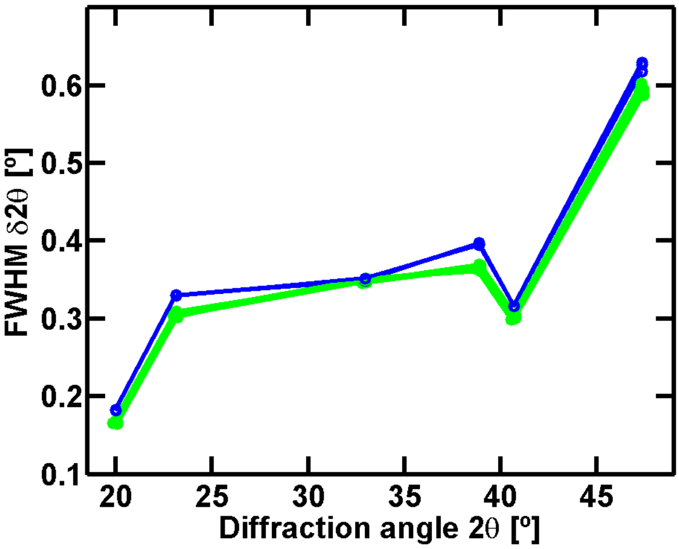

Figure 126: WH plot of eleven different NC-Nickel samples in their as prepared situation. For colors, see text.

WH analysis

Performing a WH analysis (see Section 2.3.5), the grain size and microstrain (RMS-strain) could be established and are presented in Figure 127. A correlation between the 111-FWHM and the microstructural parameters obtained from the WH analysis is evident. Samples with a FWHM of the 111 peak, which is smaller than 0.17° have a bigger grain size and a smaller RMS-strain and vice versa.

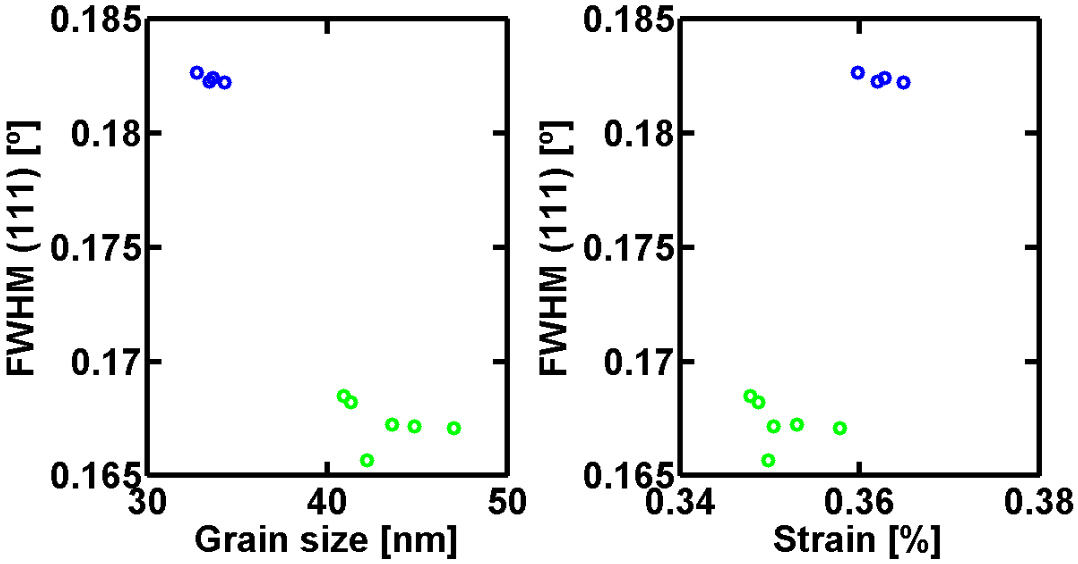

Figure 127: Grain size and RMS-strain from the WH analysis of several NC-Nickel samples. The analysis is performed by the use of the integrated with from the 111 family with the Cauchy-Gaussian deconvolution.

Microstructure

The differences presented above between the two sample sides in the WH analysis are evident. However, in TEM pictures, which are presented in Figure 128, these differences are not so clear. The cross section bright field images presented there originate from a place close to one and the other side of the as prepared sheet. For possible variations, only speculation can be performed and an intensive investigation would be necessary.

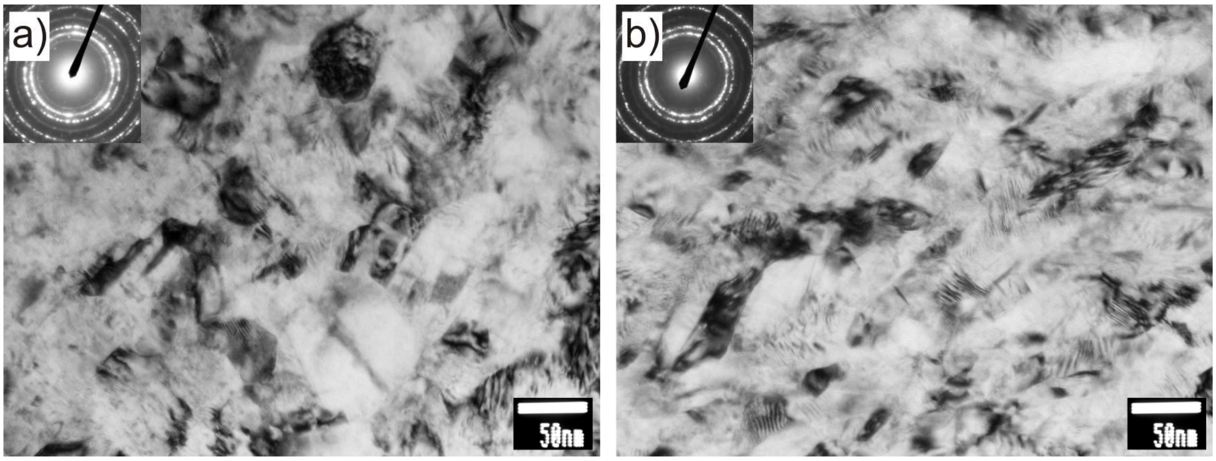

Figure 128: Cross sectional view on the ED-NC Nickel. Both a) and b) TEM bright field images are close to a surface. The insets show their corresponding diffraction pattern.

As opposed to the two TEM pictures, the results from the WH analysis, could establish significant differences between the two sides of the investigated ED Nickel sheet. However, these dissimilarities do not seem to affect any possible observation except an absolute change of the peak width during any loading cycle. To verify this, in Figure 129 the 111 peak broadening during loading of several samples are presented.

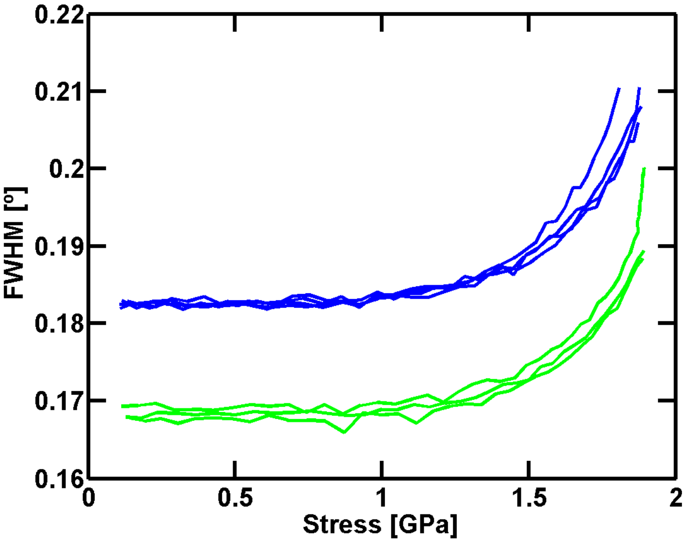

Figure 129: 111 FWHM values versus applied stress from the same eleven samples presented in Figure 126.

Summary

With diffraction pattern analysis and TEM investigation, it could be shown that there are differences between the two sides of the purchased NC-Nickel sheet. These differences can be recognized in the peak broadening which probably origins from the grain size and the RMS-strain which are empirically related [70]. These revealed differences apparently do not influence the deformation curve and the relative diffraction peak behavior of NC-Nickel.

References

1. Feynman R., *There's Plenty of Room at the Bottom*. 1959, American Physical Society: California Institute of Technology (Caltech)
2. Gleiter, H., *Nanocrystalline materials.* Progress in Materials Science, 1989. **33**(4): p. 223-315.
3. Meyers, M.A., A. Mishra, and D.J. Benson, *Mechanical properties of nanocrystalline materials.* Progress in Materials Science, 2006. **51**(4): p. 427-556.
4. Hirth, J.P. and J. Lothe, *Theory of Dislocations (2nd edition)*. 1982, New York: John Wiley and Sons. 857.
5. Hull, D. and D.J. Bacon, *Introduction to Dislocations*. Fourth Edition ed. 2001, Oxford: Butterworth-Heinemann.
6. Wertmann, J. and J.R. Wertmann, *Elementary Dislocation Theory*. 1964, New York,: Macmillan.
7. Bronkhorst, C.A., S.R. Kalidindi, and L. Anand, *Polycrystalline Plasticity and the Evolution of Crystallographic Texture in Fcc Metals.* Philosophical Transactions of the Royal Society of London Series a-Mathematical Physical and Engineering Sciences, 1992. **341**(1662): p. 443-477.
8. Heripre, E., et al., *Coupling between experimental measurements and polycrystal finite element calculations for micromechanical study of metallic materials.* International Journal of Plasticity, 2007. **23**(9): p. 1512-1539.
9. Hall, E.O., *The Deformation and Ageing of Mild Steel .3. Discussion of Results.* Proceedings of the Physical Society of London Section B, 1951. **64**(381): p. 747-753.
10. Petch, N.J., *The Cleavage Strength of Polycrystals.* Journal of the Iron and Steel Institute, 1953. **174**(1): p. 25-28.
11. Dao, M., et al., *Toward a quantitative understanding of mechanical behavior of nanocrystalline metals.* Acta Materialia, 2007. **55**(12): p. 4041-4065.
12. Palumbo, G., S.J. Thorpe, and K.T. Aust, *On the contribution of triple junctions to the structure and properties of nanocrystalline materials.* Scripta Metallurgica et Materialia, 1990. **24**(7): p. 1347-1350.
13. Wang, N., et al., *On the persistence of four-fold triple line nodes in nanostructured materials.* Scripta Metallurgica et Materialia, 1993. **28**(2): p. 253-256.
14. Derlet, P.M., S. Van Petegem, and H. Van Swygenhoven, *Calculation of x-ray spectra for nanocrystalline materials.* Physical Review B (Condensed Matter and Materials Physics), 2005. **71**(2): p. 024114-8.
15. Schiotz, J., F.D. Di Tolla, and K.W. Jacobsen, *Softening of nanocrystalline metals at very small grain sizes.* Nature, 1998. **391**(6667): p. 561-563.
16. Van Swygenhoven, H. and A. Caro, *Plastic behavior of nanophase Ni: A molecular dynamics computer simulation.* Applied Physics Letters, 1997. **71**(12): p. 1652-1654.
17. Van Swygenhoven, H. and A. Caro, *Plastic behavior of nanophase metals studied by molecular dynamics.* Physical Review B, 1998. **58**(17): p. 11246.
18. Conrad, H. and J. Narayan, *On the grain size softening in nanocrystalline materials.* Scripta Materialia, 2000. **42**(11): p. 1025-1030.
19. Yip, S., *Nanocrystals: The strongest size.* Nature, 1998. **391**(6667): p. 532-533.
20. Yip, S., *Nanocrystalline metals: Mapping plasticity.* Nat Mater, 2004. **3**(1): p. 11-12.

21. Chokshi, A.H., et al., *On the validity of the hall-petch relationship in nanocrystalline materials.* Scripta Metallurgica, 1989. **23**(10): p. 1679-1683.
22. Schuh, C.A., T.G. Nieh, and T. Yamasaki, *Hall-Petch breakdown manifested in abrasive wear resistance of nanocrystalline nickel.* Scripta Materialia, 2002. **46**(10): p. 735-740.
23. Elsherik, A.M., et al., *Deviations from Hall-Petch Behavior in as-Prepared Nanocrystalline Nickel.* Scripta Metallurgica Et Materialia, 1992. **27**(9): p. 1185-1188.
24. Sanders, P.G., C.J. Youngdahl, and J.R. Weertman, *The strength of nanocrystalline metals with and without flaws.* Materials Science and Engineering A, 1997. **234-236**: p. 77-82.
25. Fougere, G.E., et al., *Grain-size dependent hardening and softening of nanocrystalline Cu and Pd.* Scripta Metallurgica et Materialia, 1992. **26**(12): p. 1879-1883.
26. Kumar, K.S., H. Van Swygenhoven, and S. Suresh, *Mechanical behavior of nanocrystalline metals and alloys.* Acta Materialia, 2003. **51**(19): p. 5743-5774.
27. Herr, U., et al., *Investigation of nanocrystalline iron materials by M[o-umlaut]ssbauer spectroscopy.* Applied Physics Letters, 1987. **50**(8): p. 472-474.
28. Keblinski, P., et al., *Structure of grain boundaries in nanocrystalline palladium by molecular dynamics simulation.* Scripta Materialia, 1999. **41**(6): p. 631-636.
29. Zhang, K., J.R. Weertman, and J.A. Eastman, *The influence of time, temperature, and grain size on indentation creep in high-purity nanocrystalline and ultrafine grain copper.* Applied Physics Letters, 2004. **85**(22): p. 5197-5199.
30. Erb, U., K.T. Aust, and G. Palumbo, *Nanostructured materials : processing, properties, and applications*, ed. C.C. Koch. 2007, Norwich, NY: William Andrew Pub. 760.
31. Nicolaus, M.M., H.R. Sinning, and F. Haessner, *Crystallization behaviour and generation of a nanocrystalline state from amorphous Co33Zr67.* Materials Science and Engineering A, 1992. **150**(1): p. 101-112.
32. Lu, K., J.T. Wang, and W.D. Wei, *A new method for synthesizing nanocrystalline alloys.* Journal of Applied Physics, 1991. **69**(1): p. 522-524.
33. Weertman, J.R., et al., *Structure and Mechanical Behavior of Bulk Nanocrystalline Materials.* Mrs Bulletin, 1999. **24**(2): p. 44-54.
34. Van Swygenhoven, H., P.M. Derlet, and A.G. Froseth, *Nucleation and propagation of dislocations in nanocrystalline fcc metals.* Acta Materialia, 2006. **54**(7): p. 1975-1983.
35. Haasen, P., *Plastic Deformation of Nickel Single Crystals at Low Temperatures.* Philosophical Magazine, 1958. **3**(28): p. 384-&.
36. Cahn, J.W., Y. Mishin, and A. Suzuki, *Coupling grain boundary motion to shear deformation.* Acta Materialia, 2006. **54**(19): p. 4953-4975.
37. Shan, Z., et al., *Grain Boundary-Mediated Plasticity in Nanocrystalline Nickel.* Science, 2004. **305**(5684): p. 654-657.
38. Gunther, B., A. Kumpmann, and H.D. Kunze, *Secondary recrystallization effects in nanostructured elemental metals.* Scripta Metallurgica et Materialia, 1992. **27**(7): p. 833-838.
39. Markmann, J., et al., *Microstructure evolution during rolling of inert-gas condensed palladium.* Scripta Materialia, 2003. **49**(7): p. 637-644.
40. Horvath, J., R. Birringer, and H. Gleiter, *Diffusion in nanocrystalline material.* Solid State Communications, 1987. **62**(5): p. 319-322.
41. Sanders, P.G., et al., *Creep of nanocrystalline Cu, Pd, and Al-Zr.* Nanostructured Materials, 1997. **9**(1-8): p. 433-440.

42. L. Lu, R.S., Z.W. Shan, M. Dao, K. Lu, S. Suresh, *Nano-sized twins induce high rate sensitivity of flow stress in pure copper.* Acta Materialia, 2005. **53**: p. 2169-2179.
43. Van Petegem, S., et al., *Internal and effective stresses in nanocrystalline electrodeposited Ni.* Applied Physics Letters, 2006. **89**(7).
44. Wang, Y.M., A.V. Hamza, and E. Ma, *Temperature-dependent strain rate sensitivity and activation volume of nanocrystalline Ni.* Acta Materialia, 2006. **54**(10): p. 2715-2726.
45. Dalla Torre, F., et al., *Deformation behaviour and microstructure of nanocrystalline electrodeposited and high pressure torsioned nickel.* Acta Materialia, 2005. **53**(8): p. 2337-2349.
46. Asaro, R.J. and S. Suresh, *Mechanistic models for the activation volume and rate sensitivity in metals with nanocrystalline grains and nano-scale twins.* Acta Materialia, 2005. **53**(12): p. 3369-3382.
47. Zhu, B., et al., *Transition of deformation mechanisms and its connection to grain size distribution in nanocrystalline metals.* Acta Materialia, 2005. **53**(18): p. 4825-4838.
48. Li, J.C.M., *Petch Relation and Grain Boundary Sources.* Transactions of the Metallurgical Society of Aime, 1963. **227**(1): p. 239-&.
49. Van Swygenhoven, H., et al., *Competing plastic deformation mechanisms in nanophase metals.* Physical Review B, 1999. **60**(1): p. 22.
50. Wu, X.-L. and E. Ma, *Dislocations in nanocrystalline grains.* Applied Physics Letters, 2006. **88**(23): p. 231911-3.
51. Wu, X., E. Ma, and Y. Zhu, *Deformation defects in nanocrystalline nickel.* Journal of Materials Science, 2007. **42**(5): p. 1427-1432.
52. Kumar, K.S., et al., *Deformation of electrodeposited nanocrystalline nickel.* Acta Materialia, 2003. **51**(2): p. 387-405.
53. Haque, M.A. and M.T.A. Saif, *Deformation mechanisms in free-standing nanoscale thin films: A quantitative in situ transmission electron microscope study.* Proceedings of the National Academy of Sciences of the United States of America, 2004. **101**(17): p. 6335-6340.
54. Haque, M.A. and M.T.A. Saif, *Thermo-mechanical properties of nano-scale freestanding aluminum films.* Thin Solid Films, 2005. **484**(1-2): p. 364-368.
55. Van Swygenhoven, H., P.M. Derlet, and A.G. Froseth, *Stacking fault energies and slip in nanocrystalline metals.* Nature Materials, 2004. **3**(6): p. 399-403.
56. Bernstein, N. and E.B. Tadmor, *Tight-binding calculations of stacking energies and twinnability in fcc metals.* Physical Review B, 2004. **69**(9): p. 094116.
57. Brandl, C., P.M. Derlet, and H. Van Swygenhoven, *General-stacking-fault energies in highly strained metallic environments: Ab initio calculations.* Physical Review B (Condensed Matter and Materials Physics), 2007. **76**(5): p. 054124-8.
58. Warner, D.H., W.A. Curtin, and S. Qu, *Rate dependence of crack-tip processes predicts twinning trends in f.c.c. metals.* Nat Mater, 2007. **6**(11): p. 876-881.
59. Wang, Y.M., et al., *Deformation twinning during nanoindentation of nanocrystalline Ta.* Applied Physics Letters, 2005. **86**(10): p. 101915-3.
60. Ebrahimi, F. and H. Li, *The effect of annealing on deformation and fracture of a nanocrystalline fcc metal.* Journal of Materials Science, 2007. **42**(5): p. 1444-1454.
61. Hasnaoui, A., H. Van Swygenhoven, and P.M. Derlet, *Cooperative processes during plastic deformation in nanocrystalline fcc metals: A molecular dynamics simulation.* Physical Review B, 2002. **66**(18): p. 184112.

62. Mishin, Y., et al., *Stick-slip behavior of grain boundaries studied by accelerated molecular dynamics.* Physical Review B (Condensed Matter and Materials Physics), 2007. **75**(22): p. 224101-7.
63. Chen, M. and X. Yan, *Comment on "Grain Boundary-Mediated Plasticity in Nanocrystalline Nickel".* Science, 2005. **308**(5720): p. 356c-.
64. Weissmuller, J., J. Loffler, and M. Kleber, *Atomic structure of nanocrystalline metals studied by diffraction techniques and EXAFS.* Nanostructured Materials, 1995. **6**(1-4): p. 105-114.
65. Haber, J.A. and W.E. Buhro, *Kinetic Instability of Nanocrystalline Aluminum Prepared by Chemical Synthesis; Facile Room-Temperature Grain Growth.* Journal of the American Chemical Society, 1998. **120**(42): p. 10847-10855.
66. Zhang, K., J.R. Weertman, and J.A. Eastman, *Rapid stress-driven grain coarsening in nanocrystalline Cu at ambient and cryogenic temperatures.* Applied Physics Letters, 2005. **87**(6): p. 061921-3.
67. X. Z. Liao, et al., *High-pressure torsion-induced grain growth in electrodeposited nanocrystalline Ni.* Applied Physics Letters, 2006. **88**(021909).
68. Gianola, D.S., et al., *Stress-assisted discontinuous grain growth and its effect on the deformation behavior of nanocrystalline aluminum thin films.* Acta Materialia, 2006. **54**(8): p. 2253-2263.
69. Z. Budrovic, et al., *Footprints of deformation mechanisms during in situ x-ray diffraction: Nanocrystalline and ultrafine grained Ni.* Applied Physics Letters, 2005. **86**(231910).
70. Eckert, J., et al., *Structural and thermodynamic properties of nanocrystalline fcc metals prepared by mechanical attrition.* Journal of Materials Research, 1992. **7**(7): p. 1751-1761.
71. Kalkman, A.J., A.H. Verbruggen, and G.C.A.M. Janssen, *Young's modulus measurements and grain boundary sliding in free-standing thin metal films.* Applied Physics Letters, 2001. **78**(18): p. 2673-2675.
72. Baker, S.P., R.P. Vinci, and T. Arias, *Elastic and anelastic behavior of materials in small dimensions.* Mrs Bulletin, 2002. **27**(1): p. 26-29.
73. Shan, Z.W., et al., *Dislocation Dynamics in Nanocrystalline Nickel.* Physical Review Letters, 2007. **98**(9): p. 095502-4.
74. D. Caillard, J.L.M., *Thermally Activated Mechanisms in Crystal Plasticity*. Pergamon Materials Series, ed. R.W. Cahn. Vol. 8. 2003, Oxford: Elsevier. 452.
75. Spatig, P., J. Bonneville, and J.L. Martin, *A New Method for Activation Volume Measurements - Application to Ni3(Al,Hf).* Materials Science and Engineering a-Structural Materials Properties Microstructure and Processing, 1993. **167**(1-2): p. 73-79.
76. Carsley, J.E., et al., *A simple, mixtures-based model for the grain size dependence of strength in nanophase metals.* Nanostructured Materials, 1995. **5**(4): p. 441-448.
77. Wang, N., et al., *Effect of grain size on mechanical properties of nanocrystalline materials.* Acta Metallurgica et Materialia, 1995. **43**(2): p. 519-528.
78. Konstantinidis, D.A. and E.C. Aifantis, *On the "Anomalous" hardness of nanocrystalline materials.* Nanostructured Materials, 1998. **10**(7): p. 1111-1118.
79. Song, H.W., S.R. Guo, and Z.Q. Hu, *A coherent polycrystal model for the inverse Hall-Petch relation in nanocrystalline materials.* Nanostructured Materials, 1999. **11**(2): p. 203-210.

80. Meyers, M.A. and E. Ashworth, *A Model for the Effect of Grain-Size on the Yield Stress of Metals.* Philosophical Magazine a-Physics of Condensed Matter Structure Defects and Mechanical Properties, 1982. **46**(5): p. 737-759.
81. Benson, D.J., H.-H. Fu, and M.A. Meyers, *On the effect of grain size on yield stress: extension into nanocrystalline domain.* Materials Science and Engineering A, 2001. **319-321**: p. 854-861.
82. Saada, G., *Hall–Petch revisited.* Materials Science and Engineering A, 2005. **400-401**: p. 146-149.
83. Asaro, R.J., P. Krysl, and B. Kad, *Deformation mechanism transitions in nanoscale fcc metals.* Philosophical Magazine Letters, 2003. **83**(12): p. 733-743.
84. Zhu, B., et al., *Effects of grain size distribution on the mechanical response of nanocrystalline metals: Part II.* Acta Materialia, 2006. **54**(12): p. 3307-3320.
85. Budrovic, Z., *Footprints of deformation mechanisms during in-situ x-ray diffraction : nanocrystalline and ultrafine grainded materials*, in *Section de sciences et génie des matériaux*. 2006, EPFL: Lausanne. p. 133.
86. Dalla Torre, F., H. Van Swygenhoven, and M. Victoria, *Nanocrystalline electrodeposited Ni: microstructure and tensile properties.* Acta Materialia, 2002. **50**(15): p. 3957-3970.
87. Mitra, R., et al., *Effect of process variables on the structure, residual stress, and hardness of sputtered nanocrystalline nickel films.* Journal of Materials Research, 2001. **16**(4): p. 1010-1026.
88. Y. M. Wang, E.M.B., J. M. McNaney, M. Victoria, A. Caro, A. M. Hodge, R. Smith, B. Torralva, B. A. Remington, C. A. Schuh, H. Jamarkani, M. A. Meyers, *Deforming nanocrystalline nickel at ultrahigh strain rates.* Applied Physics Letters, 2006. **88**(061917).
89. Z. Budrovic, H.V.S., P. M. Derlet, S. Van Petegem, B. Schmitt, *Plastic Deformation with Reversible Peak Broadening in Nanocrystalline Nickel.* Science, 2004. **304**: p. 273-276.
90. Erb, U., *Electrodeposited nanocrystals: Synthesis, properties and industrial applications.* Nanostructured Materials, 1995. **6**(5-8): p. 533-538.
91. Tjong, S.C. and H. Chen, *Nanocrystalline materials and coatings.* Materials Science and Engineering: R: Reports, 2004. **45**(1-2): p. 1-88.
92. Koch, C.C., *Synthesis of nanostructured materials by mechanical milling: problems and opportunities.* Nanostructured Materials, 1997. **9**(1-8): p. 13-22.
93. Ebrahimi, F. and Z. Ahmed, *The effect of substrate on the microstructure and tensile properties of electrodeposited nanocrystalline nickel.* Materials Characterization, 2002. **49**(5): p. 373-379.
94. Van Petegem, S., et al., *Free volume in nanostructured Ni.* Scripta Materialia, 2003. **48**(1): p. 17-22.
95. El-Sherik, A.M. and U. Erb, *Synthesis of bulk nanocrystalline nickel by pulsed electrodeposition*, in *Journal of Materials Science*. 1995. p. 5743-5749.
96. Jang, D. and M. Atzmon, *Grain-boundary relaxation and its effect on plasticity in nanocrystalline Fe.* Journal of Applied Physics, 2006. **99**(8): p. 083504-7.
97. Dalla Torre, F., *Microstructure and mechanical properties of nanocrystalline Ni produced by three different synthesis techniques*, in *Section de physique*. 2002, EPFL: Lausanne. p. 254.
98. Valiev, R.Z., et al., *Producing bulk ultrafine-grained materials by severe plastic deformation.* Jom, 2006. **58**(4): p. 33-39.

99. Van Swygenhoven, H., et al., *Following peak profiles during elastic and plastic deformation: A synchrotron-based technique.* Review of Scientific Instruments, 2006. **77**(1).
100. Sharpe, W.N., *Murray lecture - Tensile testing at the micrometer scale: Opportunities in experimental mechanics.* Experimental Mechanics, 2003. **43**(3): p. 228-237.
101. LaVan, D. and W. Sharpe, *Tensile testing of microsamples.* Experimental Mechanics, 1999. **39**(3): p. 210-216.
102. Hemker, K.J. and W.N. Sharpe, *Microscale Characterization of Mechanical Properties.* Annual Review of Materials Research, 2007. **37**(1): p. 93-126.
103. Sharpe W.N.Jr, Dale D., and LaVan D.A., *Microspecimen Tensile Test of A533-B Steel.* ASTM STP, Small specimens test techniques, 1998. **1329**.
104. Peterson, R.E., *Stress concentration factors*. 1974: Wiley-Interscience publication. 317.
105. Sharpe, W., *The interferometric strain gage.* Experimental Mechanics, 1968. **8**(4): p. 164-170.
106. Havner, K.S., *On the onset of necking in the tensile test.* International Journal of Plasticity, 2004. **20**(4-5): p. 965-978.
107. Bronstein, I.N., et al., *Taschenbuch der Mathematik*. 2000, Thun: Harri Deutsch
108. Grabe, M., *Measurement Uncertainties in Science and Technology*. 2005: Springer. 270.
109. Gibbs, G.B., *Creep and Stress Relaxation Studies with Polycrystalline Magnesium.* Philosophical Magazine, 1966. **13**(122): p. 317-&.
110. Kalidindi, S.R., A. Abusafieh, and E. ElDanaf, *Accurate characterization of machine compliance for simple compression testing.* Experimental Mechanics, 1997. **37**(2): p. 210-215.
111. Cullity, B.D. and S.R. Stock, *Elements of X-ray diffraction*. 2001, New Jersey: Prentice Hall.
112. WARREN, B.E., *X-Ray diffraction*. Metallurgy and Materials, ed. M. Cohen. 1969: Addison-Wesley Publishing Company. 381.
113. Klug, H.P. and L.E. Alexander, *X-ray diffraction procedures*. 2 ed. 1974, New York: John Wiley & Sons.
114. Patterson, B.D., et al., *The Materials Science Beamline at the Swiss Light Source: design and realization.* Nuclear Instruments & Methods in Physics Research Section a-Accelerators Spectrometers Detectors and Associated Equipment, 2005. **540**(1): p. 42-67.
115. Schmitt, B., et al., *Mythen detector system.* Nuclear Instruments and Methods in Physics Research Section A: Accelerators, Spectrometers, Detectors and Associated Equipment, 2003. **501**(1): p. 267-272.
116. Huber, P.J., *Robust Statistics*. Wiley Series in Probability and Statistics. 1981, New York: John Wiley & Sons.
117. Scherrer, P., Göttinger Nachrichten, 1918. **2**(98).
118. Stokes, A.R. and A.J.C. Wilson, *A method of calculating the integral breadths of Debye-Scherrer lines.* Proceedings of the Cambridge Philosophical Society, 1942. **38**: p. 313-322.
119. Williamson, G.K. and W.H. Hall, *X-ray line broadening from filed aluminium and wolfram.* Acta Metallurgica, 1953. **1**(1): p. 22-31.
120. Halder, N.C. and C.N.J. Wagner, *Separation of Particle Size and Lattice Strain in Integral Breadth Measurements.* Acta Crystallographica, 1966. **20**: p. 312-&.

121. Bertaut, F., *Signification De La Dimension Cristalline Mesuree Dapres La Largeur De Raie Debye-Scherrer.* Comptes Rendus Hebdomadaires Des Seances De L Academie Des Sciences, 1949. **228**(2): p. 187-189.
122. Warren, B.E. and B.L. Averbach, *The Effect of Cold-Work Distortion on X-Ray Patterns.* Journal of Applied Physics, 1950. **21**(6): p. 595-599.
123. Krivoglaz, M.A. and K.P. Ryaboshapka, Fizika metallov i metallovedenie, 1963. **15**: p. 18-31.
124. Wagner, C.N.J., *X-Ray Study of Low-Temperature Cold Work in Silver and Aluminum.* Acta Metallurgica, 1957. **5**(9): p. 477-482.
125. Wagner, C.N.J., *Stacking Faults by Low-Temperature Cold Work in Copper and Alpha-Brass.* Acta Metallurgica, 1957. **5**(8): p. 427-434.
126. Ungar, T. and A. Borbely, *The effect of dislocation contrast on x-ray line broadening: A new approach to line profile analysis.* Applied Physics Letters, 1996. **69**(21): p. 3173-3175.
127. Ungar, T., et al., *Dislocations, grain size and planar faults in nanostructured copper determined by high resolution X-ray diffraction and a new procedure of peak profile analysis.* Acta Materialia, 1998. **46**(10): p. 3693-3699.
128. Scardi, P. and M. Leoni, *Fourier modelling of the anisotropic line broadening of X-ray diffraction profiles due to line and plane lattice defects.* Journal of Applied Crystallography, 1999. **32**(4): p. 671-682.
129. Mittemeijer, E.J. and P. Scardi, *Diffraction Analysis of the Microstructure of Materials*. Materials Science, ed. R. Hull, et al. 2004, Berlin: Springer. 549.
130. M.K. Miller, A.C., M.G. Hetherington, G.D.W. Smith, *Atom Probe Ion Microscopy*. Monographs on the physics and chemistry of materials. 1996, OXFORD: Clarendon Press. 509.
131. Blavette, D., et al., *The tomographic atom probe: A quantitative three-dimensional nanoanalytical instrument on an atomic scale.* Review of Scientific Instruments, 1993. **64**(10): p. 2911-2919.
132. Bas, P., et al., *A General Protocol for the Reconstruction of 3d Atom-Probe Data.* Applied Surface Science, 1995. **87-8**(1-4): p. 298-304.
133. Turner, P.J., et al., *Use of a channelled image intensifier in the field-ion microscope.* Journal of Physics E: Scientific Instruments, 1969. **2**(8): p. 731-733.
134. Frenkel, D. and B. Smit, *Understanding Molecular Simulation: From Algorithms to Applications*. Computational Science, ed. D. Frenkel, et al. 1996: Academic Press, Inc. 443.
135. Voronoi, M.G., *Reserches sur les parallelloedres primitifs*. Journal für die reine und angewandte Mathematik, 1908. **134**: p. 198-287.
136. Honeycutt, J.D. and H.C. Andersen, *Molecular-Dynamics Study of Melting and Freezing of Small Lennard-Jones Clusters.* Journal of Physical Chemistry, 1987. **91**(19): p. 4950-4963.
137. Refson, K., *Moldy: a portable molecular dynamics simulation program for serial and parallel computers.* Computer Physics Communications, 2000. **126**(3): p. 310-329.
138. Mishin, Y., et al., *Interatomic potentials for Al and Ni from experimental data and ab initio calculations.* Material Research Society Symposium Proceedings, 1999. **538**: p. 535-540.
139. Parrinello, M. and A. Rahman, *Polymorphic transitions in single crystals: A new molecular dynamics method*. 1981, AIP. p. 7182-7190.

140. Cormier, J., J.M. Rickman, and T.J. Delph, *Stress calculation in atomistic simulations of perfect and imperfect solids.* Journal of Applied Physics, 2001. **89**(1): p. 99-104.
141. Wang, Y.M., et al., *Effects of annealing and impurities on tensile properties of electrodeposited nanocrystalline Ni.* Scripta Materialia, 2004. **51**(11): p. 1023-1028.
142. Klement, U., et al., *Thermal stability of nanocrystalline Ni.* Materials Science and Engineering A, 1995. **203**(1-2): p. 177-186.
143. Thuvander, M., et al., *Thermal stability of electrodeposited nanocrystalline nickel and iron-nickel alloys.* Materials Science and Technology, 2001. **17**: p. 961-970.
144. Conrad, H., *Thermally Activated Deformation of Metals.* Jom-Journal of Metals, 1964. **16**(7): p. 582-&.
145. Fitzpatrick, M.E. and A. Lodini, *Analysis of Residual Stress by Diffraction using Neutron and Synchrotron Radiation*. 2003, London: Taylor & Francis. 354.
146. Stoller, R.E. and S.J. Zinkle, *On the relationship between uniaxial yield strength and resolved shear stress in polycrystalline materials.* Journal of Nuclear Materials, 2000. **283**: p. 349-352.
147. Kruml, T., et al., *Stress reduction experiments during constant-strain-rate tests in Cu and Ge.* Philosophical Magazine Letters, 2003. **83**(11): p. 651-658.
148. Brandstetter, S., et al., *Grain coarsening during compression of bulk nanocrystalline nickel and copper.* Scripta Materialia, 2008. **58**(1): p. 61-64.
149. Frøseth A.G., Derlet P.M., and Van Swygenhoven H., *Twinning in Nanocrystalline fcc Metals.* Advanced Engineering Materials, 2005. **7**(1-2): p. 16-20.
150. Froseth, A., H. Van Swygenhoven, and P.M. Derlet, *The influence of twins on the mechanical properties of nc-Al.* Acta Materialia, 2004. **52**(8): p. 2259-2268.
151. Hasnaoui, A., H. Van Swygenhoven, and P.M. Derlet, *On non-equilibrium grain boundaries and their effect on thermal and mechanical behaviour: a molecular dynamics computer simulation.* Acta Materialia, 2002. **50**(15): p. 3927-3939.
152. Maeder, G., J.L. Lebrun, and J.M. Sprauel, *Present Possibilities for the X-Ray-Diffraction Method of Stress Measurement.* Ndt International, 1981. **14**(5): p. 235-247.
153. Allen, A.J., et al., *Neutron-Diffraction Methods for the Study of Residual-Stress Fields.* Advances in Physics, 1985. **34**(4): p. 445-473.
154. Oliver, E.C., *The Generation of internal stresses in single and two phase materials*, in *Faculty of Science and Engineering*. 2002, University of Manchester: Manchester. p. 185.
155. Oliver, E.C., M.R. Daymond, and P.J. Withers, *Interphase and intergranular stress generation in carbon steels.* Acta Materialia, 2004. **52**(7): p. 1937-1951.
156. Voigt, W., *Uber die Beziehung zwischen den beiden Elastizitatskonstanten isotroper Korper.* Wiedemann's Annalen, 1889. **38**: p. 573-587.
157. Reuss, A., *Berechnung der Fliessgrenze von Mischkristallen auf Grund der Plastizitatsbedingung fur Einkristalle.* Zeitschrift Fur Angewandte Mathematik Und Mechanik, 1929. **9**: p. 49-58.
158. Mabelly, P., et al., *Role of the internal stresses on the diffraction peak's broadening*, in *ECRS4* 1996: ENSAM Cluny p. 941.
159. Wang, Y.-D., et al., *The development of grain-orientation-dependent residual stressess in a cyclically deformed alloy.* Nat Mater, 2003. **2**(2): p. 101-106.
160. Wang, Y.-D., et al., *Grain-to-Grain Stress Interactions in an Electrodeposited Iron Coating.* Advanced Materials, 2005. **17**(10): p. 1221-1226.

161. Korsunsky, A.M., K.E. James, and M.R. Daymond, *Intergranular stresses in polycrystalline fatigue: diffraction measurement and self-consistent modelling.* Engineering Fracture Mechanics, 2004. **71**(4-6): p. 805-812.
162. Korsunsky, A.M. and K.E. James, *Intergranular stress evolution in fcc polycrystals during high cycle fatigue.* ISIS Annual Report, 2001(12180).
163. Ungar, T., et al., *The contrast factors of dislocations in cubic crystals: the dislocation model of strain anisotropy in practice.* Journal of Applied Crystallography, 1999. **32**: p. 992-1002.
164. Brandstetter, S., et al., *Williamson-Hall anisotropy in nanocrystalline metals: X-ray diffraction experiments and atomistic simulations.* Acta Materialia, 2008. **56**(2): p. 165-176.
165. Ungar, T., A. Revesz, and A. Borbely, *Dislocations and grain size in electrodeposited nanocrystalline Ni determined by the modified Williamson-Hall and Warren-Averbach procedures.* Journal of Applied Crystallography, 1998. **31**: p. 554-558.
166. Fantozzi, G., et al., *Internal-Friction and Microdeformation Due to the Intrinsic-Properties of Dislocations - the Bordoni Relaxation.* Progress in Materials Science, 1982. **27**(3-4): p. 311-451.
167. Brandstetter, S., et al., *From micro- to macroplasticity.* Advanced Materials, 2006. **18**(12): p. 1545-+.
168. *In Standard Test Methods for Tension Testing of Metallic Materials [Metric]*. American Society for Testing and Materials, originally approved in 1924. **PA 2004**(Designation ASTM E 8M-04).
169. Youssef, K.M., et al., *Ultratough nanocrystalline copper with a narrow grain size distribution.* Applied Physics Letters, 2004. **85**(6): p. 929-931.
170. Argon, A.S., *Strengthening Mechanisms in Crystal Plasticity*. Oxford series on materials modeling, ed. A.P.F. Sutton and E.R. Rudd. Vol. 4. 2008, Oxford: Oxford University Press.
171. Haasen, P., *Physical Metallurgy*. 1996, Melbourne: Camerbridge University Press.
172. Kaur, I., Y. Mishin, and W. Gust, *Fundamentals of Grain and Interphase Boundary Diffusion*. 1995, Chichester, West Sussex: Wiley.
173. Purja Pun, G.P. and Y. Mishin, *A molecular dynamics study of self-diffusion in the core of a screw dislocation in Al.* Defect and Diffusion 2007. **266**: p. 49-62.
174. Legros, M., et al., *Observation of Giant Diffusivity Along Dislocation Cores.* Science, 2008. **319**(5870): p. 1646-1649.
175. Huang, X., N. Hansen, and N. Tsuji, *Hardening by Annealing and Softening by Deformation in Nanostructured Metals.* Science, 2006. **312**(5771): p. 249-251.
176. Brandstetter, S., et al., *Temperature-dependent residual broadening of x-ray diffraction spectra in nanocrystalline plasticity.* Applied Physics Letters, 2005. **87**(23).
177. Clausen, B., *Characterisation of Polycrystal Deformation by Numerical Modelling and Neutron Diffraction Measuremnts*, in *Materials Research Department*. 1997, Technical University of Denmark: Roskilde. p. 85.
178. Marschall, C.W. and R.E. Maringer, *Dimensional instability*. International series on materials science and technology. 1977, Oxford: Pergamon Press.
179. Rajagopalan, J., J.H. Han, and M.T.A. Saif, *Plastic Deformation Recovery in Freestanding Nanocrystalline Aluminum and Gold Thin Films.* Science, 2007. **315**(5820): p. 1831-1834.

180. Yang, B., et al., *Strain effects on the coarsening and softening of electrodeposited nanocrystalline Ni subjected to high pressure torsion.* Scripta Materialia, 2008. **58**(9): p. 790-793.
181. Conrad, H. *High-strength materials : proceedings of the Second Berkeley International Materials Conference*. in *High-Strength Materials - Present Status and Anticipated Developments*. 1965. University of California, Berkeley: Wiley.
182. Evans, A.G. and R.D. Rawlings, *Thermally Activated Deformation of Crystalline Materials.* Physica Status Solidi, 1969. **34**(1): p. 9-&.
183. Elsener, A., et al., *A local chemical potential approach within the variable charge method formalism.* Modelling and Simulation in Materials Science and Engineering, 2008. **16**(2): p. 025006.
184. Seeger, A., et al., *Work-Hardening and Work-Softening of Face-Centred Cubic Metal Crystals.* Philosophical Magazine, 1957. **2**(15): p. 323-&.
185. Li, J.C.M., *Dislocation Dynamics in Deformation and Recovery.* Canadian Journal of Physics, 1967. **45**(2P2): p. 493-&.
186. Dalla Torre, F.H., E.V. Pereloma, and C.H.J. Davies, *Strain hardening behaviour and deformation kinetics of Cu deformed by equal channel angular extrusion from 1 to 16 passes.* Acta Materialia, 2006. **54**(4): p. 1135-1146.
187. Kruml, T., O. Coddet, and J.L. Martin, *About the determination of the thermal and athermal stress components from stress-relaxation experiments.* Acta Materialia, 2008. **56**(3): p. 333-340.
188. Mills, M.J., J.C. Gibeling, and W.D. Nix, *A dislocation loop model for creep of solid solutions based on the steady state and transient creep properties of Al-5.5 at.% Mg.* Acta Metallurgica, 1985. **33**(8): p. 1503-1514.
189. Milicka, K., *Creep behaviour of long range ordered Cu50Zn alloy.* Acta Materialia, 1999. **47**(6): p. 1831-1843.
190. Blum, W. and A. Finkel, *New technique for evaluating long range internal back stresses.* Acta Metallurgica, 1982. **30**(8): p. 1705-1715.
191. Orowan, E., *Problems of plastic gliding.* Proceedings of the Physical Society, 1940. **52**: p. 8-22.
192. Zacharias, J., *The temperature dependence of Young's modulus for nickel.* Physical Review, 1933. **44**(2): p. 116-122.
193. Farraro, R. and R.B. McLellan, *Temperature-Dependence of Youngs Modulus and Shear Modulus of Pure Nickel, Platinum, and Molybdenum.* Metallurgical Transactions a-Physical Metallurgy and Materials Science, 1977. **8**(10): p. 1563-1565.
194. Schoeck, G., *Activation Energy of Dislocation Movement.* Physica Status Solidi, 1965. **8**(2): p. 499-&.
195. Cagnon, M., *Role of Entropy in Thermally Activated Deformation - Application of Study of Irradiation Hardening in Lif.* Philosophical Magazine, 1971. **24**(192): p. 1465-&.

List of Publications

Work included in this dissertation has been presented in the following publications:

S. Brandstetter, Z. Budrovic, S. Van Petegem, B. Schmitt, E. Stergar, P. M. Derlet, and H. Van Swygenhoven, Temperature-dependent residual broadening of X-ray diffraction spectra in nanocrystalline plasticity, Applied Physics Letters 87 (23) (2005).

S. Brandstetter, H. Van Swygenhoven, S. Van Petegem, B. Schmitt, R. Maaß, and P. M. Derlet, From micro- to macroplasticity, Advanced Materials 18 (12), 1545 (2006).

S. Brandstetter, P. M. Derlet, S. Van Petegem, H. Van Swygenhoven, Williamson-Hall anisotropy in nanocrystalline metals: X-ray diffraction experiments and atomistic simulations, Acta Materialia 56 (2008) 165.

S. Brandstetter, K. Zhang, A. Escuadro, J.R. Weertman, H. Van Swygenhoven, Grain coarsening during compression of bulk nanocrystalline nickel and copper, Scripta Materialia 58 (2008) 61

S. Van Petegem, **S. Brandstetter**, H. Van Swygenhoven, and J. L. Martin, Internal and effective stresses in nanocrystalline electrodeposited Ni, Applied Physics Letters 89, 073102 (2006).

H. Van Swygenhoven, B. Schmitt, P. M. Derlet, S. Van Petegem, A. Cervellino, Z. Budrovic, **S. Brandstetter**, A. Bollhalder, andM. Schild, Following peak profiles during elastic and plastic deformation: A synchrotronbased technique, Review of Scientific Instruments 77 (1) (2006).

Acknowledgements

At first, I would like to thank my supervisor Prof. Helena Van Swygenhoven for here guidance and constant encouragement in this work over the last years. I am grateful to her for showing me the amazing secrets of scientific work and for the exposure to international research. I thank Prof. A. Mortensen, Prof. G. Saada and Prof. R. Pippan for reading this thesis and for their presence in the Examination Committee, and Prof. H. Hofmann for presiding the Exam Committee.

Steven Van Petegem and Peter Derlet have helped me throughout the time of my PhD thesis and so contributed substantially to my scientific education, for which I am sincerely thankful. From my colleagues Zeljka Budrovic, Robert Maaß, Christian Brandl, Andreas Elsener, Erik Bitzek, Samuele Chiesa, and Anders Froseth I have learnt everything else I needed in order to fulfill my PhD studies. Xavier Sauvage from Rouen, France, I would like to thank for his help with the Atomic Probe and Danièle Laub for all her help in the Lab whenever I needed it in Lausanne, Switzerland. Jean-Luc Martin from the EPFL I would like to thank for his scientific expertise he so willingly shared. A special thank you goes to Erika Menamkat whose presence at the EPFL allowed a smooth communication with the Administration. The people from the Material Science Beamline at the SLS have always been willing to help, not only during beamtimes. I would particularly like to thank Bernd Schmitt for his readiness to make sacrifices. The experience of all the Technical Staff at PSI has been crucial in the development of the equipment needed for my experiment. In particularly I would like to thank Alex Bollhalder and Marcel Schild. From the ASQ group at PSI I would like to greatly acknowledge Gabriel Frei who helped every time I had any computer request and I am extremely grateful to our wonderful secretary Renate Bercher.

I owe a huge thanks to all my friends in Switzerland. Especially I would like to thank Ana, for the color and salt you brought to my life. The reason why I was able to reach this point was through the absolute support from my parents during my whole life. Thanks!

Curriculum Vitae

Name	Stefan Brandstetter	
Date of birth	27th of June, 1977	
Place of birth	Wiener Neustadt, Austria	
School	1983-1987	Elementary school, Pernitz, Austria
	1987-1991	Secondary school, Pernitz, Austria
	1991-1996	High school, Technical high school for electronics, Wiener Neustadt, Austria
Military service	1996-1997	Wiener Neustadt, Austria
Higher Education	1997-2003	M.Sc Materials Science, University of Leoben, Austria
	2000–2001	Exchange Student, University of Luleå, Sweden
	since 2004	PhD candidate at the Ecole Polytechnique Fédérale de Lausanne, working at the Paul Scherrer Institute, Switzerland
Publications	[43, 68, 99, 148, 164, 167, 176]	